

SEISMIC ANISOTROPY AND ITS IMPLICATIONS FOR THE FORMATION AND
EVOLUTION OF CRATONS

by

XIAORAN CHEN

A Dissertation submitted to the

School of Graduate Studies

Rutgers, The State University of New Jersey

In partial fulfillment of the requirements

For the degree of

Doctor of Philosophy

Graduate Program in Earth and Planetary Sciences

Written under the direction of

Vadim Levin

And approved by

New Brunswick, New Jersey

OCTOBER, 2020

ABSTRACT OF THE DISSERTATION

Seismic Anisotropy and Its Implications for the Formation and Evolution of Cratons

by

XIAORAN CHEN

Dissertation Director:

Vadim Levin

My research focuses on understanding seismic anisotropy from the perspective of theoretical development and exploring the upper mantle anisotropic structures beneath the Superior craton and the Yilgarn craton to set constraints to the craton formation processes. In Chapter I, I performed shear wave splitting measurements to explore the anisotropic structure in the upper mantle in Eastern North America. For Chapter II, I did theoretical development and built up a Matlab package to predict the seismic body wave propagation through horizontally stratified anisotropic media using the most general parameterization of the elastic tensor. Based on that package, I was able to explore the S-P and P-S conversions at the anisotropic boundaries and shear wave splitting in a medium composed of pure olivine. Chapter III is built up on the first two chapters, where I included part of the data analysis results from Chapter I and adopted the Matlab code package from Chapter II. Thus, I am able to carry out a comparative study between the Superior craton in North America and the Yilgarn craton in West Australia using a combination of two different groups of techniques and figure out the implications for the craton formation process.

For the array from James Bay to Fundy Basin in eastern North America, I find the fast polarizations concentrate between N60°E and N90°E with an average of N80°E and change systematically with backazimuth. In addition, I observed a lateral increase in delay time from 0.56 ± 0.25 s at the NW end of the array to 0.90 ± 0.41 s at the SE end. The location of lateral change in delay time does not match geological boundaries on the surface but seems to match the geophysical boundary at depth of 160 km. I interpret this boundary in splitting values to be the edge of cratonic lithosphere at depth. The observations suggest that the anisotropic structure beneath my study area is complex and possibly both multilayered and laterally variable.

Based on a comparative study between the Superior craton and Yilgarn craton, I find that the cratonic lithospheres at both cratons are not homogenous domains, instead, they are different from site to site within the same cratons. At all the sites in both cratons, I find there are back azimuthal variations of the fast polarizations and NULL measurements from nearly all the back azimuths where the measurements are made. Besides, I can identify multiple anisotropic boundaries in the lithosphere at all the sites in both cratons, most of which are mainly above ~ 100 km with the rest between 120 km and 160 km. However, no consistent anisotropic patterns are observed between two cratons. Thus, I consider cratons are different from each other and each craton is composed of different building blocks. Before building blocks came together, they were far apart and went through different kinds of tectonic evolution, through which they obtained different anisotropic fabrics. After this, those building blocks came together to form the craton. After the formation of the craton, the anisotropic fabrics got preserved in the lithosphere without further modification. Thus,

different fabrics preserved in the craton now are actually those obtained before the formation of the current craton.

DEDICATION

To my parents, Jingbin Chen and Zanhong Wang, for their love and support,
to my sister, Jie Chen and her husband Zhaojie Wang, for their encouragement,
and to my lovely nephew, Xiuhao Wang, for bringing happiness into our family.

ACKNOWLEDGMENTS

First of all, I would like to thank my advisor Vadim Levin, who offered me this great chance five years ago to start my graduate study in the Department of Earth and Planetary Sciences at Rutgers University, the State University of New Jersey. He is a great advisor who provides students with different opportunities, and fully supports them through their academic journey. Moreover, he not only cares about the students' research but also their life and career path. Thus, I am truly thankful for his complete support, advices and his valuable time throughout my study.

I would also like to thank all my other committee members, G. Mountain, S. Tikoo-Schantz and J. Park for their time and providing me with very helpful suggestions and encouragements, especially during the early stages of my PhD study. I especially thank J. Park for helping me solve all my confusions about the reflectivity algorithm and providing me with valuable suggestions to my second chapter. I would also like to thank G. Mountain for helping me understand the knowledge I was not familiar with in Marine Geology, and providing support and suggestions to my dissertation. Moreover, I feel very grateful to S. Tikoo-Schantz for encouraging me before my qualifying exam and very kindly introducing me to potential post-doc advisor in Stanford. I also would like to thank H. Yuan for hosting me during a short-term research in the University of Western Australia, and for providing access to his dataset, as well as advises on both my research and life. In addition, I would like to thank Y. Li for her help in co-developing a standard rule for the shear wave analysis, which is very important for both my first and third chapter, as well as for her support. Then, I want to thank M. Klaser for his help in requesting and archiving the dataset from the

Canadian sites, as well as for his work that inspired the ideas in my last chapter. Lastly, I would like to thank IRIS PASSCAL and DMC for providing data for this dissertation.

I am also very grateful to all members of the Department of Earth and Planetary Sciences for their help and support during my graduate study at Rutgers University. I would like to thank K. Miller, J. Wright, J. Gross, C. Herzberg and J. Browning for their help and suggestions throughout my PhD study. I would especially like to thank members in the seismology research group: B. Dunham, Z. Xie, J. Bourke, A. Servali, A. Razi, M. Klaser for their good advice and help.

I also would like to thank my friends and fellow graduate students in the EPS. Many thanks go to M. Needle, J. Setera, C. Sequeira, W. Si, M. Yu, M. Makarova, J. Stanley and L. Podrecca. In addition, many thanks to Y. Cai, X. Li, X. Huang, K. Ren and Z. Zhang for their help and support, especially during the time of pandemic. At the same time, I would like to thank our staff members, A. Pavlis, J. Pappas, K. Myers, W. Rodriguez and T. Rufus, for helping me solve administrative issues patiently and efficiently.

Above all, I want to thank my family for their love and support in me while doing a graduate study in the United States. For my parents, I feel very grateful that they have respected my choices and encouraged me to explore my own career path. For my sister's family, they have been very helpful to me in dealing with both my professional and private issues. Specially for my lovely nephew, we are all so happy to have you in the family.

Finally, I gratefully acknowledge the funding sources that made my PhD research possible. This dissertation was supported by fellowship from the Graduate School of Rutgers University, TA/RA assistantship and Off-Campus Dissertation Professional Development award.

PREFACE

The formation of continents is a distinct aspect of the Earth's planetary evolution compared to other rocky planets in the Solar System. Different from the oceanic lithosphere which is much simpler and younger, the continental lithosphere is more complicated and composed of different pieces of different ages, thus it preserves the records of the deformation processes that used to shape the Earth during different stages. Seismic anisotropy is the dependence of seismic wave velocity on direction of propagation. Systematic rock deformation in the upper mantle leads to anisotropy in seismic properties. Seismic anisotropy can thus be used as a proxy for the deformation process within the Earth and it resides both in the lithosphere and the asthenosphere. Seismic anisotropy can lead to splitting in shear waves. Observation and interpretation of shear wave splitting is one of the most widely adopted methods for the study of seismic anisotropy. When a shear wave propagates through an anisotropic medium, it will split into two orthogonally polarized components traveling at different velocities. As they propagate, a delay time between the fast and the slow components will accumulate, in proportion to the length of their path, as well as the strength of anisotropy of the medium.

In Chapter 1 of this thesis, I performed shear wave splitting measurements along a linear array extending from James Bay in Quebec to the Fundy basin in Maine. This array went through the major tectonic regions in eastern North America, including the part of the oldest Superior craton (more than 2.7 Ga), the Grenville Province (~1.0 Ga) and the youngest Appalachians (~0.4 Ga). For the shear wave splitting results, I observed that the delay times at the sites in the Superior craton are much smaller compared to the much

younger areas crossed by the array which are around only half of the global average of ~ 1s.

Observations performed in Chapter 1 also reveal a complicated anisotropic structure beneath the eastern North America. The ability to simulate seismic wave propagation through anisotropic media is thus necessary in order to have a better understanding of the real observations. Existing forward modelling packages either require extensive computational resources or rely on older computer languages and are thus hard to maintain. In Chapter 2, I simulated seismic wave propagation through anisotropic media using a reflectivity algorithm. Compared to others, this algorithm does not put a heavy load on the computational resources, computes seismograms with relatively high frequencies, and does not require knowing the source function of the seismic wave. Moreover, this new code is developed in Matlab, ensuring it will be easier to share with others. Called ANIMATIVITY (Anisotropic Matlab Reflectivity), it can accept different parameterizations of anisotropic medium, from the most general 81-component tensor to the Backus Notation that uses only 5 parameters for special cases. Applications of ANIMATIVITY has enabled me to understand seismic body wave conversions at the anisotropic boundaries (both P to S and S to P) and shear wave splitting in more detail.

Cratons are large domains of the continental crust which experienced little internal deformation and maintained long-term stability since their formation during the Archean epoch. Nearly all continents contain cratons that are composed of numerous different terranes formed in relatively early stages in the Earth's history. Different from the oceanic regions which are created and then recycled back into the interior of the Earth, cratons have existed on Earth for over 3 Ga. Their long-term stability makes them the only places on

Earth that potentially keep the geological records from the first half of the Earth's existence. The weak anisotropy observed in the Superior craton motivated me to explore if this is a common feature among different cratons and what it suggests about the possible mechanisms of craton formation. The Yilgarn craton in Western Australia has never been in contact with the Superior craton, which makes them a good pair for comparative studies. In Chapter 3, I investigated their anisotropic structure by combining shear wave splitting techniques and receiver function analysis, which is a method sensitive to the abrupt changes in seismic properties at depth, and discussed the corresponding implications for the craton formation process.

Chapter 1

For the first Chapter, working with Y. Li and V. Levin, I performed shear wave splitting measurements using observations of core-refracted waves recorded by a ~1,300-km-long array extending from James Bay in Quebec to the Fundy basin in Maine, with lateral spacing of 10–100 km between instruments. The object of this project is to understand the anisotropic structure of the upper mantle beneath this study area. The instruments had a relatively close spacing making it possible to associate anisotropic properties at depth with geological boundaries on the surface.

V. Levin and previous students in Rutgers Seismology Lab M. Klaser, A. Servali and B. Dunham did a tremendous amount of field work operating the seismic array during 2013 – 2015. M. Klaser also helped request seismic records from the permanent sites of the Canadian network that were integrated in the temporary array. Y. Li helped me carry out the shear wave splitting measurements on the dataset and together we developed a set

of standard rules of measuring the shear wave splitting and identifying NULL measurements.

My contribution to this chapter included dataset processing, carrying out shear wave splitting measurements on the whole dataset, interpreting the observations and comparing them with other geological and geophysical measurements. I examined seismograms recorded at 64 seismic stations, including both permanent and temporary observatories. The starting dataset included 662 station-event records (some records contain more than one core-refracted phase) from 24 different earthquakes from 2012 to 2015 ($M_w > 6.8$) at distances 90° to 150° away from the study area.

I found that the fast polarizations concentrate between $N60^\circ E$ and $N90^\circ E$ with an average of $N70^\circ E$ and change systematically with backazimuth almost everywhere along the line. The average of the fast polarizations is close to the direction of Absolute Plate Motion. In addition, I observed a lateral increase in splitting delay time from ~ 0.5 s in the older part of the study region (the Superior craton) to ~ 0.90 s in the much younger Appalachian orogen. The location of lateral change in delay time does not match geological boundaries on the surface but seems to match the geophysical boundary (a change in seismic velocity) at depth of 160 km. I interpreted this boundary in splitting values represent the edge of cratonic lithosphere at depth. In addition to the broad regional pattern in splitting delay values, observations at individual locations suggest that the anisotropic structure beneath our study area is laterally variable on a relatively small lateral scale, and likely multilayered.

This chapter has resulted in one published paper:

- **Chen, X.,** Li, Y., & Levin, V. (2018). Shear wave splitting beneath eastern North American continent: evidence for a multilayered and laterally variable anisotropic structure. *Geochemistry, Geophysics, Geosystems*, 19(8), 2857-2871.

Chapter 2

In this chapter, working with J. Park and V. Levin, I used computer modeling of seismograms to understand how the anisotropic structure of the medium influences the seismic waveforms. This forward modelling development focuses on simulating seismic wave propagation through anisotropic media with different types of parameterizations using a reflectivity algorithm, which finally led to a code distribution ANIMATIVITY (ANIsotropic MATlab reflectIVITY). Moreover, I also provided a detailed documentation of a theoretical basis for the algorithm by combining developments from previous literature.

Based on the commercial software package Matlab, the ANIMATIVITY software can compute synthetic seismograms using anisotropic models described either by a full tensor or common notations for an elastic tensor with a symmetry axis. This algorithm enables us to simulate wave propagation with high frequency components and consider all transmission and reflection coefficients in one step (thus the “reflectivity” name). I validate the ANIMATIVITY code predictions for body wave propagation in layered anisotropic media using legacy reflectivity codes, and perform a number of computational experiments that showcase its capabilities. In one example I used models with vertical gradients in anisotropic properties, finding that that features of the resulting seismic waveforms could be misconstrued as caused by dipping interfaces.

Also, I find that S-to-P converted waves have the potential to constrain anisotropy at depth via the directional variation of Sp-phase amplitude on the vertical component. Finally, ANIMATIVITY simulations of shear-wave splitting includes S-P converted waves that precede the split SKS wave.

This chapter has resulted in a manuscript ready to be submitted to Pure and Applied Geophysics:

- **Chen, X.**, Park, J., & Levin, V. Anisotropic Layering and Seismic Body Waves: Deformation Gradients, Initial S-Polarizations, and Converted-Wave Birefringence

Chapter 3

For this chapter, working with V. Levin, H. Yuan, M. Klaser and Y. Li, I carried out a comparative study between the anisotropic structures of the Superior craton in North America and the Yilgarn craton in West Australia. I adopted a combination of shear wave analysis and receiver function analysis to characterize the anisotropic structure beneath four sites in each craton.

I did an integration of three different techniques for the shear wave analysis, which includes the shear wave splitting, splitting intensity and single-layer inversion utilizing the synthetic seismogram code developed in Chapter II. These three different methods are internally connected metrics which provide a more nuanced description of the anisotropic properties beneath the sites we have studied, and make the comparisons of different locations more meaningful. In the Yilgarn craton, we examined seismic records at four permanent stations from 55 earthquakes between 2010 and 2019 with magnitudes above 6. In total, this yielded 223 measurements. In the Superior craton, we made shear wave

splitting measurements on seismograms at 3 permanent stations and 3 temporary stations. We analyzed records collected from 144 earthquakes between 2005 and 2015 with magnitudes above 5.5, which led to an overall of 263 measurements.

I also applied receiver function analysis to improve the vertical resolution. In the Yilgarn craton, we analyzed overall 1314 records, selected from earthquakes between 2008 and 2019 with magnitudes above 6, at distances 20 to 180 degrees. In the Superior craton, we used a total of 646 records collected from earthquakes with magnitudes above 5.5 between 2005 and 2019 at distances 30 to 180 degrees. I developed a systematic way to identify reliable anisotropic boundaries and to calculate their attributes, such as the orientations of the anisotropic symmetry axes, and their depths. For the shear wave splitting patterns, I compared it with the geological boundaries on the surface and the plate motion at depth. For the anisotropic boundaries, I compared them with the previous tomography studies and the vertical extent of the continental lithosphere proposed by seismic tomography and thermal models.

Combining all the observations together, I can see there are both similarities and differences between the two cratons. First, I find that the cratonic lithospheres of both regions are not homogenous domains, instead, they vary from site to site within the same craton. At all the sites in both cratons, we find there are directional variations of in shear wave splitting measurements, suggestive of vertical layering in anisotropic properties. Second, I can identify multiple anisotropic boundaries in the lithosphere at all the sites in both cratons, most of which are mainly above ~ 100 km with the rest between 120 km and 160 km. However, no consistent anisotropic boundaries or splitting patterns can be

identified for two cratons and in fact, beneath each site, the anisotropic layering and splitting pattern is different from others.

Thus, I consider a craton to be composed of different building blocks. Before building blocks came together, they were far apart and went through different kinds of tectonic evolution, through which they obtained different anisotropic fabrics. After this, those building blocks came together to form the craton. After the formation of the craton, the anisotropic fabrics got preserved in the lithosphere without further modification. Thus, different fabrics preserved in the craton now are actually those obtained before the formation of the current craton. In this sense, continents in general and specially cratons can work as records of the Earth's history of more than 3.5 Ga.

Chapter 3 is being prepared for publication and the results were reported at the 2019 AGU Fall Meeting:

- Chen, X., Li, Y., Yuan, H., & Levin, V. L. (2019). The Tale of Two Cratons: Upper Mantle Anisotropy under the Superior and West Australian Cratons. AGUFM, 2019, S43A-05.

TABLE OF CONTENTS

ABSTRACT OF THE DISSERTATION	ii
DEDICATION	v
ACKNOWLEDGMENTS	vi
PREFACE	viii
TABLE OF CONTENTS	xvi
CHAPTER 1.....	1
SHEAR WAVE SPLITTING BENEATH EASTERN NORTH AMERICAN CONTINENT: EVIDENCE FOR A MULTI-LAYERED AND Laterally VARIABLE ANISOTROPIC STRUCTURE.....	
1.1 ABSTRACT	1
1.2 INTRODUCTION	2
1.3 METHODS AND DATA	4
1.4 RESULTS	7
1.4.1 Shear wave splitting values.....	7
1.4.2 NULL measurements	11
1.4.3 Comparison with previous studies	11
1.5 DISCUSSION	14
1.5.1 Comparison with absolute plate motion (APM)	14
1.5.2 Possible thickness of the anisotropic layer.....	15
1.5.3 Evidence for more than one layer of anisotropy	16
1.5.4 Possible contribution of anisotropy from the lowermost mantle	17
1.5.5 A laterally variable anisotropic structure	18
1.5.6 Interpretation of the possible edge of the craton at depth	20
1.6 SUMMARY	21

1.7 ACKNOWLEDGMENTS	22
1.8 REFERENCES	23
1.9 FIGURE CAPTIONS.....	26
1.10 SUPPLEMENTARY FIGURE CAPTIONS	30
1.11 FIGURES	31
1.12 SUPPLEMENTARY FIGURES	39
1.13 CRITERIA FOR DATA SELECTION.....	45
CHAPTER 2.....	48
BODY WAVE PROPAGATION THROUGH HORIZONTALLY STRATIFIED ANISOTROPIC MEDIA IN DIFFERENT PARAMETERIZATIONS: SYNTHETICS AND POTENTIAL APPLICATIONS	48
2.1 ABSTRACT	48
2.2 INTRODUCTION	49
2.3 METHODOLOGY	51
2.3.1 Conventions and Model Setup	52
2.3.2 Plane Wave Propagation in Anisotropic Media.....	54
2.3.3 A Recursive Procedure for Computation	63
2.3.4 Conventions and Parameters in Fourier Transform	65
2.3.5 Other Parameterization of Anisotropy	66
2.4 APPLICATIONS	68
2.4.1 Examples of Outcome	69
2.4.2 Synthetic P-to-S Receiver Functions	69
2.4.3 Anisotropic Effects of S-to-P Conversions	74
2.4.4 Shear-wave Splitting Analysis	82
2.5 SUMMARY	84
2.6 ACKNOWLEDGMENTS	85
2.7 REFERENCES	86

2.8 FIGURE CAPTIONS.....	89
2.9 SUPPLEMENTARY FIGURE CAPTIONS	93
2.10 TABLE CAPTIONS	94
2.11 FIGURES	97
2.12 SUPPLEMENTARY FIGURES	108
2.13 TABLES	110
2.14 GLOSSARY	114
2.15 APPENDIX	118
CHAPTER 3.....	143
A COMPARATIVE STUDY OF UPPER MANTLE ANISOTROPY BETWEEN THE YILGARN CRATON AND THE SUPERIOR CRATON AND ITS IMPLICATIONS FOR THE CRATON FORMATION PROCESS.....	143
3.1 ABSTRACT	143
3.2 INTRODUCTION	144
3.3 GEOLOGICAL BACKGROUND.....	147
3.3.1 Yilgarn Craton (Western Australia).....	147
3.3.2 Superior Craton (Eastern North America)	149
3.4 METHODOLOGY AND DATA	150
3.4.1 Shear-wave Studies	150
3.4.2 Receiver Functions and their Harmonic Decomposition	158
3.5 RESULTS	168
3.5.1 Shear-Wave Studies	168
3.5.2 Receiver-function Analysis.....	181
3.5.3 Comparison between Two Cratons	193
3.6 DISCUSSION	196
3.6.1 Comparison with Previous Seismological Studies.....	196
3.6.2 Comparison with Global and Local Models	200

3.6.3 Layering of the Cratonic Lithosphere	202
3.6.4 Comparison with Geophysical Attributes and Geological Settings on the Surface.....	204
3.6.5 Possible Interpretations of the Anisotropic Structures beneath the Cratons	207
3.6.6 Anisotropic Fabrics and Mechanisms for Craton Formation Process.....	209
3.6.7 Implication for the Formation of the craton	210
3.7 SUMMARY	212
3.8 ACKNOWLEDGEMENTS	213
3.9 REFERENCE:.....	214
3.10 FIGURE CAPTIONS.....	220
3.11 SUPPLEMENTARY FIGURE CAPTIONS	229
3.12 TABLE CAPTIONS	229
3.13 FIGURES	230
3.14 SUPPLEMENTARY FIGURES	243
3.15 TABLES	245

Chapter 1

Shear wave splitting beneath eastern north American continent: evidence for a multi-layered and laterally variable anisotropic structure

This chapter has resulted in the following publication:

- Chen, X., Li, Y. & Levin, V., 2018. Shear Wave Splitting Beneath Eastern North American Continent: Evidence for a Multilayered and Laterally Variable Anisotropic Structure, 19, 2857-2871.

1.1 Abstract

Eastern North America records a tectonic history of over 3Ga in duration. Much of this record is preserved within the lithosphere, and may be unraveled by detailed studies of its interior structure. Past episodes of tectonic activity likely left their imprints in the form of anisotropy-forming rock fabric presently preserved in lithosphere of the continent. We perform shear wave splitting measurements using observations of core refracted waves collected from a ~1300 km long array extending from James Bay in Quebec to the Fundy basin in Maine, with lateral spacing of 10 ~ 100 km between instruments. Close spacing of instruments helps us associate anisotropic properties with geological boundaries. We find that the fast polarizations concentrate between N60°E and N90°E with an average of N80°E and change systematically with backazimuth. In addition, we observe a lateral increase in delay time from 0.56 ± 0.25 s at the NW end of the array to 0.90 ± 0.41 s at the SE end. The location of lateral change in delay time does not match geological boundaries on the surface but seems to match the geophysical boundary at depth of 160

km. We interpret this boundary in splitting values to be the edge of cratonic lithosphere at depth. Our observations suggest that the anisotropic structure beneath our study area is complex and possibly both multi-layered and laterally variable.

1.2 Introduction

Eastern North America contains some of the thickest lithosphere on Earth within the cratonic core of the continent, as well as the record of the two most recent Wilson cycles corresponding to the assembly and breakup of the supercontinents Rodinia and Pangea. Thus, it is an ideal place to study the formation and evolution of continents through geological time.

Seismic anisotropy, a directional dependence of seismic velocity, is a property that can be used as a proxy for deformation in the deep interior of the Earth, and thus can provide constraints on the processes of continental formation and evolution. Olivine is the most abundant mineral in the upper mantle, and it is intrinsically anisotropic (Christensen, 1984; Kumazawa & Anderson, 1969; Ribe, 1989). The orientation of its crystals will align with the strain direction when it is deformed (Zhang & Karato, 1995). Both lithosphere and asthenosphere can contribute to seismic anisotropy in the upper mantle (Silver, 1996; Vinnik et al., 1989). Thus, by developing constraints on mantle anisotropy, we can infer both the past deformation reflected by rock fabric frozen into the lithosphere, as well as the present deformation due to shearing of the asthenosphere by plate motion or mantle flow (Forte et al., 2010; Long & Becker, 2010), or a combination of both.

Our study area (Figure 1(a)) includes all major tectonic units and boundaries of eastern North America. The Superior Province is an Archean craton which has been stable since 2.8 – 2.5 Ga (Card, 1990; Percival, 2007). Tectonic subprovinces in the Superior

craton are trending nearly east to west and are surrounded by early Proterozoic orogens (Calvert & Ludden, 1999; Hoffman, 1988). The boundary between the Archean and the Proterozoic terranes, the Grenville Front was formed during the assembly of the supercontinent Rodinia between ~ 1.19 and 0.98 Ga (Hynes & Rivers, 2010; Rivers, 1997; Whitmeyer & Karlstrom, 2007). The Grenville Province is the oldest post-Archean terrane. It consists of rocks with high degree of metamorphism and includes both old Archean material and relatively younger volcanic arc material (Rivers, 2015). The Appalachians were formed by a sequence of orogenies: Taconic, Acadian-Neoacadian, and Alleghanian (Hatcher, 2010) that together resulted in the assembly of the supercontinent Pangea. Multiple tectonic boundaries can be recognized within the Appalachian Orogen, most of which separate terranes with distinct tectonic histories, such as Meguma, Gander, and Avalon (e.g. Hibbard et al., 2007). The Appalachian Front marks the boundary between the Appalachian Orogen and the Grenville Province on the surface. However, Grenville-aged rocks likely extend east of the Appalachian Front at depth, so the surface geology and deep crustal lithology of Appalachian Orogen likely do not match (Hynes & Rivers, 2010).

Although numerous previous studies have explored seismic anisotropy in the same or neighboring regions using shear wave splitting (Barruol et al., 1997; Darbyshire et al., 2015; Eaton et al., 2004; Fouch et al., 2000; Gilligan et al., 2016; Levin et al., 1999; Long et al., 2016) and surface wave inversions (Darbyshire & Lebedev, 2009; Yuan & Romanowicz, 2010), studies of anisotropy that cover the entire region (Darbyshire et al., 2015; Yuan & Romanowicz, 2010) typically lack the lateral sampling necessary to associate anisotropic structure with elements of the regional tectonic structures. In other cases, a number of studies that did have good lateral sampling (Long et al., 2016; Yang et

al., 2017) were limited to parts of the region. This makes comparison between different tectonic units difficult.

In this study, we perform shear wave splitting measurements using observations of core-refracted shear waves on a 1300 km long array crossing the eastern part of the North American continent, from James Bay to the Fundy basin (Figure 1(a)). Inter-station spacing between 10 and 100 km along this continent-scale array allows us to relate lateral variations in observed properties to specific tectonic boundaries and geological units. Having operated our instruments for 2-3 years, we have enough observations to explore likely vertical variations in anisotropic structure.

1.3 Methods and data

Shear wave splitting (Long & Silver, 2009; Silver & Chan, 1991; Vinnik et al., 1989) is one of the most widely adopted methods for the study of seismic anisotropy in the Earth. When a shear wave propagates through an anisotropic medium, it will split into two orthogonally polarized components travelling at different velocities. As they propagate, a delay time between the fast and the slow components will accumulate, in proportion to the length of their path, as well as the strength of anisotropy of the medium. Under the subcontinental upper mantle conditions, the fast polarization is expected to align with the direction of deformation (Long & Silver, 2009; Park & Levin, 2002). Core-refracted phases including SKS, SKKS, SKIKS and PKIKS (called XKS hereafter) are commonly used in this method to avoid source-side contamination of the signal (Savage, 1999). In addition, since teleseismic waves have nearly vertical travel paths beneath the receiver, shear wave splitting provides very good lateral resolution. By analyzing the estimated splitting parameters, we are able to examine lateral changes in anisotropic properties and make

comparisons between anisotropic structures at depth and tectonic divisions evident on the surface.

We adopt the SplitLab software and choose Rotation-Correlation (called RC hereafter) method (Figure 2) to estimate the shear wave splitting parameters (fast polarization and delay time). This method searches for the coordinate system where two components of the split shear wave are most similar by rotating horizontal seismograms into a sequence of test coordinate systems and comparing their pulse shapes via cross-correlation (Wüstefeld & Bokelmann, 2007). To assess the reliability of the splitting parameters we also estimate them using a Minimum Transverse Energy (called SC hereafter) method (Silver & Chan, 1991), which seeks to minimize the power of the horizontal (SH) component in the observed shear wave. We established a set of criteria concerning the splitting parameters and the quality of measurements by taking into consideration measurements from both methods. A detailed description of criteria of analysis in this study (Text S1) along with examples of measurements of different qualities (Figure S1) is provided in the supplement.

In this study, we examined seismograms recorded at 64 seismic stations, including both permanent and temporary observatories (Canadian National Seismograph Network; POLARIS stations in Quebec (<http://ds.iris.edu/mda/PO>); New England Seismic Network; USArray Transportable Array; temporary network deployed in the framework of the EarthScope project). Our starting data set included 662 station-event records (some records contain more than one XKS phase) from 24 different earthquakes from 2012 to 2015 ($M_w > 6.8$) at distances 90° to 150° away from our region (Figure 1(b)). A table listing event information is in the Supplement (Table S1). Of these, XKS phases from 13 events (yellow

in Figure 1(b)) were observed over the entire 1300 km length of our array, while the remaining 11 events yielded XKS phases for parts of the array only.

Visual inspection for the clarity of signals, low SNR traces, gaps in records or no data being recorded at all reduced the dataset to 900 records of individual XKS phases that were subsequently analyzed. To estimate splitting parameters using SplitLab, we choose time windows for the target XKS phases manually. Bandpass filters were applied depending on the signal to noise ratio (SNR) of the raw data. In this study, the lower corner of the filter was mostly 0.01 Hz or 0.02 Hz, and the upper corners varied from as low as 0.05 Hz to no filter at all. Measurements were given qualities ranked by the analyst as “good”, “fair” or “poor” on the basis of criteria such as the SNR, and the stability of measurements when filter settings or time windows were changed. For interpretation in this paper, we included the measurements of all qualities. We verified that “fair” and “poor” measurements do not show systematic differences from “good” measurements (Figure S2 and S3)). In the dataset consisting of 900 records, 639 yielded observations of splitting (Figure 2(i)) and 261 were designated as NULLs (Figure 2(ii)).

Theoretically, NULL measurements can be assigned when 1) we have an observation of a rectilinear particle motion without correction for anisotropy; 2) both RC and SC methods yield nearly zero delay times; or 3) there is no energy on transverse component before correction for anisotropy. In this study, since we combine measurements made using two methods, we adopt one more criterion in addition to the three mentioned above. According to the synthetic test by Wüstefeld and Bokelmann (2007), characteristic differences between RC and SC methods can be identified when the backazimuths are near the true fast polarization. In that case, RC method tends to yield fast polarizations with

$\pm 45^\circ$ from true fast polarization, and the delay times are close to 0. However, SC method yields a large scatter of fast polarization values, and delay values close to the maximum of the search range (3 s in our study). Levin et al. (2007) documented a similar disparity of measurement results for synthetic seismograms simulated in models with very small amount of anisotropy. Thus, in this study NULL measurements can also be identified when measurements using the two different methods yield very different answers. When applied to real data, this criterion should be considered together with three other criteria so that NULL measurements can be distinguished from those where the splitting parameters can be measured but the quality is poor.

1.4 Results

1.4.1 Shear wave splitting values

We find that evidence of splitting in XKS records can be observed at all stations along the entire length of our array. Figure 3(a) shows all shear wave splitting measurements obtained from 24 earthquakes. Fast polarizations measured along the array are similar, though not completely the same, and generally fall into a range from N50°E to N120°E. In Figure 3(c), we plot the unweighted mean fast polarization at each station. We treat the fast polarizations as scalars varying from N0°E to N180°E and calculate the arithmetic average of all fast polarizations estimated at each station using RC method. This procedure excludes NULL measurements from the average. Given the uneven distribution of sources with backazimuth (mainly West, North and East), an unweighted average of all values at a station makes implicit assumptions that directional variability is not systematic, that there is only one set of true splitting parameters, and that the scatter in the values

reflects noise in the measurements. Averaged fast polarizations do not vary significantly from station to station (Figure 3(c)), however systematic differences may be seen between sections of the linear array. Stations in the NW half of the array have mean fast polarizations generally close to E-W. This is most clear at the stations in the Superior Province. For stations in the SE half of the array, fast polarizations are close to N80°E.

At each station, fast polarizations measured from different earthquakes are not consistent with each other, but vary from event to event. To better show that fast polarizations at each station will change according to backazimuths of incoming rays, we plot splitting patterns for individual earthquakes in Figures 4(a)-(d). Splitting patterns for all 24 earthquakes can be found in Figure S2. We select 4 XKS phases that come from 4 earthquakes of different directions and that were observed at most of the stations along the array. In Figure 4(a), event 2013.321 has a backazimuth of N167°E, and the fast polarizations at stations along the transect are ~N125°E. In Figure 4(b), event 2014.202 has a backazimuth of N269°E. Fast polarizations measured from this event are not very consistent: most stations yield fast polarizations N30°E~N70°E with a few others yield ~N-45°E. Figure 4(c) shows measurements from event 2015.150 with a backazimuth of N330°E. Most fast polarizations are ~N100°E. In Figure 4(d), fast polarizations measured from event 2014.043 with a backazimuth of N21°E are ~N65°E. We thus find a systematic change in fast polarizations with backazimuth. Specifically, shear waves arriving from the south and the NW show similar splitting patterns, while arrivals from west and NE produce significantly different ones.

A significant change in the values of the splitting delay times can be observed along the array. We find a lateral increase in delay times from the NW end of the array to the SE

end. This can be seen in the individual splitting values measured from all events (Figures 3(a)-(b)). In Figure 3(a), we find that delay times measured at the stations in the NW part of the array are generally close to ~ 0.5 s. Moving toward to the SE along the line, delay times start to increase to ~ 1 s, then decrease to ~ 0.5 s in a relatively narrow area in the Grenville Province north of the Appalachian Front. Stations in the SE section of the array tend to have larger delay times of over 1 s, except for the circled area in Figure 3(b) where delay times are less than 1 s but still larger than those measured in the NW half of the array. It is also noticeable that the delay times measured at stations close to the coast are much larger than along the rest of the array, reaching values of 1.5 s.

To examine the lateral change in delay times in detail, we average the measurements at individual stations, as shown in Figure 3(c), and estimate their standard deviations (Figure 5). As was done previously with fast polarizations, we average all delays irrespective of the direction of wave propagation, making the implicit assumption of a single uniform source of splitting. However, in Figures 3(a)-(b) and Figure S3, we notice that delay times at many sites vary according to backazimuth. Moreover, for certain stations we only have a few measurements. And as a result, relatively large error bars are not surprising. While this limits our ability to tell how statistically different delay times are at individual stations, it is not contradictory to our general observation that there is a lateral increase in both the mean delay value and the size of the error bar from the NW end of the array to the SE end (Figure 5). We only use averaged delay values in the following discussion.

In Figure 5, delay times measured at stations between 0 ~ 600 km along the transect (corresponding to the NW half of the array) are generally consistent and have an average

of ~ 0.5 s. From ~ 600 km to ~ 790 km (corresponding to the circled area in Figure 3(a)), delay times increase southward, reaching ~ 1 s at 700 km along the transect, and then decrease to ~ 0.5 s at 790 km. From ~ 790 km southward (corresponding to the SE section of the array), delay times increase once again. In this part, delay times separate into two trends. One trend of the delay times is ~ 1 s to ~ 1.2 s, whereas the other trend of delay times is ~ 0.5 s to ~ 0.8 s. Delay times measured in the circled area in Figure 3(b) are marked with the cyan diamonds in Figure 5 and they correspond to the trend of delay times varying from 0.5 s to 0.8 s. Here we divide the splitting values based both on delay times measured from individual events before averaging, and the mean values after unweighted averaging. The exact location where this lateral change happens is hard to identify. In Figure 3(a) we identify a region where the delay times appear to vary from site to site, not forming a clear trend. We present statistics of delay times in these three sections in detail in the Discussion section.

We can also observe the lateral change in delay times in measurements from individual events. For each event observed over the entire length of the array, the pattern of delay times is not exactly the same as the averaged pattern, however the lateral increase in delay times is still very obvious. In Figures 6(a)-(b), the increase in delay times from NW to the SE can be seen very clearly. The nature of change in delay values with distance along the array is not always the same, and appears to be a function of event backazimuth. For example, delay times measured from event 2014.103 (Figure 6(a)) are ~ 1.0 s from array position 500 km southward, then are scattered near the Appalachian Front, and subsequently grow to nearly 2 s at the Atlantic coast. Event 2015.132 (Figure 6(b)) yields

splitting values that increase steadily from ~ 0.5 s to 1 s at the Appalachian Front, and then continue to increase to ~ 1.5 s near the coast.

1.4.2 NULL measurements

Apart from the splitting signals, NULL measurements can also be observed over the entire length of the array (Figure 7(a)). Stations in the NW half of the array tend to have more NULL measurements per station than those at the other end. We had 261 NULL measurements in total, which includes 127 NULL measurements at 18 stations in the NW half of the array and the rest 134 NULL measurements at 50 stations in the SE half of the array. If we calculate the average of NULL measurements per station, we have ~ 7 NULL measurements per station in the NW, and less than 3 NULL measurements per station in the SE. This result is very well illustrated by a comparison between stations QM78 (in the NW half of array) and QM34 (in the SE half of array) shown in Figures 7(b)-(c).

We also look at the NULL measurements in individual events. In Figures 4(a)-(b), we can observe NULL measurements at most stations along the transect. Those earthquakes are from nearly south and west of our study area. We can also observe NULL measurements at stations from earthquakes that come from the north of our study area (Figures 4(c)-(d)), but those observed NULL measurements are either limited to a small region of the study area, or the number of NULL measurements are smaller compared to what we have from the earthquakes coming from the south or the west.

1.4.3 Comparison with previous studies

We compare our observations with previous studies in the neighboring areas and make a station to station comparison when possible (Table S2). Our measurements do

match the general statistics of those from previous studies (Figure 3(c)). Surveys of shear wave splitting in the southern part of our region by Long et al. (2016) measure an average fast polarization of N77°E and Yang et al. (2017) shows mostly E-W fast polarizations, with some local variations. A study by Darbyshire et al. (2015) covers approximately the same area as our study does, and reports a range of fast polarizations varying from ENE-WSW to ESE-WNW. Delay times reported in the Superior Province by Darbyshire et al. (2015) are generally less than 1 s, similar to the range we report in this study, while results for the Appalachian Orogen by Long et al. (2016) and Yang et al. (2017) are closer to 1-1.5 s on average, once again in line with our findings.

A station-to-station comparison with previous studies of splitting parameters measured from the same individual events is documented in Table S2. We first compare our measurements with those from Darbyshire et al. (2015). The averaged fast polarizations at sites measured in our study and that of Darbyshire et al. (2015) are generally within $\sim 10^\circ$. Our averages are closer to E-W. For the only event measured by both studies (2013.134) at stations LATQ and MATQ we find close matches in observed splitting values. It is worth mentioning that splitting averages at stations DMCQ and A64 included in both studies are very similar even though we use two completely different datasets without any event overlap. We do not find systematic differences in fast polarizations when comparing our results with Long et al. (2016) and Yang et al. (2017). We note that nearly all of our averaged delay times are systematically smaller than those of the other two studies. For event 2014.103, sites G64A and H66A (SKKS phase in our study) yield very close measurements between this study and Long et al. (2016) (fast polarizations: less than 3° different; delay times: less than 0.02 s different) whereas G65A yields very different

measurement especially a much larger delay time in their study of 2 s. Compared with Yang et al. (2017), we have very close matches from event 2013.271 at stations F61A, G63A and G64A (fast polarizations: less than 5° different; delay times: less than 0.1 s different), but a discrepancy at station H66A (fast polarizations: $\sim 30^\circ$ different; delay times: ~ 0.3 s different). For event 2015.132, we have close matches in fast polarizations at stations E61A, D63A, G63A and G65A (less than 5°), but the differences in delay times are around 0.1 s \sim 0.2 s. For other events, whether there are close matches or large discrepancies depends on specific stations. For instance, for event 2015.150, D61A shows large discrepancies in both splitting parameters (fast polarizations: $\sim 25^\circ$ different; delay times: 0.4 s different) whereas G63A shows close matches (fast polarizations: $\sim 7^\circ$ different; delay times: 0.1 s different).

There are several reasons for discrepancies between our study and previous studies. First, we include datasets in different time frames. Second, there is a difference in the selection of time windows, filters, and how the analysts decided whether a measurement is a NULL. Third, choices of teleseismic phases to measure are different. For instance, we include four types of XKS phases whereas Long et al. (2016) includes only the SKS phase. Even within the same event, different phases have different ray paths and thus sample different parts of Earth. Finally, different methods of measurements can lead to different results. For instance, in Long et al. (2016), only measurements for which RC and SC methods yielded close results were retained and averaged, while we use the data measured by RC method, and utilize SC method for quality assessment and for declaring NULLs. Both Darbyshire et al. (2015) and Yang et al. (2017) adopt SC method. Wüstefeld & Bokelmann (2007) show that RC method that we have adopted tends to yield relatively

smaller absolute values of delays in cases where the noise level is high. We should also note that at stations with only a few measurements, the averages are easily influenced by extreme values and thus give quite different averaged splitting values.

1.5 Discussion

1.5.1 Comparison with absolute plate motion (APM)

Observations of shear wave splitting reflect the cumulative effects of anisotropic structure along the ray path, combining effects of the lithospheric mantle, the asthenosphere and the lowermost mantle. We first compare the fast polarizations with the mantle flow patterns in the asthenosphere. While the details of the mantle flow beneath a continent may be complex (e.g., Forte et al., 2007), we can compare fast polarizations of split shear waves with the absolute plate motion (APM), which reflects the motion of the North American plate relative to the deeper part of the upper mantle. Figure 8(a) shows a histogram of fast polarizations along the entire array computed on the basis of all observations of splitting. NULL measurements are not included in this calculation.

Figure 8(a) shows that while fast polarizations measured in this study fall into a very wide range, from N0°E to N160°E, there is a single well-defined peak between N60°E to N90°E. The average value of all fast polarizations measured is N80°E. According to the NUVEL1A-HS3 model the APM in our area is N249°E, and varies by less than 10° along the array (Gripp & Gordon, 2002).

Based on the similarity between the average fast polarization and the APM in the HS3 reference frame, we conclude that the shearing of the asthenosphere is a major contributor to the seismic anisotropy in our study area.

1.5.2 Possible thickness of the anisotropic layer

To test this inference further, we also estimate the possible thickness of the anisotropic layer responsible for the observed splitting signal. Based on Helffrich (1995), the thickness of a single homogeneous horizontal anisotropic layer can be estimated as $L \cong \delta t \times V_s / dV_s$, where δt is delay time, V_s is the shear wave velocity, and dV_s is the percentage of velocity change due to anisotropy. For estimation, we use a shear wave velocity of 4.5 km/s and an average anisotropy strength of 4% (Savage, 1999), which are the representative numbers for the parameters in the subcontinental upper mantle. Average delay times for the NW and SE ends of the array are 0.56 ± 0.25 s and 0.90 ± 0.41 s, respectively. The middle section of the array has an average delay value of 0.79 ± 0.31 s. Figures 8(b)-(d) show histograms of delays within each section and specify the extent of each section. Correspondingly, the thickness of a single anisotropic layer will be 63 ± 28 km in the NW section, 89 ± 35 km in the middle section and 101 ± 46 km in the SE section.

The change in the vertical extent of the anisotropic layer from the NW to the SE is consistent with constraints on the vertical extent of the lithosphere. Under the central part of the North American craton it extends to the depths of 200 – 250 km (Gung et al., 2003; Jaupart et al., 1998; Romanowicz, 2009; Rudnick et al., 1998), while it is about 90 – 110 km at the eastern North America continental margin (Abt et al., 2010; Rychert et al., 2005; Rychert et al., 2007).

Thus, we find that first-order lateral change in the strength of the splitting signal may be explained by the laterally variable vertical extent of the asthenospheric mantle deformed by the motion of the North American plate.

1.5.3 Evidence for more than one layer of anisotropy

Fast polarization measurements forming a clear peak between N60°E to N90°E in the histogram shown in Figure 8(a) make up only 56% of all observations. While noise in the data likely impacts the values, the width of the distribution and the fact that nearly half of the measurements fall outside the main peak suggest that there should be additional contributions of anisotropy from another source besides the mantle flow in the asthenosphere.

In Figure 4, we document systematic changes of fast polarizations according to the backazimuths of the incoming rays. We can also observe such changes with backazimuths in data from events that were observed at subsets of our array. Figures 7(b)-(c) and Figure S3 illustrate values of fast polarization changes with backazimuth at individual sites. Directional dependence of splitting parameters is an expected consequence of multi-layered anisotropic structure (e.g., Silver & Savage, 1994), which means besides the anisotropic contribution from the asthenosphere, there has to be another contribution, possibly from the fossil fabrics in the lithosphere.

Apart from splitting measurements of individual events, NULL measurements also provide the evidence of a complicated anisotropic structure since our observation of NULL measurements is contradictory to the pattern predicted by a simple one-layered anisotropic model. We find NULL measurements from many directions (Figures 4 and 7), while in case of a single layer of anisotropy we expect them to concentrate at two orthogonal directions (cf. Savage, 1999), coincident with either the fast polarization or the slow polarization.

Presence of multiple (up to three) layers of seismic anisotropy has been previously proposed for this region. Yuan and Romanowicz (2010) used seismic tomography combining surface waves and SKS splitting data to argue for multiple layers of anisotropic material within the North American lithosphere. In particular, their model suggests that there are two different anisotropic layers beneath the North America craton, including the region where our array was deployed. Levin et al. (1999) analyzed shear wave splitting values in the Appalachians and built a two-layered anisotropic model by matching the observed values and the predicted ones generated by synthetic seismograms. A subsequent study by Yuan and Levin (2014) confirmed the presence of these layers using two decades of XKS observations at sites near the Atlantic coast. Other studies of shear wave splitting results in neighboring areas (e.g. Darbyshire et al., 2015; Long et al., 2016) also interpret the corresponding areas to have more than one layer of anisotropy. Thus, combining the results from previous studies, the contribution of anisotropy from the past deformation processes preserved in the lithosphere cannot be neglected.

1.5.4 Possible contribution of anisotropy from the lowermost mantle

Theoretically, anisotropy measured from shear wave splitting integrates the contribution starting from the lowermost mantle to the upper mantle. In addition to the frozen fabric in the lithosphere and the mantle flow in the asthenosphere, the anisotropic contribution from the D'' layer cannot be neglected. Since SKS and SKKS phases sample different portions of the lower mantle and similar portions of the upper mantle, the discrepancies in splitting values between these two phases measured at the same station from the same event can be interpreted as evidence for anisotropy in the D'' layer (Lynner & Long, 2014). In our study, we pick three events (Table S3) to check the anisotropy from

the lowermost mantle. For event 2014.043, we cannot identify any discrepancy between SKS and SKKS pairs. However, for event 2014.103, we find similar fast polarizations between measurements made from SKS and SKKS phases, and SKKS phase yields larger delay times from 0.2 s to 0.4 s except at QM15 and F61A. For event 2014.305, SKS and SKKS phases have similar fast polarizations but SKKS generally yields smaller delay times than SKS phase except at QM38. Thus, we conclude that while a contribution from the D'' layer is possible, we do not see a clear evidence for it in the data set we have analyzed.

1.5.5 A laterally variable anisotropic structure

Out of 24 events analyzed in this study, 13 produced XKS phases observed over the entire 1300 km length of our array (Figure 1(b)). Measurements made on the same phase exclude likely complications from different paths taken through the Earth. Lateral changes in anisotropic parameters measured from the same phase have to reflect variations in earth structure beneath our region. Comparing average measurements from 13 events to those obtained using a full dataset we confirm that the splitting values (delay values and fast directions) are very similar. The fast polarizations are N60°E to N90°E, NULL measurements are more common at the NW end of the array and an increase in delay time from the NW end to the SE end of the array is clearly manifested. Our ability to see the same behavior in individual continuously observed phases (Figure 4) and in averaged values (Figure 5) adds confidence to the lateral variations we report below.

1.5.5.1 Variation in delay time

Histograms of delay times for three sections of the array (Figures 8(b)-(d)) document significant scatter of values, especially in the SE section (790~1300 km). This

scatter can also be seen in station mean values shown in Figure 5. This relatively scattered pattern at the SE end of array is not consistent with a notion of a single source of anisotropy at depth being the smoothly flowing upper mantle material. Considering the complicated tectonic history of the Appalachians it is likely that rock fabric frozen into the lithospheric mantle varies between distinct terranes composing the orogen. It is interesting to note that there are noticeable along-strike changes in delay values in the Appalachians (Figure 3(b)). These changes in delay values over relatively short distances provide additional support for the presence of anisotropy in both the lithosphere and the asthenosphere. If the vertical extent of the anisotropic layer in the asthenosphere beneath the Appalachians is at the higher end of our estimate (over 100 km), average delays smaller than 1 s will imply a partial cancellation of its signature. The opposite scenario is also possible, with an asthenospheric contribution being amplified locally so that the average delays significantly exceed 1 s.

On the other hand, within the Superior and Grenville Provinces delay histograms show well-defined single peaks, and station averages are more uniform. Small delay values (<0.6 s) are especially common in the NW of the array, over the Archean craton.

1.5.5.2 Delay time comparison with geological settings on the surface

We compare changes in delay times along the array with the geological boundaries that can be observed on the surface. We find the smallest average delay times in the Superior Province. Delay times remain consistently small (less than 0.6 s) across the Grenville Front and through most of the Grenville Province. Delay times over 1 s appear in the Appalachians. It is also very interesting to see that though we cannot identify the exact location where the lateral change in delay time takes place, it is clear that this lateral

change in delay time does not correspond to any of the geological boundaries on the surface. In Figure 3(a), we circle the region where we identify a lateral change, and in Figure 5 we mark this section on the transect. While it is close to the Appalachian Front, it clearly is not coincident with this major tectonic boundary. The change in delay values takes place over a zone ~200 km wide (600 km to 790 km along the array) within the Grenville Province, to the northwest of the area affected by the Appalachian orogeny.

The fact that the change in the size of the splitting delay, from ~0.6 s on average to ~0.9 s on average (Figures 5 and 8) takes place over a distance of 200 km or less, is in general agreement with the rapid lateral decrease of the thickness of the continental lithosphere towards the eastern coast of North America (Artemieva, 2006; van der Lee & Nolet, 1997; Yuan et al., 2014).

1.5.6 Interpretation of the possible edge of the craton at depth

The change in delay times between 600 and 790 km along our array does not correspond to major tectonic boundaries on the surface. More generally, none of the tectonic boundaries seem to coincide with a significant change in shear wave splitting. We thus seek possible links with continental lithosphere structure at depth. In Figure 9, we compare shear wave splitting measurements with the distribution of shear wave velocity and anisotropic properties. We show values for the depth of 160 km which is within the lithosphere beneath the craton, but in the asthenosphere under the Appalachians. We plot velocity values from Yuan et al. (2014) and anisotropy values from Yuan et al. (2011).

Sites at the NW end of this array, which have smaller delay times, correspond to a relatively higher velocity area ($V_s > 4.7$ km/s, or 4% faster than the global model IASP91, (Kennett, 1991)), with very weak anisotropy. Conversely, sites at the SE end, which have

larger delay times, correspond to a relatively lower velocity area (V_s is 4.5-4.6 km/s, or within 2% of IASP91) with stronger anisotropy. As Figure 9 shows, the place where we find the change in delay time corresponds to the changes in both the shear wave velocity and the azimuthal anisotropy. The tomography model of Yuan et al., (2011) has a lateral resolution of ~500 km. Therefore, even though we can see a transition from higher velocity to lower velocity, it is hard for us to locate where the transition happens. However, because the measurements from shear wave splitting provide very good lateral resolution, they put a better constraint on the change of properties at depth. Since the lateral change in delay times agrees with both the 4.65 km/s contour of shear wave velocity and 0.25% contour of azimuthal anisotropy, we interpret this boundary to be the edge of cratonic lithosphere at the depth of 160 km.

1.6 Summary

In this paper, we present shear wave splitting measurements of core-refracted shear waves on a 1300 km long array crossing the eastern part of the North American continent from James Bay to the Fundy Basin. We compare the shear wave splitting values with the absolute plate motion direction, tectonic boundaries on the surface and geophysical boundaries at depth.

We find splitting signals at all stations of this array, with predominant fast polarizations falling between N60°E and N90°E. The close similarity between this dominant value and the direction of the absolute plate motion suggests that the deformation of the asthenosphere is the primary source of the signal we detect.

At each station, the polarizations are similar within each observed event, but are different from event to event, and a systematic change of fast polarizations can be observed

at all stations along the array. This suggests the possibility of a structure with more than one layer of anisotropy beneath our study area, in agreement with previous studies. Delay times are relatively consistent at each individual station, and increase from ~ 0.5 s in the Superior Province to ~ 1 s in the Appalachian Province. The change takes place in the Grenville Province near the Appalachian Front.

We observe a smaller delay time over a much thicker lithosphere. This finding may imply an absence of anisotropy in the old cratonic lithosphere, or alternatively an efficient cancellation of contributions from it and the underlying asthenosphere. We favor the first choice as we do not find any examples of strong splitting at our stations on the craton. In the presence of two layers with near-orthogonal anisotropy orientations we would expect to detect strong splitting from events that arrive along the symmetry axis of one of them.

The lateral change in delay times is located approximately 100 km northwest of St. Lawrence River, and does not correspond to any major geologic structures at the surface. Rather, it appears to match the boundary where the shear wave velocity and the strength of azimuth anisotropy change at the depth of 160 km, which can be interpreted as the edge of cratonic lithosphere at that depth.

Splitting results in our study area rule out the possibility of a single layer of anisotropy and suggests the anisotropic structure beneath the eastern North America to be both multi-layered and laterally variable.

1.7 Acknowledgments

This work was supported by the NSF Earthscope grant EAR-1147831 and the graduate fellowship for the first author from the Rutgers School of Graduate Studies. Aresty Undergraduate Research Assistantship for Yiran Li was instrumental for her

participation in the work. Data can be accessed at the Data Management Center (DMC) of the Incorporated Research Institutions for Seismology (IRIS) and Portable Observatories for Lithospheric Analysis and Research Investigating Seismicity (POLARIS). Figures are drafted using GMT (Wessel & Smith, 1991). We thank two anonymous reviewers for their comments and suggestions.

1.8 References

- Albuquerque Seismological Laboratory (ASL)/USGS (1994): New England Seismic Network. International Federation of Digital Seismograph Networks. Other/Seismic Network. 10.7914/SN/NE
- Barruol, G., Silver, P. G., & Vauchez, A. (1997). Seismic anisotropy in the eastern United States: deep structure of a complex continental plate. *Journal of Geophysical Research: Solid Earth*, 102(B4), 8329-8348. doi:10.1029/96JB03800
- Calvert, A. J., & Ludden, J. N. (1999). Archean continental assembly in the southeastern Superior Province of Canada. *Tectonics*, 18(3), 412-429. doi:10.1029/1999tc900006
- Card, K. D. (1990). A Review of the Superior Province of the Canadian Shield, a Product of Archean Accretion. *Precambrian research*, 48(1-2), 99-156. doi:10.1016/0301-9268(90)90059-Y
- Christensen, N. I. (1984). The magnitude, symmetry and origin of upper mantle anisotropy based on fabric analyses of ultramafic tectonites. *Geophysical Journal International*, 76(1), 89-111. doi:10.1111/j.1365-246X.1984.tb05025.x
- Darbyshire, F., Bastow, I., Forte, A., Hobbs, T., Calvel, A., Gonzalez-Monteza, A., & Schow, B. (2015). Variability and origin of seismic anisotropy across eastern Canada: Evidence from shear wave splitting measurements. *Journal of Geophysical Research: Solid Earth*, 120(12), 8404-8421. doi:10.1002/2015JB012228
- Darbyshire, F., & Lebedev, S. (2009). Rayleigh wave phase-velocity heterogeneity and multilayered azimuthal anisotropy of the Superior Craton, Ontario. *Geophysical Journal International*, 176(1), 215-234. doi:10.1111/j.1365-246X.2008.03982.x
- Eaton, D., Frederiksen, A., & Miong, S. K. (2004). Shear-wave splitting observations in the lower Great Lakes region: Evidence for regional anisotropic domains and keel-modified asthenospheric flow. *Geophysical Research Letters*, 31(7). doi:10.1029/2004GL019438
- Forte, A., Mitrovica, J., Moucha, R., Simmons, N., & Grand, S. (2007). Descent of the ancient Farallon slab drives localized mantle flow below the New Madrid seismic zone. *Geophysical Research Letters*, 34(4). doi:10.1029/2006GL027895
- Forte, A., Moucha, R., Simmons, N., Grand, S., & Mitrovica, J. (2010). Deep-mantle contributions to the surface dynamics of the North American continent. *Tectonophysics*, 481(1), 3-15. doi:10.1016/j.tecto.2009.06.010

- Fouch, M. J., Fischer, K. M., Parmentier, E., Wyssession, M. E., & Clarke, T. J. (2000). Shear wave splitting, continental keels, and patterns of mantle flow. *Journal of Geophysical Research: Solid Earth*, 105(B3), 6255-6275. doi:10.1029/1999JB900372
- Geological Survey of Canada (1989): Canadian National Seismograph Network. International Federation of Digital Seismograph Networks. Other/Seismic Network. 10.7914/SN/CN
- Gilligan, A., Bastow, I. D., Watson, E., Darbyshire, F. A., Levin, V., Menke, W., . . . Liddell, M. V. (2016). Lithospheric deformation in the Canadian Appalachians: evidence from shear wave splitting. *Geophysical Journal International*, 206(2), 1273-1280. doi:10.1093/gji/ggw207
- Gripp, A. E., & Gordon, R. G. (2002). Young tracks of hotspots and current plate velocities. *Geophysical Journal International*, 150(2), 321-361. doi:10.1046/j.1365-246X.2002.01627.x
- Hatcher, R. D. (2010). The Appalachian orogen: A brief summary. *Geological Society of America Memoirs*, 206, 1-19. doi:10.1130/2010.1206(01)
- Hibbard, J. P., Van Staal, C. R., & Rankin, D. W. (2007). A comparative analysis of pre-Silurian crustal building blocks of the northern and the southern Appalachian orogen. *American Journal of Science*, 307(1), 23-45. doi:10.2475/01.2007.02
- Hoffman, P. F. (1988). United plates of America, the birth of a craton: Early Proterozoic assembly and growth of Laurentia. *Annual Review of Earth and Planetary Sciences*, 16(1), 543-603. doi:10.1146/annurev.ea.16.050188.002551
- Hynes, A., & Rivers, T. (2010). Protracted continental collision—evidence from the Grenville Orogen This article is one of a series of papers published in this Special Issue on the theme Lithoprobe—parameters, processes, and the evolution of a continent. *Canadian Journal of Earth Sciences*, 47(5), 591-620. doi:10.1139/E10-003
- IRIS DMC (2012), Data Services Products: SWS-DBs Shear-wave splitting datasets, <https://doi.org/10.17611/DP/SWS.1>.
- IRIS Transportable Array (2003): USArray Transportable Array. International Federation of Digital Seismograph Networks. Other/Seismic Network. 10.7914/SN/TA
- Kumazawa, M., & Anderson, O. L. (1969). Elastic moduli, pressure derivatives, and temperature derivatives of single-crystal olivine and single-crystal forsterite. *JOURNAL OF GEOPHYSICAL RESEARCH*, 74(25), 5961-5972. doi:10.1029/JB074i025p05961
- Levin, V., Menke, W., & Park, J. (1999). Shear wave splitting in the Appalachians and the Urals: a case for multilayered anisotropy. *Journal of Geophysical Research: Solid Earth*, 104(B8), 17975-17993. doi:10.1029/1999JB900168
- Levin, V., Okaya, D., & Park, J. (2007). Shear wave birefringence in wedge-shaped anisotropic regions. *Geophysical Journal International*, 168(1), 275-286. doi:10.1111/j.1365-246X.2006.03224.x
- Long, & Becker, T. W. (2010). Mantle dynamics and seismic anisotropy. *Earth and Planetary Science Letters*, 297, 341-354. doi:10.1016/j.epsl.2010.06.036
- Long, Jackson, K. G., & McNamara, J. F. (2016). SKS splitting beneath Transportable Array stations in eastern North America and the signature of past lithospheric

- deformation. *Geochemistry Geophysics Geosystems*, 17(1), 2-15.
doi:10.1002/2015gc006088
- Long, & Silver, P. G. (2009). Shear wave splitting and mantle anisotropy: measurements, interpretations, and new directions. *Surveys in Geophysics*, 30(4-5), 407-461.
doi:10.1007/s10712-009-9075-1
- Lynner, C., & Long, M. D. (2014). Lowermost mantle anisotropy and deformation along the boundary of the African LLSVP. *Geophysical Research Letters*, 41(10), 3447-3454. doi:10.1002/2014GL059875
- Park, J., & Levin, V. (2002). Seismic anisotropy: tracing plate dynamics in the mantle. *Science*, 296(5567), 485-489. doi:10.1126/science.1067319
- Percival, J. (2007). *Geology and metallogeny of the Superior Province, Canada. Mineral deposits of Canada: a synthesis of major deposit-types, district metallogeny, the evolution of geological provinces, and exploration methods*, 903-928.
- Ribe, N. M. (1989). Seismic anisotropy and mantle flow. *Journal of Geophysical Research: Solid Earth*, 94(B4), 4213-4223. doi:10.1029/JB094iB04p04213
- Rivers, T. (1997). Lithotectonic elements of the Grenville Province: review and tectonic implications. *Precambrian research*, 86(3-4), 117-154. doi:10.1016/S0301-9268(97)00038-7
- Rivers, T. (2015). Tectonic Setting and Evolution of the Grenville Orogen: An Assessment of Progress Over the Last 40 Years. *Geoscience Canada*, 42(1), 77-124. doi:10.12789/geocanj.2014.41.057
- Savage, M. (1999). Seismic anisotropy and mantle deformation: what have we learned from shear wave splitting? *Reviews of Geophysics*, 37(1), 65-106.
doi:10.1029/98RG02075
- Silver. (1996). Seismic anisotropy beneath the continents: probing the depths of geology. *Annual Review of Earth and Planetary Sciences*, 24(1), 385-432.
doi:10.1146/annurev.earth.24.1.385
- Silver, & Chan, W. W. (1991). Shear-Wave Splitting and Subcontinental Mantle Deformation. *Journal of Geophysical Research-Solid Earth*, 96(B10), 16429-16454. doi:10.1029/91jb00899
- Silver, & Savage, M. K. (1994). The Interpretation of Shear-Wave Splitting Parameters In the Presence of Two Anisotropic Layers. *Geophysical Journal International*, 119(3), 949-963. doi:10.1111/j.1365-246X.1994.tb04027.x
- Vinnik, L. P., Farra, V., & Romanowicz, B. (1989). Azimuthal anisotropy in the Earth from observations of SKS at Geoscope and NARS broadband stations. *Bulletin of the Seismological Society of America*, 79(5), 1542-1558.
- Wessel, P., & Smith, W. H. F. (1991). Free software helps map and display data. *Eos, Transactions American Geophysical Union*, 72(41), 441-446.
doi:10.1029/90EO00319
- Whitmeyer, S. J., & Karlstrom, K. E. (2007). Tectonic model for the Proterozoic growth of North America. *Geosphere*, 3(4), 220-259. doi:10.1130/Ges00055.1
- William Menke, Vadim Levin, Fiona Darbyshire (2012): Deep Structure of Three Continental Sutures in Eastern North America. *International Federation of Digital Seismograph Networks. Other/Seismic Network*. 10.7914/SN/X8_2012

- Wüstefeld, A., & Bokelmann, G. (2007). Null detection in shear-wave splitting measurements. *Bulletin of the Seismological Society of America*, 97(4), 1204-1211. doi:10.1785/0120060190
- Yang, B. B., Liu, Y., Dahm, H., Liu, K. H., & Gao, S. S. (2017). Seismic azimuthal anisotropy beneath the eastern United States and its geodynamic implications. *Geophysical Research Letters*, 44(6), 2670-2678. doi:10.1002/2016GL071227
- Yuan, H., French, S., Cupillard, P., & Romanowicz, B. (2014). Lithospheric expression of geological units in central and eastern North America from full waveform tomography. *Earth and Planetary Science Letters*, 402, 176-186. doi:https://doi.org/10.1016/j.epsl.2013.11.057
- Yuan, H., & Levin, V. (2014). Stratified seismic anisotropy and the lithosphere-aesthenosphere boundary beneath eastern North America. *Journal of Geophysical Research: Solid Earth*, 119(4), 3096-3114. doi:10.1002/2013JB010785
- Yuan, H., & Romanowicz, B. (2010). Lithospheric layering in the North American craton. *Nature*, 466(7310), 1063-1068. doi:10.1038/nature09332
- Yuan, H., Romanowicz, B., Fischer, K. M., & Abt, D. (2011). 3-D shear wave radially and azimuthally anisotropic velocity model of the North American upper mantle. *Geophysical Journal International*, 184(3), 1237-1260. doi:10.1111/j.1365-246X.2010.04901.x
- Zhang, S., & Karato, S.-i. (1995). Lattice preferred orientation of olivine aggregates deformed in simple shear. *Nature*, 375(6534), 774-777. doi:10.1038/375774a0

1.9 Figure Captions

Figure 1:

(a) Map of our study area in the eastern North America: black lines with teeth show the Grenville Front (GF) and the Appalachian Front (AF), brown lines show terranes of the Appalachian Orogen. Seismic stations used in this paper are dark red. JB: James Bay; FB: Fundy Basin; SLR: St. Lawrence River. (b) Locations of 24 earthquakes (Table S1) from 2012 to 2015 with magnitudes over 6.8 used in this paper (yellow:13 earthquakes with phases observed by the entire array, blues: additional 11 earthquakes; see text for details). This map is centered on our study area.

Figure 2:

Examples of (i) a splitting measurement (at station LATQ) and (ii) a NULL measurement (at station QM76) exported from SplitLab. Plots (a)-(f) are similar in

examples (i) and (ii). (a) ENZ components of the seismogram with predicted SKS (red solid line) and Sdiff (blue solid line) phases and the time window (time duration between ‘Start’ and ‘End’ as shown in the plot) marked with two black dashed lines. (b) RTZ components of the seismogram (same convention is adopted as ENZ components). In this figure, positive radial component is pointing away from the source whereas the positive radial component in Splitlab is pointing toward the source. Same conventions are adopted both in splitting and NULL examples. (c) Fast (blue solid line) and slow (red solid line) components after correction of delay time. (RC method is adopted in this example.) (d) Radial (blue solid line) and transverse (red solid line) components after correction of strength of anisotropy. (e) Particle motions before (blue solid line) and after (red solid line) correction of anisotropy. Black line here stands for the direction of backazimuth. (f) Map of correlation coefficient.

Figure 3:

Splitting values measured from 24 earthquakes at 64 stations along the transect (red solid line). Orientations of the blue sticks show the fast polarizations and lengths of the blue sticks are proportional to measured delay times. Orange circles stand for stations that are used in this study. (a) Splitting values of all the stations. (b) An amplified plot of splitting values of the stations in the SE half of the array. Same convention is adopted for tectonic settings as in Figure 1. (c) unweighted mean splitting measurements in this study (blue sticks) plotted on the background of the mean splitting values from the observations of published studies (orange sticks). Data from previous studies acquired using a global shear-wave splitting database (IRIS DMC, 2012).

Figure 4:

Splitting values and NULL measurements along the transect for selected events. Dates (Julian Days) of different events are in the corresponding figure titles. Meanings of different sticks are the same as those in Figure 3. Green sticks stand for NULL measurements. Their directions are aligned with the backazimuths plotted starting from the stations, and lengths are chosen to be 0.5 s. Red arrows stand for ray propagation directions from different earthquakes.

Figure 5:

Unweighted mean fast polarizations and delay times plotted from NW end of the array to the SE end of the array according to the distances away from the 79W, 52N. The blue circles: mean fast polarizations; red diamonds: mean delay times. Cyan diamonds identify sites circled in Figure 3(b). In both figures, error bars are one standard deviation in each direction. Vertical grey lines, represent tectonic boundaries: GF: Grenville Front, AF: Appalachian Front. Red rectangle marks the circled area in Figure 3(a).

Figure 6:

(a) and (b) are splitting values and NULL measurements for selected events. (Conventions of (a) and (b) are the same as similar plots in Figures 3-5). (c) and (d): splitting values of fast polarization and delay time measured from two selected events. Red lines in both upper panels stand for the polarizations aligned with the backazimuths. Grey lines in both upper panels stand for the averaged fast polarizations at all events. Black triangles stand for NULL measurements. For other symbols, blue circles, red diamonds and the vertical grey lines in the lower panels follow the same convention as Figure 5.

Figure 7:

Examples of NULL measurements. (a) NULL measurements from 24 earthquakes at 64 stations along the transect (red solid line). Green sticks are aligned with backazimuths of the earthquakes (same convention as in Figure 4). Orange circles stand for stations that are used in this study. (b) Stereoplot of all splitting values and NULL measurements at QM78. (c) Stereoplot of all splitting values and NULL measurements at QM34. Stereoplots show splitting values as a function of backazimuth (positive clockwise from north) and incidence angle (positive outward from center, grid lines from 0 to 18° every 3°) of their respective rays. Red sticks stand for the splitting measurements using RC method and black circles stand for NULL measurements. Orientations of the red sticks stand for the corresponding fast polarizations and their lengths are proportional to delay times. The black stick on the right of each plot stands for 1 s delay time.

Figure 8:

Histograms of all the fast polarizations and delay times in three sections of the array. For convenience, we subtract 180° from the true APM direction and plot N69°E onto the histogram instead. (a) Histogram of all fast polarizations in the data set. The red line is the average of all fast polarizations; the black line is an average of absolute plate motion directions estimated at all stations using the HS3-NUVEL1A model and HS3 reference frame. (b) Histogram of delay times at the NW end of the array (stations from 0 km to 600 km); (c) Histogram of delay times at stations between 600 km and 790 km; (d) Histogram of delay times at the SE end of the array (stations from 790 ~ 1300 km). Both red lines mark the average delay times in the corresponding section of the array. Ranges of the transect distances used in three histograms are marked at the upper right corner of each figure.

Figure 9:

Comparison of shear wave splitting values with contours (red lines) of (a) shear wave velocity (unit is km/s) from Yuan et al. (2014) and (b) azimuthal anisotropy amplitude (unit is %) at the depth of 160 km from Yuan et al. (2011). Orientations of blue sticks which are centered at the stations represent averaged fast polarizations, while the lengths are proportional to the corresponding averaged delay times. In (a), only contours of 4.7 km/s and 4.65 km/s are shown. In (b), only contours of 0.15% and 0.25% are shown. Velocity decreases from the NW to the SE. and the strength of azimuthal anisotropy increases from the NW to the SE.

1.10 Supplementary Figure Captions

Supplementary Figure 1:

Examples of measurements of different qualities exported by SplitLab software. (a) “good” measurement (05/14/2013 at LATQ) (b) “fair” measurement (04/12/2014 at QM78) (c) “poor” measurement (03/29/2015 at QM68). The diagram in the upper left corner in each figure shows the original waveforms of radial (blue line) and transverse (red line) components and the shaded area stands for the selected window width. Black sticks stand for arrival times of different XKS phases predicted with a chosen Earth model. The diagram in the upper right corner shows the results of three measurements. The azimuth of each bar shows the fast polarization, and the length of each is proportional to the measured splitting time (green bar stands for splitting result from RC method, red bar stands for splitting result from SC method, and the blue bar stands for splitting result from EV method). There are two rows of panels in the lower part of each plot. For each row, the panels from left to right

are: 1) Fast (blue solid line) and slow (red solid line) components after correction for delay time; 2) Radial (blue solid line) and transverse (red solid line) components after correction for strength of anisotropy; 3) Particle motions before (blue solid line) and after (red solid line) correction for anisotropy. Black line here stands for the direction of back azimuth; 4) Map of correlation coefficient for RC method and map of energy for SC method.

Supplementary Figure 2:

Splitting patterns for individual events. Measurements of different qualities are colored differently. Purple sticks are good non-NULL measurements, green sticks are fair non-NULL measurements and red sticks are poor non-NULL measurements. Lengths of those sticks are proportional to the corresponding delay times. Black sticks are NULL measurements, aligned with corresponding back azimuths. Their lengths are equivalent to a delay of 0.5 s.

Supplementary Figure 3:

Splitting patterns at individual sites. Stereoplots show splitting values as a function of backazimuth (positive clockwise from north) and incidence angle (positive outward from center, grid lines from 0 to 18° every 3°) of their respective rays. Measurements of different qualities are colored differently. Conventions for non-NULL measurements are the same as in Figure S2. Black circles are NULL measurements. The vertical black stick at right in each plot stands for 1s delay time.

1.11 Figures

Figure 1:

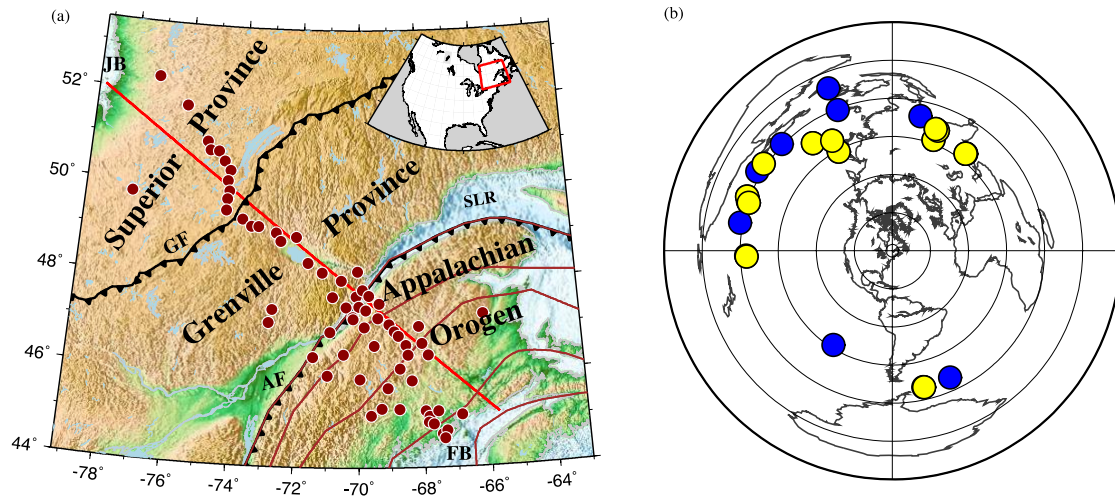


Figure 2:

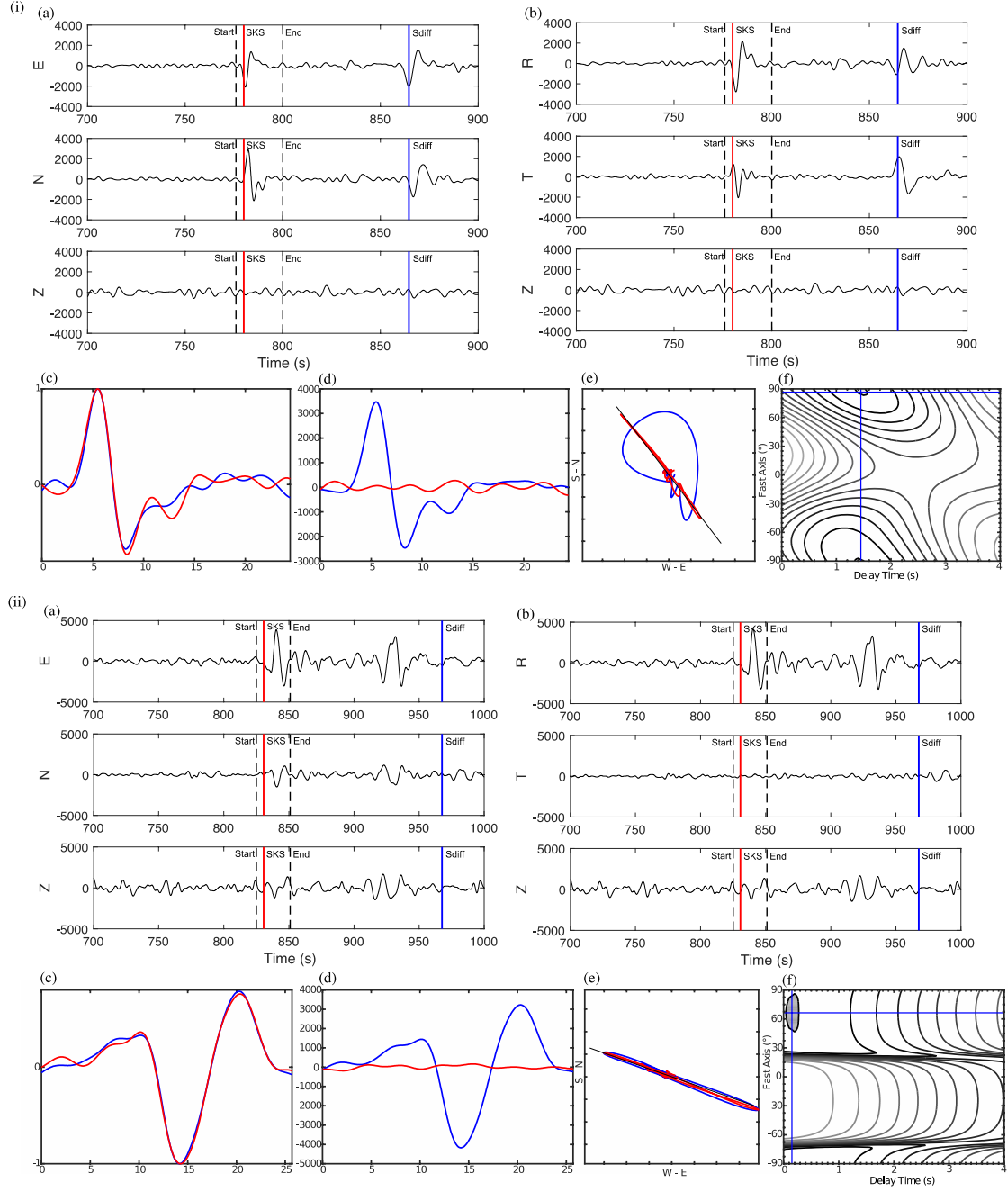


Figure 3:

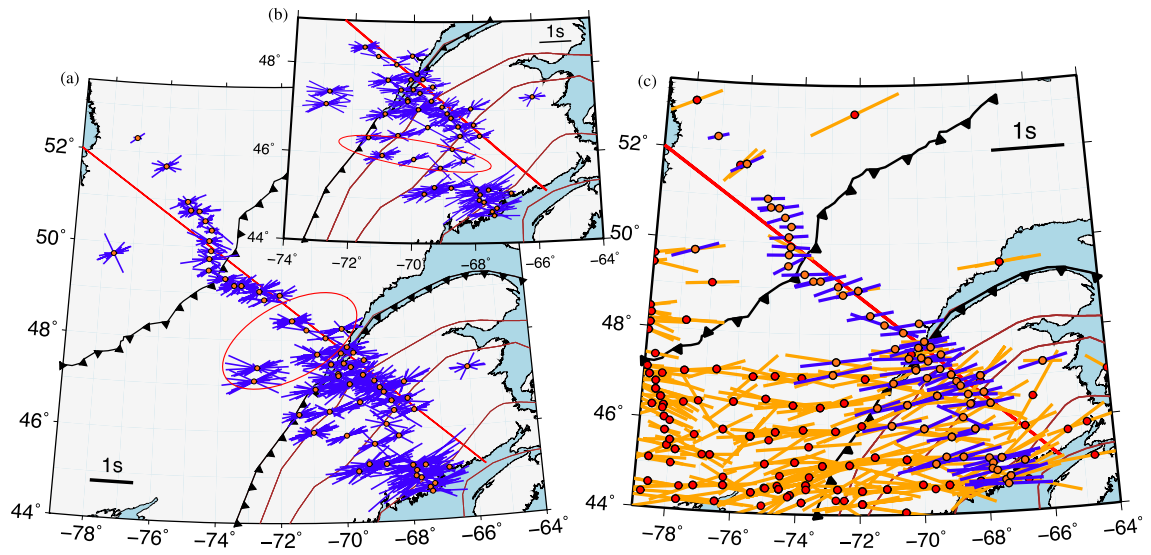


Figure 4:

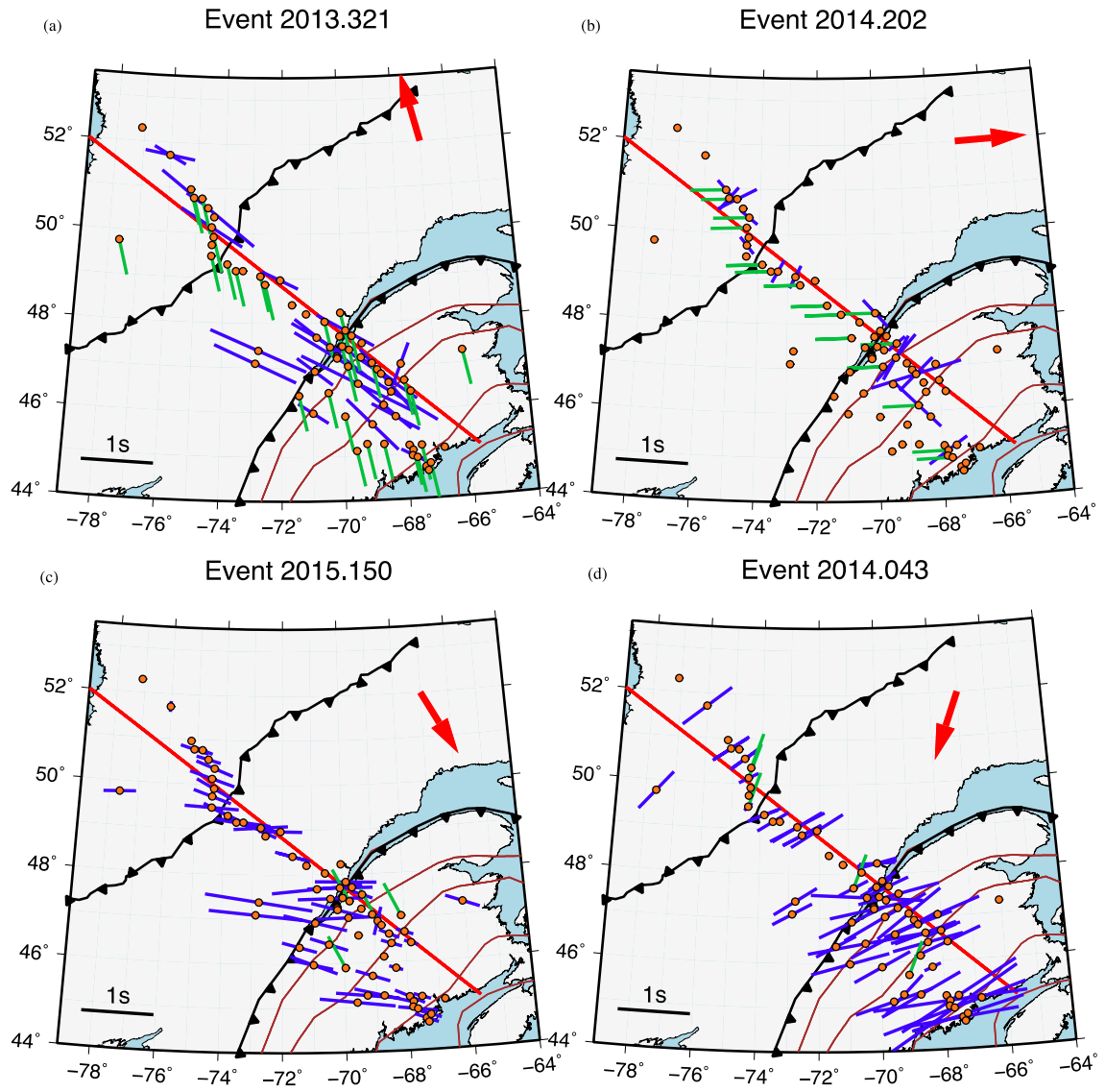


Figure 5:

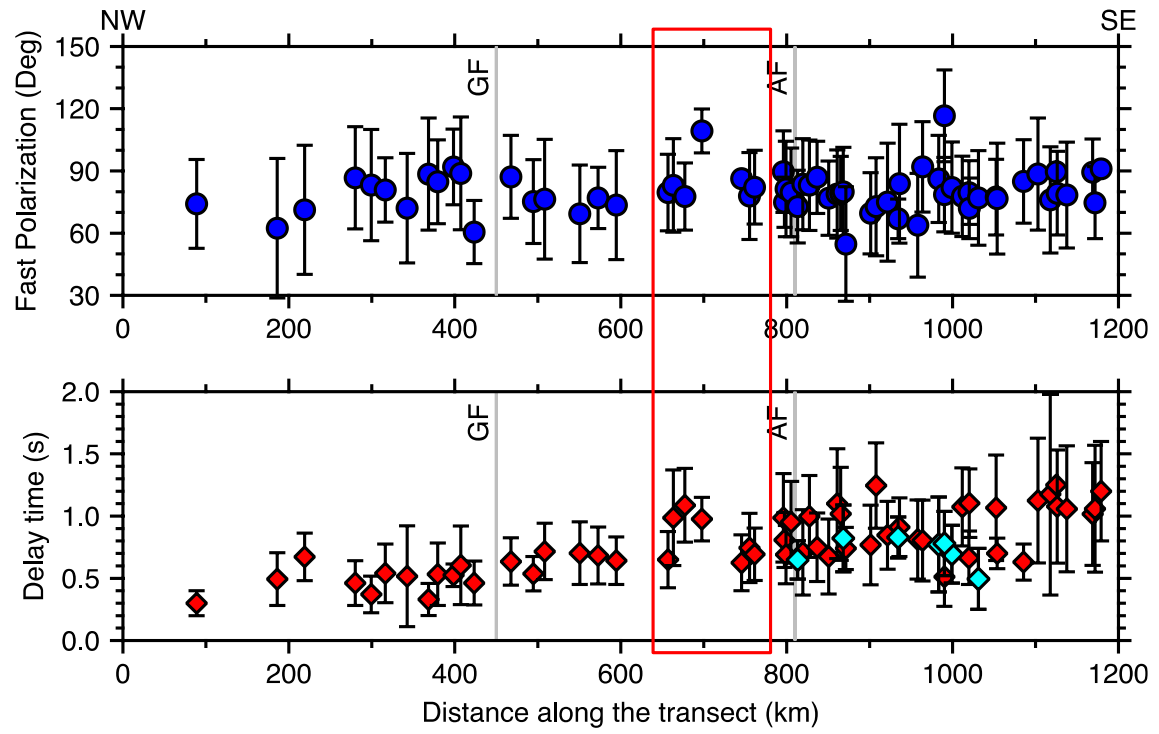


Figure 6:

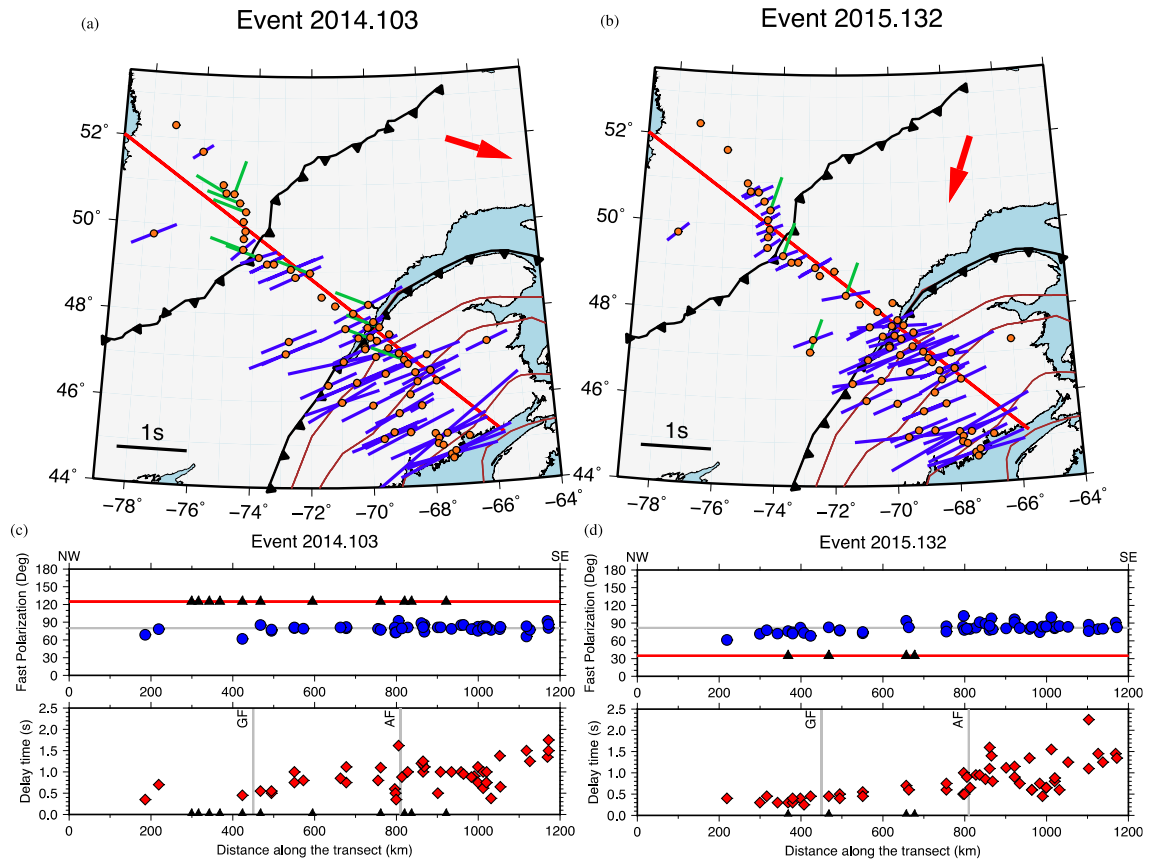


Figure 7:

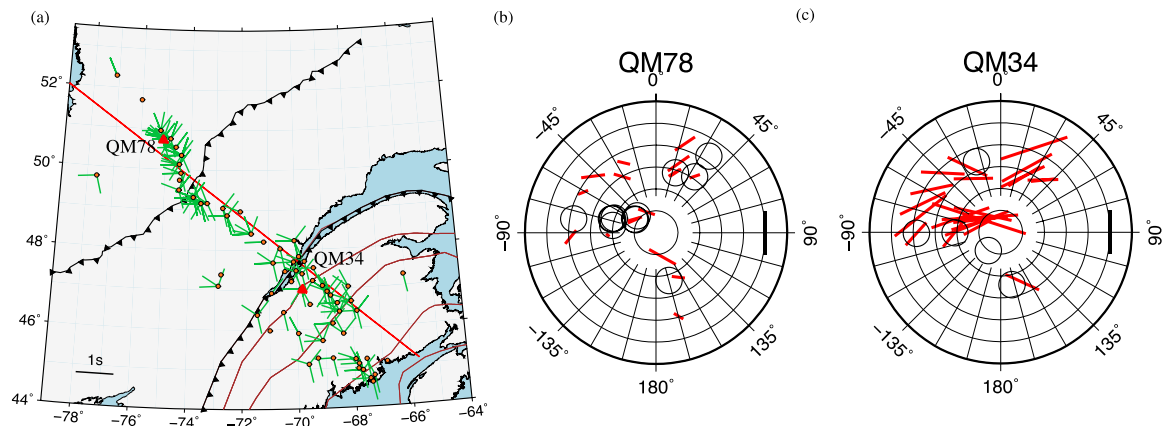


Figure 8:

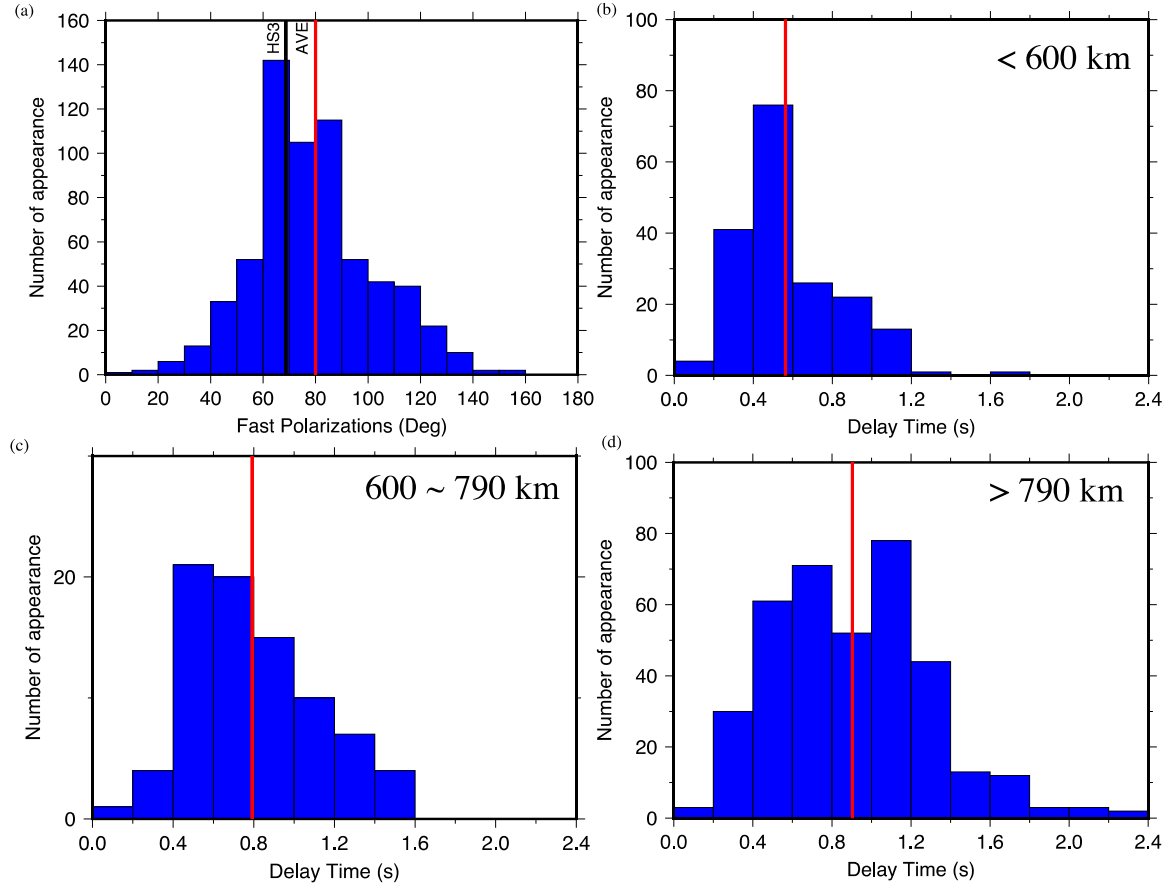
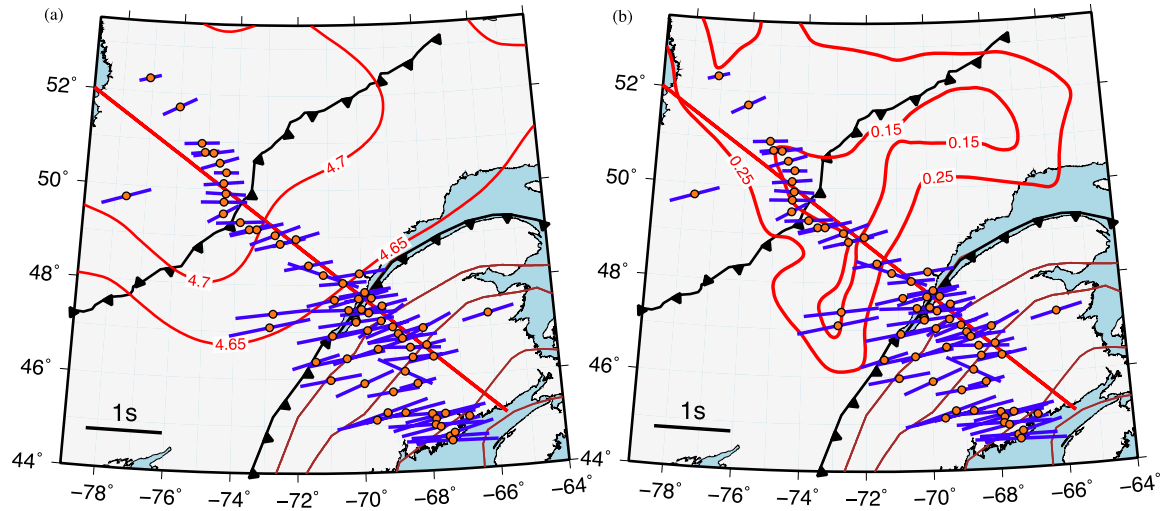
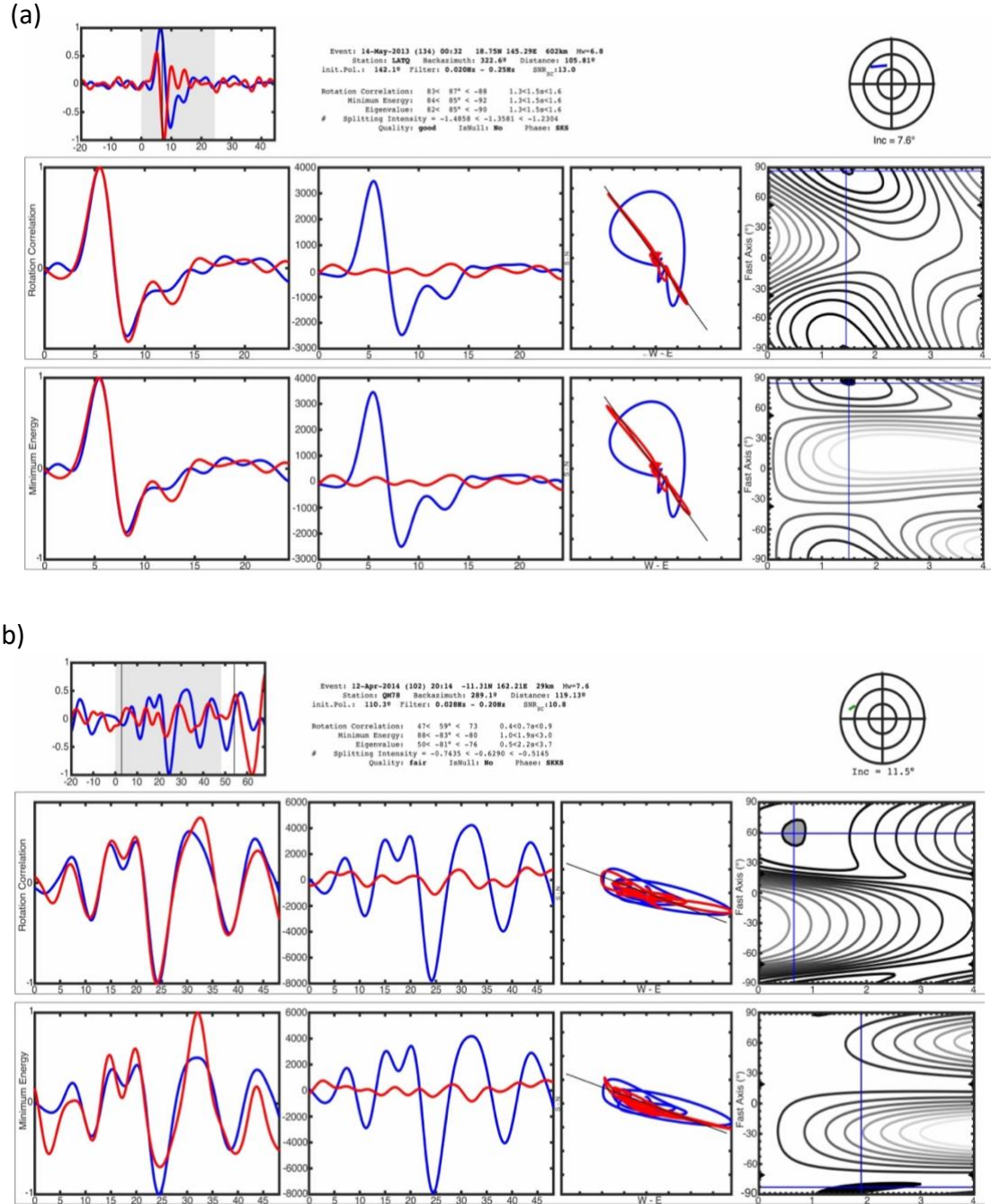


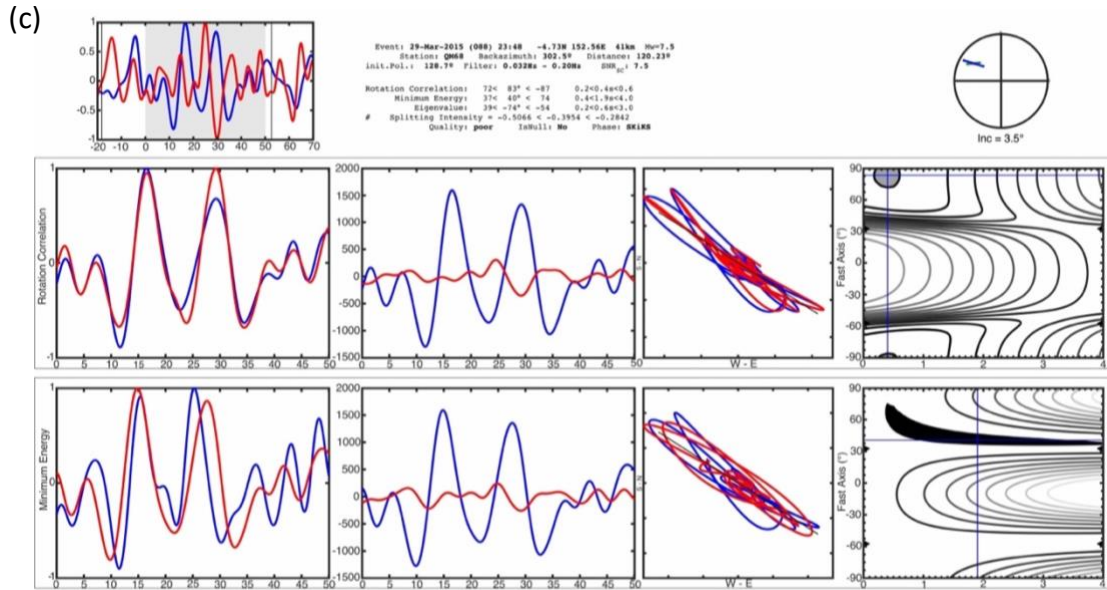
Figure 9:



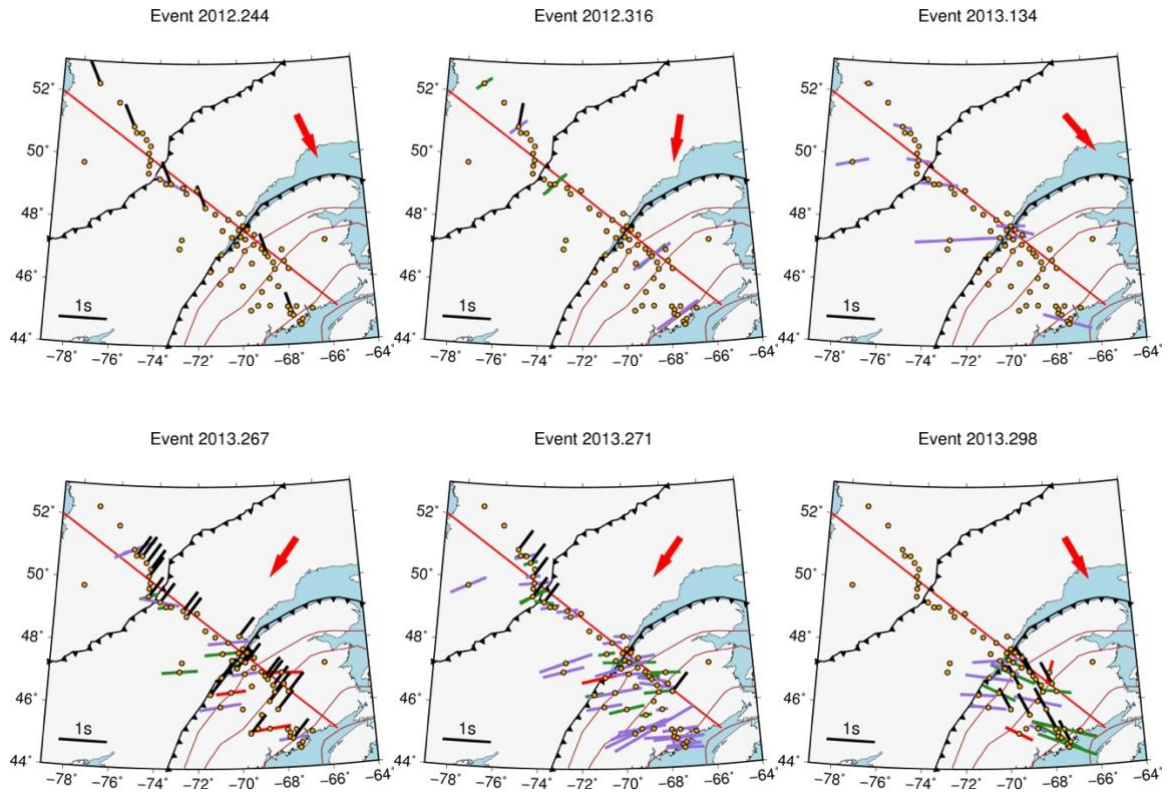
1.12 Supplementary Figures

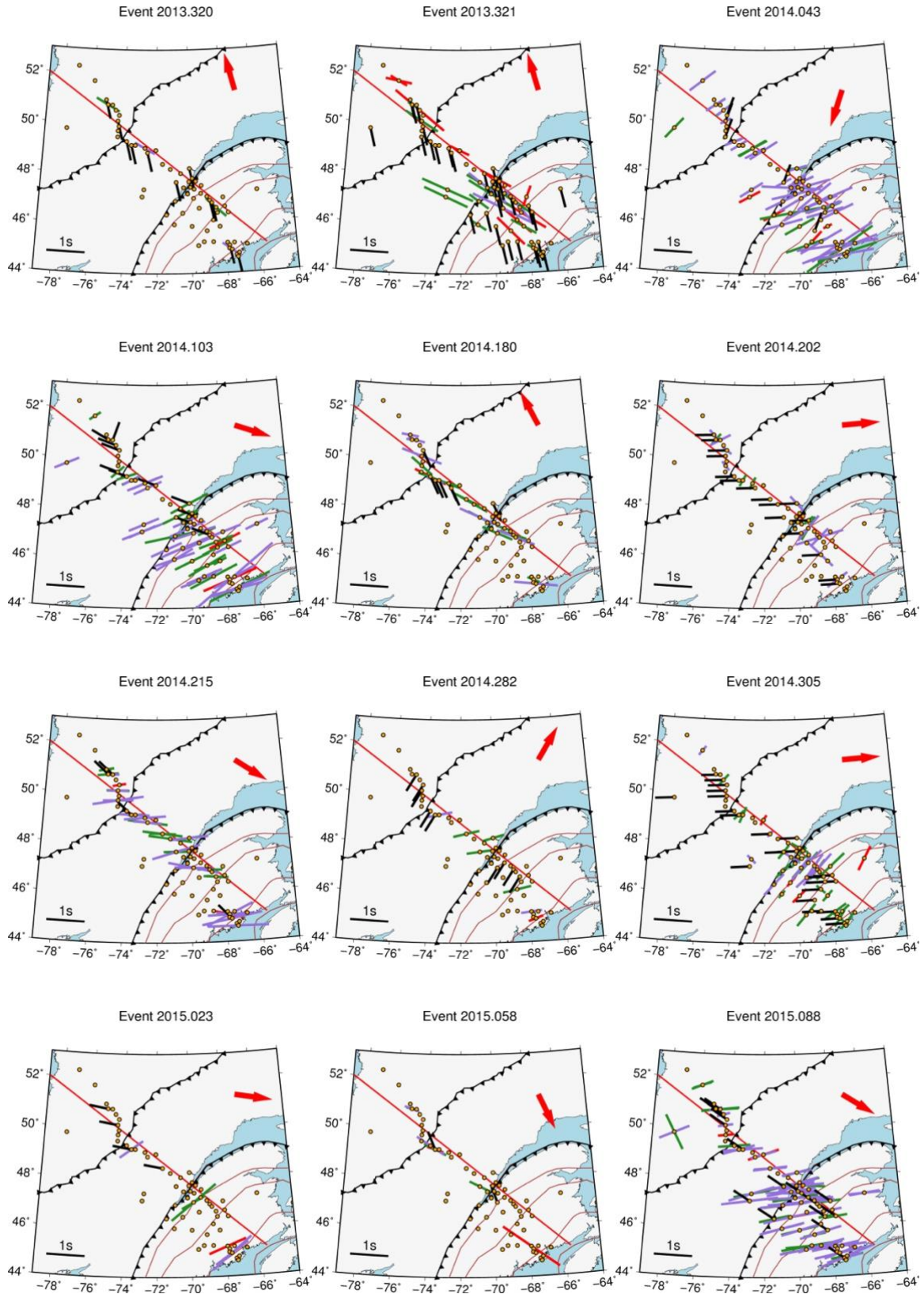
Supplementary Figure 1:

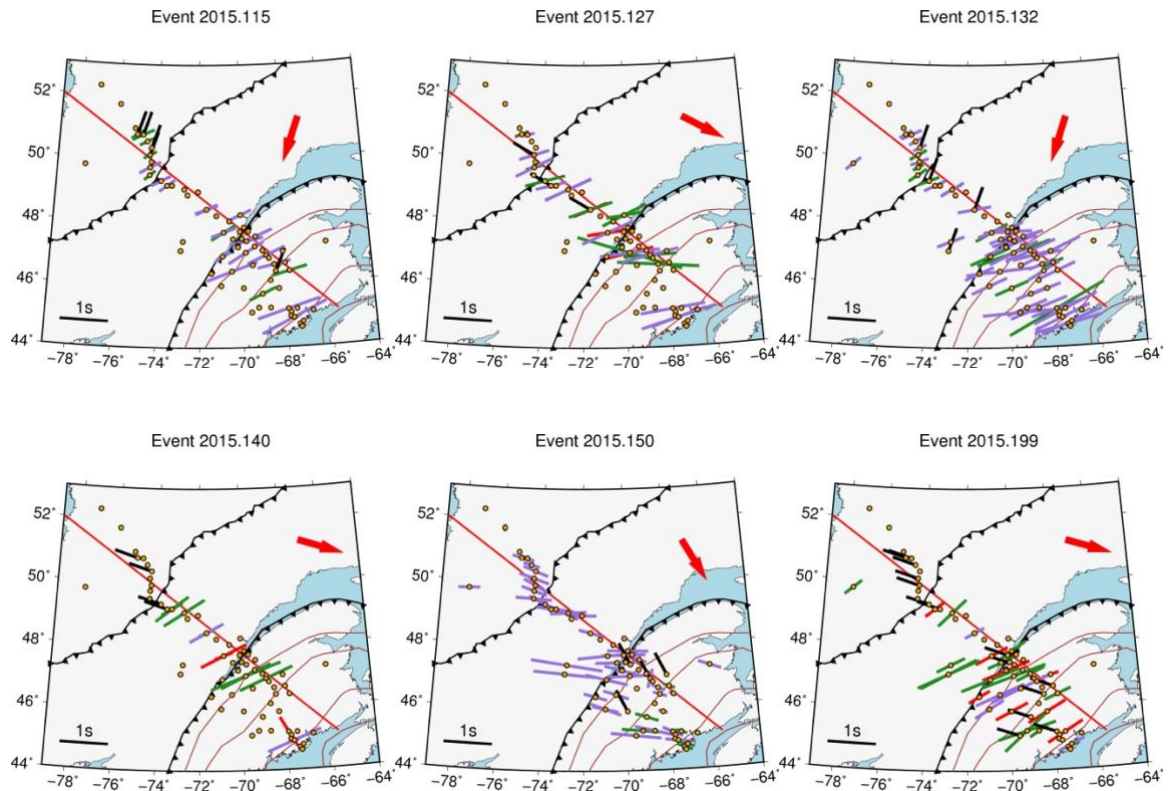




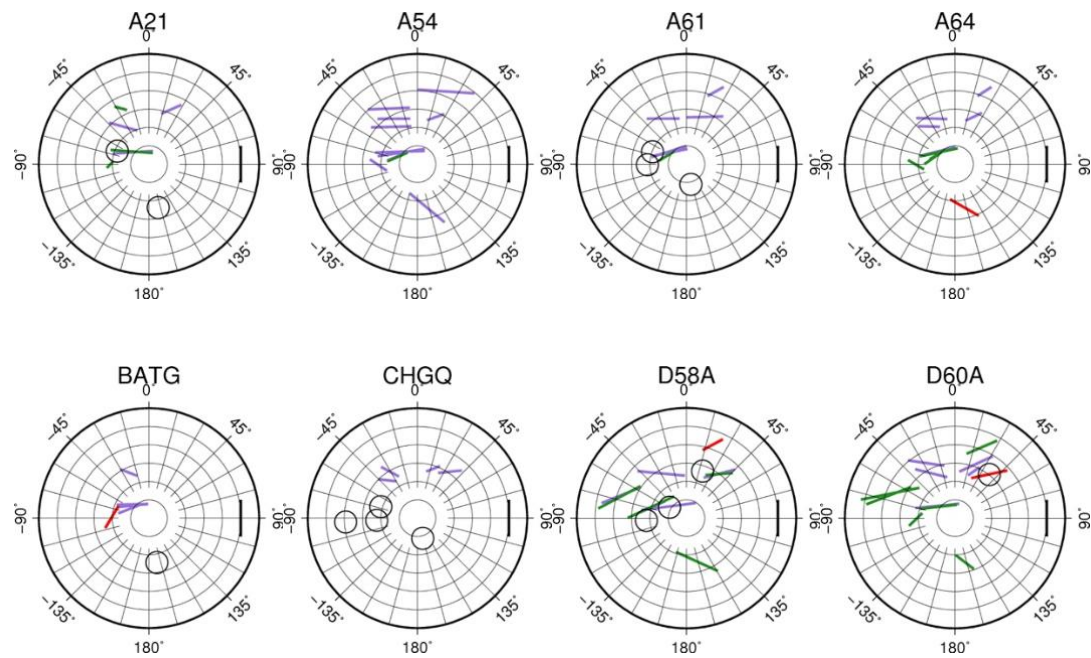
Supplementary Figure 2:

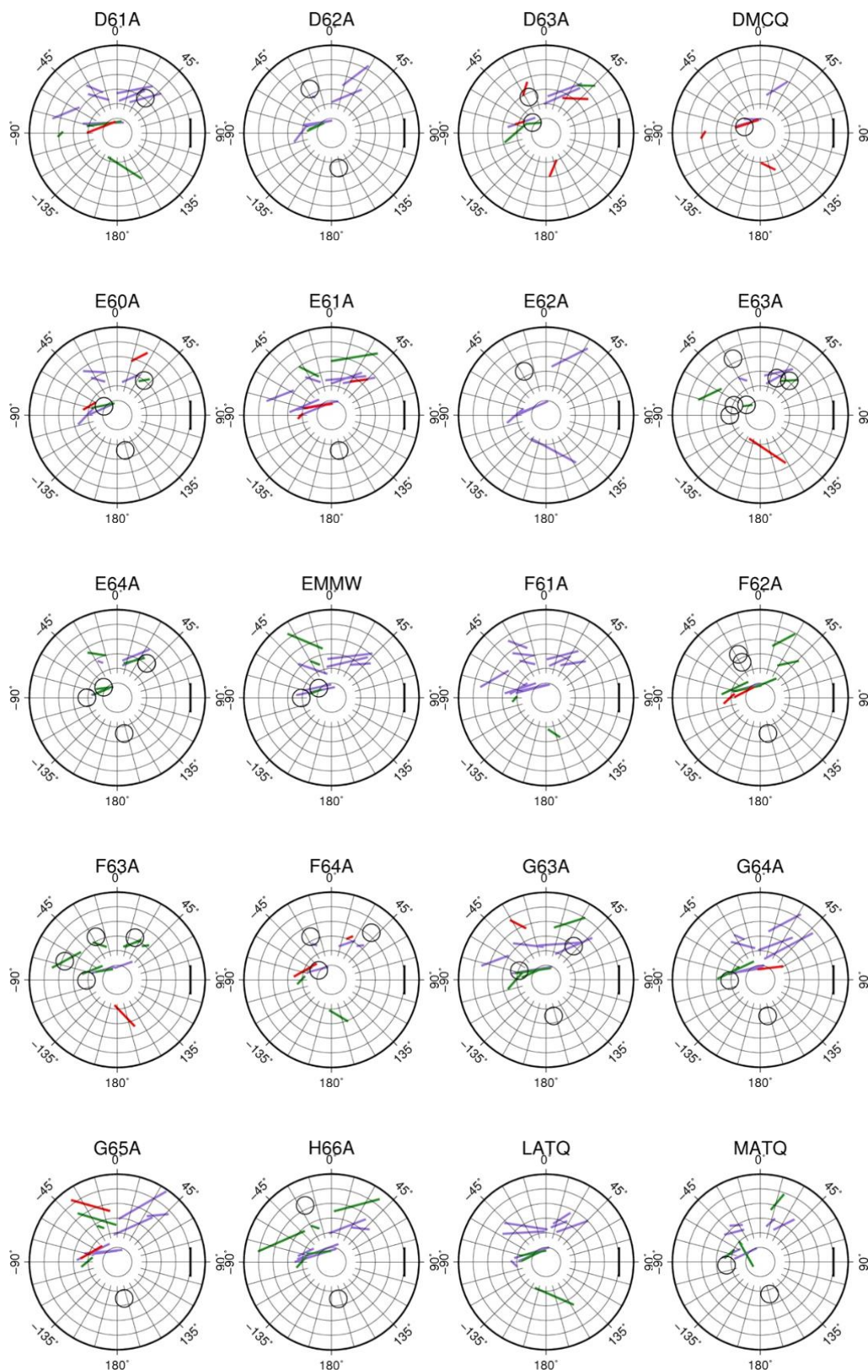


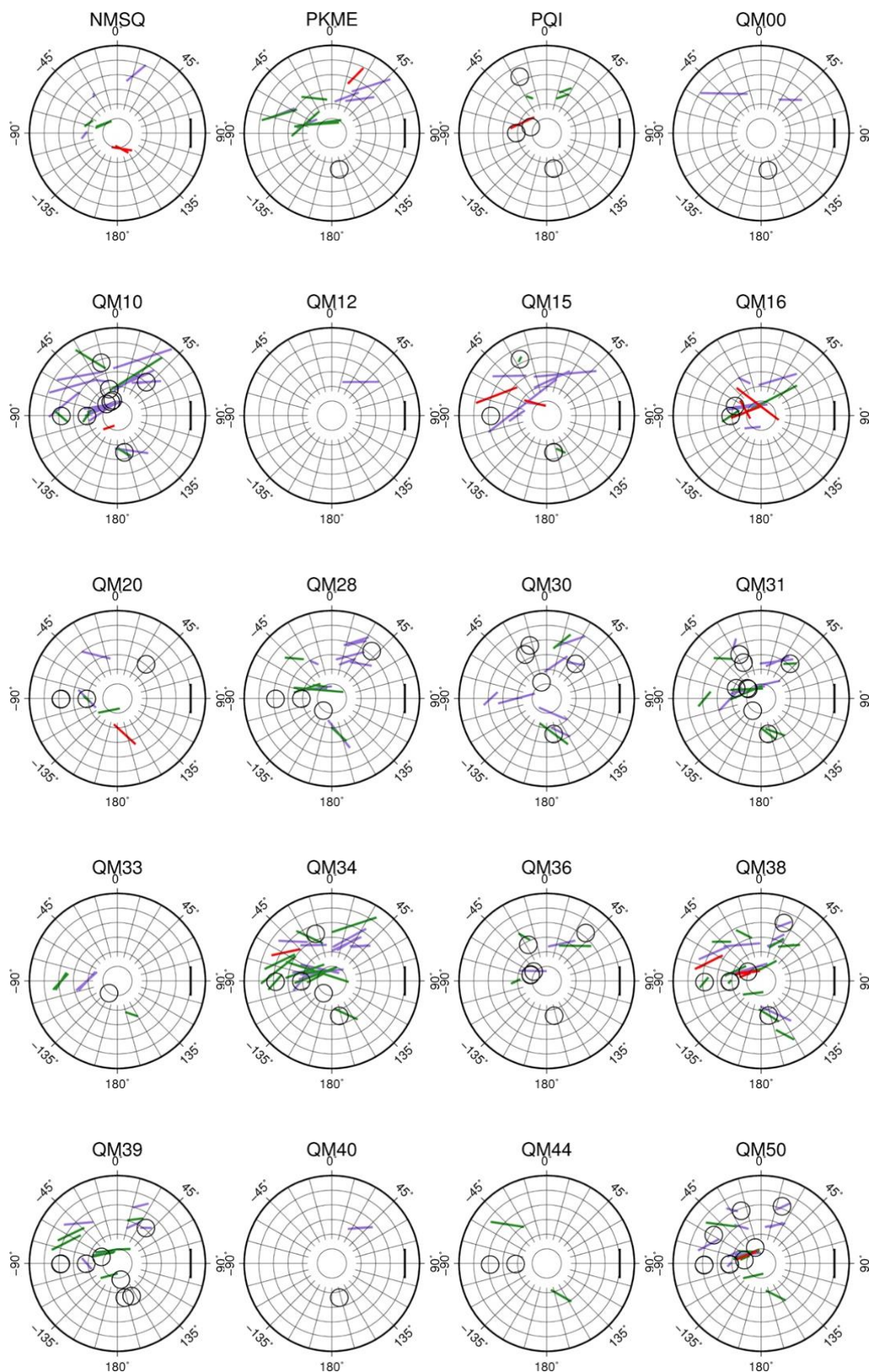


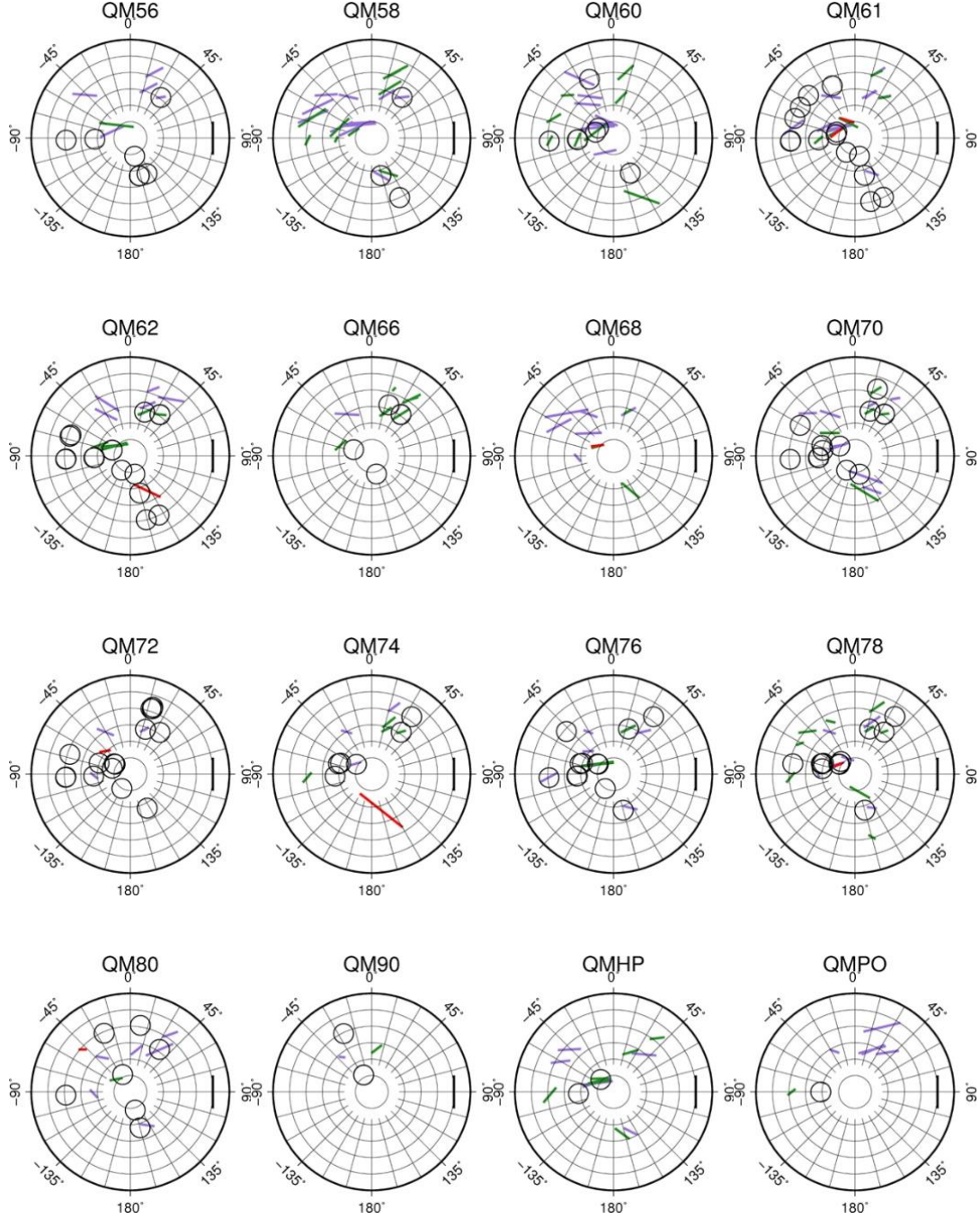


Supplementary Figure 3:









1.13 Criteria for data selection

In our analysis, we included data with all levels of quality ranked from “good” to “fair” to “poor”. We applied different types of frequency filters to them. The lower corner of the filter is mostly 0.01 Hz or 0.02 Hz, and the upper corner was chosen based on signal

to noise ratio (SNR) of the raw data. Selection of the time window requires the inclusion of a complete waveform of the chosen phase. Figure S1(a)-(c) shows examples of “good”, “fair” and “poor” non-NUL measurements. Specific criteria for ranking those measurements adopted by the analyst in this paper are described below:

1) The size and shape of the maximum (shaded in the plot) in the error surface on the map of the correlation coefficient values.

A “good” measurement should have a small maximum, while “fair” and “poor” measurements will have much larger, often elongated, maxima.

2) Particle motions before and after the correction for chosen splitting parameters.

If the particle motion has a relatively regular, elliptical, and clean shape before correction and becomes rectilinear after correction, this measurement will be identified as “good” (shown in Figure S1 (a)). For “fair” and “poor” measurements, particle motion diagrams look distorted and irregular both before and after the correction (examples shown in Figure S1 (b) and (c)).

3) The stability of the measurements with different choices of filters and different window selections.

After we apply different filters and slide our windows back and forth in a certain range, if we can still get the similar answer, it means we have a “good” measurement.

4) The degree of agreement between the two techniques used by Splitlab.

A “good” measurement typically has two measurement methods (rotation correlation (RC) and minimization of the transverse component (SC) method) returning similar fast polarizations (within their respective error ranges). Details of the methods are in Wüstefeld & Bokelmann (2007), and also Levin et al. (2017). Exceptions to this rule include events with very clear waveforms that do not result in consistent splitting parameters.

While we are doing the measurements, we will consider all four criteria together and make a decision instead of being restricted by a specific standard. The difference between “fair” and “poor” is not very easy to tell. Our criteria are as below: the “poor” measurements are mainly based on higher noise level and have less stable results with respect to filtering and window selection.

Chapter 2

Body Wave Propagation through Horizontally Stratified Anisotropic Media in Different Parameterizations: Synthetics and Potential Applications

This chapter has resulted in a manuscript ready to be submitted to Pure and Applied Geophysics:

Chen, X., Park, J., & Levin, V. Anisotropic Layering and Seismic Body Waves: Deformation Gradients, Initial S-Polarizations, and Converted-Wave Birefringence

2.1 Abstract

Seismic anisotropy, or the directional dependence of seismic velocity, is a proxy for the past and present deformation processes in the crust and the upper mantle. It is commonly investigated using methods based on observations of splitting in shear waves and the conversion of energy between P and S waves. In this paper, we present synthetic seismograms generated for plane wave propagation through horizontally stratified anisotropic media using a reflectivity algorithm. This algorithm enables us to simulate wave propagation with high frequency components and consider all transmission and reflection coefficients in one step. Instead of focusing on a specific type of parameterization of seismic anisotropy, we adopt the most general description of seismic anisotropy, an elastic tensor composed of 21 independent parameters, which will exactly characterize the anisotropic properties of the medium. We also discuss special cases of commonly used anisotropic parameterizations such as the Backus notation. We discuss a number of examples illustrating the use of this algorithm for simulating results of receiver function analysis based on both P-to-S and S-to-P converted waves, and also for results of shear wave splitting analysis.

2.2 Introduction

Anisotropy is the dependence of seismic velocity upon the direction of wave propagation and a commonly adopted proxy for deformation processes within the Earth (Long and Becker, 2010). Anisotropic structures exist widely in different parts of the Earth, for instance, the crust (Backus, 1962, Mainprice and Nicolas, 1989, Weiss et al., 1999), the upper mantle (Hess, 1964, Vinnik et al., 1989, Silver, 1996, Barruol et al., 1997), the D'' layer (Long, 2009, Wookey and Kendall, 2007), and the inner core (Karato, 1999, Beghein and Trampert, 2003). Many different mechanisms can lead to anisotropy, for instance, the layering of isotropic materials with alternating properties (Backus, 1962), oriented cracks (Crampin, 1994, Holtzman et al., 2003) and the systematic orientation of the intrinsically anisotropic crystals (Christensen, 1984). Having a better understanding of the anisotropic properties of the Earth not only explains the discrepancies between the observations and the isotropic models, but also helps us understand the internal deformation processes.

Anisotropic structures are likely to be thin or change over short distances, for instance, the fine layering of different lithologies in the crust (Kern et al., 2008), boundaries in the upper mantle (Yuan and Levin, 2014), and mantle wedges in subduction zones (Peyton et al., 2001, Long and van der Hilst, 2006). To simulate anisotropic structures in these tectonic settings requires the inclusion of high frequency components in seismic waves. Here in this paper, we present synthetic seismograms generated using a “reflectivity” algorithm originally proposed by Fuchs and Müller (1971). As anisotropy is commonly detected in the Earth, e.g. by splitting of a shear wave into two orthogonally polarized arrivals with different speeds (Long and Silver, 2009, Silver and Chan, 1991, Vinnik et al., 1989) and by the conversion from P to SH waves at sharp gradients (Bostock, 1997, Farra

and Vinnik, 2000, Park and Levin, 2000) we present a variant of this algorithm for horizontally stratified arbitrarily anisotropic medium.

To describe an anisotropic medium, a fourth-order elastic tensor is adopted which consists of 81 parameters (e.g. Anderson, 1989). Based on the symmetry properties of the strain and stress, only 21 out of 81 parameters are independent. Furthermore, this number will decrease depending on different degrees of anisotropy. For instance, we use 2 Lamé parameters to describe the isotropic medium which has the highest degree of symmetry; we adopt Thomsen parameters (Thomsen, 1986) to describe the Transversely Isotropic medium with a vertical symmetry axis (VTI) where only 5 independent parameters are necessary; similarly, Backus notation (Backus, 1965) consisting of 5 parameters is adopted to describe the hexagonal symmetry with a horizontal axis. However, not all anisotropic structures have such high degrees of symmetry and most often, we will have to consider minerals of lower degrees of symmetry like olivine or even a combination of different minerals. In this paper, we choose to describe the anisotropic medium using a full tensor which provides the exact characterization of anisotropy. At the same time, descriptions using the Backus notation and the Thomsen parameters are also included as special cases.

As the global seismic network coverages becomes more dense, large amounts of data have accumulated. At the same time, more advanced algorithms have been developed to help improve the results of seismic inversions. These growing volumes of data and emerging methods usually require fast iteration speeds, which sets the requirement that the synthetic seismograms should be generated efficiently and accurately. The reflectivity algorithm can be a good choice since it computes all the reflections and transmissions of

seismic waves in one procedure without putting a heavy load on the computing resources. Thus, in this paper, we will first present the theoretical background for a reflectivity algorithm in an anisotropic medium described by a full tensor, and then will discuss its applications in different parameterizations combined with commonly adopted teleseismic body wave analysis methods.

2.3 Methodology

The reflectivity algorithm was originally proposed by Fuchs (1968) and was extended to include transmission losses and time shifts in Fuchs and Müller (1971). It is a wavenumber-integral method, and as implied by its name reflectivity, the integrands are the transmission and reflection coefficients of the layered medium. This name is still adopted although the integrand can be computed in other ways, for example using a propagator matrix (Richards, 1971, Gilbert and Backus, 1966). Chapman and Orcutt (1985) reviewed and compared the theoretical backgrounds of reflectivity algorithm and other algorithms in great detail. Kennett and Kerry (1979) and Kennett (2013) proposed recursive schemes with a source at any depth, and expressed the integrand as the reflectivity of the multi-layered medium. Fryer and Frazer (1987) provided analytical solutions for wave propagation in stratified anisotropic media of specific symmetries. Apsel and Luco (1983) and Luco and Apsel (1983) solved the problem of wave propagation in viscoelastic media with an arbitrary buried source. Crampin (1970) and Crampin and Taylor (1971) derived expressions for surface wave propagation through a stratified azimuthal anisotropic medium, and Keith and Crampin (1977a-c) applied the same algorithm to plane wave propagation. Park (1996) derived the representations of surface wave propagation through multi-layered anisotropic medium with arbitrarily oriented symmetry axes. Levin and Park

(1997) extended the derivation for surface wave propagation Park (1996) to include body wave propagation. Wu and Chen (2016) improved the algorithm and proposed a more stable computation of the effects of low-velocity zones on surface-wave dispersion.

In this section, we will present the theoretical background of the reflectivity algorithm for plane wave propagation in a horizontally stratified anisotropic medium described by a full elastic tensor. All terms and symbols used in the derivations presented below are defined in a “glossary” that is included in Supplementary Materials. Moreover, a step-by-step derivation is presented in the Appendix.

2.3.1 Conventions and Model Setup

In this algorithm, we generate synthetic seismograms for plane wave propagation in a vertical plane through a stack of horizontal anisotropic layers above an infinite isotropic half space (Figure 1(a)). Each layer within the model has elastic properties described by density, isotropic P and S wave velocities, and anisotropy parameters that may be given by either a full fourth-order elastic tensor or by an equivalent parameterization for a specific symmetry, such as Backus parameterization (Backus, 1965) for hexagonal symmetry and Thomsen parameters (Thomsen, 1986) for VTI media. Isotropic P and S wave velocities are not needed if a complete elastic tensor and density of the corresponding material are provided. All the elastic properties remain constant within each layer and only change with depth.

We compute the displacements $u = \mathbf{A} e^{i(\mathbf{k} \cdot \mathbf{x} - \omega t)}$ at different interfaces by only considering the variations due to the changes with depth, which means we assume that the receivers at different interfaces have a shared phase-shift factor $e^{-i\omega p x}$, where p is the ray parameter, ω is the radial frequency and x is the downrange horizontal distance (Figure

1(a)). The shared phase-shift function $e^{-i\omega p x}$ enforces boundary conditions for all x , if satisfied at $x=0$, and effectively defines Snell's Law for seismic rays.

In seismology, a commonly adopted right-handed RTZ coordinate system follows the convention below: the radial axis R is positive pointing from the source to the receiver along the surface of the Earth, the vertical axis Z is positive upwards and the transverse axis T is 90° counter-clockwise from the radial axis in map view (Figure 1(b)). In our algorithm, however, we adopt a right-handed Cartesian coordinate system XYZ which is slightly different from the normal RTZ coordinate system. As illustrated in Figure 1(b), in which the X axis points in the radial direction, the Y axis points in the anti-transverse direction and the Z axis points in the anti-vertical direction, aka downwards. The free surface is at the depth of zero and the depth is positive downward. In our algorithm, an incoming wave (either P or S) is incident at the lowermost interface with a given ray parameter p or at a given incidence angle as controlled by the properties of the isotropic half space (Figure 1(a)). Each type of the waves generated thereafter (qP , qS_1 , qS_2) is separated into upgoing waves and downgoing waves, all of which share the same ray parameter as the incident wave. We use qP and qS nomenclature to reflect the fact that in an anisotropic medium these waves are not purely compressional or purely shear. To define the polarity of particle motion with each wave, we follow the convention of Aki and Richards (2002) and define a positive particle motion when this motion's component in the radial direction has the same sign as the ray parameter (Figure 2).

In our convention, when the wave propagates from the North (0° back azimuth), the X axis points to the South and the Y axis points to the West.

2.3.2 Plane Wave Propagation in Anisotropic Media

For all the derivation steps in this paper, we adopt the Einstein notation and thus, the indices i, j, k and l represent the indices permuting from 1 to 3. Our derivation below combines elements from Kennett (2013) and Chen (1993) while maintaining uniform nomenclature and consistent definitions of terms (see glossary in the Supplementary Materials).

2.3.2.1 Christoffel Equations and Christoffel Matrix

Considering Hooke's law and Newton's second law, we have relationships between stress and strain, and between stress and displacement, as given below:

$$\tau_{ij} = C_{ijkl} \epsilon_{kl} \quad (1)$$

$$\rho \ddot{u}_i = \tau_{ij,j}$$

where τ_{ij} is the stress tensor, ϵ_{kl} is the strain tensor, and C_{ijkl} is the elastic tensor. The summation convention over vector and tensor components i, j, k, l is used throughout. The equation of motion relates the product of density ρ and acceleration \ddot{u}_i to the divergence of stress $\tau_{ij,j}$. Since the solution for plane wave propagation has a known form, we can write it out as below, for particle-motion polarization vector \mathbf{U} , as:

$$u_k(\mathbf{x}, t) = A U_k e^{i(k_j x_j - \omega t)} \quad (2)$$

Here A is the scalar amplitude of the overall displacement, and U_k is the corresponding component of the unit polarization vector \mathbf{U} . The wavenumber vector $\mathbf{k}=(k_1, k_2, k_3)$ defines the wavefront normal, and $\mathbf{x}=(x_1, x_2, x_3)=(x, y, z)$ is the position in space. In

isotropic media, the unit polarization vector \mathbf{U} is wavefront-normal for P waves and wavefront-parallel for S waves. In anisotropic media the plane-wave polarizations can be hybrids of these geometries. The polarization vector determines how the overall displacement is projected onto different coordinate axes at layer boundaries, where boundary conditions must be met.

Combining (1) and (2), we obtain the Christoffel Equation:

$$(C_{ijkl}k_jk_l - \rho\omega^2\delta_{ik})u_k = 0 \quad (3)$$

To solve the Christoffel Equation is to solve an eigenvalue problem. Solutions to the equation are the eigenvalues and eigenvectors of the Christoffel Matrix defined in (4) as below:

$$\mathbf{M}_{ik} = k_j \cdot \mathbf{C}_{ijkl} \cdot k_l \quad (4)$$

The Christoffel Matrix is a 3×3 matrix containing the information of wave propagation direction and elements of the elastic tensor. The eigenvalues of the Christoffel Matrix are the vertical slownesses of the different seismic waves and the corresponding eigenvectors are their polarizations.

Given the relationship between wavenumber k and wave slowness s ,

$$s = \frac{k}{\omega} \quad (5)$$

we cancel out the angular frequency ω and have the Christoffel Equation as below:

$$(\mathbf{C}_{ijkl} s_j s_l - \rho \delta_{ik}) u_k = 0 \quad (6)$$

We further adopt an adjusted version of the Christoffel Matrix by using the elastic tensor and the components of the slowness vectors as below:

$$G_{ik} = s_j \cdot C_{ijkl} \cdot s_l - \rho \delta_{ik} \quad (7)$$

We thus can simplify the notation of the Christoffel Matrix by using the product of the elastic tensor and two components of the slowness vector. Because our problem is restricted to a vertical plane containing the ray of the incoming plane wave, we assume that $s=(s_1, s_2, s_3)=(p, 0, v)$, with p and v respectively, the horizontal and vertical slowness values. Below we will provide a simpler version of notation for the elastic tensor so that we can write out the explicit representation of the Christoffel Matrix and Equation in our derivation. The fourth-rank elastic tensor C_{ijkl} can be rearranged into a 6x6 matrix C_{pq} with the following transformation (Aki and Richards, 2002):

$$p = i\delta_{ij} + (1 - \delta_{ij})(9 - i - j) \quad (8)$$

$$q = i\delta_{kl} + (1 - \delta_{kl})(9 - k - l)$$

Combine equations (7) and (8) we have:

$$\begin{aligned}
 G_{11} &= C_{1jk1} s_j s_k - \rho \delta_{11} \quad (9) \\
 &= C_{1111} s_1 s_1 + C_{1121} s_1 s_2 + C_{1131} s_1 s_3 + C_{1211} s_2 s_1 \\
 &\quad + C_{1221} s_2 s_2 \\
 &\quad + C_{1231} s_2 s_3 + C_{1311} s_3 s_1 + C_{1321} s_3 s_2 + C_{1331} s_3 s_3 \\
 &\quad - \rho \\
 &= C_{11} s_1^2 + C_{16} s_1 s_2 + C_{15} s_1 s_3 + C_{61} s_1 s_2 + C_{66} s_2^2 \\
 &\quad + C_{65} s_2 s_3 \\
 &\quad + C_{51} s_3 s_1 + C_{56} s_3 s_2 + C_{55} s_3^2 - \rho
 \end{aligned}$$

Due to the symmetry of the elastic tensor, the Christoffel Matrix is also symmetrical, we only calculate the six independent components of the Christoffel Matrix as below:

$$\begin{aligned}
 G_{11} &= C_{11} p^2 + 2C_{15} p v + C_{55} v^2 - \rho \quad (10) \\
 G_{12} &= G_{21} = C_{16} p^2 + (C_{14} + C_{56}) p v + C_{54} v^2 \\
 G_{13} &= G_{31} = C_{15} p^2 + (C_{13} + C_{55}) p v + C_{53} v^2 \\
 G_{22} &= C_{66} p^2 + 2C_{64} p v + C_{44} v^2 - \rho \\
 G_{23} &= G_{32} = C_{65} p^2 + (C_{63} + C_{45}) p v + C_{43} v^2 \\
 G_{33} &= C_{55} p^2 + 2C_{53} p v + C_{33} v^2 - \rho
 \end{aligned}$$

Thus, we rearrange the Christoffel Matrix based on the common factors of the slowness components, and rewrite the representation of the Christoffel Matrix as follows:

$$G = p^2 \mathbf{T} + pv \mathbf{S} + v^2 \mathbf{R} - \rho \mathbf{I} \quad (11)$$

$$\mathbf{T} = \begin{bmatrix} C_{11} & C_{16} & C_{15} \\ C_{16} & C_{66} & C_{65} \\ C_{15} & C_{65} & C_{55} \end{bmatrix}$$

$$\mathbf{S} = \begin{bmatrix} 2C_{15} & C_{14} + C_{56} & C_{13} + C_{55} \\ C_{14} + C_{56} & 2C_{64} & C_{63} + C_{45} \\ C_{13} + C_{55} & C_{63} + C_{45} & 2C_{53} \end{bmatrix}$$

$$\mathbf{R} = \begin{bmatrix} C_{55} & C_{54} & C_{53} \\ C_{54} & C_{44} & C_{43} \\ C_{53} & C_{43} & C_{33} \end{bmatrix}$$

Solutions of the Christoffel Equation can be found by solving the quadratic eigenvalue problem above. As the solution, we can get six eigenvalues and six corresponding eigenvectors. The physical meaning of the solution to the Christoffel Equation is that each eigenvalue is the vertical slowness v of one of the six modes of the plane waves (upgoing qP , qS_1 , qS_2 waves and downgoing qP , qS_1 , qS_2 waves). The corresponding eigenvectors are the polarization vectors of these phases. Since the horizontal slowness p , equivalent to the ray parameter, is given, solving the eigenvalue problem can help us compute the phase velocities of all plane waves that reflect, transmit and convert at horizontal interfaces.

Notice that solving for the eigenvalues and eigenvectors, we do not need to know the specific description of seismic anisotropy symmetry. This solution is based on the

description of anisotropy in 21 parameters, which means it can work for any given kind of seismic anisotropy.

2.3.2.2 Computation of the displacement-stress matrix

To compute the effect of a layered structure, referred to as the reflectivity response, on an upgoing waveform, we compute the initial amplitude and phase spectra of the upgoing wave in the isotropic half space. By multiplying the amplitude and phase spectra of the incident wave with the reflectivity response, we can compute the spectrum of the wavefield observed on the surface. We start the derivation from the frequency domain by specifying the desired frequency range. Conventions for Fourier Transform which transforms the time series into frequency domain and corresponding parameters for the time series in our study are described at the end of Section 2. For a chosen frequency ω and horizontal slowness p within a layer with constant elastic properties, we express the seismic wavefield as a sum of six plane waves, with polarizations and vertical slowness values determined by the eigenvalues and eigenvectors of the Christoffel Matrix. For each type of the elastic wave, we define the displacement-stress vector \mathbf{b} as a 6-component vector partitioned into three-component displacement \mathbf{u} and three-component traction on horizontal surfaces $\hat{\mathbf{t}} = \hat{\mathbf{z}} \cdot \boldsymbol{\tau}$, in that, $\hat{\mathbf{z}}$ is the unit vector in the vertical direction.

$$\mathbf{b} = (\mathbf{u}, \mathbf{t})^T \quad (12)$$

We combine the displacement-stress vectors of the following types of waves into a 6 by 6 displacement-stress matrix $\mathbf{B}(\mathbf{z})$: downgoing qP wave, qS₁ wave, qS₂ wave; upgoing qP wave, qS₁ wave, qS₂ wave. Displacement-stress vectors are ordered in columns. Here we divide the matrix into two different blocks corresponding to downgoing waves and

upgoing waves, and note that the internal ordering of different types of body waves will not influence the results. Matrix \mathbf{B} can be written as the product of three matrices as in

$$\mathbf{B}_z^j = \mathbf{E}^j \mathbf{\Lambda}_z^j \mathbf{W}_z^j \quad (13)$$

All the superscripts stand for the j th layer. \mathbf{E}^j is the matrix whose columns are the eigenvectors of the Christoffel Matrix and the components of the elastic tensor or other equivalent parameterizations. It is constant within each layer of the model medium. $\mathbf{\Lambda}_z$ is a depth-dependent diagonal matrix of exponential factors of depth and frequency that “propagate” the wavefield vertically by expressing either the phase oscillation, or exponential decay and growth, of the upgoing and downgoing waves. They are expressed in terms of $\exp(i\omega v_k^j(z - z_j))$, $\exp(-i\omega v_k^j(z - z_j))$ (Chen, 1993). Thus, “zero” distance at a single depth z_j or at the boundary that each wave propagates from, depends on the directions of the waves: for downgoing waves the “zero” is at z_{j-1} and for upgoing waves the “zero” is at z_j . \mathbf{W}_z^j is a matrix that contains the amplitudes of the waves. Within one layer of material with constant properties, \mathbf{B} and $\mathbf{\Lambda}$ are both depth dependent while \mathbf{E} and \mathbf{W} are constant with depth.

2.3.2.3 Plane Wave Transmission and Reflection at Interfaces

Since we have derived the displacement-stress matrix within one layer of anisotropic medium, we can also derive the reflection and transmission coefficients by satisfying the boundary conditions where the tractions and displacements are both continuous at the interface between the j th and $(j+1)$ th layer.

The continuity of displacement and traction at the interface leads to a relationship between the relationship between the stress-displacement vectors of all upgoing and downgoing waves in the j th and $(j+1)$ th layer.

$$\mathbf{E}_{z_j}^j \mathbf{\Lambda}_{z_j}^j \mathbf{W}_{z_j}^j = \mathbf{E}_{z_j}^{j+1} \mathbf{\Lambda}_{z_{j+1}}^{j+1} \mathbf{W}_{z_j}^{j+1} \quad (14)$$

1) Solid-solid interface

As mentioned previously, any displacement-stress matrix could be written out as the product of three matrices. At the depth of z ($z_{j-1} < z < z_j$), we can write the three matrices as below (subscripts D and U stand for down-going and upgoing families of waves):

$$\mathbf{B}_z^j = \begin{bmatrix} \mathbf{E}_{11}^j & \mathbf{E}_{12}^j \\ \mathbf{E}_{21}^j & \mathbf{E}_{22}^j \end{bmatrix} \begin{bmatrix} \mathbf{\Lambda}_D^j & \mathbf{0} \\ \mathbf{0} & \mathbf{\Lambda}_U^j \end{bmatrix} \begin{bmatrix} \mathbf{W}_D^j \\ \mathbf{W}_U^j \end{bmatrix} \quad (15)$$

For the convenience of the subsequent derivation, we divide the matrix \mathbf{E} into 4 sub-matrices, which represents the coefficients of the displacements and stress for the downgoing and upgoing waves. In addition, we adopt diagonal matrix $\mathbf{\Lambda}^j$ expressed in factors of $\exp(i\omega v_k^j(z - z_j))$, $\exp(-i\omega v_k^j(z - z_j))$ as below (Chen, 1993, Kennett, 1974):

$$\mathbf{\Lambda}_D^j = \begin{bmatrix} \exp[i\omega v_1^j(z - z_j)] & 0 & 0 \\ 0 & \exp[i\omega v_2^j(z - z_j)] & 0 \\ 0 & 0 & \exp[i\omega v_3^j(z - z_j)] \end{bmatrix} \quad (16)$$

$$\Lambda_U^j = \begin{bmatrix} \exp[-i\omega v_1^j(z - z_j)] & 0 & 0 \\ 0 & \exp[-i\omega v_2^j(z - z_j)] & 0 \\ 0 & 0 & \exp[-i\omega v_3^j(z - z_j)] \end{bmatrix}$$

Solving equation (16) we have:

$$\begin{bmatrix} \mathbf{W}_D^{j+1} \\ \mathbf{W}_U^j \end{bmatrix} = \begin{bmatrix} \mathbf{E}_{11}^{j+1} & -\mathbf{E}_{12}^j \\ \mathbf{E}_{21}^{j+1} & -\mathbf{E}_{22}^j \end{bmatrix}^{-1} \begin{bmatrix} \mathbf{E}_{11}^j & -\mathbf{E}_{12}^{j+1} \\ \mathbf{E}_{21}^j & -\mathbf{E}_{22}^{j+1} \end{bmatrix} \begin{bmatrix} \Lambda_D^j & \mathbf{0} \\ \mathbf{0} & \Lambda_U^{j+1} \end{bmatrix} \begin{bmatrix} \mathbf{W}_D^j \\ \mathbf{W}_U^{j+1} \end{bmatrix} \quad (17)$$

After all the waves propagate through the interface, amplitudes of six kinds of waves will change due to transmission and reflection at the boundary.

$$\begin{bmatrix} \mathbf{W}_D^{j+1} \\ \mathbf{W}_U^j \end{bmatrix} = \begin{bmatrix} \mathbf{T}_D^j & \mathbf{R}_U^j \\ \mathbf{R}_D^j & \mathbf{T}_U^j \end{bmatrix} \begin{bmatrix} \mathbf{W}_D^j \\ \mathbf{W}_U^{j+1} \end{bmatrix} \quad (18)$$

In equation (18), $\begin{bmatrix} \mathbf{T}_D^j & \mathbf{R}_U^j \\ \mathbf{R}_D^j & \mathbf{T}_U^j \end{bmatrix}$ stands for the generalized transmission and reflection coefficients. Take \mathbf{R}_U^j for instance, we define it as the reflection coefficient between the amplitude of the waves that leave one interface downward and the amplitudes of the upgoing waves that impinge on the same interface from below.

Comparison with (17) shows that we can get the transmission and reflection coefficients as follows:

$$\begin{bmatrix} \mathbf{T}_D^j & \mathbf{R}_U^j \\ \mathbf{R}_D^j & \mathbf{T}_U^j \end{bmatrix} = \begin{bmatrix} \mathbf{E}_{11}^{j+1} & -\mathbf{E}_{12}^j \\ \mathbf{E}_{21}^{j+1} & -\mathbf{E}_{22}^j \end{bmatrix}^{-1} \begin{bmatrix} \mathbf{E}_{11}^j & -\mathbf{E}_{12}^{j+1} \\ \mathbf{E}_{21}^j & -\mathbf{E}_{22}^{j+1} \end{bmatrix} \begin{bmatrix} \Lambda_D^j & \mathbf{0} \\ \mathbf{0} & \Lambda_U^{j+1} \end{bmatrix} \quad (19)$$

2) Free surface

For the free surface, $j=0$ in the above equations. There are no upgoing or downgoing waves above the free surface, so that the amplitudes in W^0 are zero, and the E^0 submatrices do not exist. Then only the equation below is meaningful:

$$\mathbf{W}_D^1 = \mathbf{R}_U^0 \mathbf{W}_U^1 \quad (20)$$

We can get the reflection coefficients at the free surface (interface 0) as below:

$$\mathbf{R}_U^0 = -(\mathbf{E}_{21}^1)^{-1} \mathbf{E}_{22}^1 \Lambda_U^1 \quad (21)$$

2.3.3 A Recursive Procedure for Computation

For a stack of horizontal layers, we can build up a recursive routine to compute the overall transmission and reflection coefficients for the upgoing waves in each layer, starting from the free surface above the top layer. This recursive routine is equivalent to that of Kennett (1974). We define generalized transmission and reflection coefficients $(\hat{\mathbf{T}}, \hat{\mathbf{R}})$ that express the waves that leave the interface solely in terms of the upgoing waves that impinge on the interface:

$$\mathbf{W}_D^{j+1} = \mathbf{T}_D^j \mathbf{W}_D^j + \mathbf{R}_U^j \mathbf{W}_U^{j+1} = \hat{\mathbf{T}}_U^j \mathbf{W}_U^{j+1} \quad (22)$$

$$\mathbf{W}_U^j = \mathbf{R}_D^j \mathbf{W}_D^j + \mathbf{T}_U^j \mathbf{W}_U^{j+1} = \hat{\mathbf{R}}_{UD}^j \mathbf{W}_U^{j+1}$$

In (22), $\hat{\mathbf{T}}_U^j$ stands for the generalized upgoing transmission coefficient, which reflects the amplitude change between the spectra of upgoing waves above and below the j th interface. $\hat{\mathbf{R}}_{UD}^j$ stands for the generalized downgoing reflection coefficient, which represents the amplitude change between downgoing waves caused by upgoing waves impinging at the j th interface and the corresponding upgoing waves. Rearranging the equation above, we have:

$$\hat{\mathbf{T}}_U^j = (\mathbf{I} - \mathbf{R}_D^j \hat{\mathbf{R}}_{UD}^{j-1})^{-1} \mathbf{T}_U^j \quad (23)$$

$$\hat{\mathbf{R}}_{UD}^j = \mathbf{T}_D^j \hat{\mathbf{R}}_{UD}^{j-1} \hat{\mathbf{T}}_U^j + \mathbf{R}_U^j$$

In this sense, we know that any downgoing waves are actually the combination of the downgoing transmitted waves from all layers above and the reflected waves of the upgoing waves within the same layer. Similarly, any upgoing waves are the combination of the upgoing transmitted waves from layers below and the reflected waves of the downgoing waves within the same layer. By computing the generalized reflection and transmission coefficients, we take the changes of amplitudes and phases into consideration in one procedure. To compute the response at the free surface, we have

$$\mathbf{W}_U^1 = \hat{\mathbf{T}}_U^1 \hat{\mathbf{T}}_U^2 \dots \hat{\mathbf{T}}_U^{N-2} \hat{\mathbf{T}}_U^{N-1} \hat{\mathbf{T}}_U^N \mathbf{W}_U^{N+1} \quad (24)$$

$$\mathbf{W}_D^1 = \hat{\mathbf{R}}_{UD}^0 \mathbf{W}_U^1$$

Finally, we compute the displacement-stress matrix at the free surface by combining (23) and (24). Synthetic seismograms can be obtained by doing the inverse Fourier Transform of the displacements.

2.3.4 Conventions and Parameters in Fourier Transform

In this algorithm, we adopt the following infinite-time convention of the Fourier Transform of functions $f(t)$ of continuous time:

$$F(\omega) = \int_{-\infty}^{\infty} e^{-i\omega t} f(t) dt \quad (25)$$

Correspondingly, the convention of inverse Fourier transform can be obtained by:

$$f(t) = \frac{1}{2\pi} \int_{-\infty}^{\infty} e^{i\omega t} F(\omega) d\omega \quad (26)$$

The inverse Fourier transform integrates plane waves of radial frequency ω and amplitude $F(\omega)$ to form the ground-motion $f(t)$ for all time. Starting from the frequency domain, we specify the maximum frequency, and determine the frequency spacing based on the duration of the time series we plan to simulate. In practical calculations, synthetic seismograms are computed at discrete time-spacing Δt and each time series has a finite

number of N points. In computations for crustal models we use a 200-s time series, $\Delta t=0.05$ s with a corresponding frequency sampling $\Delta f=0.005$ Hz on the interval $0 \leq f \leq 10$ Hz. If plane waves that reverberate in the layered structure have significant amplitude at times later than the end of the computed time series, they suffer a “wraparound effect” and are aliased to the start of the time series. One remedy for rogue pulses in the initial portion of a synthetic seismogram is to compute the reflectivity solution at finer frequency spacing, and to compute a longer time series (if the frequency spacing is Δf , the duration of the inverse Fourier transform is $T=(\Delta f)^{-1}$).

2.3.5 Other Parameterization of Anisotropy

While the algorithm we have developed anisotropy parametrization in terms of an elastic tensor in a general form, numerous studies of seismic anisotropy are based on simplified formulations for specific symmetry systems. In this section, we document relationships that convert these more restrictive parametrizations into the elements of a general elastic tensor. Here we specially focus on the Backus Notation (Backus, 1965) while leaving the Thomsen parameters (Thomsen, 1986) and corresponding examples in the Supplementary Materials.

Backus (1965) proposed that five independent anisotropic parameters (A , B , C , D , E) are enough to describe an anisotropic medium with hexagonal symmetry and a horizontal axis for the case of head wave propagation. Using a similar formulation, Park (1996) introduced the corresponding relationship between the seismic wave velocity and the anisotropic coefficients as below:

$$\rho\alpha^2 = A + B\cos(2\xi) + C\cos(4\xi) \quad (27)$$

$$\rho\beta^2 = D + E\cos(2\xi)$$

Here ξ is the angle between the axis of hexagonal symmetry and the direction of wave propagation and B, C, and E are peak to peak values of P/S wave anisotropy in percent. In this case the axis does not have to be horizontal, and the corresponding directional distribution of seismic velocity is a function of the axis orientation and the angle ξ . If $B=C=E=0$, then A and D are the Lamé parameters. Based on this notation, the elastic tensor can be written as below (Park and Levin, 2016):

$$\Lambda = A\Lambda_A + B\Lambda_B + C\Lambda_C + D\Lambda_D + E\Lambda_E \quad (28)$$

Using Einstein notation, we have:

$$\Lambda_{Aijkl} = \delta_{ij}\delta_{kl} \quad (29)$$

$$\Lambda_{Bijkl} = \hat{w}_{ij}\delta_{kl} + \delta_{ij}\hat{w}_{kl}$$

$$\Lambda_{Cijkl} = 8\hat{w}_{ij}\hat{w}_{kl} - \delta_{ij}\delta_{kl}$$

$$\Lambda_{Dijkl} = \delta_{kj}\delta_{il} + \delta_{lj}\delta_{ki} - 2\delta_{ij}\delta_{kl}$$

$$\begin{aligned} \Lambda_{Eijkl} = & 2(\hat{w}_{kj}\delta_{il} + \delta_{kj}\hat{w}_{il} - 2\hat{w}_{lj}\delta_{ki} - 2\delta_{lj}\hat{w}_{ki}) + \delta_{kj}\delta_{il} + \delta_{lj}\delta_{ki} \\ & - 2\delta_{ij}\delta_{kl} \end{aligned}$$

In that:

$$\hat{w}_{ij} = \hat{w}_i \hat{w}_j - \frac{1}{2} \delta_{ij} \quad (30)$$

\hat{w} is a unit column vector, and its components are the projections of the symmetry axis on the corresponding coordinate axes. An explicit representation can be found in Park and Levin (2016). In our algorithm, we convert this general 81-component elastic tensor to a 36-component tensor with 21 by Voigt notation (Aki and Richard, 2002).

2.4 Applications

In this section, we present and discuss applications of reflectivity computations: body wave mode conversion in layered anisotropic media, and birefringence in shear waves propagating through an anisotropic material. For the body wave mode conversion, we look at the P-S receiver functions and S-P records specially only the Z component. We consider the time series as a linear combination of delta functions and convolve them with source functions, here understood to describe the shape of the wave coming into the layered medium from below. As a result, a source function is not necessary for the computation which makes reflectivity a perfect tool for forward-modelling results of receiver function analysis (Chapter III for detailed introduction of methodology) and shear-wave splitting studies (Chapter I for detailed introduction of methodology) where the source functions are usually unknown or not important.

We use different descriptions of seismic anisotropy for the following examples to make it easier for interpretation purposes. Synthetic records and receiver functions are generated for a stack of anisotropic layers with hexagonal symmetry described using Backus notation (Backus, 1965). A shear-wave splitting simulation is performed for an SKS wave propagation in a layer of pure olivine, with anisotropy parameterized using a

general form of the elastic tensor that is oriented by means of a rotation matrix (see Supplementary Materials).

2.4.1 Examples of Outcome

Figure 3(a) and (c) show the example with P wave incident from the half space. The transmitted P wave (direct P) will arrive first at the receiver, following it is the P-to-S converted phase at the Moho, which we can observe clearly on the Radial component in Figure 3(c). We can also observe three major crustal multiples with conversions between P and S waves at different portions of their ray paths. We also look at the example with S wave incidence. The first phase arrives at the receiver is the S-to-P converted phase at the Moho given a faster speed of P wave. The direct S wave will arrive later and due to anisotropy in the crust, this S wave will split based on the strength of anisotropy and the thickness of the crust, thus two different phases can be observed. Similar as the P wave incidence case, we also look at three different crust multiples. Since the crustal multiples have much longer ray paths compared to the direct S wave, the delay times between the split shear waves will accumulate as shown in Figure 3(d).

2.4.2 Synthetic P-to-S Receiver Functions

2.4.2.1 Sharp Anisotropic Transitions within the Crust

In this model, we have three different layers in a 70-km-thick crust above a half space of isotropic mantle. We use this case to mimic a thick multi-layered anisotropic crust, similar to that of the Tibetan Plateau (e.g. Levin et al., 2008, Liu and Park, 2016). We adopt the Backus notation (Backus, 1965) in this example since it is more closely related to the symmetrical properties of the media and thus is easier for interpretation. Similar to Levin

and Park (1998) we set parameter $C=0$, which yields perfectly elliptical surfaces describing directional variation of seismic velocity.

To generate the receiver functions, we first compute synthetic seismograms with an incident P wave from an angular distance of 90° , and for all back azimuths from 0° to 350° , with a step of 5° . The sampling rate of synthetic seismograms is 20 sps, and a cosine-squared taper is applied to the final spectrum in the frequency domain to avoid the ringing effects after the inverse Fourier transform. Since the synthetic seismograms are noise-free, we can compute the synthetic receiver functions by simple spectral division (Ammon, 1991), which computes spectral ratios of the radial and transverse components over the vertical component and reduces the 3-component time series into 2-component receiver functions. Receiver functions are shown in Figure 4 at the spacing of 5° from 0° to 350° without any overlap or smoothing. Receiver functions generated in the paper have the same patterns as those produced by *rfsyn*, a synthetic receiver function simulator built on *anirec*, a forward modelling software package (in FORTRAN) to predict seismic wave propagation in layered anisotropic media (Levin and Park, 1997). Comparison figures and full references for the older software (<http://seiscode.iris.washington.edu/projects/rfsyn>) are in the Supplementary Materials.

In Figure 4(a), only radial receiver functions exist due to the isotropic properties of the material. In the radial receiver functions, clear P-S conversions from three different interfaces at the depths of 35 km, 50 km and 70 km arrive at approximately 4.4 s, 6.2 s and 8.8 s. All receiver function pulses have a positive polarity due to an increase in impedance with depth at all interfaces. For each interface, all pulses are perfectly aligned and do not change with back azimuth.

In Figure 4(b), the anisotropic receiver functions behave differently and both radial and transverse receiver functions can be observed. Pulses from three interfaces seen in radial receiver functions are present. On the Radial component phases P_{35s} and P_{50s} (conversions from 35 and 50 km depths) arrive at the same time as in the isotropic model, however their polarity changes to negative between 120° and 300° (directions normal to the orientation of the symmetry axis within the layer between 35 and 50 km). However, for P_{70s} , the arrival times shift according to the changes in back azimuths with the maximum at 9.2 s from back azimuths of 90° and 270° , and the minimum at 8.6 s from back azimuths of 0° and 180° . This conversion (labeled P_{70s}) clearly shows the effects of shear-wave splitting. On the transverse component, a two-lobed pattern (Levin and Park, 1997; Park and Levin, 2016) can be observed for P_{35s} , consistent with an expected effect of the dipping symmetry axis. Inversions of phase polarity happen at back azimuths of 30° and 210° corresponding to the direction of the symmetry axis. Similarly, a four-lobed pattern (Levin and Park, 1997; Park and Levin, 2016) in transverse receiver functions can be observed for P_{70s} with polarity changes roughly around 0° , 90° , 180° and 270° , aligned with and normal to the orientation of the symmetry axis in the lower anisotropic layer. For the mid-crust interface at the depth of 50 km the pattern is more complicated compared to the other two interfaces. Since this interface has the influence from both the dip and the orientation of the anisotropy symmetry axes, the two-lobed and four-lobed patterns are combined, and changes in polarity occur around back azimuths 15° and 235° .

2.4.2.2 Smooth Anisotropic Transitions within the Crust

In section 3.2.1, we present a model with sharp anisotropic transitions between anisotropic layers crust in the crust, which is a formulation commonly used in studies of lithospheric anisotropy. However, in certain scenarios, a sharp transition in elastic

properties is not the best choice. One possible example of a gradual change in properties is the distributed shear at the brittle-ductile transition between the upper and lower crust. In this section, we present receiver functions generated using models with smooth anisotropic transitions and compare them with those with sharp changes at the interfaces.

Similar to section 3.2.1, we use a model with three different layers in a 70-km-thick crust above a half space of isotropic mantle, which mimics a multi-layered anisotropic crust composed of different materials on continents. We insert a 10-km-thick transition zone between the depths of 40 km and 50 km within the anisotropic layer that extends from 35 to 50 km. We further divide this smooth transition zone into ten sublayers 1 km thick. In these layers, seismic velocities and densities remain the same as those of the original layer above the boundary at 50km, but the anisotropic parameters change in a systematic manner.

Three different situations are simulated with a smooth transition zone and the corresponding plots are shown in Figure 5(a)-(c). Comparison with anirec output (Levin & Park, 1997) can be found in the Supplementary Materials. In all cases we set $B=E=5\%$ in all sub-layers within the transition zone.

We follow the same procedures of generating P receiver functions as in section 3.2.1 and compare the results generated using models with and without a smooth transition zone. In Figure 5(a), we keep the same parameters as in Table 2 and change the symmetry axis tilt angle by 6° in each successive sublayer. It is obvious that the P to S conversions generated from the depth of 35 km and 70 km are the same as those in both radial and transverse receiver functions in Figure 4(b), however, the P to S conversions from the depth of 50km and from within the smooth transition zone are more complicated. For radial receiver functions, though P_{50s} appears at the same time as in Figure 4(b), instead of narrow

pulses we observe relatively wide ones, which reflects the influence of the smooth transition zone above the 50 km interface. Moreover, due to the existence of a smooth transition zone, those wide phases can be observed on all traces between ~ 4.9 s and ~ 6.2 s and their shapes are mostly not symmetric. Transverse receiver functions have directional patterns similar to the radial receiver functions, with a phase shift of 90° in back azimuth (cf. Park and Levin, 2016). Transverse components of the P_{50S} phase are enhanced with positive amplitudes from back azimuths ranges $0^\circ \sim 90^\circ$ and $150^\circ \sim 250^\circ$.

In Figure 5(b), we keep the same parameters as in Table 2 and change the symmetry axis azimuth from 30° to 90° in 6° steps. Similar to Figure 4(b), P to S conversion from the depth of 50 km can be observed around 6.2 s but from back azimuths $0^\circ \sim 180^\circ$, it is enhanced with a positive polarity on the Radial component and is weakened on the Transverse. Similar wide phases are observed between ~ 4.9 s and ~ 6.2 s. Different from Figure 4(b), the pulse shape of P_{50S} is relatively sharper and the wide pulses between P_{35S} and P_{50S} have a plateau-like shape.

In Figure 5(c), we gradually change both the tilt angle and the azimuth of the symmetry axis. The P_{50S} phase has a four-lobed pattern at ~ 6.2 s on both radial and transverse components, a significant difference with respect to cases shown in Figures 5(a)-(b). Broad pulses between ~ 4.9 s and ~ 6.2 s represent the energy radiated by the waves scattered from the interfaces within the smooth transition zone. These pulses have both symmetric plateau-like shape as in Figure 5(b) and non-symmetric shape as those in Figure 5(a), which seem to reflect the combined influence from both tilting and variation of azimuths of the symmetry axes in the smooth transition zone.

Putting Figures 5(a)-(c) together, it is interesting to notice that due to the smooth transitions zone between the depths of 40 km and 50 km, each interface between those thin layers generates P to S conversions and the scattered waves from those interfaces modify the original patterns of the receiver functions. The patterns at the smooth transition zone are very close on both radial and transverse receiver functions, however, there is always a directional phase difference between the radial and transverse receiver functions. In real data, those patterns in Figure 5(a)-(c) can hardly be distinguished from each other, thus the behavior in these synthetic cases suggests that a broader range of crustal models has the potential to represent similar behavior in crustal receiver functions.

2.4.3 Anisotropic Effects of S-to-P Conversions

The back azimuthal variations of the P-to-S conversions have been commonly adopted to explore the anisotropic properties in the Earth (Levin and Park, 1997, Liu and Niu, 2012, Park and Levin, 2016). A reverse conversion, from S to P, is a popular observation for studies of lower lithosphere (e.g. Ford et al., 2010, Abt et al., 2010, Hopper and Fischer, 2018), however the S-to-P conversions within the anisotropic media are not often explored. Having a better understanding of the back azimuthal variations of the S-to-P converted phases will help explain the observed patterns in time series and in Sp receiver functions, which would be especially useful when researchers are trying to understand the anisotropic properties associated with Earth's crust, the Lithosphere-Asthenosphere Boundary (LAB) and the Mid-Lithospheric Discontinuity (MLD) (Fischer et al., 2010). Here in this chapter, we adapt the synthetics to explore the back azimuthal variations of the Sp converted phase. We explore three different types of model with the anisotropic layer in the middle, bottom of the crust as well as the entire crust and for each model, we discuss

cases of vertically (SV) and horizontally (SH) polarized incident S waves. A cut-off frequency of 5Hz is adopted in the synthetics, which helps characterize the anisotropic patterns clearly. Most teleseismic S waves do not possess much energy at high frequencies, and therefore cannot easily resolve detailed layering within the Earth's crust. However, these simulations highlight physical behaviors that apply as well to coarser layering within Earth's deeper interior, such as within the lithospheric mantle and the asthenosphere.

We adopt the same isotropic parameters for all the cases that follow in this section, and we will only list the different anisotropic parameters in the corresponding models.

2.4.3.1 Anisotropic Layer in the Middle Crust

In Figure 6, we insert an anisotropic layer in the middle of the isotropic crust and discover the back azimuthal variations of S-to-P converted phases and the direct S phase at the free surface. Parameters adopted in this experiment are listed in Tables 4 and 5. In Figure 6(b), we observe a consistent negative phase from all back azimuths at around 8.7 s, which represents the S-to-P converted phase at the Moho. It is consistent since the layer above the Moho is isotropic and thus no back azimuthal variations in converted-wave amplitude are expected. This is further confirmed by Figure 6(c) where the incident shear wave is SH-type and thus no P wave is generated at around 8.7 s.

At ~10.2s, we observe a four-lobed pattern in Figure 6(b) with polarity changes at 10° , 80° , 190° and 260° . This phase represents the S-to-P conversion at the bottom of the anisotropic layer. In Figure 6(c), a four-lobed pattern is also detected but with polarity changes at 45° , 135° , 225° and 315° , which clearly reflects the effects of the horizontal strike of the symmetry axis being 45° . Compared to the same phase generated by an incident SV-type shear wave, this pattern has a polarity change which varies more regularly. At ~12.4 s, we observe a negative phase from all the back azimuths in Figure 6(b) but we

can still observe changes in the back azimuths and arrival times at around 100° , 160° , 270° and 330° . This negative phase implies that, for SV incidence, the influence of the impedance contrasts on Sp converted phases competes with the influence of anisotropy. In Figure 6(c), the four-lobed pattern is much clearer. The polarity changes for incident SH occur at the same back azimuths for interfaces at the top and bottom of the anisotropic layer, but the corresponding polarities are opposite.

The phase with the latest arrival at ~ 14.9 s represents the direct S wave. Similar to the SV-interaction with both internal crustal interfaces, the negative phase in Figure 6(b) represents the combined influence from the impedance contrasts and the horizontal orientation of the symmetry axis. In Figure 6(c), in addition to having a 4-lobed directional pattern, incident SH waves generate a phase of two different polarities which represent the two split waves as the incident shear wave propagates through the anisotropic layer within the crust.

Similar as in Figure 6, we insert an anisotropic layer in the middle of isotropic crust but instead of a horizontal symmetry axis, we tilt it to 45° from the vertical (Table 6). Similar as Figure 6(b) and 6(c), at ~ 8.7 s, we can observe a consistent negative phase in Figure 7(a) but no corresponding phase at all in Figure 7(b), which is consistent with the S-to-P converted phase at Moho that is also the bottom of an isotropic layer. However, the S-to-P phases converted at the bottom of the anisotropic layer arriving at around 10.2 s are quite different from those in Figure 6(b) and 6(c). In Figure 7(a), compared to a four-lobed pattern caused by a horizontal orientation of the symmetry axis, we observe a skewed two-lobed pattern with polarity changes at 165° and 285° which reflect the effects from the tilted symmetry axis. In Figure 7(b), this phase does have a symmetrical two-lobed pattern

with polarity changes at 45° and 225° . In Figure 7(a) at ~ 12.4 s, we observe strong negative pulses from 90° to 360° and much weaker positive pulses from the rest of the back azimuthal range. In Figure 7(b), this phase has a much clearer two-lobed pattern with polarity changes at the same back azimuths as the S-to-P converted phase at 8.7 s. At 15 s, we observe similar behaviors of the S wave as in Figure 6. In Figure 7(a), we observe a negative phase of shear wave and Figure 7(b) shows a four-lobed pattern for incident SH waves, with two split shear waves due to the anisotropic layer in the crust.

2.4.3.2 Anisotropic Layer in the Lower Crust

In this simulation we keep the same isotropic parameters of the crust but insert the anisotropic layer in the lower crust so that its bottom corresponds to the Moho (Table 7). In Figure 8(b), all converted phases have negative amplitudes which implies the effects from the impedance contrasts overwhelm those from anisotropy, however, we can still observe the anisotropic effects in both amplitudes and the arrival times. In Figure 8(b) at ~ 8.7 s, a relatively symmetrical two-lobed pattern can be observed. In Figure 8(c), different from examples in Figures 6 and 7, an incident S wave of SH polarization will generate a P wave at the Moho given the anisotropic layer at the bottom of the crust. A clear four-lobed pattern can be observed with polarity changes at 45° , 135° , 225° and 315° . Similarly, at 10.1 s, the S-to-P converted phase at the top of the anisotropic layer in the crust shows a two-lobed pattern in Figure 8(b) and a clear four-lobed pattern in Figure 8(c). In Figure 8(b) at ~ 12.4 s we observe negative phases of same amplitudes but different arrival times from different back azimuths. This is expected since the phase is the S-to-P conversion at the top of the isotropic layer which leads to no change in amplitudes and the different arrival times represent the effects of traversing the anisotropic layer in different directions. At the same time in Figure 8(c), we can observe two converted phases. Those two phases

are P waves converted at the top of the isotropic layer from a small SV wave formed by recombining two split shear waves generated when the SH wave propagates through the anisotropic layer. This conversion is much weaker compared to the other phases. Moreover, the converted P waves also have polarity changes at the same back azimuths as the previous two phases. At ~ 15 s, similar to Figure 6 and 7, we observe a negative phase in Figure 8(b) and two split phases in Figure 8(c).

We keep the same parameters of the model adopted in Figure 8 and only change the symmetry axis from horizontal to 45° tilted from the vertical. At 8.7 s, we observe a predominantly negative phase except between 195° and 255° in Figure 9(a), which reflects the effects of the tilted symmetry axis. At ~ 10.2 s, we also observe a two-lobed pattern with polarity changes at 130° and 320° . In Figure 9(b), at 8.6 s and 10.1 s, we find two symmetrical two-lobed patterns with opposite polarities but same polarity changes at 45° and 225° . Compared to the incident SV case in Figure 9(a), both converted phases in Figure 9(b) represent the effects from a tilted axis. A negative phase arrives at ~ 12.4 s in Figure 9(a). This phase has a consistent amplitude from all back azimuths but the arrival times shift slightly due to the anisotropic layer at the bottom. Correspondingly at the same time in Figure 9(b), we can observe two converted P waves generated by the two split shear waves from the anisotropic layer. Since the split phases from anisotropy are not as strong, the converted P waves do not show large amplitudes but their polarities do vary systematically according to the back azimuths. At around 15 s, which is similar as in Figure 8(b) and 8(c), we observe a negative phase in Figure 9(a) and a skewed four-lobed pattern for the direct S phases of different polarities in Figure 9(b).

2.4.3.3. Whole-crustal Anisotropy

Different from two previous models which only have parts of the crust being anisotropic, in Figure 10, we keep the same isotropic parameters in the crust but make the whole crust anisotropic as listed in Table 9. In Figure 10(b), incident SV waves generate four negative phases. The first is a S-to-P converted phase from the Moho that arrives at 8.8 s which is later compared to two previous examples given the anisotropic layer in this model is much thicker. Similar as in Figure 9(b), the converted phase at the Moho shows a two-lobed pattern but the changes in polarity are largely dominated by the impedance contrasts. For the incident SH waves at the same time in Figure 10(c), the converted P wave has a clear four-lobed pattern with polarity changes at 45° , 135° , 225° and 315° . In Figure 10(b), at time 10.2 s, the negative phases have similar amplitudes but different arrival times. The arrival times are relatively larger between $100^\circ \sim 190^\circ$ and $270^\circ \sim 340^\circ$, which also corresponds with the large negative amplitudes at 8.7 s. At ~ 12.5 s, we can observe the negative S-to-P phase converted from the shallowest interface. This phase also shows different arrival times at different back azimuths but compared to the phase at 10.2 s, the differences in arrival times are much larger. For the incident SH waves in Figure 10(c), we can observe two four-lobed patterns with polarity changes at 45° , 135° , 225° and 315° at the 10.2 s and 12.5 s. Within each of the pattern, the converted phase has two different pulses which come from the two split shear waves from the anisotropic layer. The converted phase at 12.5 s has a similar polarity as that at 10.2 s but the amplitudes are much larger. Between 14 s and 16 s, we find clear split shear waves in Figure 10(b). The differences in the arrival times are less than 1 s and the amplitudes of the two phases vary roughly every 90° . For the incident SH waves in Figure 10(c), two split phases can be

observed and they have a four-lobed pattern, however, the polarities of the phases are opposite.

In Figure 11, we still keep the whole crust anisotropic, however, we change the symmetry axis from horizontal to 45° tilted from the vertical, as done in the previous examples. At 8.6 s, incident SV waves generate weak positive pulses between the back azimuthal range of 195° and 255° and much stronger negative pulses beyond that range in Figure 11(a). Compared to Figure 10(b), this phase is not pure negative which represents the effects from the tilted symmetry axis. For incident SH waves at the same time in Figure 11(b), a clear two-lobed pattern is observed at 45° and 225° . The two-lobed pattern is different from the previous examples given that the arrival times differ according to the back azimuths. The arrival times increase for back azimuths close to 225° but decrease when they are close to 45° . We observe a similar pattern of the pulses at 10.2 s and 12.4 s for incident SV waves in Figure 11(a). Similar as Figure 11(a), both phases are negative from all back azimuths and the arrival times vary according to the back azimuths. Moreover, the differences between the arrival times at different back azimuths are larger at 12.4 s compared to 10.2 s. For incident SH waves in Figure 11(b), the converted phase at the top of the third layer is very weak and we can barely observe it. At 12.4 s, we can observe P waves converted from the split shear waves from the two middle anisotropic layers and it shows a four-lobed pattern. In Figure 11(b), between 14 s and 15 s, we find direct S waves with different arrival times however we do not observe as clearly the shear wave splitting analogous to Figure 10(b), which may indicate that the tilting of the symmetry axis may cancel out part of the anisotropic effects from the horizontal variation of the symmetry axis. In Figure 11(b), a similar four-lobed pattern as in Figure 10(c) can be observed with

polarity changes at 45° , 135° , 225° and 315° and the phase for individual back azimuth also has pulses at opposite polarities.

Based on the observations just described above, we find that when a shear wave propagates through anisotropic media, the amplitudes and the arrival times of S-to-P converted phases will vary according to the back azimuths. This observation is valid no matter what the initial polarization of the shear motion is. As we compare the vertical components of the time series generated using the same collection of models with both SV and SH-type incident shear waves, the patterns turn out to be quite different. For the SV-type incident waves, we find that the amplitudes of the phases are influenced by the impedance contrasts, which is not the case for the SH-type wave incidence. Thus, a broad selection of back azimuths with SH-incident waves might provide a clear simple anisotropic pattern in the time series. Moreover, both the four-lobed and two-lobed patterns generated with an incident SH-type wave are more clear and easier to identify. Once the isotropic effect is accounted for the anisotropic amplitude variation of the SV-to-P converted phase is phase-shifted with respect to the SH-to-P converted-wave amplitude. This offers the opportunity to detect anisotropy at a deep interface with Sp waves generated from varying initial polarizations. Though exploring the exact formulas for the converted phases with SV and SH-type of incident waves has been outside the scope of this chapter, the anisotropic patterns of the two cases are distinguishable in synthetic seismogram examples we produced. Because most teleseismic S waves are longer-period than those we model here, the behavior in these synthetics should transfer to cases where the interfaces are deeper and the layers thicker. For example, we can test whether the LAB and various boundaries proposed for the lithosphere in the 70 ~ 250-km depth range are associated

more with changes in anisotropic orientation, or else represent gradients in composition or partial-melt content (Fischer et al., 2010, Eaton et al., 2009).

2.4.4 Shear-wave Splitting Analysis

In this section, we present synthetic seismograms and discuss the effect of shear-wave splitting due to anisotropy caused by the alignment of olivine crystals. Olivine has an orthorhombic crystal system (Kumazawa and Anderson, 1969, Zhang and Karato, 1995), and in this paper, the initial setting of the olivine lattice is as below: a axis aligns with the X axis (radial axis), b axis aligns with the Y axis (anti-transverse axis) and c axis aligns with the Z axis (anti-vertical axis). We adopt Euler angles to describe the elastic tensor rotation from this original setting. Corresponding conventions and necessary formulae can be found in the Supplementary Materials. By default, the incident ray has a back azimuth of 0° , thus the X axis points to the South.

In the simulation, we focus on the ray-based system, keep our incoming ray fixed, and rotate the tensor to study the effects of anisotropy due to crystal alignments.

In the simulation of synthetic seismograms, anisotropic seismic properties of the medium are described by a 6 x 6 tensor (the exact tensor can be found in the Supplementary Materials) with elastic constants for the olivine crystal tensor obtained from Table 11 in Abramson et al. (1997).

In this simulation, we have a mantle model with a 50-km-thick anisotropic layer composed of pure olivine above a half space of isotropic mantle made of peridotite. The crystal lattice of olivine has the orientation as in the initial setting described previously. An SV-polarized plane wave simulating an SKS phase is incident from the half space into the anisotropic layer. We rotate the elastic tensor describing the properties of olivine, and

observe the corresponding effects on horizontal components of synthetic seismograms caused by the changes in the angle between the symmetry axis and the direction of SKS wave propagation. We simulate an SKS wave with an angular distance of 90° and calculate the ray parameter using iasp91 model in TauP toolkit (Crotwell et al., 1999). All other attributes of the time series are the same as those in Sections 3.1-3.3. To make the time series more realistic, we convolve the synthetics with a 1 s long sine-squared function.

Theoretically if the SKS wave is propagating along or orthogonal to the a axis of the olivine crystal lattice, no shear-wave splitting should be observed. As shown in Figures 12(a) and (c), no waveform can be observed on the transverse component in either of the two cases. Instead, only a converted compressional Sp wave with a small amplitude and a direct S wave are observed. Converted Sp wave arrives around 6 s and direct S wave arrives around 10.1 s in Figure 12(a), as the wave propagates along the a (fast) axis of the olivine crystal. In Figure 12(c), however, where the olivine tensor is rotated 90° and the wave travels along the relatively slow axis of the crystal, both phases arrive later compared to those in Figure 12(a).

In Figure 12(b), we rotate the orientation of the olivine crystal lattice 30° from the X axis to Y axis. Different from the synthetics in Figure 12(a) and (c), we can observe clear waveforms on the transverse component with the fast shear wave coming around 10.3 s and the slow shear wave coming around 11.6 s, thus a 1.3-second-delay is accumulated as the wave propagates. In this example, the analytical delay time can be calculated given the solutions of the Christoffel Equation which yield speeds of quasi-shear fast and slow waves of 4.94km/s and 4.39km/s. By using $\frac{h}{v_s} \times \cos j_s - \frac{h}{v_f} \times \cos j_f$ (where h is the thickness of the layer above the half space, j is the angle the ray path makes with the vertical, v is the shear

wave velocity, and subscripts s and f stand for slow and fast quasi shear waves, respectively), the angle can be calculated using the shear wave velocities and the horizontal slowness, finally we get a delay time of 1.3 s which is the same as what is shown in Figure 12(b).

In Figure 12(d), we show the synthetics generated by two layers of pure olivine with different geometries of the elastic tensor, as described in Table 11(b). We can see four distinct pulses appear on both radial and transverse components reflecting splitting of the shear waves in each of the layers. Since we rotate the tensor in the bottom layer by 90° , the slower b axis is aligned with the wave propagation direction, which causes the pulses in the radial component to slow down. This is reflected in Figure 12(d), where the most significant phase in transverse component precedes the corresponding phase in the radial component at the free surface. The other details in Figure 12(d) are not easy to interpret. This, at the same time, implies the potential of our algorithm in its applications to simulate wave propagation in anisotropic materials with low degrees of symmetry and build a direct link between seismic wave propagation and the mineral composition of the medium.

2.5 Summary

We provide the theoretical background for plane wave propagation through horizontally stratified anisotropic media and the synthetic seismograms using a reflectivity algorithm, which is light, fast and can simulate seismic wave propagation containing higher frequency components. Different from previous studies which focuses on a specific type of seismic anisotropy, we include the synthetics generated using anisotropic models described by a full tensor. We also include expressions for the Backus notation, a commonly used parameterizations describing higher orders of symmetry in the elastic

tensor. In the end, we present and discuss three potential applications of this algorithm: shear-wave splitting in a medium characterized by the full elastic tensor of olivine, and synthetic receiver functions as well as records for a hexagonally symmetric horizontally layered medium. Specially, we simulate receiver functions using models with a smooth transition zone and compare it with models only containing sharp interfaces. Moreover, we make different crustal models to explore the anisotropic effects of S-to-P conversions. These applications of reflectivity algorithm will be helpful for us to have a better understanding of the real observations and identify effects from different types of anisotropic structures.

2.6 Acknowledgments

This work was supported by the Rutgers School of Graduate Studies for the first author. Part of the figures are drafted using GMT (Wessel & Smith, 1999). The synthetic code and its corresponding waveforms are done using Matlab R2016a.

2.7 References

- Abramson, E.H., Brown, J.M., Slutsky, L.J. & Zaug, J., 1997. The elastic constants of San Carlos olivine to 17 GPa, *Medium: X*; Size: pp. 12253-12264.
- Abt, D., Fischer, K., French, S., Ford, H., Yuan, H. & Romanowicz, B., 2010. North American lithospheric discontinuity structure imaged by Ps and Sp receiver functions, *J. Geophys. Res.*, 115, B09301.
- Aki, K. & Richards, P.G., 2002. *Quantitative seismology*, edn, Vol., pp. Pages.
- Ammon, C.J., 1991. The isolation of receiver effects from teleseismic P waveforms, *Bulletin of the Seismological Society of America*, 81, 2504-2510.
- Anderson, D.L., 1989. *Theory of the Earth*, edn, Vol., pp. Pages, Blackwell scientific publications.
- Apfel, R.J. & Luco, J.E., 1983. On the Green's functions for a layered half-space. Part II, *Bulletin of the Seismological Society of America*, 73, 931-951.
- Backus, G.E., 1962. Long-wave elastic anisotropy produced by horizontal layering, *Journal of Geophysical Research*, 67, 4427-4440.
- Backus, G.E., 1965. Possible forms of seismic anisotropy of the uppermost mantle under oceans, *Journal of Geophysical Research*, 70, 3429-3439.
- Barruol, G., Silver, P.G. & Vauchez, A., 1997. Seismic anisotropy in the eastern United States: deep structure of a complex continental plate, *Journal of Geophysical Research: Solid Earth*, 102, 8329-8348.
- Beghein, C. & Trampert, J., 2003. Robust Normal Mode Constraints on Inner-Core Anisotropy from Model Space Search, *Science*, 299, 552.
- Bostock, M.G., 1997. Anisotropic upper-mantle stratigraphy and architecture of the Slave craton, *Nature*, 390, 392-395.
- Chapman, C.H. & Orcutt, J.A., 1985. The computation of body wave synthetic seismograms in laterally homogeneous media, 23, 105-163.
- Chen, X., 1993. A systematic and efficient method of computing normal modes for multilayered half-space, *Geophysical Journal International*, 115, 391-409.
- Christensen, N.I., 1984. The magnitude, symmetry and origin of upper mantle anisotropy based on fabric analyses of ultramafic tectonites, *Geophysical Journal International*, 76, 89-111.
- Crampin, S., 1970. The Dispersion of Surface Waves in Multilayered Anisotropic Media, *Geophysical Journal International*, 21, 387-402.
- Crampin, S., 1994. The fracture criticality of crustal rocks, *Geophysical Journal International*, 118, 428-438.
- Crampin, S. & Taylor, D.B., 1971. The Propagation of Surface Waves in Anisotropic Media, *Geophysical Journal International*, 25, 71-87.
- Crotwell, H.P., Owens, T.J. & Ritsema, J., 1999. The TauP Toolkit: Flexible Seismic Travel-time and Ray-path Utilities, *Seismological Research Letters*, 70, 154-160.
- Eaton, D.W., Darbyshire, F., Evans, R.L., Grütter, H., Jones, A.G. & Yuan, X., 2009. The elusive lithosphere–asthenosphere boundary (LAB) beneath cratons, *Lithos*, 109, 1-22.
- Farra, V. & Vinnik, L., 2000. Upper mantle stratification by P and S receiver functions, *Geophysical Journal International*, 141, 699-712.
- Fischer, K.M., Ford, H.A., Abt, D.L. & Rychert, C.A., 2010. The Lithosphere–Asthenosphere Boundary, 38, 551-575.

- Ford, H.A., Fischer, K.M., Abt, D.L., Rychert, C.A. & Elkins-Tanton, L.T., 2010. The lithosphere–asthenosphere boundary and cratonic lithospheric layering beneath Australia from Sp wave imaging, *Earth and Planetary Science Letters*, 300, 299-310.
- Fryer, G.J. & Frazer, L.N., 1987. Seismic waves in stratified anisotropic media — II. Elastodynamic eigensolutions for some anisotropic systems, *Geophysical Journal International*, 91, 73-101.
- Fuchs, 1968. The Reflection of Spherical Waves from Transition Zones with Arbitrary Depth-dependent Elastic Moduli and Density, *Journal of Physics of the Earth*, 16, 27-41.
- Fuchs & Müller, G., 1971. Computation of synthetic seismograms with the reflectivity method and comparison with observations, *Geophysical Journal International*, 23, 417-433.
- Gilbert, F. & Backus, G.E., 1966. Propagator matrices in elastic wave and vibration problems, *Geophysics*, 31, 326-332.
- Hess, H.H., 1964. Seismic Anisotropy of the Uppermost Mantle under Oceans, *Nature*, 203, 629.
- Holtzman, B., Kohlstedt, D.L., Zimmerman, M.E., Heidelbach, F., Hiraga, T. & Hustoft, J.J.S., 2003. Melt segregation and strain partitioning: Implications for seismic anisotropy and mantle flow, 301, 1227-1230.
- Hopper, E. & Fischer, K.M., 2018. The Changing Face of the Lithosphere-Asthenosphere Boundary: Imaging Continental Scale Patterns in Upper Mantle Structure Across the Contiguous U.S. With Sp Converted Waves, 19, 2593-2614.
- Karato, S.-i., 1999. Seismic anisotropy of the Earth's inner core resulting from flow induced by Maxwell stresses, *Nature*, 402, 871-873.
- Keith, C.M. & Crampin, S., 1977a. Seismic body waves in anisotropic media: propagation through a layer, *Geophysical Journal International*, 49, 209-223.
- Keith, C.M. & Crampin, S., 1977b. Seismic body waves in anisotropic media: reflection and refraction at a plane interface, *Geophysical Journal International*, 49, 181-208.
- Keith, C.M. & Crampin, S., 1977c. Seismic body waves in anisotropic media: synthetic seismograms, *Geophysical Journal International*, 49, 225-243.
- Kennett, 2013. Seismic wave propagation in stratified media, edn, Vol., pp. Pages, ANU Press.
- Kennett & Kerry, N.J., 1979. Seismic waves in a stratified half space, *Geophysical Journal International*, 57, 557-583.
- Kennett, B.L.N., 1974. Reflections, rays, and reverberations, *Bulletin of the Seismological Society of America*, 64, 1685-1696.
- Kern, H., Ivankina, T.I., Nikitin, A.N., Lokajíček, T. & Pros, Z., 2008. The effect of oriented microcracks and crystallographic and shape preferred orientation on bulk elastic anisotropy of a foliated biotite gneiss from Outokumpu, *Tectonophysics*, 457, 143-149.
- Kumazawa, M. & Anderson, O.L., 1969. Elastic moduli, pressure derivatives, and temperature derivatives of single-crystal olivine and single-crystal forsterite, *Journal of Geophysical Research*, 74, 5961-5972.

- Levin, V. & Park, J., 1997. P-SH conversions in a flat-layered medium with anisotropy of arbitrary orientation, *Geophysical Journal International*, 131, 253-266.
- Levin, V. & Park, J., 1998. P-SH conversions in layered media with hexagonally symmetric anisotropy: a cookbook, *Pure and Applied Geophysics*, 151, 669-697.
- Levin, V., Roecker, S., Graham, P. & Hosseini, A., 2008. Seismic anisotropy indicators in Western Tibet: Shear wave splitting and receiver function analysis, *Tectonophysics*, 462, 99-108.
- Liu, H. & Niu, F., 2012. Estimating crustal seismic anisotropy with a joint analysis of radial and transverse receiver function data, *Geophysical Journal International*, 188, 144-164.
- Liu, Z. & Park, J., 2016. Seismic receiver function interpretation: Ps splitting or anisotropic underplating?, *Geophysical Journal International*, 208, 1332-1341.
- Long & Becker, T.W., 2010. Mantle dynamics and seismic anisotropy, *Earth and Planetary Science Letters*, 297, 341-354.
- Long & Silver, P.G., 2009. Shear wave splitting and mantle anisotropy: measurements, interpretations, and new directions, *Surveys in Geophysics*, 30, 407-461.
- Long, M.D., 2009. Complex anisotropy in D'' beneath the eastern Pacific from SKS-SKKS splitting discrepancies, *Earth and Planetary Science Letters*, 283, 181-189.
- Long, M.D. & van der Hilst, R.D., 2006. Shear wave splitting from local events beneath the Ryukyu arc: Trench-parallel anisotropy in the mantle wedge, *Physics of the Earth and Planetary Interiors*, 155, 300-312.
- Luco, J.E. & Apsel, R.J., 1983. On the Green's functions for a layered half-space. Part I, *Bulletin of the Seismological Society of America*, 73, 909-929.
- Mainprice, D. & Nicolas, A., 1989. Development of shape and lattice preferred orientations: application to the seismic anisotropy of the lower crust, *Journal of Structural Geology*, 11, 175-189.
- Park & Levin, V., 2016. Anisotropic shear zones revealed by backazimuthal harmonics of teleseismic receiver functions, *Geophysical Journal International*, 207, 1216-1243.
- Park, J., 1996. Surface waves in layered anisotropic structures, *Geophysical Journal International*, 126, 173-183.
- Park, J. & Levin, V., 2000. Receiver Functions from Multiple-Taper Spectral Correlation Estimates, *Bulletin of the Seismological Society of America*, 90, 1507-1520.
- Peyton, V., Levin, V., Park, J., Brandon, M., Lees, J., Gordeev, E. & Ozerov, A., 2001. Mantle flow at a slab edge: Seismic anisotropy in the Kamchatka Region, 28, 379-382.
- Richards, P.G., 1971. Elastic wave solutions in stratified media, *Geophysics*, 36, 798-809.
- Silver & Chan, W.W., 1991. Shear-Wave Splitting and Subcontinental Mantle Deformation, *Journal of Geophysical Research-Solid Earth*, 96, 16429-16454.
- Silver, P., 1996. Seismic anisotropy beneath the continents: probing the depths of geology, *Annual Review of Earth and Planetary Sciences*, 24, 385-432.
- Thomsen, L., 1986. Weak elastic anisotropy, *Geophysics*, 51, 1954-1966.
- Vinnik, L.P., Farra, V. & Romanowicz, B., 1989. Azimuthal anisotropy in the Earth from observations of SKS at Geoscope and NARS broadband stations, *Bulletin of the Seismological Society of America*, 79, 1542-1558.

- Weiss, T., Siegesmund, S., Rabbel, W., Bohlen, T. & Pohl, M., 1999. Seismic velocities and anisotropy of the lower continental crust: a review. in *Seismic Exploration of the Deep Continental Crust*, pp. 97-122 Springer.
- Wookey, J. & Kendall, J.-M.J.W.D.A.G.U.G.M.S., 2007. Seismic anisotropy of post-perovskite and the lowermost mantle, 174, 171-189.
- Wu, B. & Chen, X., 2016. Stable, accurate and efficient computation of normal modes for horizontal stratified models, *Geophysical Journal International*, 206, 1281-1300.
- Yuan, H. & Levin, V., 2014. Stratified seismic anisotropy and the lithosphere-asthenosphere boundary beneath eastern North America, *Journal of Geophysical Research: Solid Earth*, 119, 3096-3114.
- Zhang, S. & Karato, S.-i., 1995. Lattice preferred orientation of olivine aggregates deformed in simple shear, *Nature*, 375, 774-777.

2.8 Figure Captions

Figure 1:

Illustrations of the model setup and the coordinate system conventions adopted in the derivation. (a) Horizontal lines stand for different interfaces with the corresponding depths marked on the right-hand side ($0 < Z_1 < Z_2 < \dots < Z_{N-1} < Z_N$). The tilted line stands for the wavefront of an incoming wave, and the black arrows show the direction of wave propagation. The red triangle stands for the receiver at the free surface. (b) conventions of the XYZ coordinate system in this algorithm are different from the normal RTZ coordinate system. A detailed description is given in the main text.

Figure 2:

Illustrations of positive polarity of the particle motion adopted in the algorithm, (view of the polarity convention in a vertical plane (Modified from Aki and Richards (2002))). The horizontal line stands for the interface which separates the elastic media above and below. Black arrows stand for the wave propagation directions, and red arrows stand for the positive polarity of particle motions for different types of waves.

Figure 3:

Illustrations of wave propagation and the corresponding 3-component waveforms generated using the same model in Table 1 with different types of incident waves. a) illustration of P wave incidence b) illustration of S wave incidence, in both cases, blue lines stand for the P wave ray paths and red lines stand for the S wave ray paths, the yellow triangles stand for the receivers. In b), we use two double arrows along the closest S wave ray path to represent the two split shear waves. In both cases, the distance of the earthquake is 90° and the back azimuth is 45° . c) waveforms generated with an incident P wave and major phases are marked with their names next them. The capital 'P' stands for the P wave incidence, the little 'p' or 's' stand for the converted wave types each time, 'm' stands the conversion at the Moho. d) waveforms generated with the S wave incidence and major phases are marked with their names next them. Conventions of the multiples are the same as in c).

Figure 4:

Radial and transverse synthetic P receiver functions. The incident P wave has an angular distance of 90° and the ray parameter is predicted using iasp91 model via the TauP toolkit (Crotwell et al., 1999). The highest frequency is limited to 10Hz. Converted phases from different interfaces are marked on the figures as P_{ds} where d is the depth of the interface in km. Parameters of the Earth model used to compute the synthetics are listed in Table 2. (a) and (b) adopt the same elastic model except in (a) the elastic materials are isotropic thus $B=C=E=0$.

Figure 5:

Radial and transverse synthetic P receiver functions generated using models in Table 3. The incident P wave has an angular distance of 90° and the ray parameter is

predicted using iasp91 model in TauP (Crotwell et al., 1999). Receiver functions are computed and plotted from 0° to 350° with a spacing of 5° without stacking or smoothing. The highest frequency is limited to 10Hz. (a) uses a model with a smooth transition zone which has a 6° -gradient in symmetry axis tilt angle. (b) uses a model with a smooth transition zone which has a 6° -gradient in symmetry axis azimuth. (c) uses a model with a smooth transition zone which has gradients of 6° in both the symmetry axis tilt angle and azimuth.

Figure 6:

Illustration of the anisotropic model and its ground motion generated by the reflectivity synthetic code. a) illustration of the model with incident shear waves at the Moho from an infinite half space, the cyan layer represents the anisotropic layer; b) vertical component of the time series for an incident S wave of SV type; c) vertical component of the time series for an incident S wave of SH type. In (b) and (c), time '0' is equivalent to time when the incident wave impinges at the Moho. All the synthetics are generated using a cut-off frequency of 5Hz.

Figure 7:

Illustration of the anisotropic model and its corresponding ground motion generated by the reflectivity code. a) vertical component of the time series of an incident S wave of SV type; b) vertical component of the time series of an incident S wave of SH type. In (a) and (b), time '0' is equivalent to time when the incident wave impinges at the Moho. All the synthetics are generated using a cut-off frequency of 5Hz.

Figure 8:

Illustration of the anisotropic model and its corresponding ground motion generated by the reflectivity code. a) illustration of the model with incident shear waves at the Moho from an infinite half space, the cyan layer represents the anisotropic layer; b) vertical component of the time series of an incident S wave of SV type; c) vertical component of the time series of an incident S wave of SH type. In (b) and (c), time '0' is equivalent to time when the incident wave impinges at the Moho. All the synthetics are generated using a cut-off frequency of 5Hz.

Figure 9:

Illustration of the anisotropic model and its corresponding ground motions generated by the reflectivity synthetic code. a) vertical component of the time series of an incident S wave of SV type; b) vertical component of the time series of an incident S wave of SH type. In (a) and (b), time '0' is equivalent to time when the incident wave impinges at the Moho. All the synthetics are generated using a cut-off frequency of 5Hz.

Figure 10:

Illustration of the anisotropic model and its corresponding ground motions generated by the synthetic code. a) illustration of the model with incident shear waves at the Moho from an infinite half space, the cyan layer represents the anisotropic layer; b) vertical component of the time series of an incident S wave of SV type; c) vertical component of the time series of an incident S wave of SH type. In (b) and (c), time '0' is equivalent to time when the incident wave impinges at the Moho. All the synthetics are generated using a cut-off frequency of 5Hz.

Figure 11:

Illustration of the anisotropic model and its corresponding ground motions generated by the reflectivity synthetic code. a) vertical component of the time series of an incident S wave of SV type; b) vertical component of the time series of an incident S wave of SH type. In (a) and (b), time '0' is equivalent to time when the incident wave impinges at the Moho. All the synthetics are generated using a cut-off frequency of 5Hz.

Figure 12:

Time series showing S wave propagated through a layer of pure olivine. (a) - (c) are simulation results using parameters in Table 11(a). (d) is the simulated results using parameters in Table 11(b).

2.9 Supplementary Figure Captions

Figure 1:

Synthetic examples for seismic wave propagation in VTI media. (a) synthetics generated by an incident P wave from the half space with an incident angle of 35° . (b) synthetics generated by an incident SV wave from the half space with an incident angle of 20° .

Figure 2:

Radial and transverse synthetic P receiver functions generated using rfsyn. Parameters are the same as in Figure 3 of the main text. The incident P wave has an angular distance of 90° and the ray parameter is predicted using iasp91 model via the TauP toolkit (Crotwell et al., 1999). The highest frequency is limited to 5Hz. Different interfaces are marked on the figures as Pds where d is the depth of the interface in km. Parameters of the Earth model used to compute the synthetics are listed in Table 1 in the main text. (a) and

(b) adopt the same elastic model except in (a) the elastic materials are isotropic thus $B=E=0$, and all the orientations of the symmetry axes and dipping axes are 0° .

Figure 3:

Radial and transverse synthetic P receiver functions generated by using the rfsyn. Parameters are the same as in Figure 4 of the main text. In Figure 2(a)-(c), a smooth transition zone is inserted between the depth of 40 and 50 km. The incident P wave has an angular distance of 90° and the ray parameter is predicted using iasp91 model in TauP (Crotwell et al., 1999). Receiver functions are computed and plotted from 0° to 350° with a spacing of 5° without stacking or smoothing. The highest frequency is limited to 5Hz. (a) uses a model with a smooth transition zone which has a 6° -gradient in symmetry axis tilt angle. (b) uses a model with a smooth transition zone which has a 6° -gradient in symmetry axis azimuth. (c) uses a model with a smooth transition zone which has gradients of 6° in both the symmetry axis tilt angle and azimuth.

2.10 Table Captions

Table 1:

Parameters of the model. From left to right are depths of the bottoms of the layers, compressional wave velocities, shear wave velocities, densities of the corresponding layers in the crust. B and E are the percentage anisotropy in Backus Notation (Backus, 1965); Tilt is the angle of the symmetry axis from the vertical and strike is the azimuth of the symmetry axis clockwise from the North.

Table 2:

Parameters of the model. From left to right are depths of the bottoms of the layers, compressional wave velocities, shear wave velocities, densities of the corresponding layers

in the crust. B and E are the percentage anisotropy in Backus Notation (Backus, 1965); Tilt is the angle of the symmetry axis from the vertical and strike is the azimuth of the symmetry axis clockwise from the North.

Table 3:

Parameters adopted in the model for generating receiver functions using the Backus notation. Notation and parameters are as in Table 2 except for a smooth transition zone in the anisotropic layer between 35 km and 50 km. Detailed description of the smooth transition zone for different cases illustrated in Figure 5 can be found in the main text.

Table 4:

Common isotropic parameters of the model. From left to right are the depths of the bottoms of the layers, compressional wave velocity, shear wave velocity and the density of the medium.

Table 5:

Parameters of the model. From left to right are depths of the bottoms of the layers, then B and E are the percentage anisotropy in Backus Notation (Backus, 1965); tilt is the angle of the symmetry axis from the vertical and strike is the azimuth of the symmetry axis clockwise from the North.

Table 6:

Parameters of the model. From left to right are depths of the bottoms of the layers, then B and E are the percentage anisotropy in Backus Notation (Backus, 1965); tilt is the angle of the symmetry axis from the vertical and strike is the azimuth of the symmetry axis clockwise from the North.

Table 7:

Parameters of the model. From left to right are depths of the bottoms of the layers, then B and E are the percentage anisotropy in Backus Notation (Backus, 1965); tilt is the angle of the symmetry axis from the vertical and strike is the azimuth of the symmetry axis clockwise from the North.

Table 8:

Parameters of the model. From left to right are depths of the bottoms of the layers, then B and E are the percentage anisotropy in Backus Notation (Backus, 1965); tilt is the angle of the symmetry axis from the vertical and strike is the azimuth of the symmetry axis clockwise from the North.

Table 9:

Parameters of the model. From left to right are depths of the bottoms of the layers, then B and E are the percentage anisotropy in Backus Notation (Backus, 1965); tilt is the angle of the symmetry axis from the vertical and strike is the azimuth of the symmetry axis clockwise from the North.

Table 10:

Parameters of the model. From left to right are depths of the bottoms of the layers, then B and E are the percentage anisotropy in Backus Notation (Backus, 1965); tilt is the angle of the symmetry axis from the vertical and strike is the azimuth of the symmetry axis clockwise from the North.

Table 11:

Parameters for the synthetic seismograms shown in Figure 12. N/A here means that the P and S wave velocities are not necessary because velocities will be computed based on the values of elastic tensor elements, orientation of the tensor symmetry axis, density,

and the direction of wave propagation. The last three columns are the Euler angles used for the tensor rotation. α is the angle describing a rotation around the z axis (anti vertical here) from X axis to Y axis. β is the angle rotating around the new X axis. γ is the angle rotating around the new Z axis. Detailed description can be found in Supplementary Materials. (a) parameters used in Figures 12(a)-(c) with three choices of α . The three values from left to right are used for Figure 12(a)-(c) correspondingly. (b) parameters used for Figure 12(d).

2.11 Figures

Figure 1:

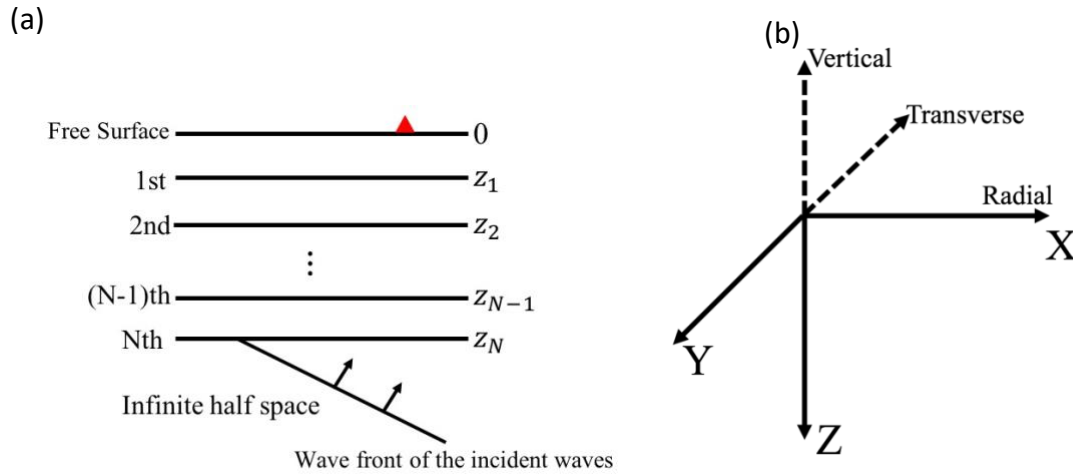


Figure 2:

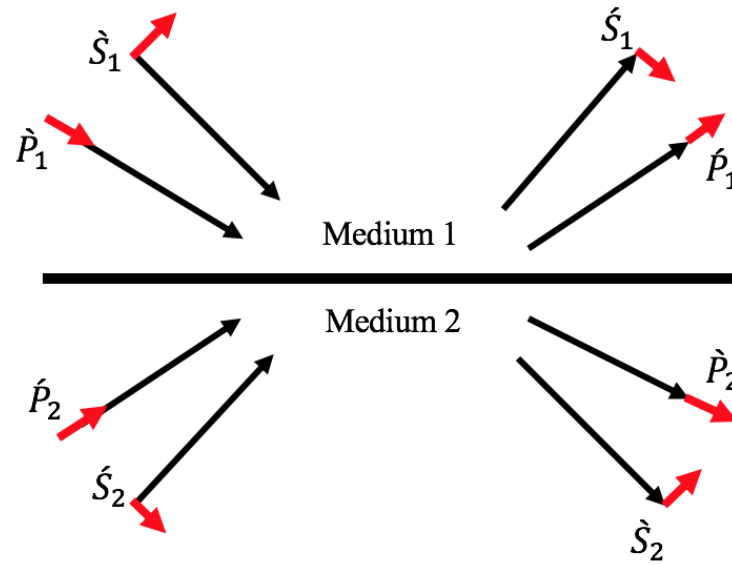


Figure 3:

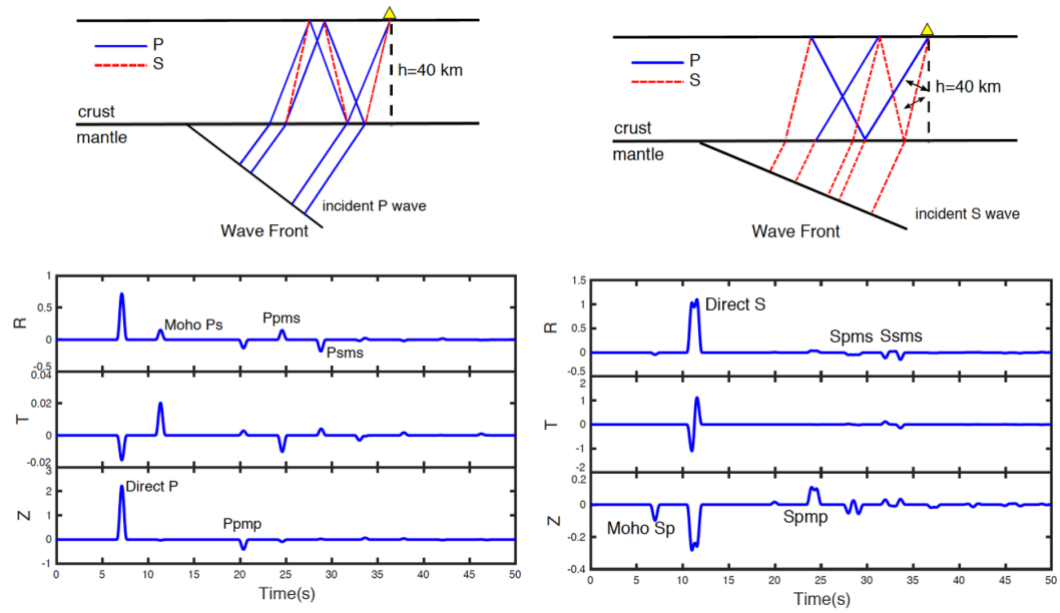


Figure 4:

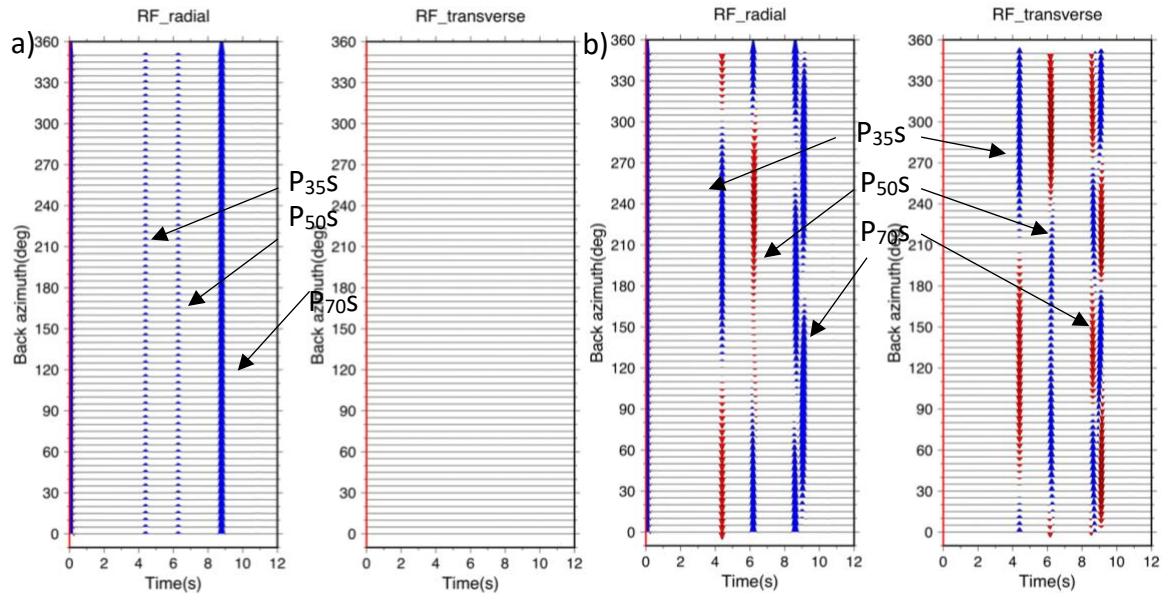
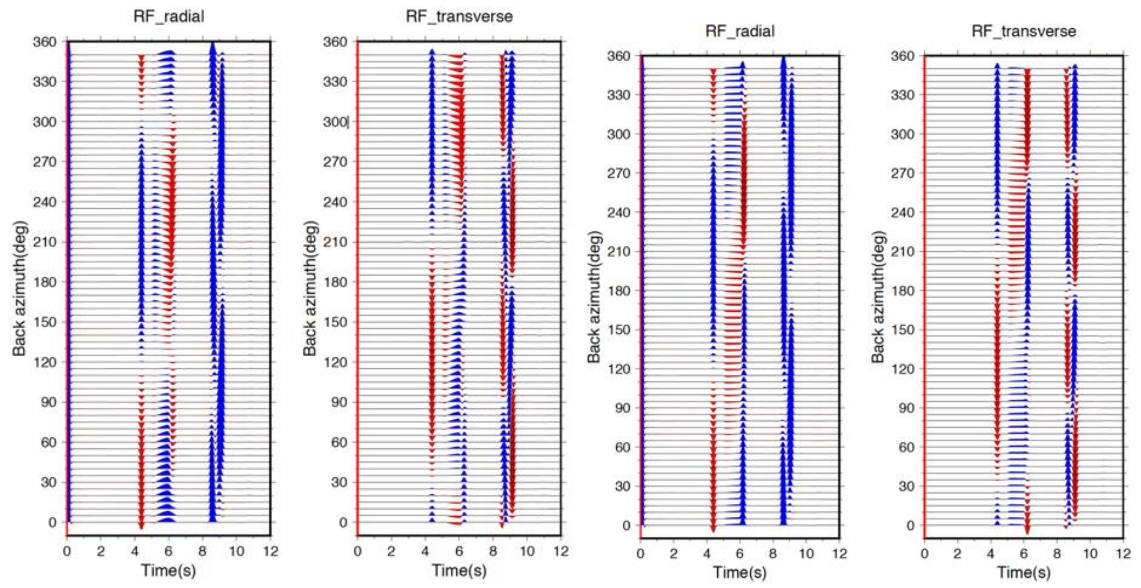


Figure 5:



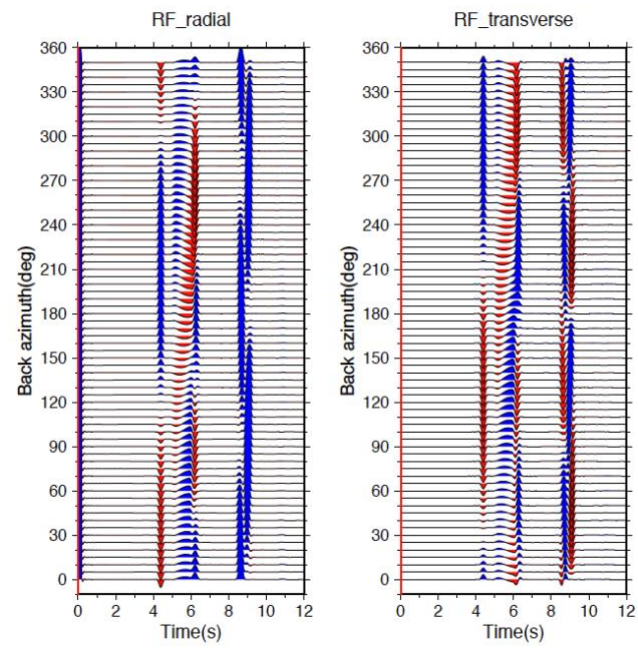


Figure 6:

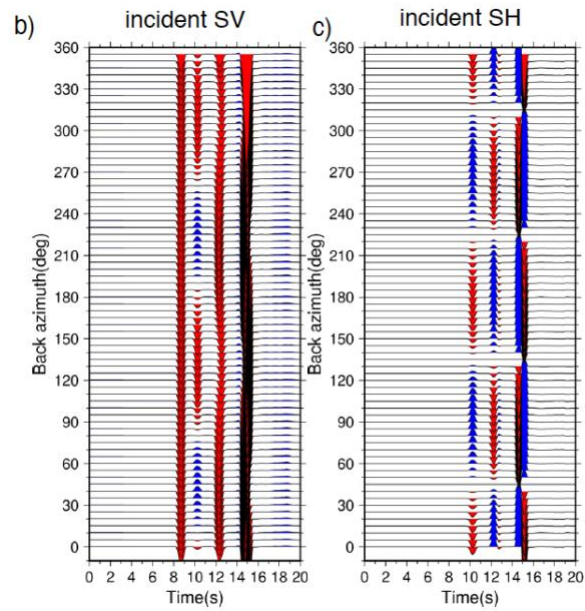
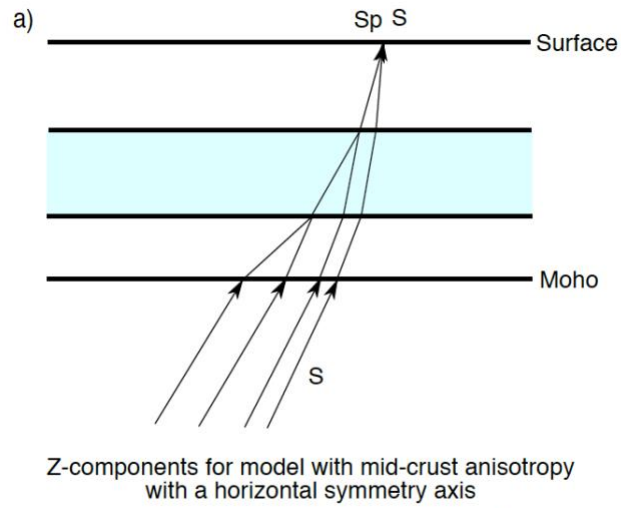


Figure 7:

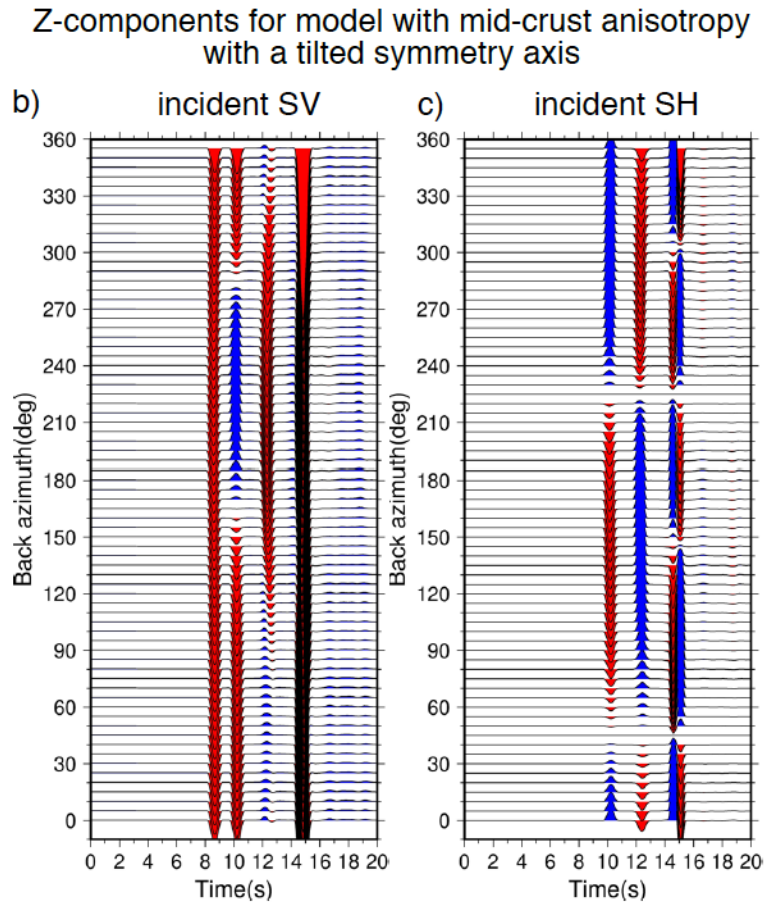


Figure 8:

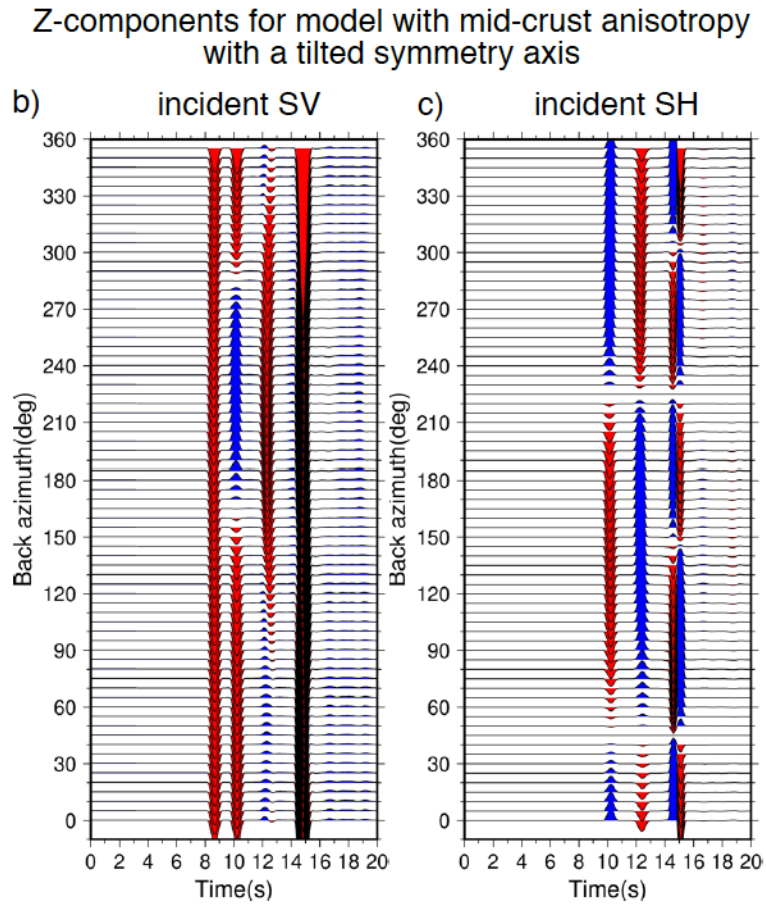
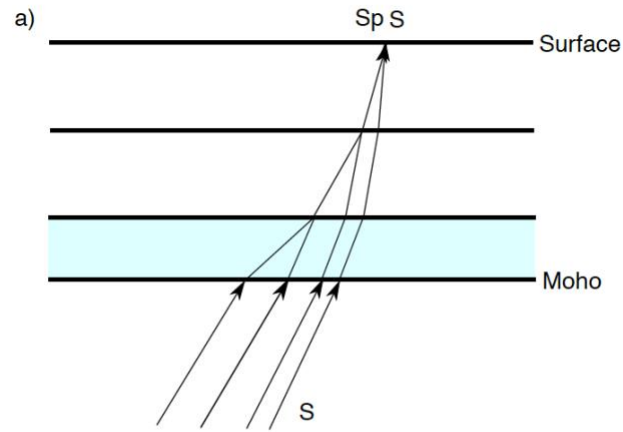


Figure 9:



Z-components for model with lower-crust anisotropy
with a horizontal symmetry axis

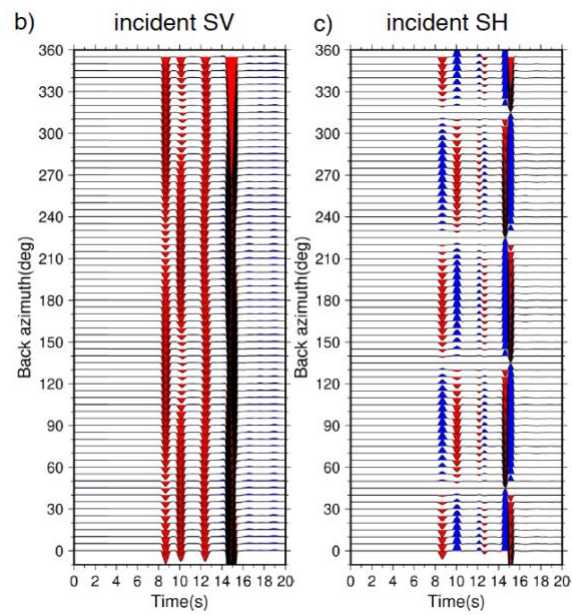


Figure 10:

Z-components for model with lower-crust anisotropy
with a tilted symmetry axis

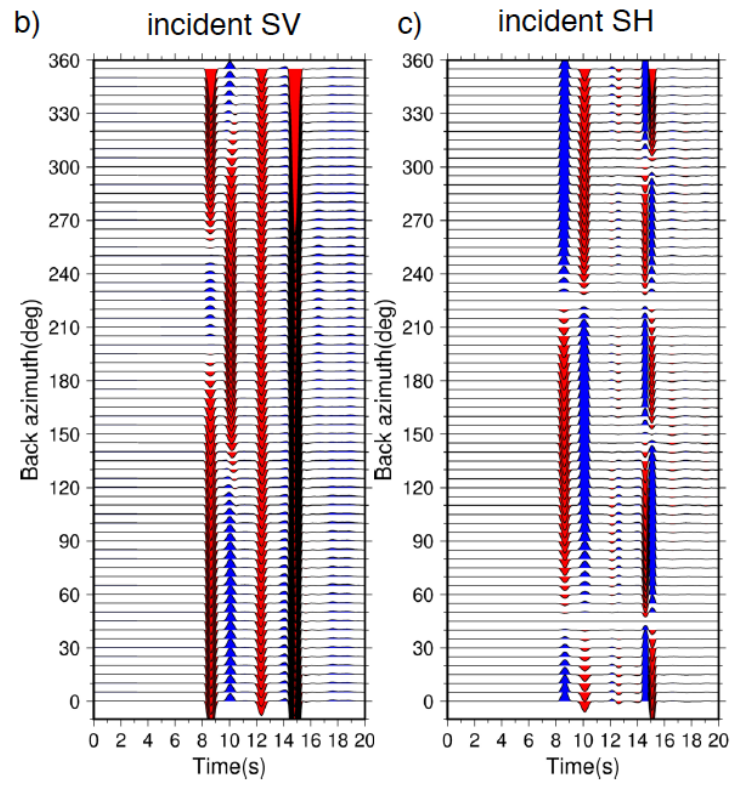
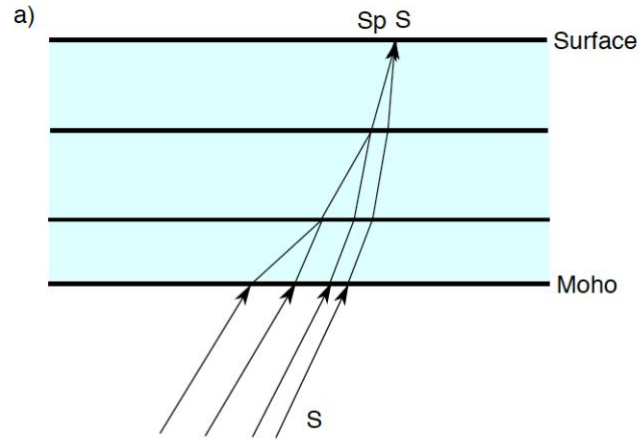


Figure 11:



Z-components for model with whole-crust anisotropy
with horizontal symmetry axes

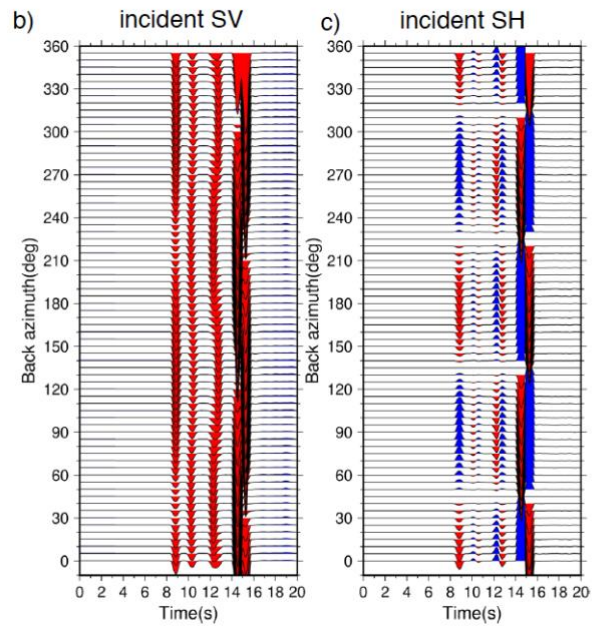


Figure 12:

Z-components for model with whole-crust anisotropy
with tilted symmetry axes

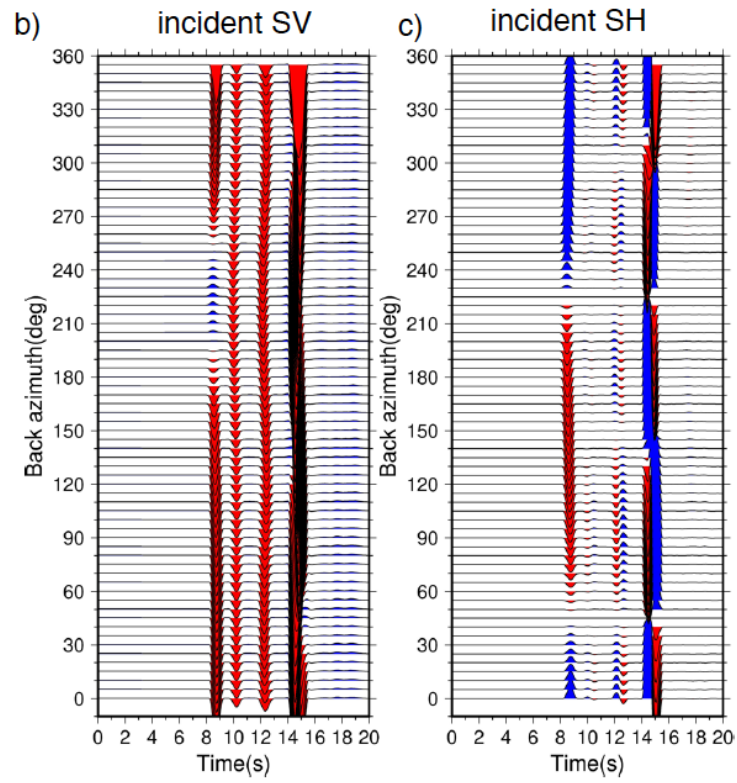
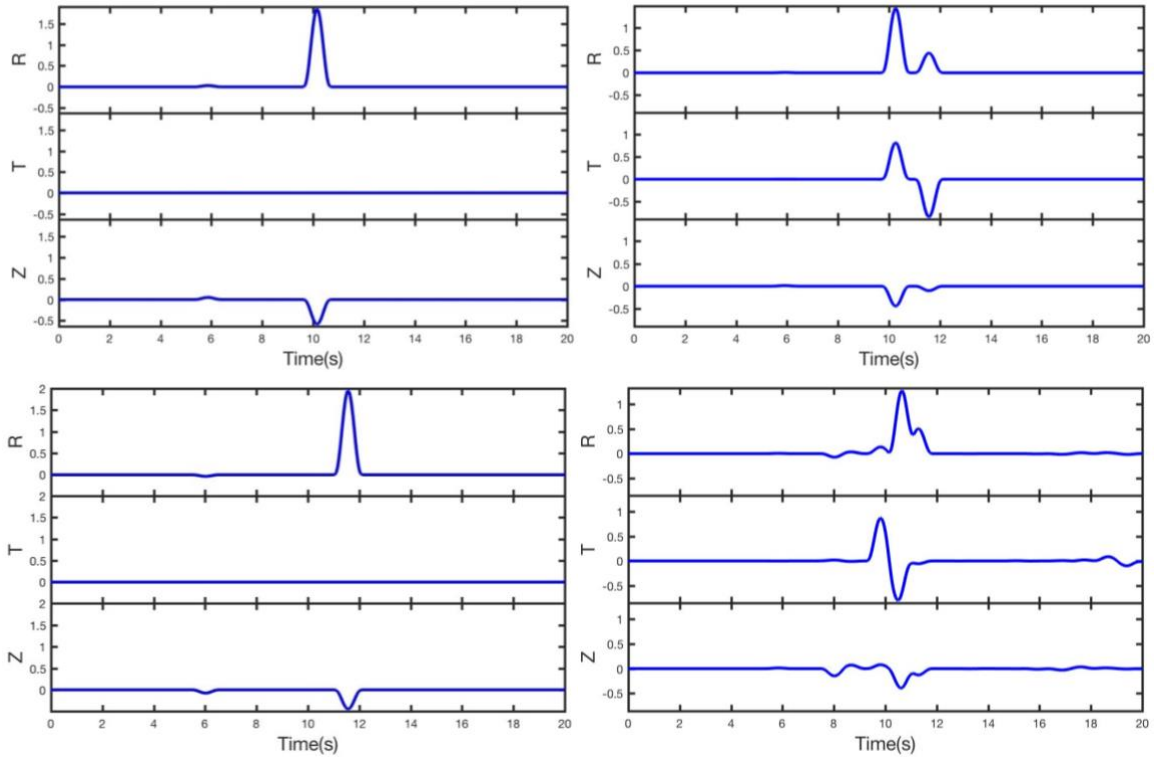
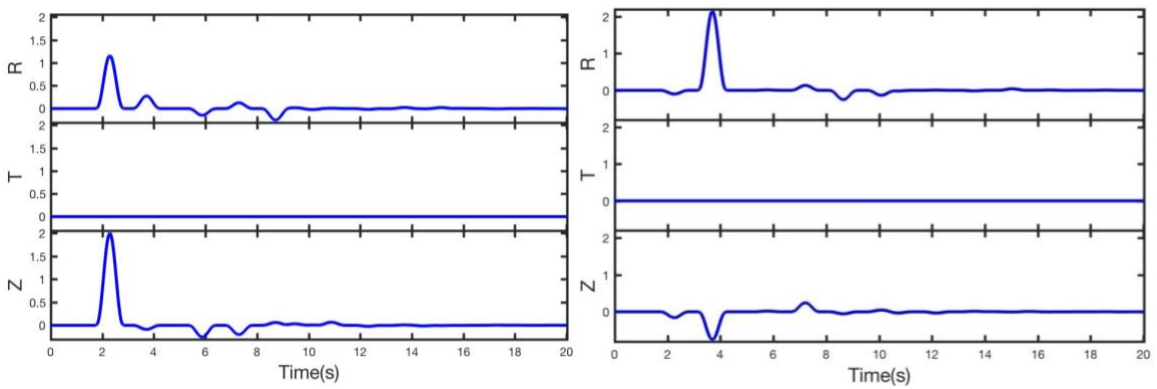


Figure 13:

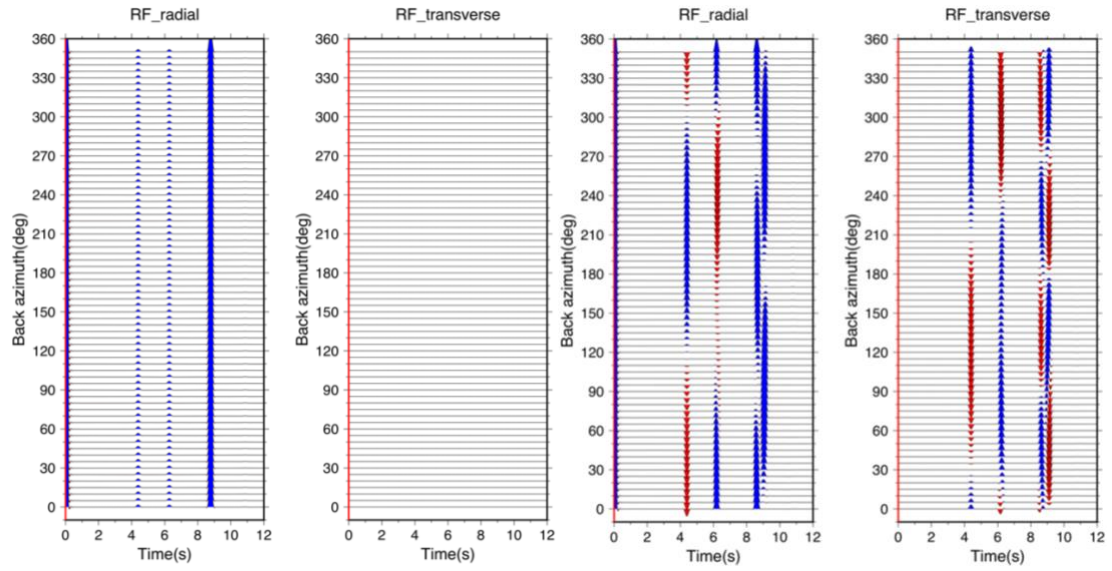


2.12 Supplementary Figures

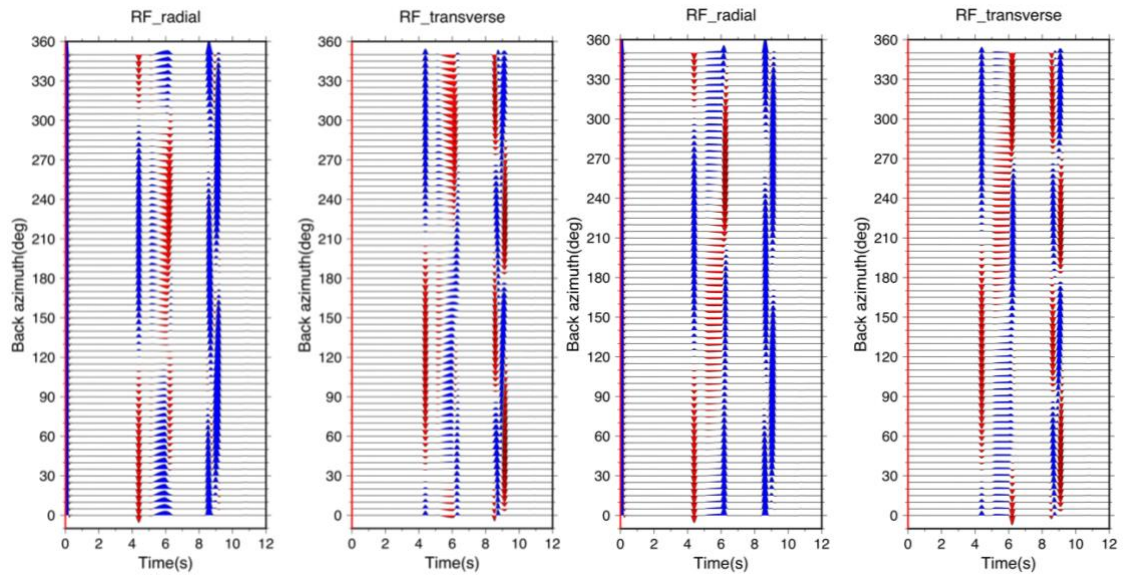
Supplementary Figure 1:

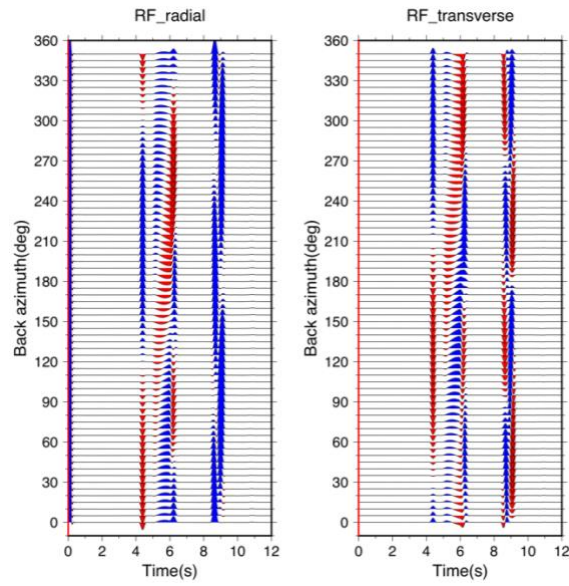


Supplementary Figure 2:



Supplementary Figure 3:





2.13 Tables

Table 1:

Depth (km)	Vp (km/s)	Vs (km/s)	Density (g/cm ³)	B/E (%)	Tilt (°)	Strike (°)
40	6.00	3.65	2.90	5	90	90
half space	8.30	4.60	3.30	0	0	0

Table 2:

Depth (km)	Vp (km/s)	Vs (km/s)	Density (g/cm ³)	B/E (%)	Tilt (°)	Strike (°)
35	6.00	3.45	2.65	0	0	0
50	6.30	3.55	2.80	5	30	30
70	6.60	3.65	2.90	-8	90	90
half space	8.30	4.60	3.30	0	0	0

Table 3:

Depth (km)	Vp (km/s)	Vs (km/s)	Density (g/cm³)	B/E (%)	Tilt (°)	Strike (°)
35	6.00	3.45	2.65	0	30	30
40	6.30	3.55	2.80	5	90	90
Smooth transition zone						
50	6.60	3.65	2.90	-8	90	90
70	6.60	3.65	2.90	-8	0	0
half space	8.30	4.60	3.30	0	0	0

Table 4:

Depth (km)	Vp (km/s)	Vs (km/s)	Density (g/cm³)
20.5	6.00	3.53	2.50
40.5	6.50	3.82	2.70
55.0	6.80	4.00	2.70
half space	8.00	4.44	3.30

Table 5:

Depth (km)	B/E (%)	Tilt (°)	Strike (°)
20.5	0	0	0
40.5	5	90	45
55.0	0	0	0
half space	0	0	0

Table 6:

Depth (km)	B/E (%)	Tilt (°)	Strike (°)
20.5	0	0	0
40.5	5	45	45
55.0	0	0	0
half space	0	0	0

Table 7:

Depth (km)	B/E (%)	Tilt (°)	Strike (°)
20.5	0	0	0
40.5	0	0	0
55.0	5	90	45
half space	0	0	0

Table 8:

Depth (km)	B/E (%)	Tilt (°)	Strike (°)
20.5	0	0	0
40.5	0	0	0
55.0	5	45	45
half space	0	0	0

Table 9:

Depth (km)	B/E (%)	Tilt (°)	Strike (°)
-----------------------	--------------------	---------------------	-----------------------

20.5	5	90	45
40.5	5	90	45
55.0	5	90	45
half space	0	0	0

Table 10:

Depth (km)	B/E (%)	Tilt (°)	Strike (°)
20.5	5	45	45
40.5	5	45	45
55.0	5	45	45
half space	0	0	0

Table 11:

Depth (km)	Vp (km/s)	Vs (km/s)	Density (g/cm ³)	α (°)	β (°)	γ (°)
50	N/A	N/A	3.3	0/30/90	0	0
half space	8.3	4.6	3.3	0	0	0

Depth (km)	Vp (km/s)	Vs (km/s)	Density (g/cm ³)	α (°)	β (°)	γ (°)
25	N/A	N/A	3.3	30	0	0

50	N/A	N/A	3.3	90	45	0
half space	8.3	4.6	3.3	0	0	0

2.14 Glossary

Parameters concerning the elastic properties of the material:

C_{ijkl} : component of the $3 \times 3 \times 3 \times 3$ elastic tensor with i, j, k, l permuting from 1 to 3; C_{pq} is a 6×6 symmetric matrix on which the 81-component elastic tensor is mapped by applying Voigt mapping rules, here p and q permute from 1 to 6

ρ : density of the elastic material

α : isotropic P wave velocity

β : isotropic S wave velocity

λ and μ : Lamè parameters

- **Backus notation:**

A, B, C, D, E : five numbers using Backus notation; A and D are Lamè parameters where $A = \lambda + 2\mu$ and $D = \mu$; B and C are peak-to-peak P wave anisotropy given by percent $\times A$; E is peak-to-peak S wave anisotropy given by percent $\times D$

ξ : the angle between the symmetry axis and the radial axis, positive if rotating from radial to the symmetry axis

Λ : elastic tensor when using Backus notation (this is to avoid the confusion with the Backus parameter C)

w : unit column vector, and its components are the projections of the symmetry axis on corresponding coordinate axes

- **Thomsen Parameter**

C : the elastic tensor for VTI media, c_{ij} is component of the corresponding elastic tensor for the VTI media

ε : half fractional change in P wave velocity , notice that this parameter does not have any subscripts so it is different from components of the strain tensor

γ : half fractional change in S wave velocity

δ : parameter that influences both P and S wave velocity at the same time

Parameters concerning the properties of the plane wave:

u_i : component of the displacement vector with i permuting from 1 to 3; \hat{u}_i represents the spectrum of u_i by using Fourier Transform

A : scalar amplitude of the total displacement for a given type of wave in plane wave solution

p_k : component of the unit polarization vector for displacement in plane wave solution with k permuting from 1 to 3

k_j : component of the wave number vector for a given type of wave with j permuting from 1 to 3

ω : angular frequency of the plane waves

p : horizontal slowness/ray parameter of the plane waves, notice that all six types of waves in the paper share the same horizontal slowness/ray parameter, this should be distinguished from p_k where a subscript is used to represent the polarization vector of the displacement in plane wave solution

v : vertical slowness of the wave

Parameters concerning the plane wave propagation:

τ_{ij} : component of the 3×3 stress tensor with i and j permuting from 1 to 3

τ_p : component of the stress vector on which the stress tensor is mapped by applying Voigt mapping rules with p permuting from 1 to 6

ε : the strain tensor, this should be distinguished from ε in Thomsen parameters specially when it is used in a general description of anisotropy

ε_{kl} : component of the 3×3 strain tensor with k and l permuting from 1 to 3

ε_p : component of the strain vector on which the stress tensor is mapped by applying Voigt mapping rules with p permuting from 1 to 6

G'_{ik} : component of the Christoffel Matrix represented by wavenumber with i and k permuting from 1 to 3

s : scalar slowness, s_j is one component of the slowness vector with j permuting from 1 to 3

G_{ik} : component of the Christoffel Matrix represented by slowness

$f(t)$: a function in time domain

$F(\omega)$: spectrum of $f(t)$ in frequency domain after Fourier Transform

\mathbf{b} : spectrum of displacement-stress vector of a given wave

$\mathbf{A}/\mathbf{A}(\mathbf{z})$: a constant matrix/coefficient for the propagator matrix

\mathbf{B}_z^j : spectrum of displacement-stress matrix for 6 types of waves; its superscript and subscript indicate that this matrix is calculated in the j th layer at the depth of z

\mathbf{E}_z^j : eigenvalue matrix for 6 types of waves; its superscript and subscript indicate that this matrix is calculated in the j th layer at the depth of z ; if its subscript is in numbers, then it represents a submatrix of the original eigenvalue matrix

$\mathbf{\Lambda}_z^j$: diagonal matrix controlling the phase change at the depth of z at the j th interface/in the j th layer; if its subscript is U/D, then this parameter is for an upgoing/downgoing wave

\mathbf{W}_z^j : spectrum of amplitude of the displacement-stress matrix in the j th layer at the depth of z ; if its subscript is U/D, then this parameter is for an upgoing/downgoing wave

$\mathbf{P}(\mathbf{z}, \mathbf{z}_0)$: propagator matrix connecting different depths from z_0 to z

\mathbf{T}_D^j : downgoing transmitted coefficients at the j th interface from the $(j-1)$ th interface including both the amplitude change and the phase change in the spectrum of displacement-stress matrix

\mathbf{R}_D^j : downgoing reflected coefficients at the j th interface from the $(j-1)$ th interface including both the amplitude change and the phase change in the spectrum of displacement-stress matrix

\mathbf{T}_U^j : upgoing transmitted coefficients at the j th interface from the $(j+1)$ th interface including both the amplitude change and the phase change in the spectrum of displacement-stress matrix; if $j=0$, it means that this interface is the free surface

\mathbf{R}_U^j : upgoing reflected coefficients at the j th interface from the $(j+1)$ th interface including both the amplitude change and the phase change in the spectrum of displacement-stress matrix; if $j=0$, it means that this interface is the free surface

$\hat{\mathbf{T}}_U^j$: generalized upgoing transmitted coefficients at the j th interface from the $(j+1)$ th interface including both transmission from below and reflection from above

$\hat{\mathbf{R}}_{UD}^j$: generalized upgoing reflected coefficients at the j th interface from the $(j+1)$ th interface including both transmission from above and reflection from below

Parameters concerning the tensor rotation option:

\mathbf{T}_1 : rotation matrix formed by rotating angle α around the z axis

\mathbf{T}_2 : rotation matrix formed by rotating angle β around the new x axis after rotating α around its corresponding axis

\mathbf{T}_3 : rotation matrix formed by rotating angle γ around the new z axis after rotating α and β around corresponding axes

\mathbf{x}' : a transformed vector after three rotations

\mathbf{x} : a vector before rotation transformation

\mathbf{T}_σ : strain transformation matrix

\mathbf{T}_ϵ : stress transformation matrix

$\boldsymbol{\tau}^t$: transformed stress tensor

\mathbf{C}^t : transformed elastic tensor

2.15 Appendix

This appendix documents all the details of how we can calculate the seismic velocity, then the displacements of seismic waves given the elastic tensor, the density of the material and the ray parameter of the incident wave.

We separate this appendix into three parts. In Part I, we will look at how to get the Christoffel Equation, since the eigenvalues of the Christoffel Equation are the velocities and the corresponding eigenvectors show the polarization of the particle motion. In Part II, we will look at how we can calculate the eigenvalues and eigenvectors in three different cases, isotropic medium (in terms of Lamé Parameters); Hexagonal symmetry (in terms of A, C, F, L, N); Orthorhombic (in terms of A, B, C, D, E) and the most general cases where we need 21 components. Here we will just assume the wave is propagating only in x-z plane. In Part III, we let the wave propagate through the medium and calculate the displacements.

Part I. Calculate the Christoffel Equation

Note: Throughout this document, we adopt the Einstein notation and here I repeat this rule again since we are going to try expanding the index notation with the permutation of 1, 2, 3 of each index.

Repeated indices are implicitly summed over, and it is a summation index. It is also called a **dummy index** since any symbol can replace it without changing the meaning of the expression provided. An index that is not summed over is a **free index** and should appear only once per term. If such an index does appear, it usually also appears in terms belonging to the same sum, with the exception of special values such as zero. We also need to make sure that the indices left after your calculation should be the same on both sides.

Two dots above one parameter means to take the second derivative of this parameter over time. If there is a comma in subscript of one parameter, it means to take the partial derivative of this parameter over certain direction, for instance, $u_{i,j} = \frac{\partial u_i}{\partial x_j}$.

We first start to derive the equation of motion, which is essentially the Newton's second law. We let u be the displacement vector of the particle motion, u_i refers to the i th component of the displacement ("i" permutates from 1 to 3). Thus we have,

$$\rho \ddot{u}_i = \sigma_{ij,j}$$

Consider Hooke's law, we relate the stress tensor with the strain tensor using the stiffness matrix and rewrite the Newton's law:

$$\sigma_{ij} = C_{ijkl} \varepsilon_{kl}$$

$$\rho \ddot{u}_i = C_{ijkl} \varepsilon_{kl,j}$$

Expand this, we have,

$$\rho \ddot{u}_i = C_{ijkl} \cdot \frac{1}{2} (u_{k,lj} + u_{l,kj}) = C_{ijkl} u_{k,jl}$$

Now we have the displacement on both sides of the equation and we know the format of the solution of the displacement, we can rewrite the equation above like:

$$u_i = A p_i e^{i(\omega t - k_i x_i)}$$

A is the amplitude of the displacement, and p_i controls how the amplitude is partitioned onto each direction, it is a unit vector. We write out the formulation on both sides, we have:

$$-\omega^2 \rho u_i = -C_{ijkl} k_j k_l u_k$$

Reorganize the equation above, we have the Christoffel Equation:

$$-\omega^2 \rho u_i = -C_{ijkl} k_j k_l u_k$$

$$(C_{ijkl} k_j k_l - \rho \omega^2 \delta_{il}) u_k = 0$$

We know that Christoffel Matrix can thus be defined as below:

$$M_{ij} = C_{ijkl} k_j k_l$$

To simplify our following derivation, we let

$$G_{il}' = C_{ijkl} k_j k_k - \rho \omega^2 \delta_{il}$$

Till now we derived the Christoffel Equation using wavenumbers, now we can convert the wavenumber into slowness. By using the following relationship, s is the slowness and k is the wavenumber, ω is the angular frequency.

$$s = \frac{k}{\omega}$$

we can rewrite the equation

$$C_{ijkl}k_jk_ku_l - \rho\omega^2u_i = 0$$

as below:

$$(C_{ijkl}s_js_k - \rho\delta_{il})u_l = 0$$

Take one step further, we have:

$$|C_{ijkl}s_js_k - \rho\delta_{il}| = 0$$

Then we ask $G_{il} = C_{ijkl}s_js_k - \rho\delta_{il}$ to simplify our notation. By looking at the order of the tensor, we know that the Christoffel matrix here or to be exact, the G_{il} is a second order matrix which should have nine components and it is symmetric at the same time due to the symmetric property of the stiffness tensor. It is enough for us to just calculate the six components.

To show the most general case, here we will just provide the example of the first component of this matrix and start from the calculation using slowness vector $s=(s_1, s_2, s_3)$.

During the derivation here, we also switch to the Voigt notation, recall the rules of the Voigt notation: 11→1, 22→2, 33→3, 23 or 32 →4, 13 or 31 →5, 12 or 21 → 6.

$$\begin{aligned}
 G_{11} &= C_{1jk1} s_j s_k - \rho \delta_{11} \\
 &= C_{1111} s_1 s_1 + C_{1121} s_1 s_2 + C_{1131} s_1 s_3 + C_{1211} s_2 s_1 + C_{1221} s_2 s_2 + C_{1231} s_2 s_3 \\
 &\quad + C_{1311} s_3 s_1 + C_{1321} s_3 s_2 + C_{1331} s_3 s_3 - \rho \\
 &= C_{11} s_1^2 + C_{16} s_1 s_2 + C_{15} s_1 s_3 + C_{61} s_1 s_2 + C_{66} s_2^2 + C_{65} s_2 s_3 + C_{51} s_3 s_1 + C_{56} s_3 s_2 \\
 &\quad + C_{55} s_3^2 - \rho
 \end{aligned}$$

In our case, since the wave only propagate in x-z plane, thus the second component of the slowness vector is zero. Now we can write out the nine components of the G as below:

$$G_{11} = C_{11} s_1^2 + 2C_{15} s_1 s_3 + C_{55} s_3^2$$

Following the same strategy, we can have all the other components and here we write them together.

$$\begin{aligned}
 G_{11} &= C_{11} s_1^2 + 2C_{15} s_1 s_3 + C_{55} s_3^2 - \rho \\
 G_{12} &= C_{16} s_1^2 + (C_{14} + C_{56}) s_1 s_3 + C_{54} s_3^2 \\
 G_{13} &= C_{15} s_1^2 + (C_{13} + C_{55}) s_1 s_3 + C_{53} s_3^2 \\
 G_{22} &= C_{66} s_1^2 + 2C_{64} s_1 s_3 + C_{44} s_3^2 - \rho \\
 G_{23} &= C_{65} s_1^2 + (C_{63} + C_{45}) s_1 s_3 + C_{43} s_3^2
 \end{aligned}$$

$$G_{33} = C_{55}s_1^2 + 2C_{53}s_1s_3 + C_{33}s_3^2 - \rho$$

If you are interested, you can do the same thing to the other three independent components (G_{21}, G_{31}, G_{32}) and you will find that

$$G_{21} = G_{12}; G_{31} = G_{13}; G_{32} = G_{23}$$

To expand with the components, $s=(p, 0, v)$, we have $s_1 = p$ and $s_3 = v$, then we can rewrite all components of G_{ij} as below:

$$G_{11} = C_{11}p^2 + 2C_{15}pv + C_{55}v^2 - \rho$$

$$G_{12} = G_{21} = C_{16}p^2 + (C_{14} + C_{56})pv + C_{54}v^2$$

$$G_{13} = G_{31} = C_{15}p^2 + (C_{13} + C_{55})pv + C_{53}v^2$$

$$G_{22} = C_{66}p^2 + 2C_{64}pv + C_{44}v^2 - \rho$$

$$G_{23} = G_{32} = C_{65}p^2 + (C_{63} + C_{45})pv + C_{43}v^2$$

$$G_{33} = C_{55}p^2 + 2C_{53}pv + C_{33}v^2 - \rho$$

Now we have the Christoffel Equation for a given stiffness matrix and if you would like to try to count the number of the independent components of the stiffness matrix, you will see that we do only need 21 components.

Part II. Calculation of eigenvalues and eigenvectors

Here we will start by using the special case of wave propagation through a homogenous isotropic medium without any interfaces. Then we will look at different kinds of symmetry of axis.

1. Isotropic medium

Following what we have in Part I, if we represent the stiffness matrix using the Lamé parameters, we will have the following matrix:

$$C_{ij} = \begin{bmatrix} \lambda + 2\mu & \lambda & \lambda & 0 & 0 & 0 \\ \lambda & \lambda + 2\mu & \lambda & 0 & 0 & 0 \\ \lambda & \lambda & \lambda + 2\mu & 0 & 0 & 0 \\ 0 & 0 & 0 & \mu & 0 & 0 \\ 0 & 0 & 0 & 0 & \mu & 0 \\ 0 & 0 & 0 & 0 & 0 & \mu \end{bmatrix}$$

We thus can calculate the Christoffel Matrix given the stiffness matrix above, to make the calculation easier, we can choose the P wave is propagation along the x axis, thus $p=1/c$:

$$G_{11} = (\lambda + 2\mu)p^2 - \rho$$

$$G_{12} = G_{21} = 0$$

$$G_{13} = G_{31} = 0$$

$$G_{22} = \mu p^2 - \rho$$

$$G_{23} = G_{32} = 0$$

$$G_{33} = \mu p^2 - \rho$$

Thus, we have the determinant to be

$$\begin{vmatrix} (\lambda + 2\mu)p^2 - \rho & 0 & 0 \\ 0 & \mu p^2 - \rho & 0 \\ 0 & 0 & \mu p^2 - \rho \end{vmatrix} = 0$$

It is thus easy to calculate the determinant as below:

$$[(\lambda + 2\mu)p^2 - \rho](\mu p^2 - \rho)^2 = 0$$

We will see the solutions are

$$\sqrt{\frac{(\lambda + 2\mu)}{\rho}}, \sqrt{\frac{\mu}{\rho}}, \sqrt{\frac{\mu}{\rho}}$$

with corresponding eigenvectors to be (1, 0, 0), (0, 1, 0), (0, 0, 1). Here we simplify our selection of the wave propagation direction to align with the x axis, and this makes our life so much easier, but here we will look at the case where we have the wave not propagating along the x axis. Remember that the eigenvalue is actually the wave speed, since we are dealing with the isotropic case at this moment, we should have the eigenvalues of the Christoffel equation the same in value, regardless of the wave propagation direction. But we need to be careful when looking at the eigenvectors since the eigenvectors will change according to the wave propagation direction, and it should align with the wavenumber direction.

To relate our results with the angle, we do a little trick here to introduce the directional dependence. We make θ to be the angle between the wavefront and positive x axis, we have the horizontal slowness $p=\sin(\theta)/v$, v is the velocity of the wave, if we times v^2 for every components in the Christoffel matrix, this will not influence the solution of the eigenvalue problem. In this case, the Christoffel Equation is as below:

$$G_{11} = (\lambda + 2\mu)\sin^2\theta + \mu\cos^2\theta - \rho v^2$$

$$G_{12} = G_{21} = 0$$

$$G_{13} = G_{31} = (\lambda + \mu)\sin\theta\cos\theta$$

$$G_{22} = \mu\sin^2\theta + \mu\cos^2\theta - \rho v^2 = \mu - \rho v^2$$

$$G_{23} = G_{32} = 0$$

$$G_{33} = \mu\sin^2\theta + (\lambda + 2\mu)\cos^2\theta - \rho v^2$$

Thus, we have the determinant to be

$$\begin{vmatrix} (\lambda + 2\mu)\sin^2\theta + \mu\cos^2\theta - \rho v^2 & 0 & (\lambda + \mu)\sin\theta\cos\theta \\ 0 & \mu - \rho v^2 & 0 \\ (\lambda + \mu)\sin\theta\cos\theta & 0 & \mu\sin^2\theta + (\lambda + 2\mu)\cos^2\theta - \rho v^2 \end{vmatrix} = 0$$

Now we calculate the determinant,

$$\begin{aligned} & [(\lambda + 2\mu)\sin^2\theta + \mu\cos^2\theta - \rho v^2](\mu - \rho v^2)[\mu\sin^2\theta + (\lambda + 2\mu)\cos^2\theta - \rho v^2] \\ & - [(\lambda + \mu)\sin\theta\cos\theta](\mu - \rho v^2)[(\lambda + \mu)\sin\theta\cos\theta] = 0 \end{aligned}$$

Apparently, $(\mu p^2 - \rho)$ occurs at both ends and this will definitely give us a solution which is $\sqrt{\frac{\mu}{\rho}}$, and the corresponding vector is $(0, 1, 0)$, and we know that is the SH wave.

Now we will just drop $\mu p^2 - \rho$ and we reorganize the equation, we have

$$[(\lambda + 2\mu)\sin^2\theta + \mu\cos^2\theta - \rho v^2][\mu\sin^2\theta + (\lambda + 2\mu)\cos^2\theta - \rho v^2] \\ = [(\lambda + \mu)\sin\theta\cos\theta]^2$$

$$[(\lambda + \mu)\sin^2\theta + \mu - \rho v^2][(\lambda + \mu)\cos^2\theta + \mu - \rho v^2] \\ = [(\lambda + \mu)\sin\theta\cos\theta]^2 + (\mu - \rho v^2)[((\lambda + \mu)(\sin^2\theta + \cos^2\theta))] + (\mu - \rho v^2)^2 \\ = [(\lambda + \mu)\sin\theta\cos\theta]^2$$

$$(\mu - \rho v^2)[((\lambda + \mu)(\sin^2\theta + \cos^2\theta))] + (\mu - \rho v^2)^2 \\ = (\mu - \rho v^2)(\lambda + \mu + \mu - \rho v^2) = 0$$

$$(\mu - \rho v^2)(\lambda + 2\mu - \rho v^2) = 0$$

Thus, we calculate two other solutions, they are $\sqrt{\frac{(\lambda+2\mu)}{\rho}}$, $\sqrt{\frac{\mu}{\rho}}$, and they have nothing to do with the direction of wave propagation. If we put them back into the matrix, we have

$$\begin{bmatrix} -(\lambda + \mu)\cos^2\theta & 0 & (\lambda + \mu)\sin\theta\cos\theta \\ 0 & (\lambda + \mu) & 0 \\ (\lambda + \mu)\sin\theta\cos\theta & 0 & -(\lambda + \mu)\sin^2\theta \end{bmatrix} \begin{bmatrix} x_1 \\ x_2 \\ x_3 \end{bmatrix} = 0$$

$$\begin{bmatrix} (\lambda + \mu)\sin^2\theta & 0 & (\lambda + \mu)\sin\theta\cos\theta \\ 0 & -(\lambda + \mu) & 0 \\ (\lambda + \mu)\sin\theta\cos\theta & 0 & (\lambda + \mu)\cos^2\theta \end{bmatrix} \begin{bmatrix} x_1 \\ x_2 \\ x_3 \end{bmatrix} = 0$$

But when we look at their corresponding eigen vectors, we have

$$\sqrt{\frac{(\lambda + 2\mu)}{\rho}} \sim (\sin\theta, 0, \cos\theta)$$

$$\sqrt{\frac{\mu}{\rho}} \sim (\cos\theta, 0, -\sin\theta)$$

Notice that the three eigenvectors are orthogonal to each other, and $(\sin\theta, 0, \cos\theta)$ is the wave propagation direction.

2. Hexagonal symmetry

Here we will switch to the hexagonal symmetry with a vertical symmetry axis (which is also the transverse isotropy). We will follow the same routine here, and start from the stiffness matrix:

$$C = \begin{bmatrix} A & A - 2N & F & 0 & 0 & 0 \\ A - 2N & A & F & 0 & 0 & 0 \\ F & F & C & 0 & 0 & 0 \\ 0 & 0 & 0 & L & 0 & 0 \\ 0 & 0 & 0 & 0 & L & 0 \\ 0 & 0 & 0 & 0 & 0 & N \end{bmatrix}$$

To calculate the components of the G, we will adopt the notation of using the angle instead of the slowness here, then we have

$$G_{11} = A\sin^2\theta + L\cos^2\theta - \rho v^2$$

$$G_{12} = G_{21} = 0$$

$$G_{13} = G_{31} = (F + L)\sin\theta\cos\theta$$

$$G_{22} = N\sin^2\theta + L\cos^2\theta - \rho v^2$$

$$G_{23} = G_{32} = 0$$

$$G_{33} = L\sin^2\theta + C\cos^2\theta - \rho v^2$$

$$\begin{vmatrix} A\sin^2\theta + L\cos^2\theta - \rho v^2 & 0 & (F + L)\sin\theta\cos\theta \\ 0 & N\sin^2\theta + L\cos^2\theta - \rho v^2 & 0 \\ (F + L)\sin\theta\cos\theta & 0 & L\sin^2\theta + C\cos^2\theta - \rho v^2 \end{vmatrix} = 0$$

Write out the determinant, we have

$$(A\sin^2\theta + L\cos^2\theta - \rho v^2)(N\sin^2\theta + L\cos^2\theta - \rho v^2)(L\sin^2\theta + C\cos^2\theta - \rho v^2) -$$

$$[(F + L)\sin\theta\cos\theta][(F + L)\sin\theta\cos\theta](N\sin^2\theta + L\cos^2\theta - \rho v^2) = 0$$

Apparently we have,

$$N\sin^2\theta + L\cos^2\theta - \rho v^2 = 0$$

We will have the one eigenvalue as $\sqrt{\frac{N\sin^2\theta + L\cos^2\theta}{\rho}}$, here I leave out the eigenvector, since the expansion of the representation is too complicated and it might be easier if you can specify the wavenumber.

Then we will look at the other part of the equation there by dropping $N\sin^2\theta + L\cos^2\theta - \rho v^2$,

$$(A\sin^2\theta + L\cos^2\theta - \rho v^2)(L\sin^2\theta + C\cos^2\theta - \rho v^2) - [(F + L)\sin\theta\cos\theta][(F + L)\sin\theta\cos\theta] = 0$$

$$(\rho v^2)^2 - (\rho v^2)(A\sin^2\theta + L\cos^2\theta + L\sin^2\theta + C\cos^2\theta) + (A\sin^2\theta + L\cos^2\theta)(L\sin^2\theta + C\cos^2\theta) - [(F + L)\sin\theta\cos\theta]^2 = 0$$

$$(\rho v^2)^2 - (\rho v^2)(A\sin^2\theta + L + C\cos^2\theta) + (AL\sin^4\theta + AC\sin^2\theta\cos^2\theta + L^2\sin^2\theta\cos^2\theta + CL\cos^4\theta - F^2\sin^2\theta\cos^2\theta - 2FL\sin^2\theta\cos^2\theta - L^2\sin^2\theta\cos^2\theta) = 0$$

The two solutions for ρv^2 is that

$$\frac{(A\sin^2\theta + L + C\cos^2\theta) \pm \sqrt{\Delta}}{2}$$

Now we calculate Δ separately, we will have

$$\begin{aligned}
\Delta &= A^2 \sin^4 \theta + C^2 \cos^4 \theta + L^2 + 2AL \sin^2 \theta + 2CL \cos^2 \theta + 2AC \sin^2 \theta \cos^2 \theta - 4AL \sin^4 \theta \\
&\quad - 4AC \sin^2 \theta \cos^2 \theta - 4CL \cos^4 \theta + 4F^2 \sin^2 \theta \cos^2 \theta + 8FL \sin^2 \theta \cos^2 \theta \\
&= A^2 \sin^4 \theta + 2AL \sin^2 \theta (1 - 2 \sin^2 \theta) + C^2 \cos^4 \theta + 2CL \cos^2 \theta (1 - 2 \cos^2 \theta) + L^2 \\
&\quad + F^2 (\sin 2\theta)^2 + 2FL (\sin 2\theta)^2 - 2AC \sin^2 \theta \cos^2 \theta \\
&= A^2 \sin^4 \theta + 2AL \sin^2 \theta \cos 2\theta + C^2 \cos^4 \theta - 2CL \cos^2 \theta \cos 2\theta - 2AC \sin^2 \theta \cos^2 \theta + L^2 \\
&\quad + F^2 (\sin 2\theta)^2 + 2FL (\sin 2\theta)^2 \\
&= (A \sin^2 \theta - C \cos^2 \theta)^2 + 2L \cos 2\theta (A \sin^2 \theta - C \cos^2 \theta) + (L \cos 2\theta)^2 + F^2 (\sin 2\theta)^2 \\
&\quad + 2FL (\sin 2\theta)^2 + L^2 - (L \cos 2\theta)^2 \\
&= (A \sin^2 \theta + L \cos 2\theta - C \cos^2 \theta)^2 + F^2 (\sin 2\theta)^2 + 2FL (\sin 2\theta)^2 + L^2 (\sin 2\theta)^2 \\
&= (A \sin^2 \theta - L \sin^2 \theta + L \cos^2 \theta - C \cos^2 \theta)^2 + (F + L)^2 \sin^2 2\theta \\
&= ((A - L) \sin^2 \theta + (L - C) \cos^2 \theta)^2 + (F + L)^2 \sin^2 2\theta
\end{aligned}$$

Now that we will have two other eigenvalues, as below:

$$\sqrt{\frac{(A \sin^2 \theta + L + C \cos^2 \theta) \pm \sqrt{\Delta}}{2\rho}}$$

In that,

$$\Delta = ((A - L)\sin^2\theta + (L - C)\cos^2\theta)^2 + (F + L)^2\sin^2 2\theta$$

We can see clearly here that the velocities do depend on the wave propagation direction. Following the same logic, we put the calculated eigenvalues back into the equation and calculate two other eigen vectors.

We first try

$$v = \sqrt{\frac{(A\sin^2\theta + L + C\cos^2\theta) + \sqrt{\Delta}}{2\rho}}$$

Thus,

$$\rho v^2 = \frac{(A\sin^2\theta + L + C\cos^2\theta) + \sqrt{\Delta}}{2}$$

Now we rewrite each term within the following matrix and we have

$$\begin{bmatrix} A\sin^2\theta + L\cos^2\theta - \rho v^2 & 0 & (F + L)\sin\theta\cos\theta \\ 0 & N\sin^2\theta + L\cos^2\theta - \rho v^2 & 0 \\ (F + L)\sin\theta\cos\theta & 0 & L\sin^2\theta + C\cos^2\theta - \rho v^2 \end{bmatrix}$$

$$A\sin^2\theta + L\cos^2\theta - \rho v^2 = \frac{1}{2}(A\sin^2\theta + L\cos 2\theta - C\cos^2\theta - \sqrt{\Delta})$$

$$(F + L)\sin\theta\cos\theta = \frac{1}{2}(F + L)\sin 2\theta$$

$$L\sin^2\theta + C\cos^2\theta - \rho v^2 = \frac{1}{2}(C\cos^2\theta - A\sin^2\theta - L\cos 2\theta - \sqrt{\Delta})$$

If we put them back into each component of the matrix, it is easy for us to find that the y component in the eigenvector is zero. We use x and z to represent the first and third components of the eigenvector and solve the following equation:

$$\frac{1}{2}(A\sin^2\theta + L\cos 2\theta - C\cos^2\theta - \sqrt{\Delta})x + \frac{1}{2}(F + L)\sin 2\theta z = 0$$

$$\frac{1}{2}(F + L)\sin 2\theta x + \frac{1}{2}(C\cos^2\theta - A\sin^2\theta - L\cos 2\theta - \sqrt{\Delta})z = 0$$

Here we use $W = A\sin^2\theta + L\cos 2\theta - C\cos^2\theta$ and $V = (F + L)\sin 2\theta$, then rewrite it

$$Vx + (-W - \sqrt{\Delta})z = 0$$

Now we make $z=1$, the eigenvector is $(\frac{V}{W+\sqrt{\Delta}}, 0, 1)$;

Repeat the same procedure, the only difference is that we need

$$\rho v^2 = \frac{(A\sin^2\theta + L + C\cos^2\theta) - \sqrt{\Delta}}{2}$$

It is easy to know that

$$Vx + (-W + \sqrt{\Delta})z = 0$$

Again we make $z=1$, the eigenvector is $(\frac{V}{W-\sqrt{\Delta}}, 0, 1)$;

Till now, we have the three corresponding pairs of eigenvalues and eigenvectors as below:

$$\sqrt{\frac{(A\sin^2\theta + L + C\cos^2\theta) + \sqrt{\Delta}}{2\rho}} \sim (\frac{V}{W+\sqrt{\Delta}}, 0, 1)$$

$$\sqrt{\frac{(A\sin^2\theta + L + C\cos^2\theta) - \sqrt{\Delta}}{2\rho}} \sim (\frac{V}{W-\sqrt{\Delta}}, 0, 1)$$

$$\sqrt{\frac{N\sin^2\theta + L\cos^2\theta}{\rho}} \sim (0, 1, 0)$$

In that

$$\Delta = ((A - L)\sin^2\theta + (L - C)\cos^2\theta)^2 + (F + L)^2\sin^2 2\theta$$

$$W = A\sin^2\theta + L\cos 2\theta - C\cos^2\theta$$

$$V = (F + L)\sin 2\theta$$

To test whether the two eigenvectors are orthogonal to each other, we calculate their inner product, we have

$$(\frac{V}{W+\sqrt{\Delta}}, 0, 1) \cdot (\frac{V}{W-\sqrt{\Delta}}, 0, 1) = \frac{V^2}{W^2 - \Delta} + 1 = \frac{V^2 + W^2 - \Delta}{W^2 - \Delta}$$

Since $L\cos 2\theta = L\cos^2\theta - L\sin^2\theta$, we can rewrite W to be

$$W = A\sin^2\theta + L\cos 2\theta - C\cos^2\theta = (A - L)\sin^2\theta + (L - C)\cos^2\theta$$

Thus it is easy to see that $V^2 + W^2 = \Delta$, the two eigenvectors are orthogonal to each other, however their absolute value will depend on the angle between the wave front and the x axis.

3. Random symmetry, the most general case

Recall the relationship between the Christoffel Equation and the stiffness matrix,

$$\begin{aligned} G_{11} &= C_{11}s_1^2 + 2C_{15}s_1s_3 + C_{55}s_3^2 - \rho \\ G_{12} &= C_{16}s_1^2 + (C_{14} + C_{56})s_1s_3 + C_{54}s_3^2 \\ G_{13} &= C_{15}s_1^2 + (C_{13} + C_{55})s_1s_3 + C_{53}s_3^2 \\ G_{22} &= C_{66}s_1^2 + 2C_{64}s_1s_3 + C_{44}s_3^2 - \rho \\ G_{23} &= C_{65}s_1^2 + (C_{63} + C_{45})s_1s_3 + C_{43}s_3^2 \\ G_{33} &= C_{55}s_1^2 + 2C_{53}s_1s_3 + C_{33}s_3^2 - \rho \end{aligned}$$

In general, we only need the following 15 components of the stiffness matrix, and they are $C_{11}, C_{15}, C_{55}, C_{16}, C_{14}, C_{56}, C_{45}, C_{31}, C_{35}, C_{66}, C_{46}, C_{44}, C_{36}, C_{34}, C_{33}$ (here we only talk about the case where the waves are propagating in x - z planes so that we leave out some terms with s_2 , where we will leave out 6 other independent components). The way it works is that we need the help of some packages or functions to calculate the eigenvalues and

eigenvectors for us. We can try to use `polyeig()` function in Matlab, as input, we need to reorganize our Christoffel Equation here, and separate them based on the order of horizontal and vertical slownesses. This solution is applicable to olivine too, but we will look at that case in the next session since we can write out the full representation and compare it with Levin and Park (1998)

$$\begin{aligned} \mathbf{G} = & p^2 \begin{bmatrix} C_{11} & C_{16} & C_{15} \\ C_{16} & C_{66} & C_{56} \\ C_{15} & C_{56} & C_{55} \end{bmatrix} + pv \begin{bmatrix} 2C_{15} & C_{14} + C_{56} & C_{55} + C_{31} \\ C_{14} + C_{56} & 2C_{46} & C_{14} + C_{36} \\ C_{55} + C_{31} & C_{45} + C_{36} & 2C_{35} \end{bmatrix} \\ & + v^2 \begin{bmatrix} C_{55} & C_{45} & C_{35} \\ C_{45} & C_{44} & C_{34} \\ C_{35} & C_{34} & C_{33} \end{bmatrix} - \rho \begin{bmatrix} 1 & 0 & 0 \\ 0 & 1 & 0 \\ 0 & 0 & 1 \end{bmatrix} = p^2 \mathbf{T} + pv \mathbf{S} + v^2 \mathbf{R} - \rho \mathbf{I} \end{aligned}$$

$\mathbf{T}, \mathbf{S}, \mathbf{R}, \mathbf{I}$ are the inputs of the function.

4. Orthorhombic symmetry, which is the case for olivine

According to J. Park (1996), for olivine, the stiffness matrix can be represented as

$$\Lambda = A\Lambda_A + B\Lambda_B + C\Lambda_C + D\Lambda_D + E\Lambda_E$$

Where each item can be written as in equation (4) in J.Park (1996):

Below is a brief overview of how tensor product work (All those examples are from Wikipedia, if you are interested type tensor product/outer product/Kronecker product):

Here I write out all the Kronecker product results as below:

$$\hat{x} \otimes \hat{x} = \begin{bmatrix} 1 & 0 & 0 \\ 0 & 0 & 0 \\ 0 & 0 & 0 \end{bmatrix}$$

$$\hat{x} \otimes \hat{z} = \begin{bmatrix} 0 & 0 & 1 \\ 0 & 0 & 0 \\ 0 & 0 & 0 \end{bmatrix}$$

$$\hat{z} \otimes \hat{z} = \begin{bmatrix} 0 & 0 & 0 \\ 0 & 0 & 0 \\ 0 & 0 & 1 \end{bmatrix}$$

$$\hat{z} \otimes \hat{x} = \begin{bmatrix} 0 & 0 & 0 \\ 0 & 0 & 0 \\ 1 & 0 & 0 \end{bmatrix}$$

$$\hat{w} \otimes \hat{w} = \begin{bmatrix} w_x^2 & w_x w_y & w_x w_z \\ w_x w_y & w_y^2 & w_y w_z \\ w_x w_z & w_y w_z & w_z^2 \end{bmatrix}$$

$$\hat{w} \otimes \hat{x} = \begin{bmatrix} w_x & 0 & 0 \\ w_y & 0 & 0 \\ w_z & 0 & 0 \end{bmatrix}$$

$$\hat{x} \otimes \hat{w} = \begin{bmatrix} w_x & w_y & w_z \\ 0 & 0 & 0 \\ 0 & 0 & 0 \end{bmatrix}$$

$$\hat{w} \otimes \hat{z} = \begin{bmatrix} 0 & 0 & w_x \\ 0 & 0 & w_y \\ 0 & 0 & w_z \end{bmatrix}$$

$$\hat{z} \otimes \hat{w} = \begin{bmatrix} 0 & 0 & 0 \\ 0 & 0 & 0 \\ w_x & w_y & w_z \end{bmatrix}$$

To get a better visualization of how each term looks like, from now on I will write out the full expression of the index notation.

$$\Lambda_{Aijkl} = \delta_{ij}\delta_{kl}$$

$$\Lambda_{Bijkl} = w_{ij}\delta_{kl} + \delta_{ij}w_{kl}$$

$$\Lambda_{Cijkl} = 8w_{ij}w_{kl} - \delta_{ij}\delta_{kl}$$

$$\Lambda_{Dijkl} = \delta_{kj}\delta_{il} + \delta_{lj}\delta_{ki} - 2\delta_{ij}\delta_{kl}$$

$$\Lambda_{Eijkl} = 2(w_{kj}\delta_{il} + \delta_{kj}w_{il} - 2w_{ij}\delta_{kl} - 2\delta_{ij}w_{kl}) + \delta_{kj}\delta_{il} + \delta_{lj}\delta_{ki} - 2\delta_{ij}\delta_{kl}$$

In that, $w_{ij} = w_i w_j - \frac{1}{2}\delta_{ij}$.

Then we can calculate the stiffness matrix and we have the 15 components

$C_{11}, C_{15}, C_{55}, C_{16}, C_{14}, C_{56}, C_{45}, C_{31}, C_{35}, C_{66}, C_{46}, C_{44}, C_{36}, C_{34}, C_{33}$ as below:

$$C_{11} = 8Cw_x^4 + (2B - 8C)w_x^2 + (A - B + C)$$

$$C_{15} = 8Cw_x^3w_z + (B - 4C)w_xw_z$$

$$C_{55} = 8Cw_x^2w_z^2 + 2Ew_x^2 + 2Ew_z^2 + (D - E)$$

$$C_{16} = 8Cw_x^3w_y + (B - 4C)w_xw_y$$

$$C_{14} = 8Cw_x^2w_yw_z + (B - 4C - 4E)w_yw_z$$

$$C_{56} = 8Cw_x^2w_yw_z + 2Ew_yw_z$$

$$C_{45} = 8Cw_xw_yw_z^2 + 2Ew_xw_y$$

$$C_{31} = 8Cw_x^2w_z^2 + (B - 4C - 4E)w_x^2 + (B - 4C - 4E)w_z^2 + (A - B + C - 2D + 2E)$$

$$C_{35} = 8Cw_xw_z^3 + (B - 4C)w_xw_z$$

$$C_{66} = 8Cw_x^2w_y^2 + 2Ew_x^2 + 2Ew_y^2 + (D - E)$$

$$C_{46} = 8Cw_xw_y^2w_z + 2Ew_xw_z$$

$$C_{44} = 8Cw_y^2w_z^2 + 2Ew_y^2 + 2Ew_z^2 + (D - E)$$

$$C_{36} = 8Cw_xw_yw_z^2 + (B - 4C - 4E)w_xw_y$$

$$C_{34} = 8Cw_yw_z^3 + (B - 4C)w_yw_z$$

$$C_{33} = 8Cw_z^4 + (2B - 8C)w_z^2 + (A - B + C)$$

Thus, we can write **T**, **S**, **R** as below:

$$\mathbf{T} = \begin{bmatrix} C_{11} & C_{16} & C_{15} \\ C_{16} & C_{66} & C_{56} \\ C_{15} & C_{56} & C_{55} \end{bmatrix}$$

$$= \begin{bmatrix} 8Cw_x^4 + (2B - 8C)w_x^2 + (A - B + C) & 8Cw_x^3w_y + (B - 4C)w_xw_y & 8Cw_x^3w_z + (B - 4C)w_xw_z \\ 8Cw_x^3w_y + (B - 4C)w_xw_y & 8Cw_x^2w_y^2 + 2Ew_x^2 + 2Ew_y^2 + (D - E) & 8Cw_x^2w_yw_z + 2Ew_yw_z \\ 8Cw_x^3w_z + (B - 4C)w_xw_z & 8Cw_x^2w_yw_z + 2Ew_yw_z & 8Cw_x^2w_z^2 + 2Ew_x^2 + 2Ew_z^2 + (D - E) \end{bmatrix}$$

$$\mathbf{S} = \begin{bmatrix} 2C_{15} & C_{14} + C_{56} & C_{55} + C_{31} \\ C_{14} + C_{56} & 2C_{46} & C_{45} + C_{36} \\ C_{55} + C_{31} & C_{45} + C_{36} & 2C_{35} \end{bmatrix}$$

$$= \begin{bmatrix} 16Cw_x^3w_z + 2(B - 4C)w_xw_z & 16Cw_x^2w_yw_z + (B - 4C - 2E)w_yw_z & 16Cw_x^2w_z^2 + (B - 4C - 2E)(w_x^2 + w_z^2) + (A - B + C - D + E) \\ 16Cw_x^2w_yw_z + (B - 4C - 2E)w_yw_z & 16Cw_xw_y^2w_z + 4Ew_xw_z & 16Cw_xw_yw_z^2 + (B - 4C + 2E)w_xw_y \\ 16Cw_x^2w_z^2 + (B - 4C - 2E)(w_x^2 + w_z^2) + (A - B + C - D + E) & 16Cw_xw_yw_z^2 + (B - 4C + 2E)w_xw_y & 16Cw_x^3w_z + 2(B - 4C)w_xw_z \end{bmatrix}$$

$$\mathbf{R} = \begin{bmatrix} C_{55} & C_{45} & C_{35} \\ C_{45} & C_{44} & C_{34} \\ C_{35} & C_{34} & C_{33} \end{bmatrix}$$

$$= \begin{bmatrix} 8Cw_x^2w_z^2 + 2Ew_x^2 + 2Ew_z^2 + (D - E) & 8Cw_xw_yw_z^2 + 2Ew_xw_y & 8Cw_xw_z^3 + (B - 4C)w_xw_z \\ 8Cw_xw_yw_z^2 + 2Ew_xw_y & 8Cw_y^2w_z^2 + 2Ew_x^2 + 2Ew_z^2 + (D - E) & 8Cw_yw_z^3 + (B - 4C)w_yw_z \\ 8Cw_xw_z^3 + (B - 4C)w_xw_z & 8Cw_yw_z^3 + (B - 4C)w_yw_z & 8Cw_z^4 + (2B - 8C)w_z^2 + (A - B + C) \end{bmatrix}$$

Here I will reorganize the three matrix and check if I can get the same presentation as equation (9) in Park and Levin (2016) as below:

$$\mathbf{T} = \begin{bmatrix} 8Cw_x^4 + (2B - 8C)w_x^2 + (A - B + C) & 8Cw_x^3w_y + (B - 4C)w_xw_y & 8Cw_x^3w_z + (B - 4C)w_xw_z \\ 8Cw_x^3w_y + (B - 4C)w_xw_y & 8Cw_x^2w_y^2 + 2Ew_x^2 + 2Ew_z^2 + (D - E) & 8Cw_x^2w_yw_z + 2Ew_yw_z \\ 8Cw_x^3w_z + (B - 4C)w_xw_z & 8Cw_x^2w_yw_z + 2Ew_yw_z & 8Cw_x^2w_z^2 + 2Ew_x^2 + 2Ew_z^2 + (D - E) \end{bmatrix}$$

$$= \begin{bmatrix} 8Cw_x^4 + 2(B - 4C - 2E)w_x^2 + (A - B + C - D + E) + 4Ew_x^2 + (D - E) & 8Cw_x^3w_y + (B - 4C - 2E)w_xw_y + 2Ew_xw_y & 8Cw_x^3w_z + (B - 4C - 2E)w_xw_z + 2Ew_xw_z \\ 8Cw_x^3w_y + (B - 4C - 2E)w_xw_y + 2Ew_xw_y & 8Cw_x^2w_y^2 + 2Ew_x^2 + 2Ew_y^2 + (D - E) & 8Cw_x^2w_yw_z + 2Ew_yw_z \\ 8Cw_x^3w_z + (B - 4C - 2E)w_xw_z + 2Ew_xw_z & 8Cw_x^2w_yw_z + 2Ew_yw_z & 8Cw_x^2w_z^2 + 2Ew_x^2 + 2Ew_z^2 + (D - E) \end{bmatrix}$$

$$= (8Cw_x^2 + 2E) \begin{bmatrix} w_x^2 & w_xw_y & w_xw_z \\ w_xw_y & w_y^2 & w_yw_z \\ w_xw_z & w_yw_z & w_z^2 \end{bmatrix} + (B - 4C - 2E)w_x \left\{ \begin{bmatrix} w_x & 0 & 0 \\ w_y & 0 & 0 \\ w_z & 0 & 0 \end{bmatrix} + \begin{bmatrix} w_x & w_y & w_z \\ 0 & 0 & 0 \\ 0 & 0 & 0 \end{bmatrix} \right\} + (A - B + C - D + E) \begin{bmatrix} 1 & 0 & 0 \\ 0 & 0 & 0 \\ 0 & 0 & 0 \end{bmatrix} + (D + 2w_x^2E - E) \begin{bmatrix} 1 & 0 & 0 \\ 0 & 1 & 0 \\ 0 & 0 & 1 \end{bmatrix}$$

$$= (8Cw_x^2 + 2E)\hat{w} \otimes \hat{w} + (B - 4C - 2E)w_x(\hat{w} \otimes \hat{x} + \hat{x} \otimes \hat{w}) + (A - B + C - D + E)\hat{x} \otimes \hat{x} + (D + (2w_x^2 - 1)E)I$$

$$\mathbf{S} = \begin{bmatrix} 16Cw_x^3w_z + 2(B - 4C)w_xw_z & 16Cw_x^2w_yw_z + (B - 4C - 2E)w_yw_z & 16Cw_x^2w_z^2 + (B - 4C - 2E)(w_x^2 + w_z^2) + (A - B + C - D + E) \\ 16Cw_x^2w_yw_z + (B - 4C - 2E)w_yw_z & 16Cw_xw_y^2w_z + 4Ew_xw_z & 16Cw_xw_yw_z^2 + (B - 4C - 2E)w_xw_y \\ 16Cw_x^2w_z^2 + (B - 4C - 2E)(w_x^2 + w_z^2) + (A - B + C - D + E) & 16Cw_xw_yw_z^2 + (B - 4C - 2E)w_xw_y & 16Cw_x^3w_z + 2(B - 4C)w_xw_z \end{bmatrix}$$

$$= \begin{bmatrix} 16Cw_x^3w_z + 2(B - 4C - 2E)w_xw_z + 4Ew_xw_z & 16Cw_x^2w_yw_z + (B - 4C - 2E)w_yw_z & 16Cw_x^2w_z^2 + (B - 4C - 2E)(w_x^2 + w_z^2) + (A - B + C - D + E) \\ 16Cw_x^2w_yw_z + (B - 4C - 2E)w_yw_z & 16Cw_xw_y^2w_z + 4Ew_xw_z & 16Cw_xw_yw_z^2 + (B - 4C - 2E)w_xw_y \\ 16Cw_x^2w_z^2 + (B - 4C - 2E)(w_x^2 + w_z^2) + (A - B + C - D + E) & 16Cw_xw_yw_z^2 + (B - 4C - 2E)w_xw_y & 16Cw_x^3w_z + 2(B - 4C - 2E)w_xw_z + 4Ew_xw_z \end{bmatrix}$$

$$= 16Cw_xw_z \begin{bmatrix} w_x^2 & w_xw_y & w_xw_z \\ w_xw_y & w_y^2 & w_yw_z \\ w_xw_z & w_yw_z & w_z^2 \end{bmatrix}$$

$$+ (B - 4C - 2E) \left[w_z \left(\begin{bmatrix} w_x & 0 & 0 \\ w_y & 0 & 0 \\ w_z & 0 & 0 \end{bmatrix} + \begin{bmatrix} w_x & w_y & w_z \\ 0 & 0 & 0 \\ 0 & 0 & 0 \end{bmatrix} \right) \right]$$

$$+ w_x \left(\begin{bmatrix} 0 & 0 & w_x \\ 0 & 0 & w_y \\ 0 & 0 & w_z \end{bmatrix} + \begin{bmatrix} 0 & 0 & 0 \\ 0 & 0 & 0 \\ w_x & w_y & w_z \end{bmatrix} \right) + 4Ew_xw_z \begin{bmatrix} 1 & 0 & 0 \\ 0 & 1 & 0 \\ 0 & 0 & 1 \end{bmatrix}$$

$$+ (A - B + C - D + E) \left(\begin{bmatrix} 0 & 0 & 0 \\ 0 & 0 & 0 \\ 1 & 0 & 0 \end{bmatrix} + \begin{bmatrix} 0 & 0 & 0 \\ 0 & 0 & 0 \\ 1 & 0 & 0 \end{bmatrix} \right)$$

$$\begin{aligned}
&= 16Cw_xw_z\hat{w}\otimes\hat{w} + (B - 4C - 2E)[w_z(\hat{w}\otimes\hat{x} + \hat{x}\otimes\hat{w}) + w_x(\hat{w}\otimes\hat{z} + \hat{z}\otimes\hat{w})] + 4Ew_xw_zI \\
&\quad + (A - B + C - D + E)(\hat{x}\otimes\hat{z} + \hat{z}\otimes\hat{x}) \\
R &= \begin{bmatrix} 8Cw_x^2w_z^2 + 2Ew_x^2 + 2Ew_z^2 + (D - E) & 8Cw_xw_yw_z^2 + 2Ew_xw_y & 8Cw_xw_z^3 + (B - 4C)w_xw_z \\ 8Cw_xw_yw_z^2 + 2Ew_xw_y & 8Cw_y^2w_z^2 + 2Ew_x^2 + 2Ew_z^2 + (D - E) & 8Cw_yw_z^3 + (B - 4C)w_yw_z \\ 8Cw_xw_z^3 + (B - 4C)w_xw_z & 8Cw_yw_z^3 + (B - 4C)w_yw_z & 8Cw_z^4 + (2B - 8C)w_z^2 + (A - B + C) \end{bmatrix} \\
&= \begin{bmatrix} 8Cw_x^2w_z^2 + 2Ew_x^2 + 2Ew_z^2 + (D - E) & 8Cw_xw_yw_z^2 + 2Ew_xw_y & 8Cw_xw_z^3 + (B - 4C - 2E)w_xw_z + 2Ew_xw_z \\ 8Cw_xw_yw_z^2 + 2Ew_xw_y & 8Cw_y^2w_z^2 + 2Ew_y^2 + 2Ew_z^2 + (D - E) & 8Cw_yw_z^3 + (B - 4C - 2E)w_yw_z + 2Ew_yw_z \\ 8Cw_xw_z^3 + (B - 4C - 2E)w_xw_z + 2Ew_xw_z & 8Cw_yw_z^3 + (B - 4C - 2E)w_yw_z + 2Ew_yw_z & 8Cw_z^4 + (2B - 8C)w_z^2 + (D - E) + (A - B + C - D + E) \end{bmatrix} \\
&= (8Cw_z^2 + 2E) \begin{bmatrix} w_x^2 & w_xw_y & w_xw_z \\ w_xw_y & w_y^2 & w_yw_z \\ w_xw_z & w_yw_z & w_z^2 \end{bmatrix} + (B - 4C - 2E)w_z \left(\begin{bmatrix} 0 & 0 & 0 \\ 0 & 0 & 0 \\ w_x & w_y & w_z \end{bmatrix} + \begin{bmatrix} 0 & 0 & w_x \\ 0 & 0 & w_y \\ 0 & 0 & w_z \end{bmatrix} \right) \\
&\quad + (D + (2w_z^2 - 1)E) \begin{bmatrix} 1 & 0 & 0 \\ 0 & 1 & 0 \\ 0 & 0 & 1 \end{bmatrix} + (A - B + C - D + E) \begin{bmatrix} 0 & 0 & 0 \\ 0 & 0 & 0 \\ 0 & 0 & 1 \end{bmatrix} \\
&= (8Cw_z^2 + 2E)\hat{w}\otimes\hat{w} + (B - 4C - 2E)w_z(\hat{w}\otimes\hat{z} + \hat{z}\otimes\hat{w}) + (A - B + C - D + E)\hat{z}\otimes\hat{z} + (D \\
&\quad + (2w_z^2 - 1)E)I
\end{aligned}$$

For a special case, if we make the wave to propagate along the positive x axis (that is $\hat{k} = \hat{x}$), we will simplify the stiffness tensor components to be (ξ is the angle between symmetry axis and the x axis):

$$C_{11} = A + B\cos 2\xi + C\cos 4\xi$$

$$C_{15} = 0$$

$$C_{55} = D + E\cos 2\xi$$

$$C_{16} = \frac{1}{2}B\sin 2\xi + C\sin 4\xi$$

$$C_{14} = 0$$

$$C_{56} = 0$$

$$C_{45} = E \sin 2\xi$$

$$C_{31} = A - B \sin^2 \xi - C(2 \cos 2\xi + 1) - 2D - 2E(2 \sin^2 \xi + 1)$$

$$C_{35} = 0$$

$$C_{66} = D + E + C(1 - \cos 4\xi)$$

$$C_{46} = 0$$

$$C_{44} = D - E \cos 2\xi$$

$$C_{36} = \frac{1}{2} B \sin 2\xi - 2E \sin 2\xi$$

$$C_{34} = 0$$

$$C_{33} = A - C$$

We thus have the Christoffel Matrix to be

$$\begin{bmatrix} A + B \cos 2\xi + C \cos 4\xi & \frac{1}{2} B \sin 2\xi + C \sin 4\xi & 0 \\ \frac{1}{2} B \sin 2\xi + C \sin 4\xi & D + E + C(1 - \cos 4\xi) & 0 \\ 0 & 0 & D + E \cos 2\xi \end{bmatrix}$$

Chapter 3

A Comparative Study of Upper Mantle Anisotropy between the Yilgarn Craton and the Superior Craton and its Implications for the Craton Formation Process

Chapter 3 is being prepared for publication and the results were reported at the 2019 AGU Fall Meeting:

Chen, X., Li, Y., Yuan, H., & Levin, V. L. (2019). The Tale of Two Cratons: Upper Mantle Anisotropy under the Superior and West Australian Cratons. AGUFM, 2019, S43A-05.

3.1 Abstract

While all cratons on Earth have participated in different stages of the supercontinent cycle, whether there exists a uniform process for the formation of different cratons is not known yet. The Yilgarn craton in Western Australia and the Superior craton in North America are two cratons that have never been in direct contact, which makes them a good pair for comparative studies. Seismic anisotropy is a proxy for the past and present deformation processes in Earth's deep interior. We integrate an analysis of shear waves, receiver functions and harmonic decomposition to characterize the anisotropic seismic structure beneath 4 sites in each craton. We observe averages of shear-wave-splitting delay times between ~ 0.4 s - ~ 0.7 s at both cratons, which are smaller than the global average of ~ 1 s. We also detect multiple anisotropic boundaries beneath each individual site within each craton. However, no common anisotropic structures can be identified within or across the cratons. Based on the observations of the two different methods, we conclude that cratons are not uniform domains and instead they are composed of different subdomains of different properties. The anisotropic layering beneath each site implies that the cratons

likely formed through processes which included horizontal movements of the preexisting lithosphere. Each distinct anisotropic structure beneath the corresponding site was emplaced and preserved before the completion of the present craton.

3.2 Introduction

Cratons are large domains of the continental crust which have experienced little internal deformation and have maintained long-term stability since their formation during the Archean epoch. Nearly all continents contain cratons that are composed of numerous different terranes formed in relatively early stages in Earth's history. Cratons usually have the lithospheric roots that are more than twice as thick as the oceanic lithosphere (Hawkesworth et al., 2017, Cawood et al., 2013). Different from the oceanic regions which are created and then recycled back into Earth's interior, cratons have existed on Earth for over 3 Gyrs. This long-term preservation of the cratons is likely due to the fact that cratonic lithosphere is lighter (Kaban et al., 2003), significantly colder (Artemieva, 2006) and even stronger (Anderson, 1995, Barrell, 1914) than those recently deformed regions. Their long-term stability makes cratons the only places on Earth that retain geological records from the first half of Earth's existence. Thus, having a better understanding of the cratons can help us to understand the early stages of Earth's evolution.

The mechanisms for craton formation and evolution are still under debate. This mainly revolves around the question of whether the style of tectonics back in the Archean epoch was similar to plate tectonics, which operates on Earth at present. In the Archean epoch, the mantle potential temperatures were up to 250°C higher than today (Davies, 1992, Korenaga, 2008, Herzberg et al., 2010, Brown, 2007), which may lead to different

behaviors of Earth's lithospheric materials and thus completely different styles of tectonics (Gerya, 2014). Based on a pre-tectonic regime, mechanisms for building cratons include large melting events triggered by upwellings or mantle plumes (Pearson et al., 1995, Lee et al., 2011), as well as successive sorting or reworking of the mantle materials due to gravity instability (Johnson et al., 2014, Robin and Bailey, 2009, Sizova et al., 2015). Alternatively, there are other studies that argue that plate tectonics operated in the early stages of craton formation (e.g. Calvert et al., 1995). Different from the vertical movements of Earth's materials in a pre-plate regime, plate tectonics involves the horizontal movement of the preexisting lithosphere. Possible plate-tectonic mechanisms include thickening or thrust stacking of the preexisting oceanic lithosphere which failed to subduct (Bostock, 1998, Jordan, 1978, Cooper et al., 2006, Gray and Pysklywec, 2010).

Different hypotheses can be explored and examined if we can understand the internal structures of the cratons and relate them to the corresponding deformation processes. Seismic anisotropy, the dependence of seismic velocity on the direction of wave propagation, can be used as a proxy for the deformation processes in Earth's interior. Olivine is the major mineral in the upper mantle and it is intrinsically anisotropic (Christensen, 1984, Kumazawa and Anderson, 1969, Ribe, 1992). In the upper mantle, both the fossil fabrics in the lithosphere and deformation in the asthenosphere can cause anisotropy (Silver, 1996, Park and Levin, 2002, Long and Becker, 2010). When the rocks in the upper mantle are systematically deformed under dry conditions, the a-axes of the olivine crystals will align with the strain direction (Zhang and Karato, 1995). Dry upper mantle is typically found beneath the cratons.

Different mechanisms may have different impacts on the formation or modification of the anisotropic structures within the cratonic lithosphere. For instance, there are hypotheses of creating a craton through a large melting event triggered by mantle plume (Pearson et al., 1995, Lee et al., 2011) or instability in gravity of the Earth materials (Robin and Bailey, 2009). Those models mainly rely on the vertical movement of the mantle materials, which is less likely to form azimuthal anisotropic mantle fabrics (where anisotropic properties vary according to the back azimuths) due to the lack of horizontal strains. However, if plate tectonics were operating as presently in the Archean epoch, given the horizontal movement of the preexisting lithosphere, the horizontal strains would leave lenses of sheared rock in the mantle. It is likely for those horizontal textures to be preserved in the lithosphere as fossil fabrics. In this paper, we explore the anisotropic structures in two different areas and relate the mantle fabrics to different mechanisms of the craton formation and evolution.

Our study areas are the Superior craton located in North America and the Yilgarn craton in West Australia. All the cratons on Earth have participated in various stages of the supercontinent cycle (Hawkesworth et al., 2013, Nance et al., 2014) and have experienced distinct deformation histories. These two cratons had different tectonic histories and were never in contact during the formation of Pangea (Muttoni et al., 2009), Rodinia (Li et al., 2008) and even earlier supercontinents Nuna and Columbia (Nance et al., 2014). Their independent formation and evolution paths made them a good pair for comparison.

In this study, we integrate the shear-wave studies which have a good lateral resolution and the receiver function analysis which is sensitive to the vertical structures in the upper mantle to build models of seismic anisotropic structures for selected stations beneath our study areas. By comparing the different anisotropic structures in both areas and associating them with their corresponding tectonic histories, we are able to set constraints on the formation and evolution of the cratons, and explore the possibility of a uniform mechanism for craton formation.

3.3 Geological Background

3.3.1 Yilgarn Craton (Western Australia)

The Yilgarn craton (Figure 1(a)) is a Meso- to Neoarchean craton in Western Australia (Griffin et al., 2004, Champion and Smithies, 2007). Together with the Paleo- to Mesoarchean Pilbara craton (Champion and Smithies, 2007), Yilgarn formed the Western Australian Craton after a series of Proterozoic orogenies, such as the 2.2 Ga Ophthalmian event (Johnson, 2013). Between the two cratons, there is a Proterozoic Capricorn Orogen that formed around 1.8 Ga (Johnson, 2013). The Yilgarn craton is composed of numerous different terranes, from the Narryer terrane in the west, Murchison terrane and the Southwest Yilgarn composite terrane in the middle, to the Eastern Goldfields super terranes (Champion and Smithies, 2007, Van Kranendonk et al., 2013).

The crustal thickness of the Yilgarn craton is generally between ~32 km and ~42 km (Yuan, 2015), which is close to the median of global crust thickness (Abbott et al., 2013). Moreover, the bulk properties of the crust in the Yilgarn craton vary spatially with those of similar physical properties confined into one particular terrane (Yuan, 2015). Surface

wave tomography suggests a multilayered anisotropic structure beneath the cratons of Australia (Debayle et al., 2016, Debayle et al., 2005, Fishwick and Reading, 2008, Simons et al., 2002, Yoshizawa, 2014). These studies proposed that shallow-lithosphere anisotropic fabrics trend east-west (Debayle et al., 2005) while in the deeper asthenosphere, the anisotropy aligns with the present-day plate motion of the continent. The thickness of the upper layers seems to correspond with the depth of mid-lithospheric discontinuity identified using S_p receiver functions (Ford et al., 2010).

We focus on three cratonic terranes within Western Australia in this study.

The Kalgoorlie Terrane is a part of the Eastern Goldfield superterrane. It is mainly composed of granites and greenstones, and surrounded by different faults (Myers, 1993). It consists of volcanic rocks formed between 2.7 Ga and 2.69 Ga (Swager, 1997). The deformation history of this terrane is different from the units next to it. Between 2.68 Ga and 2.65 Ga, Kalgoorlie Terrane experienced three episodes of deformation, after which it obtained a pronounced NNW-SSE tectonic pattern in the region, and some of terrane boundary faults were reactivated (Myers, 1993).

The Murchison Terrane is composed of granites (~ 2.7 Ga - 2.6 Ga) and greenstones (~ 3.0 Ga) that are metamorphosed in greenschist facies (Myers, 1990, Watkins and Hickman, 1990). This terrane experienced four different stages of deformation and during this period between 2.68 -2.64Ga, rocks were repeatedly deformed and folded together with Narryer Terrane (Myers, 1993). Finally, at the last stage of deformation, a major north-south shear zone was formed.

The Southwest Yilgarn Composite Terrane formed between 2.7 Ga and 0.6 Ga, there were repeated episodes of aggregation and dispersal of crust materials in the southwestern

part of Australia (Myers, 1990). In this area, Southwest Yilgarn Composite Terrane is composed of a number of small greenstone belts and high-grade gneisses (Myers, 1993).

3.3.2 Superior Craton (Eastern North America)

The Superior craton (Figure 1(b)) is an Archean craton, and together with other Archean cratons and Proterozoic orogens, it is a part of the Archean core of the Canadian Shield (Hoffman, 1988, Card, 1990, Percival et al., 2006). Its formation was associated with the closure of an ancient ocean basin and it finally stabilized near the end of the Late Archean from 2.8-2.5 Ga (Card, 1990). It can be divided into linear subprovinces of distinctive lithological and structural character: northern and southern high-grade gneiss subprovinces, and a central subprovince of alternating granite-greenstone and metasedimentary belts (Percival, 2007, Card, 1990, Card and Ciesielski, 1986).

In the Superior craton, the thickness of the crust is between 30 km and 40 km when approaching to the northeastern edge close to the Grenville Front (Levin et al., 2017). Moreover, the lithosphere thickness beneath the central Superior craton is around 200-250 km (Jaupart et al., 1998, Rudnick et al., 1998, Gung et al., 2003, Romanowicz, 2009). Similar to the Yilgarn craton, Yuan and Romanowicz (2010) also suggest that the anisotropic structure beneath North America is multi-layered. In that, two distinct lithospheric layers are identified which are later interpreted to consist of a stack of two layers with a chemical layer on top of a thermal layer.

We focus on three Archean terranes within the Superior Craton in this study.

Abitibi Terrane is the largest Archean greenstone terrane with much less deformation or erosion compared to other terranes during Archean epoch (Green et al., 1990). It can be separated into three different regions with distinct rock types: volcanic assemblages (~ 2.74

Ga – 2.72 Ga) with layered intrusions in the North (~ 2.79 Ga); plutonic rocks in the central Abitibi Terrane (~ 2.75 Ga) and relatively younger sedimentary-volcanic deposits in the South (~ 2.67 Ga) (Percival, 2007). These three regions have overlapping stratigraphic histories. In this terrane, there is also a shear zone which is trending east to west extending to hundreds of kilometers (Peschler et al., 2004).

La Grande Subprovince is composed of the submarine volcanic rock (2.75 Ga – 2.73 Ga) and a sedimentary sequence overlying gneiss basement (3.36–2.79 Ga) with some ultramafic intrusions (Percival, 2007). There is a Neoarchean W-NW trending fault that separates the La Grande Subprovince from others (Mercier-Langevin et al., 2012). La Grande Subprovince went through at least four major deformation events during the Archean times which includes mechanisms like thrusting, folding and shearing (Goutier et al., 2001, Mercier-Langevin et al., 2012).

The Opatica Subprovince is a belt that lies directly to the south of low-grade Abitibi greenstone belt (Calvert and Ludden, 1999, Percival, 2007). It consists of tonalitic gneiss (~2.82 Ga), volcanic arc and back-arc assemblages (~2.77 Ga – 2.70 Ga) together with some granodiorite and granitic plutons (Sawyer and Benn, 1993, Boily and Dion, 2002). This area went through different stages of deformation processes and it has relatively younger south-verging structures overprinting on a shear zone that is west-verging (Sawyer and Benn, 1993).

3.4 Methodology and Data

3.4.1 Shear-wave Studies

3.4.1.1 Shear-wave Splitting

Systematic rock deformation in the upper mantle can produce seismic anisotropy. As a shear wave propagates through the anisotropic media in the upper mantle, it will split into

two orthogonally polarized fast and slow components. Under the most-common upper-mantle conditions, the fast polarization aligns with the direction of rock deformation (Long and Silver, 2009, Park and Levin, 2002). A splitting delay time will accumulate depending on the strength of anisotropy and the length of the ray path. Shear-wave splitting (Long and Silver, 2009, Silver and Chan, 1991, Vinnik et al., 1989) is a commonly adopted technique to explore seismic anisotropy in the upper mantle. It measures the integral effect of anisotropy along the ray path of a birefringent S wave. Core-refracted shear phases (SKS, SKKS, PKS) are used in this technique to avoid the potential anisotropic contamination from the source side (Savage, 1999). Due to nearly vertical incidence angles of these teleseismic waves, this method provides a good lateral resolution of the overall anisotropy beneath the corresponding site.

In this study, we adopt the SplitLab software and measure shear-wave splitting of core-refracted phases SKS, SKKS, SKIKS and PKS (called XKS hereafter) using the Rotation Correlation Method following a systematic procedure adopted in Chen et al. (2018) and Li et al. (2019). The splitting parameter pairs (fast polarization and delay time) are estimated when the horizontal components of the shear waves before and after a series of test rotations have the most similar pulse shapes via cross correlation (Wüstefeld and Bokelmann, 2007). NULL measurements are assigned when no energy is observed on the transverse component or a nearly rectilinear particle motion is observed without correction for anisotropy. We also use the Minimum Transverse Energy method (Silver and Chan, 1991), which minimizes the energy on the SH component of the shear wave, to ensure the reliability of the measurements. Thus, NULL measurements can also be identified when both methods yield nearly zero delay times or very different results.

3.4.1.2 Splitting Intensity

Shear-wave splitting can be estimated for individual station-event pairs, which enables us to examine the back-azimuth variation of anisotropic properties beneath each site. As an extra constraint for the upper-mantle anisotropy in our study areas, we also adopt a multi-record approach proposed by Chevrot (2000) that utilizes all station-event pairs simultaneously. In this method, a parameter called splitting intensity (SI) is defined as the ratio between the transverse component and the derivative of the radial component. For a simple case of anisotropy with a horizontal symmetry axis, SI values are expected to form a sinusoidal pattern with back azimuth described by the following formula:

$$SI = \delta t * \sin [2(\phi - \phi_0)] \quad (2)$$

where δt and ϕ_0 stand for the delay time and fast polarization, respectively, of a vertically propagating SV-polarized wave, and ϕ is the back azimuth of the corresponding measurement.

The best-fit combination of the fast polarization δt and the delay time ϕ_0 is estimated by fitting a sinusoidal curve to the set of back azimuth and SI value pairs using a least-squares method. We use the same datasets for both shear-wave splitting and splitting-intensity measurements. We carried out the measurements on seismic records using the SplitLab software (Wüstefeld et al., 2008) with modifications by Deng et al. (2017) that enable the estimation of SI values and corresponding error ranges calculated given a 95% confidence interval.

3.4.1.3 Single-layer Inversion

In addition to the two time series analysis methods mentioned previously, we also perform a full waveform inversion using reflectivity synthetic seismograms (Levin and Park, 1998) and the cross-convolution technique (Menke and Levin, 2003) to find the best-fitting anisotropic parameters of a layer of anisotropic mantle rock with a horizontal symmetry axis. We consider seismograms as convolutions of a source-wavelet function and the structure response. Given a model of earth structure, we can predict radial and transverse components of a set of N synthetic seismograms, $V_i^{\text{pre}}(\mathbf{m}, t)$ and $H_i^{\text{pre}}(\mathbf{m}, t)$, where ‘ $i=1,2,\dots,N$ ’ stands for individual seismogram sets, ‘ \mathbf{m} ’ stands for the model, v^{pre} and h^{pre} represent model responses to the propagation of a plane wave, and s^{true} stands for the source wavelet.

$$\begin{aligned} V_i^{\text{pre}}(\mathbf{m}, t) &= s_i^{\text{true}}(t) * v_i^{\text{pre}}(\mathbf{m}, t) \\ H_i^{\text{pre}}(\mathbf{m}, t) &= s_i^{\text{true}}(t) * h_i^{\text{pre}}(\mathbf{m}, t) \end{aligned} \quad (2)$$

At the same time, we can represent observed radial and transverse components of the corresponding data records as V^{obs} and H^{obs} , where h^{true} and v^{true} are hypothetical responses of the real Earth structure:

$$\begin{aligned} V_i^{\text{obs}}(t) &= s_i^{\text{true}}(t) * v_i^{\text{true}}(t) \\ H_i^{\text{obs}}(t) &= s_i^{\text{true}}(t) * h_i^{\text{true}}(t) \end{aligned} \quad (3)$$

If the model used to predict synthetic seismograms is close to real Earth properties, functions V^{pre} and v^{true} should be similar, and functions H^{pre} and h^{true} should be similar. Since s^{true} is present in both observed and predicted waveforms, a relationship below should be satisfied (Menke and Levin, 2003):

$$H_i^{\text{pre}}(\mathbf{m}, t) * V_i^{\text{obs}}(t) \approx V_i^{\text{pre}}(\mathbf{m}, t) * H_i^{\text{obs}}(t) \quad (4)$$

To find the best-fitting model, we simulate synthetic seismograms for a range of parameter values in the model \mathbf{m} and construct cross-convolved timeseries of observed and predicted components, as shown above. We then assess the degree of misfit in timeseries representing two sides of eq (4), using the following expression:

$$E(\mathbf{m}) = \left(\frac{1}{N}\right) \sum_{i=1}^N ||H_i^{\text{pre}}(\mathbf{m}, t) * V_i^{\text{obs}}(t) - V_i^{\text{pre}}(\mathbf{m}, t) * H_i^{\text{obs}}(t)||^2 * w \quad (5)$$

We choose a weighted least squares method shown in eq (5), with weights w based on the quality of the data assigned by an analyst in the course of routine shear-wave-splitting parameter estimation using SplitLab (Wüstefeld et al., 2008). For a good measurement, we give 100% weight, and we assign 75% and 50% weights to fair and poor measurements correspondingly. At the end of the procedure, the best-fitting model with the least error will be returned.

We predict synthetic seismograms in horizontally layered model with a 40-km isotropic crust and a 100-km upper-mantle anisotropic layer with a fast symmetry axis. We adopt the Backus Notation (Backus, 1965) for the description of upper-mantle anisotropy. We compute synthetic seismograms for different combinations of the symmetry axis

orientation (from 0 to 170 in 10-degree steps) and the anisotropy strength (from 1 to 8% in 1% steps). After we find the best-fitting pair of model parameters, we carry out a detailed local search, changing the azimuth spacing to 5° within $\pm 10^\circ$ of the current optimal fast-axis direction, and the percentage of anisotropy to every 0.5% within $\pm 1\%$ of the current optimal percentage of anisotropy. Figure 1(c) shows an example of the error surface E (m) resulting from the grid search for best-fitting values of axis orientation and anisotropy strength.

3.4.1.4 An Integration of Methodologies in Shear-wave Studies

All three methods that are adopted in this study assume the existence of only one anisotropic layer with a horizontal symmetry axis, which is a simplified representation of the real anisotropic structure beneath a study area. The first two methods provide estimates of the ‘apparent’ anisotropic properties for the study area while the single-layer inversion adds an extra constraint on the “apparent” splitting parameters. Taken together, these internally connected metrics provide a more nuanced description of the anisotropic properties beneath the sites we have studied, and make the comparisons of different locations more meaningful. A further explanation of the workflow and its corresponding logic is described using the example of site KMBL shown in Figure 2.

We first measure shear-wave splitting on the dataset collected for site KMBL and plot the fast polarizations and delay times according to their back azimuths as in Figure 2(a). Since this method assumes there is only one anisotropic layer with a horizontal symmetry axis beneath the site, agreement with the assumption can be identified if consistent splitting measurements according to the back azimuths are made and NULL measurements concentrate on two orthogonal back azimuths (Savage, 1999). This metric can provide a good view of the anisotropic property variations according to the back azimuths by

showing all individual measurements. As Figure 2(a) shows, we can observe a certain degree of back-azimuth variation of the fast polarization at site KMBL. Following common procedures in shear-wave-splitting studies (cf. Long and Silver, 2009) we compute simple averages for fast polarization ϕ and delay time δt using all non-NULL values obtained for the site (Figure 2(d)). We then examine results of SI measurements which provide an estimate of the best-fitting combination of delay and fast-axis values for this site (Figure 2(d)).

We also predict the SI sinusoidal function on the basis of ϕ and δt averages estimated from non-NULL measurements for this site and compare it to the sinusoid obtained by fitting the observed SI data. A good match implies an agreement with the one layer of anisotropy assumption, a likely case at site KMBL (Figure 2(b)). If a mismatch exists between the sinusoids, different interpretations are possible, such as the relatively high noise level, or the complexity of the anisotropic structure at depth. SI measurements and corresponding best-fit splitting parameters include all observations, while averages of individual splitting measurements are based on non-NULL values only.

Finally, we compare two pairs of splitting parameters obtained by time-series analysis to the estimate of anisotropic properties from a waveform inversion (Figure 2(d)). The shape of the error surface provides a way to assess how well the strength of anisotropy and the direction of the fast axis are constrained (Figure 2(c)). For instance, at site KMBL the range of fast-axis values yielding errors within 5% of the best solution is 60° to 90° , while the range of anisotropy strength values is from 1.5% to 4.5%. A comparison to the estimates of fast polarization from RC and SI methods shows a close match. Estimating a likely delay in a split shear wave propagating through a model with best-fit anisotropy strength of 3%,

we obtain 0.75 s, a value in good agreement with RC and SI delays. An estimate of 0.75 s assumes that a 100-km-thick anisotropic layer with 4% anisotropy will yield ~ 1 s delay between fast and slow components of a typical SKS wave travelling through upper-mantle material with isotropic speed of 4.5 km/s.

Thus, a comparison of results from three different techniques confirms that site KMBL lies above a relatively simple anisotropic structure that can be approximated by a single layer of anisotropy.

3.4.1.5 Data

In the Yilgarn craton, we examined seismic records at four permanent stations (Australian National Seismograph Network, <http://ds.iris.edu/mda/AU>, Table S1) from 55 earthquakes between 2010 and 2019 with magnitudes above 6 (Figure 3(a)). In total, this yielded 223 measurements of splitting intensity. Of these, 85 of the records returned non-NULL splitting measurements, and 138 returned NULL measurements.

In the Superior craton, we estimated shear-wave splitting on seismograms at 3 permanent stations (POLARIS stations in Quebec, <http://ds.iris.edu/mda/PO>) and 3 temporary stations (QMIII Flexible Array, <http://ds.iris.edu/mda/X8>) (Table S1). Given the relatively short operating time of temporary stations and thus the limited numbers of measurements, we combined the measurements at the 3 temporary stations into a composite-location called ‘merged’. We analyzed records collected from 144 earthquakes between 2005 and 2015 with magnitudes above 5.5 (Figure 3(b)). Overall, we made 263 measurements of splitting intensity, with 142 of them corresponding to non-NULL splitting measurements and 121 corresponding to NULL measurements.

For both regions, we used data sets developed for individual sites to invert waveforms from multiple events for one-layer anisotropic model parameters. The core-refracted

phases were preprocessed with the same time window and frequency filters chosen to measure the SI values and Splitting Parameters in SplitLab by the analyst.

3.4.2 Receiver Functions and their Harmonic Decomposition

3.4.2.1 Receiver Function Analysis

In addition to the shear-wave studies that provide an integral measurement of anisotropic properties along the ray path but do not have a good vertical resolution, we use the receiver function (RF) analysis method (Ammon, 1991) to develop constraints on the vertical distribution of anisotropic properties in the upper mantle beneath our study areas. Receiver functions (RFs) represent the response of the layered earth structure beneath the site to the propagation of a plane wave. Given the existence of vertical gradients in impedance, anisotropy, or both, mode-converted shear phases will be generated when teleseismic compressional (P) waves pass through them (e.g. Burdick and Langston, 1977, Levin and Park, 1997), and will arrive closely after these P wave arrivals. Relative arrival times between those converted phases and the original P wave contain information on the depths of the boundaries, while their amplitudes are controlled by the contrasts in the properties across the boundaries.

Assuming that the waveform of the teleseismic P wave represents the signature of the earthquake source, and that the later-arriving converted shear waves have similar pulse shapes, P-to-S receiver functions are computed by deconvolving the vertical component timeseries from the horizontal components of seismic records. To better isolate the P wave, prior to deconvolution the three-component records are transformed into the LQT coordinate system, where L is along the P-wave incidence angle (and thus captures the compressional wave), Q is normal to the L component with maximum projection into the vertical plane, and T is the usual transverse component, orthogonal to both L and Q.

Although T aligns with the SH polarization, Q deviates from the SV polarization at the same horizontal slowness of the P wave, because the S-wave ray has steeper incidence than the P-wave ray.

We adopt the multi-taper spectral correlation (MTC) technique of Levin et al. (2000) that combines records from multiple earthquakes to develop spectrally averaged RFs. Relative timing of the P-to-S converted waves depends on the ray parameter of the incident P wave (Cassidy, 1992, Gurrola et al., 1995) and hence on the source distance. We use move-out corrections in the spectral domain to align all RFs to the vertical incidence angle prior to averaging, and consequently form back-azimuth and epicentral gathers that we use to identify phases likely associated with seismic boundaries at depth (e.g. Figure 4(b-c)). The reliability of MTC RF waveforms is highest at the start of the timeseries, presenting a challenge for phases with larger (15-20 s) delays (Park and Levin, 2000, 2016b). This is the time when phases from depths in excess of 100 km beneath our sites are expected. To make our RFs more reliable, we migrate all RFs to the chosen target depth in order to emphasize the deeper features in the upper mantle. After migration, time '0' corresponds to the delay time of the vertically incident P to S converted phase that originates at the target depth. Detailed procedures for move-out correction and migration can be found in Park and Levin (2016b).

Once receiver function timeseries are constructed, individual pulses within them may be examined for the properties of the boundaries they (likely) represent. The picked delay time can be converted into depth using the following equation:

$$h = \frac{t}{\sqrt{\frac{1}{v_s^2} - p^2} - \sqrt{\frac{1}{v_p^2} - p^2}} \quad (6)$$

where t is the delay time of the P-to-S converted phases, v_p and v_s are P and S velocities from corresponding models and p is the ray parameter.

3.4.2.2 Harmonic-decomposition Analysis

Based on the studies of synthetic seismograms (e.g. Levin and Park, 1997) and theoretical considerations (Park and Levin, 2016a), anisotropy of seismic velocity will lead to directional variations in the amplitudes and polarities of P-to-S converted waves. Depending on whether the boundary and the symmetry axis of anisotropy are both horizontal, or whether either one is dipping, two-lobed (proportional to $\sin(\text{baz})$ or $\cos(\text{baz})$) and four-lobed (proportional to $\sin(2(\text{baz}))$ or $\cos(2(\text{baz}))$) directional patterns are expected (Levin and Park, 1998, Park and Levin, 2016a). To separate effects caused by seismic anisotropy and dipping interfaces from those caused by the presence of noise and scattering, we adopt the harmonic-decomposition analysis (Park and Levin, 2016a, Xie et al., 2019).

Anisotropy or dipping interfaces result in systematic patterns of converted wave amplitude on both the T and Q components of the receiver functions, such that the SH component (T) has a 45° or 90° directional phase lag compared to the SV component (Q) of the receiver functions:

$$Q \sim T(\text{baz} + 90^\circ) + T(\text{baz} + 45^\circ) \quad (7)$$

In our analysis, both Q and T RFs computed using all records are fitted simultaneously in the spectral domain using a sum of five harmonic functions of the back azimuth. The fitting operation generates five time-varying coefficients: ‘const’, which reflects the effects from the isotropic impedance contrast; ‘cos1’ and ‘sin1’ for two-lobed directional patterns caused by the effects of dipping interfaces and/or symmetry axes; and ‘cos2’, ‘sin2’ for four-lobed directional patterns representing the effects of the horizontal symmetry axes:

$$\begin{aligned}
 \text{QRF}(t) &= \text{const}(t) + \cos1(t) \cos(\text{baz}) + \sin1(t) \sin(\text{baz}) + \cos2(t) \cos(2(\text{baz})) \\
 &\quad + \sin2(t) \sin(2(\text{baz})) \\
 \text{TRF}(t) &= 0 + \cos1(t) \cos(\text{baz} + 90^\circ) + \sin1(t) \sin(\text{baz} + 90^\circ) \\
 &\quad + \cos2(t) \cos(2(\text{baz} + 45^\circ)) + \sin2(t) \sin(2(\text{baz} + 45^\circ))
 \end{aligned} \tag{8}$$

In the above “baz” represents the back-azimuth of an observed seismic record.

To evaluate the total energy represented by pairs of corresponding terms we compute the vector-length amplitudes of periodic components (Olugboji and Park, 2016):

$$\begin{aligned}
 \text{Amplitude}_{2\text{lobed}}(t) &= \sqrt{(\sin1(t))^2 + (\cos1(t))^2} \\
 \text{Amplitude}_{4\text{lobed}}(t) &= \sqrt{(\sin2(t))^2 + (\cos2(t))^2}
 \end{aligned} \tag{9}$$

Amplitudes of individual harmonic components are controlled by the orientation of the anisotropic symmetry axis. In case of a dipping axis (and hence a 2-lobed pattern) axis orientation ξ may be estimated by the following formula (Olugboji and Park, 2016):

$$\xi = \text{tg}^{-1} \left(\frac{\cos 1}{\sin 1} \right) \quad (10)$$

If the symmetry axis is horizontal, coefficients $\cos 2$ and $\sin 2$ are used instead, and the resulting orientation is determined to within 90° , subject to knowing whether the axis is fast or slow (Xie et al., 2019).

Not all energy in the observed RFs can be explained by P-to-S conversion from boundaries at depth. Some will arise as a consequence of noise in the records or the scattering from lateral inhomogeneities at depth. To evaluate the significance of these other contributions to the RF wavefield, we develop “Unmodelled” harmonic components and compare them to those representing expected P-to-S converted wave behavior.

The unmodeled components are constructed with an opposite sense of the directional phase shift (Park and Levin, 2016a):

$$Q \sim T(\text{baz} - 90^\circ) + T(\text{baz} - 45^\circ) \quad (11)$$

Correspondingly, the harmonic decomposition can be written as follows:

$$\begin{aligned} \text{QRF}(t) = & \text{uconst}(t) + \text{ucos1}(t) \cos(\text{baz}) + \text{usin1}(t) \sin(\text{baz}) + \text{ucos2}(t) \cos(2(\text{baz})) \\ & + \text{usin2}(t) \sin(2(\text{baz})) \\ \text{TRF}(t) = & 0 + \text{ucos1}(t) \cos(\text{baz} - 90^\circ) + \text{usin1}(t) \sin(\text{baz} - 90^\circ) \\ & + \text{ucos2}(t) \cos(2(\text{baz} - 45^\circ)) + \text{usin2}(t) \sin(2(\text{baz} - 45^\circ)) \end{aligned} \quad (13)$$

The amplitudes of directionally varying components can be calculated using the vector-length formula:

$$\begin{aligned} \text{UAmplitude}_{2\text{lobed}} &= \sqrt{(\sin 1(t))^2 + (\cos 1(t))^2} \\ \text{UAmplitude}_{4\text{lobed}} &= \sqrt{(\sin 2(t))^2 + (\cos 2(t))^2} \end{aligned} \quad (14)$$

In the above representations, ‘u’ before ‘uconst’, ‘ucos1/2’, ‘usin1/2’ and ‘uamplitude’ stands for ‘unmodeled’, which is to distinguish from the anisotropic or dipping-interface contributions. An example of timeseries of harmonic-decomposition coefficients, and the corresponding vector-length plots, is presented in Figures 3(d) and 3(e).

3.4.2.3 A Systematic Data Analysis Workflow

In this section, we combine receiver-function timeseries and their corresponding harmonic decompositions in a systematic procedure to identify signals most likely representing the planar boundaries within anisotropic seismic velocity at depth. By combining different representations of RFs, we examine possible choices for the converted waves, and apply a set of standards informed by synthetic seismogram simulations in layered anisotropic medium (Levin and Park, 1998, Xie et al., 2019, Chen et al., 2018). In Chapter II of this dissertation, we simulate the teleseismic wave propagation through layered anisotropic medium using the reflectivity algorithm (Fuchs and Müller, 1971) and code it in Matlab (R2016a).

Below is a detailed explanation of the corresponding procedure.

1) We start by computing receiver functions for each station and constructing back-azimuth gathers for the Q and T components. We combine multiple observations at each site in the

spectral domain to form 30° -wide back-azimuth bins with 50% overlap. We perform the analysis for different values of maximum frequency. We find that RFs containing frequencies up to 0.25Hz yield good results for the targets in the upper mantle. Figure 4(a) shows an example of a back-azimuth gather.

2) To have a better alignment of converted phases in records that have different ray parameters and thus different incidence angles, we correct RF time series to vertical incidence using station-specific velocity models of the crust and the upper mantle (Yuan, 2015, Levin et al., 2017). In the MTC method, the receiver-function features within the first $\frac{1}{4}$ of the input time window are constrained the best (Levin et al., 2000). Our input time windows are 80 s long thus we have the highest confidence in receiver function within 20 s before and after the “0” time. For the purpose of this study, we focus on potential discontinuities in the upper mantle, between depths 50 and 250 km, with expected delay times for P-to-S converted phases in the range 5-25 s. To focus our analysis at these delay times, we carry out a depth migration procedure (Park and Levin, 2016b) that shifts the target depth from the surface to the depth of 50 km in the mantle. After migration, time ‘0’ is equivalent to the predicted vertical-incidence delay of the P-to-S converted wave that originates from 50 km, while converted phases originating above 50 km are represented by receiver-function waveforms at negative times, -6 s to 0 (Figure 4(b)). A comparison with results from step 1 (Figure 4(a)) confirms that major features of the wavefield are the same, but also shows that migrated pulses in the time range 5 – 15 s in Figure 4(b) are more energetic than corresponding ones in the (unmigrated) time range 10 – 20 s.

3) We next compute the epicentral gathers of receiver functions (Figure 4(c)). Since RFs vary with direction, especially on the T component, we assemble such gathers for BAZ ranges with consistent polarity of the pulses we are interested in. We gather individual records in epicentral distance bins 10° wide with 50% overlap. These plots will help us further examine and check the properties of potential choices of anisotropic boundaries.

4) For each frequency in the spectra of individual receiver functions we compute back-azimuth harmonic-decomposition coefficients for both “anisotropy/dip” and “unmodelled” components. Collecting coefficients for individual frequencies into full spectra, we transform them into the time domain and plot resulting timeseries for the five coefficients representing effects of layered anisotropic structure (const, sin1, cos1, sin2 and cos2) and five coefficients representing noise and scattering (uconst, usin1, ucos1, usin2, ucos2). An example is in Figure 4(d).

5) We compute the vector-length amplitudes of the harmonic function pairs which represent the total amount of the energy in the corresponding periodic terms (Figure 4(e)). We also compute vector-length amplitudes for the unmodeled components. By comparing the relative amplitudes of modelled and unmodelled parts, we can identify harmonic components of the receiver-function wavefield that should be interpreted further.

6) The crust-mantle transition is the strongest contrast we expect to find, and waves multiply reflected within the crust are likely to be present in the observed RFs. We use known values for the thickness of and seismic velocities within the crust to estimate delay

times for the wave converted from the crust-mantle boundary (Ps) and waves bouncing once within the crust (Ppms+Psmp, Psms). We adjust these estimates for the effects of the moveout correction and the time shift to a delay corresponding to 50 km depth. We plot resulting predictions on all representations of our RFs, either as lines tracing the expected wave arrival time (Figure 4(d)) or a range of possible delay times (Figure 4(a-c) and 3(e)).

3.4.2.4 Using Multiple Constraints to Identify Anisotropic Boundaries

In this study, we combine observations from different kinds of analysis described in the workflow section 3.2.3 to make decisions on whether the converted phases we observe represent sub-horizontal boundaries in anisotropic seismic velocity. We base our interpretation on expectations from synthetic seismograms (Cassidy, 1992, Levin and Park, 1997, Xie et al., 2019, Park and Levin, 2016a), as follows:

We expect a P-to-S converted wave from an abrupt change in properties across a planar boundary to have a pulse-like shape, with the peak of the pulse at its theoretically predicted arrival time. A planar interface is expected to generate converted waves with the same delay from all directions. We expect changes in impedance (velocity x density) to be reflected by P-to-SV converted waves that will be recorded on the Q components of the receiver function and on the “const” component of harmonic expansions. An increase of impedance with depth is represented by a positive pulse, and vice versa. We expect changes in anisotropic properties (either strength of anisotropy or sense/direction of the axis, or both) to be reflected by the P-to-SH converted waves, and to appear primarily on the T component and the periodic (2-lobed and 4-lobed) harmonic components. Polarity of T component RFs depends on both impedance and anisotropy changes, while directions

where changes in their polarity occur are expected to coincide with orientations of anisotropic symmetry axes or else be at 90° angle to them.

1) We first check the amplitudes (vector length measurements) for both 2-lobed and 4-lobed patterns in Figure 4(e). If the amplitudes of the modelled part are more than twice as large as those of the unmodeled part, we mark them as possible choices for a boundary. As an example, In Figure 4(e) we mark a prospective 2-lobed phase at delay time ~ 2.5 s, and we note a prospective 4-lobed phase at the same time.

2) We confirm that the individual harmonic components (Figure 4(d)) have clear energy at 2.5 s, and use the amplitudes of cos1 and sin1 component to evaluate the likely orientation of the symmetry axis, in this case $\sim 50^\circ$.

3) After the first two steps, we look for the marked phase in back-azimuth and epicentral gathers of receiver functions (Figures 3(b-c)). In the back-azimuth gather we note the presence of energy at 2-3 s delay, and changes in polarity of the T component phase, at 40° and 220° . In the epicentral gather we note the clear phase with near-constant delay of ~ 2 s, confirming that this is a converted wave that was correctly aligned in the course of correction for the incidence angle. Figure 4(c) also shows an exceptionally clear example of crustal multiples that should not be interpreted.

4) Having confirmed that this phase satisfies selection criteria, we evaluate the depth of the interface where it forms as ~ 80 km.

3.5 Results

3.5.1 Shear-Wave Studies

3.5.1.1 Yilgarn Craton

We detect weak anisotropy in the Yilgarn craton by looking at the averaged shear-wave splitting. At sites KMBL, MEEK and MORW in the Yilgarn craton (Figure 5), the fast polarizations are close to each other and they are $\sim 70^\circ$ whereas at site MUN it is $\sim 103^\circ$, which is nearly 30° away from the other three sites. The simple averages of delay times at different sites are relatively consistent and overall fall into the range between 0.5 s and 0.7 s (Figure 5(a)). Comparing both approaches, the fast polarizations are relatively stable and insensitive to the change of methods (Figure 5(b)). The variations between two methods in estimating fast polarizations are up to 10° . However, the delay times vary by as much as 0.3 s except for site KMBL where two estimates are within 0.1 s. Overall, no matter which methods we choose to estimate the splitting delays in the Yilgarn craton, we always find relatively weak anisotropy compared to the global average of ~ 1 s (Silver, 1996, Savage, 1999, Long and Silver, 2009) which was based on a statistic analysis of 332 observations in Silver (1996).

We also look at the statistical characteristics of the splitting parameters in Figure 5. The standard deviations of the delay time at each individual site are relatively consistent and around 0.3 s. The fast polarizations spread differently at different sites. Fast polarizations at MEEK have the largest standard deviation of around 50° while those of site KMBL have the smallest value which is around 20° . Moreover, the fractions of NULL measurements are all above 50% at the sites in the Yilgarn craton.

In addition to looking at the overall splitting parameters alone, we also focus on the results at each individual site using an integration of three methods in this shear-wave study.

Site KMBL

Site KMBL has overall 45 measurements from nearly all the back azimuths except between 240° and 300° (Figure 6(a)). Of these, 23 are assigned as NULL, so it has a balanced assignment of NULL and non-NULL measurements which leads to a ratio of NULL over non-NULL measurements being 1.0. Fast polarizations at KMBL are roughly consistent with an average of 76° and a standard deviation of 24° . Delay times are up to 1.2 s with an average of 0.7 s and a standard deviation of 0.3 s. NULL measurements can be observed from nearly all directions where measurements are made except from 0° to 45° and they mainly cluster in back-azimuth ranges of $150^\circ \sim 180^\circ$ and around 60° . We can observe a good agreement between the two sinusoids estimated by all SI values and predicted using only split measurements (Figure 6(b)). The differences between the two sets of splitting parameters are minor in fast polarizations of less than 1° and the delay times of less than 0.1 s. This agreement shows that a single layer of anisotropy can be used to approximate the anisotropic structure beneath this site. In the error surface plot (Figure 6(c)), it is clear that the best-fitting pairs are relatively well constrained with a weak anisotropy of 3% and fast polarization of 75° , which are close to the estimates using two other methods. In all, site KMBL seems to have a relatively simple anisotropic structure that can be approximated by only one layer of weak anisotropy and a fast polarization that is around 75° clockwise from N.

Site MEEK

In the stereoplot (Figure 6(d)), MEEK has a complete coverage of the back azimuth. This site yielded 64 measurements in total including 46 NULL measurements. MEEK has the highest NULL vs non-NULL ratio of 2.6 compared to all the other sites. Fast polarizations at this site are not consistent with average of the fast polarizations being 76° and the standard deviation being 50° . Delay times are not consistent either. Though the delay time has a small average of 0.6 s given most of the measurements yielded smaller values, the standard deviation is 0.4 s. NULL measurements can be observed from all back azimuths except from $0^\circ - 30^\circ$. This is similar to site KMBL where no NULL measurements are observed from this range of back azimuths. We compare two sinusoidal curves for the SI values and find a clear mismatch (Figure 6(e)). There is only a minor phase shift between the fast polarizations (average and best-fit values are 76° and 67° , respectively), but the delay time predicted by fitting all SI values (0.2 s) is much smaller than the average of individual splitting measurements (0.6 s). This is likely due to the inclusion of the NULL measurements in the SI sinusoid fit. In the error surface (Figure 6(f)), we can observe a pattern that suggests very weak anisotropy (best-fit value is 2%) but also does not offer a good constraint on α as it includes 0 as a possible solution. The range of equally well-fitting fast polarizations is broad, from 40° to 100° , with a preference for 60-80 range if anisotropy is stronger. The pattern is very different from site KMBL that has a well-defined minimum with a closed oval shape of the 2% error range.

The mismatch of sinusoids and the nature of the error surface both suggest that the anisotropic structure cannot be approximated by a single anisotropic layer with a horizontal axis. Alternatives include laterally variable anisotropy, significantly dipping symmetry, or fortuitous arrangement of multiple horizontal layers that lead to a cancellation of splitting.

Site MORW

We made a total of 60 measurements at site MORW and designated 38 of them as NULL. It has the second highest NULL to Non-NULL ratio of 1.7. Similar to MEEK, site MORW does not have a consistent pattern of the fast polarizations, instead, the range of the variation of the fast polarizations nearly covers $0^\circ \sim 180^\circ$. A number of measurements with a fast polarization between 0° and 15° are observed from the events coming from the North (Figure 6(g)). The average of the fast polarization is 64° with a standard deviation of 29° . Delay times are not consistent and go up to 1.6 s. An average of the delay times is 0.6 s and the standard deviation is 0.3 s. NULL measurements are observed from nearly all back azimuths where the data exist except between 330° and 360° . At this site, we can observe fast polarizations trending nearly N-S with large delays. In Figure 6(h), we observe a mismatch between the sinusoidal curves similar to that seen at site MEEK. The sinusoid estimated by fitting all SI values corresponds to a delay time of 0.3 s, which is ~ 0.3 s smaller than the average of non-NULL delay values. Fast polarization values are fairly similar, 64° and 70° for averaged and best-fit curves. The error surface from the waveform inversion shows a range of anisotropy strength values from 0 to 4%, with best-fitting value of 2%. A range of fast polarization values from 40° to 100° produces similar fit, with values

$\sim 70^\circ$ preferred when the anisotropy strength is higher. Similar to site MEEK, the degree of constraint on the properties of anisotropy is not as good as at KMBL (Figure 6(i)). Results from the waveform inversion yield a fast polarization that is within 10° of the two other estimates, and the delay time predicted for best-fit anisotropy strength of 2% falls between those of two other methods (Table 1). Overall, MORW has a similar set of observations as site MEEK. Both are significantly different from site KMBL and both cannot be approximated using a simple layer of anisotropy with a horizontal axis of symmetry.

Site MUN

Measurements at site MUN cover almost all back azimuths from 0° to 360° except for the range between 255° and 300° (Figure 6(j)). In total, 50 measurements were made and 29 of them were identified as NULL. This site has the second smallest ratio of NULL versus non-NULL of being 1.4. Unlike site KMBL where a consistent pattern of fast polarizations is seen, or the other two sites where a spread of the fast polarizations is very large, site MUN has two groups of fast polarizations: $\sim 10^\circ$ in data from the northwest and $\sim 135^\circ$ in data from the most other directions.

The average fast polarization at this site is 104° and a standard deviation of 38° . The best-fit sinusoid for the SI measurements corresponds to a fast polarization of 114° . These values are $\sim 30^\circ$ different from what is observed at the other three sites. Delay times are generally around ~ 0.5 s except for a few large measurements up to ~ 1 s. NULL

measurements can be observed from all back azimuths where the measurements are made. Similar to site MEEK and MORW, we observe a mismatch between the two sinusoidal curves in Figure 6(k). The sinusoid fitted using all SI measurements show a much weaker anisotropy with a delay time ~ 0.4 s smaller than the average of non-NUL measurements. The waveform inversion yields a best-fit percentage of anisotropy of ~ 1.5 % which is equivalent to a delay of ~ 0.375 s, the smallest value among the four sites in the Yilgarn craton. Inversion results suggest a fast polarization of $\sim 110^\circ$, close to the values from other methods, but do not have a strong constraint on it, with similar fit obtained for values in the range from 60° to 160° (Figure 6(l)).

Splitting in the Yilgarn Craton

Overall, four locations in the Yilgarn Craton show evidence for a modest degree of anisotropy in the upper mantle. Waveform inversions assuming a 100 km layer return best-fit anisotropy values from 1% (MUN) to 3% (KMBL), corresponding to delays of 0.25 – 0.75 s.

Using inversion results together with patterns of single-event measurements we can separate our sites into three different groups.

Group 1: KMBL forms its own group since its behavior is obviously distinct from the other three sites within the same craton. Properties beneath this site can be approximated with a single layer of anisotropy with a horizontal symmetry axis. All three methods yield

consistent results showing an agreement with the assumption and this site has the best constraint on the splitting parameters in the error surface.

Group 2: MEEK and MORW show similar patterns as measured using a combination of three different techniques. Overall, both sites suggest anisotropy that is significantly weaker than site KMBL. MEEK and MORW have the same amount of anisotropy (2%) which are close to the average of the four stations. Moreover, the mismatches between the two sinusoids and weak constraints on splitting parameters from the waveform inversions clearly separate them from site KMBL. They also have distinguishable splitting patterns in the stereoplots. Fast polarizations at both sites are not consistent and they have a large deviation. In addition, NULL measurements can be observed at almost every back azimuth, and they also have the two highest ratios of NULL versus non-NULL observations.

Group 3: MUN also stands apart from other sites. It has a relatively similar pattern as sites MEEK and MORW in that it has a mismatch between the two sinusoids and less-constrained splitting parameters in single-layered inversion, which means a single layer of anisotropy is not appropriate for the description of the structure at site MUN. However, it has different properties in its back-azimuth variation of the fast polarizations compared to MEEK and MORW. MUN shows a fast axis of 110° , compared to $60-80^\circ$ obtained for all other sites. Fast polarizations generally focus on two ranges of orientations instead of being quite scattered as MEEK and MORW. MUN has the weakest anisotropy of 1.5% and it has a smaller NULL to non-NULL ratio compared to MEEK and MORW but still larger than KMBL.

3.5.1.2 Superior Craton

In the Superior craton, we examine the anisotropy in the upper mantle by looking at the averages of the splitting parameters. Overall, the two averaging methods show good agreement with each other. The differences between the two averaged fast polarizations are up to around 5° and the variations in delay times are generally within ~ 0.1 s. The simple averages of the fast polarizations in the Superior craton fall into the range between $\sim 50^\circ$ and $\sim 85^\circ$ and the simple averages of the delay times vary from ~ 0.4 s - ~ 0.65 s.

In Figure 7, we also plot out the statistical metrics of the splitting parameters at corresponding stations. The standard deviations of the averaged fast polarizations at all sites are relatively consistent and all around 25° . This metric in the Superior craton is relatively more consistent and overall smaller compared to that of the Yilgarn craton. The standard deviations of the averaged delay times at the four sites vary from ~ 0.15 s to ~ 0.3 s. All four stations have percentages of NULL measurements above 25% but less than 50% except for site WEMQ which has more than half of the measurements designated as NULL.

Here we examine the anisotropic properties of each site in detail.

Site MATQ

We made 84 shear-wave-splitting measurements including 30 NULL measurements and 54 non-NULL measurements, or a NULL versus non-NULL ratio of 0.6. Given the imbalanced distribution of the shear-wave sources, the measurements mainly concentrate in two back-azimuth ranges: $-120^\circ \sim 30^\circ$ and $135^\circ \sim 180^\circ$ (Figure 8(a)). Fast polarizations

at site MATQ are relatively consistent with an average of 72° and a standard deviation of 27° . Delay times have an average of 0.6 s and a standard deviation of 0.30 s. NULL measurements can be detected from nearly all back azimuths where the observations are available. We also observe a good match between the sinusoid functions fitting and predicting Splitting-intensity values. In Figure 8(b), differences in fast polarizations estimated using two methods are around 5° and those of delay times are within 0.1 s. In Table 2, we have consistent estimates of splitting parameters using three different methods. However, in Figure 8(c), we see that fast polarization orientation is a relatively well constrained (best-fit value of 80° and a range from 60° to 90°) while the percentage of anisotropy varies broadly, from 1% to 5%. Overall, site MATQ shows consistency in the three metrics and is reasonable to be approximated using a single layer of anisotropy.

Site NMSQ

In total, there are 73 measurements made at site NMSQ and 31 of them are designated as NULLs, resulting in a ratio of NULL versus non-NULL measurements of being 0.7. Measurements at site NMSQ concentrate on two back-azimuth ranges: $-120^\circ \sim 30^\circ$ and $150^\circ \sim 180^\circ$ (Figure 8(d)). Fast polarizations are generally consistent around 50° with an average of 51° and a standard deviation of 25° . Delay times at site NMSQ are as large as 1.3 s, with an average of 0.6 s and a standard deviation of 0.3 s. In Figure 8(e), we can see a good match between the two sinusoids estimated using different techniques. The difference in fast polarization values is less than 1° and the delay time estimated by fitting all SI values is ~ 0.1 s smaller than the average of non-NULL measurements. The

waveform inversion returns a best-fit anisotropy strength of 2% (corresponding to a vertical shear-wave delay of 0.5 s), with a range of similar fits for values from 1% to 4% (Figure 8(f)). Constraints on the fast polarization are relatively weak, with a range of acceptable values from 20° to 80° for smaller anisotropy strengths. Overall, all three techniques provide consistent results, suggesting relatively simple anisotropic structure at depth.

Site WEMQ

At site WEMQ, we made in total 46 shear-wave-splitting measurements which includes 29 NULL measurements and 17 non-NULL measurements, resulting in a NULL versus non-NULL ratio of 1.7, which is quite different from sites MATQ and NMSQ. Most of the measurements are made using events from nearly northwest and south-southeast of the study area. In Figure 8(g), fast polarizations observed at site WEMQ are relatively consistent and mainly cluster on three groups of orientations: fast polarizations from north-northeast are around 50° - 60°; those from the north-northwest are around 90° - 100°; and measurements from the south are nearly trending 30° - 45°. The average of the fast polarizations is 58° and the standard deviation is 25°. Delay times have an average of 0.5 s and standard deviation of 0.3 s. In Figure 8(h), the two sinusoids agree well with each other, where they have the same fast polarizations and the difference in delay times is less than 0.1 s. The waveform inversion results (Figure 8(i)) suggest fast polarization varying from 40° - 80°, with a best-fit value of 60°, and the percentage of anisotropy varying from 1% to 3%, with a best-fit value being 2% (or correspondingly, a delay of 0.5 s). Overall splitting parameters at site WEMQ are consistent for all three methods. This suggests that

site WEMQ has a relatively simple anisotropic structure that can be approximated using a single layer of anisotropy that is weaker than at sites MATQ and NMSQ.

Site ‘merged’ (QM76, QM78 and QM80)

A combination of measurements from three nearby temporary sites yielded 56 measurements in total with 27 assigned as NULL measurements, which leads to a ratio of NULL versus non-NULL measurements of 0.9. In Figure 8(j), fast polarizations are not very consistent but generally vary between 50° and 100° , with an average of 85° and a standard deviation of 25° . Delay times are significantly smaller than 1 s. The average of the delay time is 0.4 s and the standard deviation is 0.2 s. NULL measurements are observed from nearly every back azimuth with data coverage. The distribution of the NULL measurements at this site is a bit different compared to the other three. Site MATQ does not have NULL measurements from back-azimuth range -45° to 90° at large incidence angles (relatively close sources). NMSQ and WEMQ do not have NULL measurements from 0° to 30° at large incidence angles. Site ‘merged’, however, has NULL measurements from all back azimuths and nearly all incidence angles which means that NULL measurements are identified from sources both close and far away. Comparison between two sinusoids in Figure 8(k) shows good agreement, with both suggesting a small delay value. Fast polarizations from two estimates differ by $\sim 3^\circ$. In Figure 8(l), both the strength of anisotropy and the fast polarization are relatively well constrained even though the area of the smallest error likely includes 0. Best-fit fast polarization is 90° (with a range from 60° to 120°), and best-fit anisotropy strength is 2%, corresponding to 0.5 s delay. As shown

in Table 2, all three methods provide consistent answers implying a single layer of weak anisotropy with nearly E-W trending symmetry axis.

Splitting in the Superior Craton

Overall, each of the four sites in the Superior craton shows a high degree of consistency among the results using three different methods, which means that a single layer of anisotropy can approximate the anisotropic structure beneath this area. Different from the sites in the Yilgarn craton, it is not easy to fully separate the sites in the Superior craton based on a combination of different metrics. Instead, given different parameters or metrics, we can separate the sites in the Superior craton in many different ways.

Based on the results from the single-layer inversion, all four stations in the Superior craton have similar patterns of the corresponding error surfaces. The contours of the error toward the global minimum (dark blue areas in Figure 8) are bell-shaped and they are elongated along the strength of anisotropy axis. This observation illustrates the fact that the azimuth of the fast axis is constrained better than the strength of anisotropy. Among the four sites, site MATQ is the worst constrained and the possible range of the percentage of anisotropy varies from 1% to 5%. Site ‘merged’ has the best constraint on the splitting parameters with the error range of the fast polarization being 20° and that of the percentage of anisotropy being 1%. The other two stations NMSQ and WEMQ fall between the two sites.

Moreover, we can detect minor differences in the strength of anisotropy among the four stations. Sites ‘merged’ and WEMQ show the weakest anisotropy, likely less than 2%, while NMSQ and MATQ suggest stronger anisotropy. MATQ suggests a 3% anisotropy and NMSQ suggests a 2.5% anisotropy. The averages of individual measurement at those locations agree with the waveform inversion results. Site ‘merged’ and WEMQ have average delay times 0.3 – 0.4 s while the other two have average delay times larger than 0.5-0.6 s. Fast axes are relatively well constrained and are different from station to station. MATQ has a fast-axis orientation of $\sim 75^\circ$, NMSQ and WEMQ show generally similar orientations of the fast axes of $\sim 50^\circ$, while the ‘merged’ site has a fast orientation of $\sim 90^\circ$.

If we focus on the splitting patterns at individual sites, the distribution of the NULL measurements at site ‘merged’ covers different back azimuths and nearly all incident angles, which means both measurements from events nearby or far away yield NULL measurements. Site NMSQ and WEMQ have similar patterns in the back-azimuth variations of fast polarization, distributions of NULL and non-NULL measurements are very similar especially from 0° to 30° , neither of the sites have NULL measurements at large incident angles. Site MATQ does not have NULL measurements with large incident angles from -45° to -90° . However, site WEMQ and NMSQ cannot be grouped together if a NULL versus non-NULL ratio is considered. WEMQ has a very high ratio of NULL versus non-NULL ratio larger than 1, whereas at the other sites, corresponding ratios are smaller than 1.

Thus, we have four locations within the superior craton, each with a somewhat different signature of the anisotropic structure beneath it.

3.5.2 Receiver-function Analysis

3.5.2.1 Yilgarn Craton

In the Yilgarn craton, we computed the RFs and their corresponding harmonic decompositions at the four permanent stations adopted in the shear-wave studies. We used 1314 records, selected from earthquakes between 2008 and 2019 with magnitudes above 6, at distances 20 to 180 degrees (Figure 9(a)). We are able to select multiple reliable anisotropic boundaries both in the shallow upper mantle and the crust at each individual site in the Yilgarn craton following the systematic procedure and selection criteria. We find that the details of the anisotropic structure differ from site to site, thus we describe them individually.

Site KMBL

In total, we picked 312 P-wave arrivals (Figure S1(a)) to compute the receiver functions and their corresponding harmonic decomposition. At site KMBL, the amplitudes of the anisotropic phases in the receiver functions are not too large and the anisotropic structure is relatively simple.

In Figure 10(a), on the Q component, largest amplitudes appear around -1.3 s which corresponds to the expected delay of Ps wave converted at the ~ 36 km deep Moho. The amplitude of the phase is relatively smaller in the back-azimuth range $120^\circ \sim 180^\circ$. We can observe a systematic variation of the polarity and size of the phases at the same time on the

transverse component. This phase changes its polarity at 135° , 45° , -5° and -60° , which implies that the Moho might be an anisotropic interface beneath site KMBL.

At delay ~ 0.7 s we identify a phase on T component of the back-azimuth gather (green arrow), as well as on 4-lobed harmonic components, with amplitude of \cos^2 component being significantly larger than \sin^2 . Correspondingly, the symmetry axis for this phase is 16° . At delay of ~ 3.4 s we identify a phase on the four-lobed terms, both individual harmonic and the vector length plot (purple arrow). The energy coming from the effects of anisotropy or dipping interfaces is nearly three times as large as that coming from the unmodeled part which we attribute to noise and scattering. Amplitudes of harmonic components (Figure 10(c)) yield horizontal orientation of the symmetry axis of -46° . This phase is not visible on the back-azimuth gather (Figure 10(a)), but is quite clear in data from the NW and N, illustrated by the epicentral gather (Figure 10(b)).

Finally, we observe a clear peak at 4.8 s in the amplitude of the coefficients for the two-lobed terms in the harmonic functions (orange arrow). The amount of energy from the effects of anisotropy of dipping interfaces is more than twice as large as the unmodeled part. Harmonic component amplitudes (Figure 10(c)) suggest a horizontal symmetry axis orientation of 76° . Both back-azimuth and epicentral gathers show this phase clearly. Interestingly, its amplitude on Q component varies significantly with direction and hence we do not see it on the constant component (Figures 9(c)-(d)).

In the vector-length measurement plot (Figure 10(d)), we can observe two more peaks: one between 9 and 10 s on the four-lobed component and the other between 13 and 14 s on the two-lobed component. Both phases fall within the time range of crustal multiples. A negative transverse pulse between 9 and 10 s does appear from back-azimuth range -60 through 90 (Figure 10(a)). Epicentral gather shows exceptionally clear crustal multiples on the Q component, and somewhat surprisingly we also observe a transverse ‘echo’ of the Psms multiple between 10 and 15 s on the T component. Since the effect from the crust multiples overprints our prospective signals arriving at the same time windows, we cannot choose them as reliable observations of anisotropic boundaries beneath site KMBL.

Site MEEK

We picked 336 phases to compute the receiver functions at site MEEK (Figure S1(b)). Compared to site KMBL, MEEK has a relatively complicated structure and overall the energy of the converted phases is much higher than those at KMBL.

First clear phase (black arrow) is seen between -5 and -4 s on T components of back-azimuth and epicentral gathers (Figures 10(a)-(b)) and both 2-lobed and 4-lobed harmonic components (Figures 10(b)-(c)). A weak phase is also present on Q component of back-azimuth gather. Q component polarity changes at back azimuth 150° while T component polarity changes twice, at 0° and 90° . Timing of observed phases implies a strong anisotropic contrast, or zone, in very shallow crust.

The Ps phase from the crust-mantle boundary at delay times -2 - 0.5 s is the largest peak on Q and const components. On Q component of the back-azimuth gather the width of this pulse decreases between 0° and 180° . This phase has energetic directionally varying pulses on the T component. Polarity changes occur around 210° (from positive to negative) and around 30° (from negative to positive). Harmonic components show energy with 2-lobed and 4-lobed patterns, and a high level of unmodeled energy as well. Width and complexity of this phase may reflect multiple closely spaced converting boundaries.

Between delays of 2 and 5 seconds back-azimuth gathers show considerable energy with directional changes in polarity on both Q and T components. Viewed in the epicentral gather two phases stand out, at 2 - 3s and between 4 and 5 s (green and orange arrows, respectively). Positive Q components (Figure 11(b)) correspond to an increase in impedance with depth, however the back-azimuth gather shows these phases to change polarity at $\sim 150^\circ$. It is thus likely that the changes in impedance are caused by vertically varying anisotropy.

Corresponding harmonic components show that the phase at 2-3 s has energy in both 2-lobed and 4-lobed components. In the later phase the 2-lobed energy is clear, while the 4-lobed component has high unmodeled part and thus cannot be considered reliable. Using amplitudes of 2-lobed components we determine horizontal symmetry axes orientations of 49° at 2.3 s and 29° for the phase between 4 and 5 s. The back-azimuth gather of T components does indeed show these phases change polarity around 30° and 200° . The fit

is not perfect to the axes determined with $\sin 1$ and $\cos 1$ component amplitudes, confirming presence of some 4-lobed energy in these phases.

Similar to our observation at site KMBL we also detect an ‘echo’ of the multiples on the transverse component at site MEEK (Figure 11(b)). From the vector length measurements of coefficients of the two-lobed terms in Figure 11(d), we can identify a peak around 10 s and a long lobe extending from 10 s to 20 s. The former likely represents the multiples. We do not see obvious phases for the later on either of the gathers (Figure 11(a)-(b)) and thus chose to not interpret it.

Site MORW

At site MORW, 371 phases are combined to calculate the receiver functions (Figure S1(c)). Site MORW has a relatively complicated anisotropic structure as numerous converted phases are observed in the -5 s through 10 s time interval of delay times.

The earlier arriving phase is between -5 and -4 s (black arrow), seen very clearly on the T components of the back-azimuth gather (Figure 12(a)) and the Q component of the epicentral gather (Figure 12(b)). Strong 2-lobed component (Figures 11(c)-(d)) is associated with it, with $\sin 1$ coefficient much larger than the $\cos 1$, consistent with a polarity change seen in back azimuth T component at $\sim 0^\circ$.

Directionally varying energy on T component between -2.5 and -1.5 s (Figure 12(d)) appears to be dominated by unmodeled energy (Figure 12(d)) and thus not interpreted. The Ps phase (largest peak on Q and const components, delay ~ -1 s) is associated with a strong 4-lobed phase and a significant level of unmodeled energy in the 2-lobed component.

We group together a number of phases appearing between 2 and 4 s delay on both Q and T components (green arrows) and associated with significant energy on both 2-lobed and 4-lobed components. Positive Q component and a clear phase on the const component at ~ 3.5 s suggest an increase in impedance with depth. Evaluating the orientation of the horizontal symmetry axis at 2.2 s we obtain -10° using 2-lobed components and 10° using 4-lobed components, which is consistent with observed switch in polarity $\sim 180^\circ$ in the T component (Figure 12(a)). A weaker phase between 6 and 7 s (orange arrow) is positive on Q and const components (Figures 11(a)-(c)), while its directional variation is uncertain as the unmodeled component is approximately the same size as that expected from anisotropy (Figure 12(d)).

Finally, a phase at ~ 10.3 s (maroon arrow) is clearly visible in the 2-lobed vector length plot (Figure 12(d)), and also in the T components of both the back-azimuth and epicentral gathers. It is exactly within the time window of the crustal multiples Ppms and Psmp, however the epicentral gather (Figure 12(b)) shows this phase to have a nearly constant time, as would be expected of an upgoing converted phase. Thus, we believe the 11 s phase is a real feature of the anisotropic structure, obscured in Q component by the multiples.

Relative size of $\sin 1$ and $\cos 1$ amplitudes (Figure 12(c)) suggests the orientation of the horizontal symmetry axis of 62°

Site MUN

We select 295 P-wave arrivals (Figure S1(d)) to carry out the receiver-function analysis. Site MUN has a distinct pattern compared to the other three sites in the Yilgarn craton. Overall, the energy of the phases in the receiver functions at site MUN is much higher, and the systematic patterns in the transverse component are the clearest. We find an alternating 2-lobed pattern from $-5 - 0$ s with a polarity change at $\sim 100^\circ$ on the T component. The Q component and the const components do not show significant energy at the time of the expected Ps phase from the Moho, which together with a strong 2-lobed variation (Figure 13(d)) may imply a dipping Moho.

Between delay times 1 and 2 s we see consistent phases in back-azimuth and epicentral gathers (Figures 12(a)-(b), green arrow). Q component is positive, implying an increase in impedance with depth. T component of back-azimuth gather changes polarity at 0° , 100° and 220° . Both 2-lobed and four lobed components (Figures 12(c)-(d)) show considerable energy. Using only 4-lobed amplitudes at 1.8 s we obtain the horizontal orientation of the symmetry axis of -20° , consistent with directional variation observed in the back-azimuth gather. Between 5 and 6 s a phase is clearly seen in the T component of the back-azimuth and epicentral gathers, as well as on the 2-lobed vector length plot (orange arrow). Some 4-lobed energy is also present. Using $\sin 1$ and $\cos 1$ coefficients at time 5 s (peak in

harmonic components, Figure 13(c)) we get the orientation of the horizontal symmetry axis of 68° . A positive Q component phase is present between 6 and 8 s on both back-azimuth and epicentral gathers (maroon arrow), and there is a corresponding broad peak on the const component. There seem to be no significant directional variation.

Between 9 and 10 s both 2-lobed and 4-lobed vector length components show pulses (cyan arrow) that considerably exceed the level of unmodeled energy, and corresponding pulses are very clear in the individual harmonic components (Figure 13(c)). In the back-azimuth gather we observe a T component phase between 9 and 10 s that changes polarity at 0° and 150° . Examination of the epicentral gather shows this phase to be distinct (earlier) than the crustal multiples (Figure 13(d)) at larger epicentral distances. The mixing of energy from the likely real anisotropic boundary and the crustal multiples (also clear in Figure 13(b)) makes determination of the horizontal symmetry axis uncertain. Using only \sin^2 and \cos^2 components at time ~ 9.3 s we get an orientation of 46° .

3.5.2.2 Superior Craton

In the Superior craton, we computed the RFs and corresponding harmonic decompositions for the permanent stations MATQ, NMSQ and WEMQ that were used for the shear-wave-splitting analysis. We also used a temporary station QM78, one of the sites combined in the “merged” data set. Receiver functions are sensitive to smaller scale features thus we cannot combine data from a number of temporary sites. We used a total of 646 records collected from earthquakes with magnitudes above 5.5 between 2005 and 2019 at distances 30 to 180 degrees. The number of data at individual locations is smaller than in Australia, both because sources of seismicity are farther away and records are less clear, and also because data were collected over different time spans. In particular, site QM78 operated

from the summer of 2013 through the summer of 2015, and site WEMQ operated from 2005 until 2013. Similarly, as our observation in the Yilgarn craton, the anisotropic structure beneath each individual site in the Superior craton is different so we have to examine and discuss the corresponding observations one by one.

Site MATQ

At site MATQ, we used 306 records (Figure S2(a)) to compute the receiver functions and the corresponding harmonic decompositions.

At delay -5 s a positive Q component phase is clear on back-azimuth and epicentral gathers (Figure 14(a), black arrow), and on the const component. It also has a T component that varies in polarity, and both 2-lobed and 4-lobed components (Figure 14(d)) display considerable energy. Around -2 s, the largest positive phase on the Q component represents the Ps converted phase from the Moho. In the back-azimuth gather its T component changes polarity at -100° , and the vector-length of the 2-lobed component (Figure 14(d)) is exceptionally large. Likely horizontal symmetry axis orientation determined from sin1 and cos1 components at -2.5 s is 70° .

At delay 1.2 s the const component shows a clear positive phase (orange arrow) implying an increase in impedance with depth. Q components of back-azimuth and epicentral gathers show this feature, although it is not very strong. It appears to be associated with directionally varying phases between 1 and 3 s, seen clearly on the sin2 component (Figure

14(c)) and the vector length of the 4-lobed component (Figure 14(d)). Using \sin^2 and \cos^2 components at 1.3 s, we obtain a horizontal axis orientation of -61° .

At delays 10 -11 s the \cos^2 component and the vector length of the 4-lobed component contain a significant peak (maroon arrow). Covered by crustal multiples on the Q component, this phase emerges on the T component of both back-azimuth and epicentral gathers. In back azimuth the polarity change is at $\sim -70^\circ$. The delay of this phase in the epicentral gather is nearly constant between 30° and 90° distance, confirming that it is a real converted wave and not a multiple. Using \sin^2 and \cos^2 harmonic components at 10.5 s to estimate the horizontal symmetry axis orientation, we obtain a value close to 1° .

Site NMSQ

In total we utilized 124 events (Figure S2(b)) to compute the receiver functions and carry out the corresponding harmonic decompositions. In Figure 15, we observe a consistent positive converted phase around -1.5 s on the Q component and the const component which corresponds to the Ps conversion at the Moho. T component energy is high for this phase (Figures 14(a)-(b)) however directional variations are not consistent with effects of anisotropy, as shown by large value of unmodeled harmonic components (Figure 15(c)-(d)).

At delay time ~ 1.9 s a consistent directionally variable phase (green arrow) is present on T components of back-azimuth and epicentral gathers, and on the 4-lobed harmonic

components. Using $\sin 2$ and $\cos 2$ amplitudes at time 1.9 s we obtain a horizontal symmetry axis orientation of 47° . At 5 s delay the Q components on back-azimuth and epicentral gathers, and the $\cos 1$ component show a clear positive phase (orange arrow). T component is not clear for this phase, although we do see some energy on the $\cos 1$ component and the corresponding 2-lobed vector length component. Using $\cos 1$ and $\sin 1$ amplitudes at 5.6 s, we obtain a horizontal symmetry axis orientation of 8° . Between delays of 7.5 and 9 s clear peaks are present on both 2-lobed and 4-lobed components (maroon arrow). The back-azimuth gather shows energy on the T component although with a complex directional variation. An epicentral gather for data from the south (backazimuths -225° through -75°) do show a consistent positive T phase at ~ 8 s, earlier than the expected crustal multiples. Using amplitudes of $\sin 2$ and $\cos 2$ harmonic components at 7.7 s we obtain a symmetry axis orientation of -13° .

We note a clear T component phase at 11 s delay in the epicentral gather (marked with a question mark). In the back-azimuth gather this feature is not as clear, thus while a plausible candidate for another boundary at depth, we choose not to interpret it.

Site WEMQ

We select 100 records (Figure S2(c)) to compute the receiver functions and the corresponding harmonic decompositions. Site WEMQ shows a much simpler structure compared to the other sites in the Superior Craton (Figure 16).

The largest Q component and const component positive phase around -1 s which represents Ps conversion at the Moho. T component has energy at the same time, and 2-lobed components (sin1 and the corresponding vector length, Figures 15(c)-(d)) suggest the crust-mantle transition has anisotropy associated with it. Between delays 0 and 2 s the vector length components contain energy suggesting an influence of anisotropy, however neither the back-azimuth nor the epicentral gather contain directionally varying phases in this time window. Between delays 2 and 4 s, a positive-negative pair of pulses is seen on Q components of back-azimuth and epicentral gathers, and on the const component (orange arrow, Figures 15(a)-(c)).

Between delay times of 7 and 8 s harmonic components (sin1, cos2, 4-lobed vector length) contain a clear phase that is much larger than the corresponding unmodeled component. In data from the northwest (shown in the epicentral gather, Figure 16(b)) there also appears to be a positive Q component, although it does not appear in the const component and thus is not directionally consistent. Using amplitudes of cos2 and sin2 components at 6.6 s we obtain a horizontal symmetry axis orientation of -49° .

Site QM78

In total, we used 117 records (Figure S2(d)) for the computation of receiver functions and harmonic decompositions. The largest Q component and const component phase at ~ -2 s represents the Ps phase from the crust-mantle boundary (Figure 17). It has a strong 2-lobed varying energy associated with, suggesting a horizontal symmetry axis orientation of -28° .

Between delays 1 and 2 s both 2-lobed and 4-lobed harmonic components show clear phases (Figures 16(c)-(d), green arrow). T component of the back-azimuth gather changes polarity at -100° and at 30° , while the epicentral gather for the northwestern quadrant (Figure 17(b)) shows this phase clearly on the T component. There is no obvious Q component associated with it. Using amplitudes of 2-lobed harmonic components at 1 s we estimate the horizontal orientation of the symmetry axis to be 52° .

Q components of back-azimuth and epicentral gathers and the const component show a positive phase at ~ 4.7 s delay. Directionally varying T component energy is present in the same time window, and harmonic components suggest the 4-lobed variation is more significant. Using \cos^2 and \sin^2 component amplitudes we evaluate the orientation of the horizontal symmetry axis as $\sim 8^\circ$.

T components of the back-azimuth gather, and the harmonic components with the 4-lobed variation suggest a phase between 8 and 10 s (maroon arrow). Using \sin^2 and \cos^2 amplitudes at 10 s we estimate the orientation of the axis as -48° . However, we do not see clear evidence for this phase in the epicentral gather and thus consider it uncertain.

3.5.3 Comparison between Two Cratons

3.5.3.1 Shear-wave Studies

From shear-wave studies, we find that the cratonic lithospheres at both cratons are not homogenous domains, instead, they are different from site to site within the same craton. At all the sites in both cratons, we find there are back-azimuth variations of the fast

polarizations and NULL measurements from nearly all the back azimuths where the measurements are made.

In the Superior craton, we can find a good agreement between the two sinusoidal curves at all the sites which are predicted by combining two different estimations of splitting parameters. Overall, the splitting parameters estimated by an integration of three techniques using shear waves are consistent, which suggests the structure beneath this craton can be estimated using one layer of anisotropy with a horizontal symmetry axis. However, each site at the Superior craton has its own distinct behavior and it is not easy to separate the four sites into different groups based a selection of fixed metrics.

In the Yilgarn craton, only at site KMBL we can detect such an agreement among the results from the three methods of estimation of splitting parameters, all the other sites show considerable mismatches and the splitting delays calculated by fitting SI measurements are larger. However, sites at this craton are easy to be separated into different groups based on different metrics, and this division corresponds with the geographic domains they belong to. The percentages of NULL measurements are different too. In the Yilgarn craton, except for KMBL where the percentage of NULL measurements is slightly above 50%, those of all other sites are much larger than 50%. However, in the Superior craton, only site WEMQ shows a NULL measurement percentage to be above 50% whereas those of the rest of the sites are below 50%.

3.5.3.2 Receiver-function Analysis

In general, the P-S conversions in receiver functions have larger amplitudes at sites in the Yilgarn craton than those detected in the Superior craton. In the crust, we can detect

anisotropic boundaries at all the sites in the Yilgarn craton whereas in the Superior craton, we can only detect crustal anisotropic boundaries at site MATQ and QM78, and in that QM78 has a relatively weaker anisotropic signal.

In the upper mantle, we can identify multiple anisotropic boundaries in the lithosphere at all the sites in both cratons, most of which are mainly above ~ 100 km with the rest between 120 km and 160 km (Figure 18). Two isotropic boundaries are identified: one at MUN with a positive impedance contrast and the other at WEMQ with a negative impedance contrast. However, within each individual craton, we cannot find a consistent pattern of the anisotropic structure across the craton and the patterns are different from site to site and do not cluster within the tectonic domains. Even though we can detect anisotropic boundaries at a similar depth among different sites, the orientations for the symmetry axes on the horizontal plane are not the same.

In the Yilgarn craton, we cannot observe anisotropic boundaries extending deeper than 100 km at sites KMBL and MEEK but we do identify deeper boundaries at site MORW and MUN (Figure 18). At sites KMBL and MEEK, only one type of anisotropic pattern can be observed whereas the anisotropic patterns at sites MORW and MUN are more complicated and both 2-lobed and 4-lobed patterns can be observed at certain depths. Compared to the Yilgarn craton, overall, sites at the Superior craton do not have as many anisotropic boundaries identified, specially depths shallower than ~ 100 km. In the Superior craton, all the sites have anisotropic boundaries deeper than 100 km. Except for site QM78 where

both 2-lobed and 4-lobed anisotropic boundaries are identified at certain depths, only one type of anisotropic pattern (mainly 2-lobed) is observed at all the other three sites.

3.6 Discussion

3.6.1 Comparison with Previous Seismological Studies

3.6.1.1 Yilgarn craton

There have been a limited number of shear-wave-splitting results reported for the Australian continent given the previous sparse coverage of the seismic networks as well as their short operation durations. Heintz and Kennett (2005) estimated shear-wave splitting across the Australian continent, reporting relatively weak anisotropy (delay of 1 s or smaller) in most locations, and stressing the complexity of shear-wave-splitting patterns. Significantly, the splitting patterns did not align with the nearly north-south Absolute Plate Motion (APM) of the Australian continent. In addition, NULL measurements were also reported at all the sites. In the Yilgarn craton in particular, to the north of 30°S latitude fast polarization directions were generally 40° ~ 50°, and aligned with regional faults, whereas to the south of 30°S a consistent fast polarization direction of 60° ~ 90° was reported for 10 sites recording a single event. Our observations are in good agreement with this study and confirm the observation of relatively weak anisotropy and abundant NULL measurements at all sites in the Yilgarn craton. Compared to Heintz and Kennett (2005) which used data collected over a 6 month period, we are able to observe more complexity in the measurements based on a 10-year-long dataset.

The crustal thickness in the Yilgarn craton has been estimated to be 32 km – 39 km using H-k stacking, a teleseismic converted wave technique that uses direct and multiply reflected waves in the crust (Yuan, 2015). Using a variant of receiver-function analysis

different from ours, Reading and Kennett (2003) reported a sharply-defined Moho at the depth of 40 km (± 2 km) in the northern Yilgarn craton. Reading et al. (2003) computed the receiver functions at sites along two transect lines from the west to the east of the Yilgarn craton. In their study, they interpreted the Moho to be dipping gently to the east. Similar results were also reported by Goleby et al. (2006) who combined results from multiple seismological techniques with different scales of sensitivity, from the continent-wide to a few km. They confirmed observations of the eastward dipping Moho and a complex, dipping mantle lithospheric body beneath the Yilgarn craton. Our observations from receiver-function analysis are generally consistent with the previous studies, as demonstrated by the good fit of predictions for the converted waves from the Moho and the crustal multiples in Figures 9-16. Moreover, we do detect a signal of a dipping Moho beneath site MUN.

Ford et al. (2010) performed the first comprehensive survey of lithospheric layering beneath Australia using S-P receiver-function analysis. Beneath the western Australian craton, they reported Mid-lithosphere Discontinuities (MLDs) between the depths of ~ 70 km and ~ 100 km, and could not identify deeper boundaries that would be consistent with the Lithosphere-asthenosphere Boundary (LAB). In our study, we are able to detect multiple anisotropic boundaries, some with a downward increase in impedance, at the depths where MLDs are identified by Ford et al. (2010). Since P-S receiver functions we have constructed use higher frequency, the downward impedance drops observed using S-P receiver functions and described as MLDs might be too gradual to be observable in our study.

Surface wave studies show that the crust of the west Australian craton is underlain by the thick lithospheric mantle extending to the depth of around 200 km and then the asthenosphere with some level of anisotropy (Kennett, 2003, Kennett et al., 2004). In addition, many studies using surface wave tomography suggest that cratonic Australia has a layered anisotropic structure (Debayle et al., 2016, Debayle et al., 2005, Fishwick and Reading, 2008, Simons et al., 2002, Yoshizawa, 2014). In those studies, it was proposed that in the upper layer, the anisotropic fabrics are trending east-west and in the lower layer, the anisotropic patterns align with the current direction of plate motion. Yoshizawa and Kennett (2015) proposed a shear-wave velocity model using surface waves which has a gradual Lithosphere Asthenosphere transition (LAT) which the authors differentiate from the Lithosphere-Asthenosphere Boundary (LAB) that is especially elusive under cratons (Eaton et al., 2009). The range of the LAT at sites in our study area is between ~ 100 km and ~ 225 km.

3.6.1.2 Superior craton

Previous studies have reported an overall weak anisotropy with fast-axis orientations subparallel to the APM in the asthenospheric mantle beneath the Superior craton using shear-wave splitting. Darbyshire et al. (2015) reported fast polarizations between ENE-WSW and ESE-WNW across our study area and delay times under 1 s at most of the sites except for a few measurements of ~ 1.3 s. A high portion of NULL measurements is identified at site WEMQ (Darbyshire et al., 2015). Similar observations of small delay times with an average of ~ 0.5 s and fast polarizations of $\sim 70^\circ$ are identified in the eastern Superior craton in Quebec (Chen et al., 2018). In that study, NULL measurements have also been observed and reported for nearly all the sites in corresponding area. In the

Superior craton to the west of our study area, Frederiksen et al. (2007) reported weak anisotropy (average of delay time of ~ 0.67 s) and an E-W fast polarization direction subparallel to the APM. Our observations in the Superior craton agree with previous work. In general, all four sites have average fast polarizations of around 70° , and the average delay time is around 0.7 s.

The properties of the crust in the Superior craton and its surrounding area have been explored using various types of receiver-function analysis. Levin et al. (2017) used timing of Ps phases from the Moho and H-k stacking to estimate the crustal thickness at sites we have used, obtaining values between 33 km and 39 km. Earlier, Thompson et al. (2015) obtained nearly identical values for sites MATQ and WEMQ. A good match of our detailed receiver functions and predicted times of the Ps phase from the Moho and the crustal multiples in Figures 9-16 is not surprising as we rely on data that significantly overlaps with these previous studies. Also, the area between sites MATQ and NMSQ was surveyed by seismic reflection profiling in the course of the LITHOPROBE program (Clowes, 2010), with crustal thickness between 35 and 40 km reported by Ludden and Hynes (2000).

Ford et al. (2016) explored cratonic lithosphere in the Wyoming and western Superior cratons with a set of receiver-function techniques very similar to those we have applied. While our areas of study do not overlap, the overall findings of multiple anisotropic boundaries in the upper 150 km of the North American lithosphere, and of strong lateral variations in the nature and position of boundaries are very similar to ours. A notable difference is in that we only detect an impedance decrease with depth that may signify an

MLD at one out of four location. Abt et al. (2010) combined P-S and S-P receiver-function analysis to understand the discontinuities in the upper mantle in North America mostly to the south of our study area. In the Superior craton (site ULM in Abt et al. (2010)), an internal low-velocity zone in the lithosphere can be identified at the depth of 101 ± 14 km using S-P receiver functions. The absence of LAB in P-S receiver functions is consistent with a thermal transition at the bottom of the lithosphere.

The seismic layering in the mantle has been explored and reported in multiple studies using surface wave tomography. Yuan and Romanowicz (2010) performed an inversion of long-period waveforms for a 3D anisotropic shear-wave velocity structure of North America. According to the model, there are two distinct layers in the lithospheric mantle which these authors interpreted as a highly depleted chemical layer (which is around 150 km thick in our study area) on top of a thermal transition layer (bottom of which is around 200 km in our study area). In the northeastern Superior craton, the fast axis of anisotropy in the chemical layer aligns with the geological sutures on the surface. Beneath the two layers, the asthenospheric layer has an anisotropic direction nearly parallel to the APM. In the Ontario section of the Superior craton to the west of our study area both vertical and lateral variations in azimuthal anisotropy were investigated using Rayleigh waves (Darbyshire and Lebedev, 2009, Darbyshire et al., 2007).

3.6.2 Comparison with Global and Local Models

We first compare our observations with the depths of the LAB estimated beneath each individual site based on a global model by Steinberger and Becker (2018), shown in Figure 19. The thickness of the lithosphere is estimated by combining a seismic tomography

model and a thermal model with a lateral grid spacing of 0.25° . In the Yilgarn craton, the depth of the LAB increases from the coast to the core of the craton. The LAB is shallowest at 160 km beneath site MUN, then around 180 km beneath MORW, and is deepest at 200 km beneath MEEK and KMBL (Figure 19(a)). In the Superior craton, the depths of the LAB are larger than 200 km everywhere (Figure 19(b)), with the site WEMQ having the thickest lithosphere of 220 km.

We compare our results with tomography models for corresponding cratons. In the Yilgarn craton, we can only detect anisotropic boundaries within the LAT (Yoshizawa, 2014, Yoshizawa and Kennett, 2015) at site MORW and MUN, while at KMBL and MEEK the deepest anisotropic boundaries identified are both shallower than the top of the LAT (Figure 20(a)). We also adopt a global model from Debayle et al. (2016) which has a lateral grid spacing of 2° ($6^\circ \sim 12^\circ$ for the azimuths of fast axes) and a vertical spacing of ~ 20 km (Figure 20(b)-(d)). The shear-wave velocity increases from 50 km to ~ 100 km and then keeps decreasing till 250 km. Interestingly, between 100 and 200 km, the strength of anisotropy is between 2% and 4% with an average of $\sim 3\%$ and the fast-axis orientation remains close to 0° .

We compare our results similarly in the Superior craton. We adopt the tomography model for North America (Yuan et al., 2014, Yuan and Romanowicz, 2010) and mark the MLD and LAB depths defined in it. Anisotropic boundaries can be identified above the MLD and sites QM78 and MATQ have anisotropic boundaries beneath it. At all sites, the profiles for different parameters of this model are similar to each other: they all have an increase in

shear-wave velocity till around 170 km ~ 180 km. Two different anisotropic layers can be identified within the upper 200 km. From 50 km to 150 km, the anisotropic layers have fast polarizations around -80° and strength of anisotropy between 0.5% and 1%. Beneath it, there is another anisotropic layer ~ 50 km thick which has very weak anisotropy. Then from 200 km to 250 km, the strength of anisotropy starts to increase and the fast axes are nearly 50° .

Overall, it is hard to detect a relationship between the anisotropic boundaries in our study and the tomography models in either of the cratons. A major reason for it is that the tomography models have limited lateral resolution for instance it could be around a few hundred kilometers and each of the profiles that we extract actually reflects an average of the corresponding properties in a much larger area on the scale of a few degrees instead of just beneath the site. This does not necessarily imply a contradiction, instead, it reflects the necessity of our study in order to have a detailed description for anisotropy at each site. Moreover, our results can work as constraints for future tomography studies.

3.6.3 Layering of the Cratonic Lithosphere

Our investigation reveals the presence of numerous sub-horizontal boundaries in seismic properties within the lithospheric mantle of two cratonic regions (Figures 17, 19, 20). Here we discuss elements of this layering that are common to both regions and thus likely reflect aspects of cratonic lithosphere in general.

Our results (Figures 19(a) and 20(a)) agree with previous work in not being able to see the lower limit of the lithosphere (cf. Fischer et al., 2010). In all locations that we have probed

the LAB remains elusive (Eaton et al., 2009). In an attempt to detect more gradual changes in vertical properties, we have constructed RFs with periods of 8 s and longer but were not able to detect downward impedance decreases at depths $\sim 200 - 250$ km suggested for the LAB by tomography (Yuan et al., 2014; Debayle et al., 2016). Using the measure of sharpness of the converting boundary proposed by Levin et al. (2016), we can be certain that the vertical changes in impedance associated with the lower limit of cratonic lithosphere take place over distances larger than 20 km (estimated as $\sim 0.6 \cdot \lambda$, where the shortest wavelength in the upper mantle $T \cdot V_s = 8 \text{ s} \cdot 4.5 \text{ km/s} = 36 \text{ km}$).

We find all observable impedance contrasts to reside above the depth of 150-170 km (Figure 18). This is in general accord with the idea that there are two distinct layers within the cratonic lithosphere (e.g. Cooper et al., 2004, Lee, 2006, Yuan et al., 2011, Yuan and Romanowicz, 2010), with the upper layer 100 – 150 km thick representing a volume of chemically distinct rocks, and the lower layer extending past the depth of 200 km representing the thermal differences between the lithosphere and the asthenosphere.

The number, arrangement and properties of seismic boundaries appear to be unique to each site. While we survey large areas, their stability over 2.5 Ga or longer forms an expectation of some common elements that would arise if material making up the cratons could deform and adjust over this time period. We do not observe such common features, a finding very similar to that of Ford et al. (2016) who used nearly identical methodology to probe two other regions of cratonic lithosphere (Wyoming and south-western Superior). Our respective studies agree in documenting unique sets of multiple anisotropic boundaries in

the upper ~150 km of the mantle, with and without impedance contrasts, at individual sites within cratons. We also agree on these sets of boundaries being characteristic for each site. Interestingly, locations we have surveyed do not seem to have consistent vertical decreases in impedance documented by Ford et al. (2016) in most of their data sets. Barring methodological issues, this finding may point to important variations in the composition layering in overall structure of the cratonic lithosphere.

One finding that is common in our results has not been a part of previous RF surveys of the cratonic lithosphere. At most locations we find at least one boundary where the impedance increases with depth. These increases reside at depths between 80 and 120 km beneath the Yilgarn craton, and between 70 and 100 km beneath the Superior. This is the depth range where a compressional wave speed increase referred to as the Hales Discontinuity is required by travel time observations in both North America and Australia (Hales et al., 1975, Hales, 1969). Unlike our findings that document a local increase in shear-wave impedance at a boundary, these earlier travel time studies require a bulk increase in seismic wave speed over a significant vertical distance.

3.6.4 Comparison with Geophysical Attributes and Geological Settings on the Surface

Shear-wave splitting integrates of the anisotropic effects accumulated along the ray path from the lower mantle till Earth's surface. In order to detangle the cumulative effects and associate the corresponding contributions of anisotropy with different sections of Earth, we compare the two estimates of averaged shear-wave splitting with other geophysical and geological boundaries both at depth and on the surface. The shearing of the asthenosphere represents the present deformation process within Earth's interior and it is commonly

treated as a source of anisotropy in the mantle. We thus compare the averaged fast polarizations with APM directions estimated using the NUVEL1A-HS3 model. The direction of APM is calculated for each site instead of using an average of the study area (Figures 21(a), 22(a)). Moreover, we also compare the averaged fast polarizations with the geological boundaries on the surface trying to explore the relationship between the anisotropic measurements and the surface geology.

In Figure 22 (a), we can see that the APM directions are quite consistent among the four sites in the Yilgarn craton, which vary from 6.5° at KMBL to 9.8° at MUN. Overall, at all sites, we can see that the averaged fast polarizations and the directions of the plate motion are nearly orthogonal with each other. At sites KMBL and MEEK, the averaged fast polarizations are around 75° , which are nearly 70° away from the direction of the APM. At site MORW, the difference between the fast polarization and APM direction is only 50° , whereas at site MUN, the difference between the two angles is nearly 90° . This is unexpected because the Australian continent is the fastest moving continent on Earth, thus the mantle flow should have a large impact on the overall anisotropic observation. In our study, however, this large deviation suggests that there must be another source of anisotropy possibly in the lithosphere that overwhelms the influence from the asthenosphere. It is also important to point out that the splitting patterns at those sites are actually complicated and the averages might be influenced by some individual measurements instead of reflecting true conditions at depth.

Similarly, we also consider a relationship between the averaged fast polarizations and the terrane boundaries on the surface. In Figure 22(b), we see that the averaged fast polarizations are nearly orthogonal to the terrane boundaries on the surface. At site KMBL, the terrane boundaries colored in green are generally trending -10° from the North and thus the angle between the two is nearly 90° . At site MUN and MEEK, the terranes boundaries are generally trending N-S, at site MEEK the angle between them is nearly 80° whereas at site MUN, it is around 100° . At site MORW, the terrane boundaries are trending around -45° , and thus they are nearly 90° away from the fast polarization direction. The mismatch between the averaged fast polarizations and the terrane boundaries implies that the geology on the surface does not reflect the anisotropic properties at depth as was proposed for more recent orogenic regions by Vauchez and Nicolas, (1991).

The relationship between the direction of plate motion and the averaged fast polarization is completely different from that of the Yilgarn craton. In the Superior craton, we can detect a good alignment between the averaged fast polarization and APM direction. The best alignment is at site WEMQ where the two estimates of fast polarization are both around 58° and the APM direction is around 245° . At site MATQ, the average of the fast polarization is around 70° and the APM direction is around 247° . The other two sites have relatively larger deviations: around 10° at site NMSQ, and $\sim 20^\circ$ at the site 'merged'. The close match between the averaged fast polarizations and the APM direction suggests a major contribution of anisotropy from the asthenosphere.

The relationship between the fast polarization and the surface terrane boundaries differs from that of the Yilgarn craton, we cannot find a systematic relationship between the two. For instance, at site MATQ, it has a fast polarization direction of around 70° which is only roughly aligned with the nearby terrane boundary. While the corresponding subprovince has a complex boundary, overall it trends E-W and therefore aligns with the averaged fast polarization at site ‘merged’. Similarly, given the irregular shape of the subprovince, it is hard to make a comparison, so we cannot draw any relationship between the averaged fast polarizations at sites WEMQ and NMSQ and their corresponding terrane boundaries. This observation suggests that the surface geological domains do not correspond to anisotropy-forming fabric at depth and neither can we cluster different sites based on their tectonic domains given that no systematic relationships are observed.

3.6.5 Possible Interpretations of the Anisotropic Structures beneath the Cratons

In the Yilgarn craton, we detect NULL measurements from nearly all the back-azimuth ranges with data coverage and find overall weak anisotropy at all sites. This is unexpected given the fact that Australia is the fastest moving continent on Earth, and we thus expect the observation of strong anisotropy from the asthenosphere. Tomography models (Debaille et al., 2016, Fishwick and Reading, 2008, Yoshizawa, 2014) suggest the presence of two anisotropic layers with orthogonal fast axes which would cancel the anisotropic effects from each other. Though this interpretation is consistent with the observations of NULL measurements, it is hard to expect all sites to have exactly the same perfect cancellation of anisotropy and it is also contradictory to the observation of different shear-wave-splitting patterns at individual sites. Besides, a number of anisotropic boundaries are detected beneath each site in this study due to a much higher vertical resolution. To

reconcile the observations from both studies, we propose that the anisotropic structure beneath the Yilgarn craton includes a number of thin layers of anisotropy. Based on Debayle et al. (2016), vertical profile shows 2-4% of anisotropy over 100 km, so we expect between 0.5 and 1 s of splitting is the fabric if perfectly aligned. With multiple thin anisotropic layers in the lithosphere, only a modest amount of splitting will be accumulated along the sub-vertical shear-wave ray paths, and detection of multiple anisotropic boundaries at depth will be explained as well. Given the layers are so thin, some of them are beyond the resolution of surface waves. Thus, differences between different sites actually reflect differences in their local structures.

For the sites in the Superior craton, the asthenosphere seems to have a more significant contribution to the accumulated anisotropy compared to the lithosphere. The averages of the fast polarizations are nearly aligned with the APM, which is consistent at all the sites. Moreover, when compared with the inversion results and SI measurements, the anisotropic structures beneath the sites in the Superior craton can be approximated relatively well using one layer of anisotropy with a horizontal symmetry axis. However, our measurements of individual shear-wave splitting show a large variation of the fast polarization orientations, and NULL measurements are observed at nearly all the back-azimuth ranges of data coverage. Then there should be another contribution of anisotropy from the fossil fabrics kept in the lithosphere. Overall, the anisotropic structure beneath the Superior craton is relatively simple and has the major contribution from asthenospheric shear, with minor contribution from the mantle fabrics preserved in the lithosphere.

3.6.6 Anisotropic Fabrics and Mechanisms for Craton Formation Process

An important element in the debate about the formation of cratons is whether the style of tectonics during the Archean time was similar to present. Assuming a pre-plate-tectonic regime with mantle potential temperatures up to 250°C higher than today (Davies, 1992, Korenaga, 2008, Herzberg et al., 2010, Brown, 2007), a craton can form through a single melting event initiated deep inside a mantle plume (Pearson et al., 1995, Lee et al., 2011). As a result, the melting of peridotite is much more extensive and thus forms very thick basaltic crust with extremely dehydrated and depleted residues accumulated beneath it. Robin and Bailey (2009) also proposed that diapirism can be dominant during the Hadean and early Archean Epochs and thus can build cratons through density inversion and sorting of Earth materials. This sorting event can also happen after the melting event. The primary crust formed this way keeps evolving toward a more felsic composition through successive re-melting and delamination, until it reaches gravitational stability. Though both mechanisms can eventually lead to a structure composed of layers of different composition, however, this kind of structure is not likely to be azimuthally anisotropic given the absence of long-range horizontal displacements and associated deformation that can align olivine crystals in the upper mantle. Moreover, this type of mechanisms tends to generate layers that are horizontal, which might not be sufficient to explain the dipping interfaces. In addition, given the mechanism of this process, the structures are more likely to be simple and consistent, so it is hard to explain our observation of distinct structures beneath different sites.

Many other hypotheses of craton formation involve horizontal movements of the preexisting lithosphere. Both thrust stacking and the amalgamation of the preexisting

lithosphere can build up a craton (Bostock, 1998, Jordan, 1978), difference between the two hypotheses only relies on the rheology of the materials. Cooper et al. (2006) used numerical modelling to confirm the feasibility of the two mechanisms. Compared with the previous group of hypotheses, this type of mechanism can provide horizontal stress which leads to the systematic orientations of the olivine crystals in the upper mantle. In addition, given the horizontal movements, it is possible to form dipping interfaces during this process, and also other complicated anisotropic structures which have different angles, thin layers and some other local variations. Compared with the previous group of hypotheses, which may lead to a large scale, homogenous and horizontal structure, this hypothesis is able to generate different types of anisotropic structures with complex local variations, dipping interfaces or embedded thin layers. For all the sites, we can observe at least two anisotropic boundaries in the upper mantle and some of them may have dipping interfaces or symmetry axes, thus it is reasonable to relate our observations to the craton formation mechanism that involves horizontal movements of the preexisting lithosphere.

3.6.7 Implication for the Formation of the craton

Based on our observations, we consider two different mechanisms for craton formation and evaluate their feasibilities correspondingly. Given our observations in both cratons, each site has a distinct anisotropic structure, we thus envision cratons to be composed of numerous smaller components with different structure at depth. We refer to them as building blocks hereafter.

In mechanism I (Figure 24), there are different building blocks of the craton and during the formation of the craton, those building blocks come together and obtain a similar

anisotropic structure with each other through a uniform formation process. However, during the process of the craton evolution, these building blocks go through different kinds of modification which somehow erases some anisotropic boundaries and adds new ones. Though plausible at the beginning, this mechanism cannot explain the absence of consistent features at any given depth. Even though there might be later stages of modifications, it is not reasonable to have all the previous anisotropic fabrics modified specially at distances on the order of a few hundreds of kilometers. Moreover, as cratons are defined as coherent domains which remain stable except maybe at their rims, large-scale modifications that penetrate so deep into the lithosphere in their interiors are not realistic. In all, this mechanism cannot explain our observations in both cratons.

In mechanism II (Figure 25), the initial conditions are the same as those in Mechanism I. However, before the building blocks came together, while apart they went through different kinds of tectonic evolution, through which they obtained different anisotropic fabrics. After this, those building blocks came together to form the craton. After the formation of the craton, the anisotropic fabrics were preserved in the lithosphere without further modification. This process kept operating till the last building block came together and finalized the craton at present. Thus, the anisotropic structures that are detected now actually reflect the deformation processes pre-dating the formation of the craton. This mechanism is actually not consistent with the insight from large-scale tomography models generated using surface waves. Tomography models show nearly uniform structure beneath each craton we examined, largely due to the limited resolution. However, this mechanism is consistent with our more-local observations. We point out that the cratons

are actually mosaics composed of different pieces with their own distinct tectonic or pre-tectonic histories. Thus, differences in the anisotropic structures actually reflect the past deformation processes before the craton formation.

3.7 Summary

In this study, we explore and compare the detailed anisotropic structures beneath four sites in Yilgarn craton of West Australia and four sites in Superior craton of North America. We combine two different types of techniques including shear-wave birefringence studies and receiver-function analysis, which provide us with sufficient resolution both laterally and in the vertical direction. We develop systematic procedures and standards in our data analysis process and we are able to detect weak anisotropy and at least two anisotropic boundaries between 50 km ~ 160 km at each individual site. By applying the same systematic approach to the dataset at each individual site, we find that the properties and depths of the anisotropic boundaries beneath each site are distinct. This suggests that the cratons are not uniform domains and no common anisotropic structures are observed between the two different cratons. Compared to the tomography models, our results reveal more details about the local variations of the anisotropic structures beneath both cratons. We compare the shear-wave-splitting patterns with the geological and geophysical boundaries. We interpret the anisotropic structure beneath the Yilgarn craton as a stack of thin anisotropic layers whereas the Superior craton has a major contribution from the asthenosphere and a minor contribution from the lithosphere. Based on different craton-formation mechanisms and corresponding anisotropic structures, we are able to set constraints on the craton formation process. We thus consider cratons have to be formed through series of horizontal

movements of the preexisting lithosphere and the distinct anisotropic structures detected at sites are actually obtained and preserved before the formation of the current craton.

3.8 Acknowledgements

This work was supported by the NSF Earthscope grant EAR-1147831, the graduate fellowship and the Off-Campus Dissertation Development Awards provided by the School of Graduate Studies of Rutgers, the State University of New Jersey for the first author. All the dataset in this study can be accessed at the Data Management Center (DMC) of the Incorporated Research Institutions for Seismology (IRIS) and Portable Observatories for Lithospheric Analysis and Research Investigating Seismicity (POLARIS). Figures are drafted using GMT (Wessel and Smith, 1991) and Matlab (R2016a).

3.9 Reference:

- Abbott, D.H., Mooney, W.D. & VanTongeren, J.A., 2013. The character of the Moho and lower crust within Archean cratons and the tectonic implications, *Tectonophysics*, 609, 690-705.
- Abt, D., Fischer, K., French, S., Ford, H., Yuan, H. & Romanowicz, B., 2010. North American lithospheric discontinuity structure imaged by Ps and Sp receiver functions, *J. Geophys. Res.*, 115, B09301.
- Ammon, C.J., 1991. The isolation of receiver effects from teleseismic P waveforms, *Bulletin of the Seismological Society of America*, 81, 2504-2510.
- Anderson, D.L., 1995. Lithosphere, asthenosphere, and perisphere, 33, 125-149.
- Artemieva, I.M., 2006. Global 1×1 thermal model TC1 for the continental lithosphere: implications for lithosphere secular evolution, *Tectonophysics*, 416, 245-277.
- Backus, G.E., 1965. Possible forms of seismic anisotropy of the uppermost mantle under oceans, *Journal of Geophysical Research*, 70, 3429-3439.
- Barrell, J.J.T.J.o.G., 1914. The strength of the Earth's crust, 22, 655-683.
- Boily, M. & Dion, C., 2002. Geochemistry of boninite-type volcanic rocks in the Frotet-Evans greenstone belt, Opatica subprovince, Quebec: implications for the evolution of Archean greenstone belts, *Precambrian Research*, 115, 349-371.
- Bostock, M.G., 1998. Mantle stratigraphy and evolution of the Slave province, 103, 21183-21200.
- Brown, M., 2007. Metamorphic conditions in orogenic belts: a record of secular change, *International Geology Review*, 49, 193-234.
- Burdick, L.J. & Langston, C.A., 1977. Modeling crustal structure through the use of converted phases in teleseismic body-wave forms, *Bulletin of the Seismological Society of America*, 67, 677-691.
- Calvert, A., Sawyer, E., Davis, W. & Ludden, J., 1995. Archean subduction inferred from seismic images of a mantle suture in the Superior Province, *Nature*, 375, 670.
- Calvert, A.J. & Ludden, J.N., 1999. Archean continental assembly in the southeastern Superior Province of Canada, *Tectonics*, 18, 412-429.
- Card, K. & Ciesielski, A., 1986. DNAG# 1. Subdivisions of the Superior Province of the Canadian shield, *Geoscience Canada*, 13.
- Card, K.D., 1990. A Review of the Superior Province of the Canadian Shield, a Product of Archean Accretion, *Precambrian Research*, 48, 99-156.
- Cassidy, J.F., 1992. Numerical experiments in broadband receiver function analysis, *Bulletin of the Seismological Society of America*, 82, 1453-1474.
- Cawood, P.A., Hawkesworth, C.J. & Dhuime, B., 2013. The continental record and the generation of continental crust, *GSA Bulletin*, 125, 14-32.
- Champion, D.C. & Smithies, R.H., 2007. Chapter 4.3 Geochemistry of Paleoproterozoic Granites of the East Pilbara Terrane, Pilbara Craton, Western Australia: Implications for Early Archean Crustal Growth. in *Developments in Precambrian Geology*, pp. 369-409, eds. van Kranendonk, M. J., Smithies, R. H. & Bennett, V. C. Elsevier.

- Chen, X., Li, Y. & Levin, V., 2018. Shear Wave Splitting Beneath Eastern North American Continent: Evidence for a Multilayered and Laterally Variable Anisotropic Structure, 19, 2857-2871.
- Chevrot, S., 2000. Multichannel analysis of shear wave splitting, *Journal of Geophysical Research: Solid Earth*, 105, 21579-21590.
- Christensen, N.I., 1984. The magnitude, symmetry and origin of upper mantle anisotropy based on fabric analyses of ultramafic tectonites, *Geophysical Journal International*, 76, 89-111.
- Clowes, R.M., 2010. Initiation, development, and benefits of Lithoprobe — shaping the direction of Earth science research in Canada and beyond This article is one of a series of papers published in this Special Issue on the theme Lithoprobe — parameters, processes, and the evolution of a continent. *Lithoprobe Contribution 1480, Canadian Journal of Earth Sciences*, 47, 291-314.
- Cooper, C., Lenardic, A., Levander, A. & Moresi, L.J.G.M.-A.G.U., 2006. Creation and preservation of cratonic lithosphere: seismic constraints and geodynamic models, 164, 75.
- Cooper, C.M., Lenardic, A. & Moresi, L., 2004. The thermal structure of stable continental lithosphere within a dynamic mantle, *Earth and Planetary Science Letters*, 222, 807-817.
- Darbyshire, F., Bastow, I., Forte, A., Hobbs, T., Calvel, A., Gonzalez-Monteza, A. & Schow, B., 2015. Variability and origin of seismic anisotropy across eastern Canada: Evidence from shear wave splitting measurements, *Journal of Geophysical Research: Solid Earth*, 120, 8404-8421.
- Darbyshire, F., Eaton, D.W., Frederiksen, A.W. & Ertolahti, L., 2007. New insights into the lithosphere beneath the Superior Province from Rayleigh wave dispersion and receiver function analysis, *Geophysical Journal International*, 169, 1043-1068.
- Darbyshire, F.A. & Lebedev, S., 2009. Rayleigh wave phase-velocity heterogeneity and multilayered azimuthal anisotropy of the Superior Craton, Ontario, *Geophysical Journal International*, 176, 215-234.
- Davies, G.F., 1992. On the emergence of plate tectonics, *Geology*, 20, 963-966.
- Debayle, E., Dubuffet, F. & Durand, S., 2016. An automatically updated S-wave model of the upper mantle and the depth extent of azimuthal anisotropy, *Geophysical Research Letters*, 43, 674-682.
- Debayle, E., Kennett, B. & Priestley, K., 2005. Global azimuthal seismic anisotropy and the unique plate-motion deformation of Australia, *Nature*, 433, 509-512.
- Deng, J., Long, M.D., Creasy, N., Wagner, L., Beck, S., Zandt, G., Tavera, H. & Minaya, E., 2017. Lowermost mantle anisotropy near the eastern edge of the Pacific LLSVP: constraints from SKS–SKKS splitting intensity measurements, *Geophysical Journal International*, 210, 774-786.
- Eaton, D.W., Darbyshire, F., Evans, R.L., Grütter, H., Jones, A.G. & Yuan, X., 2009. The elusive lithosphere–asthenosphere boundary (LAB) beneath cratons, *Lithos*, 109, 1-22.
- Fischer, K.M., Ford, H.A., Abt, D.L. & Rychert, C.A., 2010. The Lithosphere–Asthenosphere Boundary, 38, 551-575.

- Fishwick, S. & Reading, A.M., 2008. Anomalous lithosphere beneath the Proterozoic of western and central Australia: A record of continental collision and intraplate deformation?, *Precambrian Research*, 166, 111-121.
- Ford, H.A., Fischer, K.M., Abt, D.L., Rychert, C.A. & Elkins-Tanton, L.T., 2010. The lithosphere–asthenosphere boundary and cratonic lithospheric layering beneath Australia from Sp wave imaging, *Earth and Planetary Science Letters*, 300, 299-310.
- Ford, H.A., Long, M.D. & Wirth, E.A., 2016. Midlithospheric discontinuities and complex anisotropic layering in the mantle lithosphere beneath the Wyoming and Superior Provinces, 121, 6675-6697.
- Frederiksen, A., Miong, S.K., Darbyshire, F., Eaton, D., Rondenay, S. & Sol, S., 2007. Lithospheric variations across the Superior Province, Ontario, Canada: Evidence from tomography and shear wave splitting, *Journal of Geophysical Research: Solid Earth*, 112.
- Fuchs & Müller, G., 1971. Computation of synthetic seismograms with the reflectivity method and comparison with observations, *Geophysical Journal International*, 23, 417-433.
- Gerya, T., 2014. Precambrian geodynamics: Concepts and models, *Gondwana Research*, 25, 442-463.
- Goleby, B.R., Blewett, R.S., Fomin, T., Fishwick, S., Reading, A.M., Henson, P.A., Kennett, B.L.N., Champion, D.C., Jones, L., Drummond, B.J. & Nicoll, M., 2006. An integrated multi-scale 3D seismic model of the Archaean Yilgarn Craton, Australia, *Tectonophysics*, 420, 75-90.
- Goutier, J., Dion, C., Ouellet, M., Mercier-Langevin, P. & Davis, D.J.M.d.R.n., Québec, RG, 2001. Géologie de la colline Masson, de la passe Awapakamich, de la baie Carbillet, et de la passe Pikwahipanan (SNRC 33F/09, 33F/10, 33F/15, et 33F/16), 10.
- Gray, R. & Pysklywec, R.N., 2010. Geodynamic models of Archean continental collision and the formation of mantle lithosphere keels, 37.
- Green, A.G., Milkereit, B., Mayrand, L.J., Ludden, J.N., Hubert, C., Jackson, S.L., Sutcliffe, R.H., West, G.F., Verpaest, P. & Simard, A., 1990. Deep structure of an Archaean greenstone terrane, *Nature*, 344, 327-330.
- Griffin, W.L., O'Reilly, S.Y., Doyle, B.J., Pearson, N.J., Coopersmith, H., Kivi, K., Malkovets, V. & Pokhilenko, N., 2004. Lithosphere mapping beneath the North American plate, *Lithos*, 77, 873-922.
- Gung, Y., Panning, M. & Romanowicz, B., 2003. Global anisotropy and the thickness of continents, *Nature*, 422, 707-711.
- Gurrola, H., Baker, G.E. & Minster, J.B., 1995. Simultaneous time-domain deconvolution with application to the computation of receiver functions, *Geophysical Journal International*, 120, 537-543.
- Hales, A.L., 1969. A seismic discontinuity in the lithosphere, *Earth and Planetary Science Letters*, 7, 44-46.
- Hales, A.L., Muirhead, K.J., Rynn, J.M. & Gettrust, J.F., 1975. Upper-mantle travel times in Australia — A preliminary report, *Physics of the Earth and Planetary Interiors*, 11, 109-118.

- Hawkesworth, C., Cawood, P. & Dhuime, B., 2013. Continental growth and the crustal record, *Tectonophysics*, 609, 651-660.
- Hawkesworth, C.J., Cawood, P.A., Dhuime, B. & Kemp, T.I.S., 2017. Earth's Continental Lithosphere Through Time, 45, 169-198.
- Heintz, M. & Kennett, B.L.N., 2005. Continental scale shear wave splitting analysis: Investigation of seismic anisotropy underneath the Australian continent, *Earth and Planetary Science Letters*, 236, 106-119.
- Herzberg, C., Condie, K. & Korenaga, J., 2010. Thermal history of the Earth and its petrological expression, *Earth and Planetary Science Letters*, 292, 79-88.
- Hoffman, P.F., 1988. United plates of America, the birth of a craton: Early Proterozoic assembly and growth of Laurentia, *Annual Review of Earth and Planetary Sciences*, 16, 543-603.
- Jaupart, C., Mareschal, J.-C., Guillou-Frottier, L. & Davaille, A., 1998. Heat flow and thickness of the lithosphere in the Canadian Shield, *Journal of Geophysical Research: Solid Earth*, 103, 15269-15286.
- Johnson, S.J.P., Western Australia, 78p, 2013. The birth of supercontinents and the Proterozoic assembly of Western Australia: Geological Survey of Western Australia.
- Johnson, T.E., Brown, M., Kaus, B.J. & VanTongeren, J.A., 2014. Delamination and recycling of Archaean crust caused by gravitational instabilities, *Nature Geoscience*, 7, 47-52.
- Jordan, T.H., 1978. Composition and development of the continental tectosphere, *Nature*, 274, 544-548.
- Kaban, M.K., Schwintzer, P., Artemieva, I.M. & Mooney, W.D., 2003. Density of the continental roots: compositional and thermal contributions, *Earth and Planetary Science Letters*, 209, 53-69.
- Kennett, B.L.N., 2003. Seismic structure in the mantle beneath Australia, 372, 7.
- Kennett, B.L.N., Fishwick, S. & Heintz, M., 2004. Lithospheric Structure in the Australian Region - A Synthesis of Surface Wave and Body Wave Studies, *Exploration Geophysics*, 35, 242-250.
- Korenaga, J., 2008. Urey ratio and the structure and evolution of Earth's mantle, *Reviews of Geophysics*, 46.
- Kumazawa, M. & Anderson, O.L., 1969. Elastic moduli, pressure derivatives, and temperature derivatives of single-crystal olivine and single-crystal forsterite, *Journal of Geophysical Research*, 74, 5961-5972.
- Lee, C., 2006. Geochemical/petrologic constraints on the origin of cratonic mantle, 164, 89.
- Lee, C.-T.A., Luffi, P. & Chin, E.J., 2011. Building and Destroying Continental Mantle, 39, 59-90.
- Levin, V. & Park, J., 1997. P-SH conversions in a flat-layered medium with anisotropy of arbitrary orientation, *Geophysical Journal International*, 131, 253-266.
- Levin, V. & Park, J., 1998. P-SH conversions in layered media with hexagonally symmetric anisotropy: a cookbook, *Pure and Applied Geophysics*, 151, 669-697.
- Levin, V., Park, J., Brandon, M.T. & Menke, W., 2000. Thinning of the upper mantle during late Paleozoic Appalachian orogenesis, *Geology*, 28, 239-242.

- Levin, V., Servali, A., VanTongeren, J., Menke, W. & Darbyshire, F., 2017. Crust-mantle boundary in eastern North America, from the (oldest) craton to the (youngest) rift, Geological Society of America Special Papers, 526, SPE526-506.
- Levin, V., VanTongeren, J.A. & Servali, A., 2016. How sharp is the sharp Archean Moho? Example from eastern Superior Province, Geophysical Research Letters, 43, 1928-1933.
- Li, Y., Levin, V., Elkington, S. & Hlavaty, J., 2019. Localized Anisotropic Domains Beneath Eastern North America, 20, 5499-5521.
- Li, Z.-X., Bogdanova, S., Collins, A., Davidson, A., De Waele, B., Ernst, R., Fitzsimons, I., Fuck, R., Gladkochub, D. & Jacobs, J., 2008. Assembly, configuration, and break-up history of Rodinia: a synthesis, Precambrian research, 160, 179-210.
- Long & Becker, T.W., 2010. Mantle dynamics and seismic anisotropy, Earth and Planetary Science Letters, 297, 341-354.
- Long & Silver, P.G., 2009. Shear wave splitting and mantle anisotropy: measurements, interpretations, and new directions, Surveys in Geophysics, 30, 407-461.
- Ludden, J. & Hynes, A., 2000. The Lithoprobe Abitibi-Grenville transect: two billion years of crust formation and recycling in the Precambrian Shield of Canada, Canadian Journal of Earth Sciences, 37, 459-476.
- MATLAB. (2016). version 9.0.0 (R2016a). Natick, Massachusetts: The MathWorks Inc.
- Menke, W. & Levin, V., 2003. The cross-convolution method for interpreting SKS splitting observations, with application to one and two-layer anisotropic earth models, Geophysical Journal International, 154, 379-392.
- Mercier-Langevin, P., Daigneault, R., Goutier, J., Dion, C. & Archer, P., 2012. Geology of the Archean Intrusion-Hosted La-Grande-Sud Au-Cu Prospect, La Grande Subprovince, James Bay Region, Québec(1,2), Economic Geology, 107, 935-962.
- Muttoni, G., Gaetani, M., Kent, D.V., Sciunnach, D., Angiolini, L., Berra, F., Garzanti, E., Mattei, M. & Zanchi, A., 2009. Opening of the Neo-Tethys Ocean and the Pangea B to Pangea A transformation during the Permian, GeoArabia, 14, 17-48.
- Myers, J.S., 1990. Precambrian tectonic evolution of part of Gondwana, southwestern Australia, Geology, 18, 537-540.
- Myers, J.S., 1993. Precambrian History of the West Australian Craton and Adjacent Orogens, 21, 453-485.
- Nance, R.D., Murphy, J.B. & Santosh, M., 2014. The supercontinent cycle: A retrospective essay, Gondwana Research, 25, 4-29.
- Olugboji, T.M. & Park, J., 2016. Crustal anisotropy beneath Pacific Ocean-Islands from harmonic decomposition of receiver functions, 17, 810-832.
- Park & Levin, V., 2016a. Anisotropic shear zones revealed by backazimuthal harmonics of teleseismic receiver functions, Geophysical Journal International, 207, 1216-1243.
- Park, J. & Levin, V., 2000. Receiver Functions from Multiple-Taper Spectral Correlation Estimates, Bulletin of the Seismological Society of America, 90, 1507-1520.
- Park, J. & Levin, V., 2002. Seismic anisotropy: tracing plate dynamics in the mantle, Science, 296, 485-489.
- Park, J. & Levin, V., 2016b. Statistics and frequency-domain moveout for multiple-taper receiver functions, Geophysical Journal International, 207, 512-527.

- Pearson, D.G., Carlson, R.W., Shirey, S.B., Boyd, F.R. & Nixon, P.H., 1995. Stabilisation of Archaean lithospheric mantle: A ReOs isotope study of peridotite xenoliths from the Kaapvaal craton, *Earth and Planetary Science Letters*, 134, 341-357.
- Percival, J., 2007. Geology and metallogeny of the Superior Province, Canada, *Mineral deposits of Canada: a synthesis of major deposit-types, district metallogeny, the evolution of geological provinces, and exploration methods*, 903-928.
- Percival, J., Sanborn-Barrie, M., Skulski, T., Stott, G., Helmstaedt, H. & White, D., 2006. Tectonic evolution of the western Superior Province from NATMAP and Lithoprobe studies 1, 2, *Can. J. Earth Sci.*, 43.
- Peschler, A.P., Benn, K. & Roest, W.R., 2004. Insights on Archean continental geodynamics from gravity modelling of granite–greenstone terranes, *Journal of Geodynamics*, 38, 185-207.
- Reading, A.M. & Kennett, B.L.N., 2003. Lithospheric structure of the Pilbara Craton, Capricorn Orogen and northern Yilgarn Craton, Western Australia, from teleseismic receiver functions, *Australian Journal of Earth Sciences*, 50, 439-445.
- Reading, A.M., Kennett, B.L.N. & Dentith, M.C., 2003. Seismic structure of the Yilgarn Craton, Western Australia, *Australian Journal of Earth Sciences*, 50, 427-438.
- Ribe, N.M., 1992. On the relation between seismic anisotropy and finite strain, *Journal of Geophysical Research: Solid Earth*, 97, 8737-8747.
- Robin, C.M.I. & Bailey, R.C., 2009. Simultaneous generation of Archean crust and subcratonic roots by vertical tectonics, *Geology*, 37, 523-526.
- Romanowicz, B., 2009. The thickness of tectonic plates, *Science*, 324, 474-476.
- Rudnick, R.L., McDonough, W.F. & O'Connell, R.J., 1998. Thermal structure, thickness and composition of continental lithosphere, *Chemical Geology*, 145, 395-411.
- Savage, M., 1999. Seismic anisotropy and mantle deformation: what have we learned from shear wave splitting?, *Reviews of Geophysics*, 37, 65-106.
- Sawyer, E.W. & Benn, K., 1993. Structure of the high-grade Opatika Belt and adjacent low-grade Abitibi Subprovince, Canada: an Archean mountain front, *Journal of Structural Geology*, 15, 1443-1458.
- Silver & Chan, W.W., 1991. Shear-Wave Splitting and Subcontinental Mantle Deformation, *Journal of Geophysical Research-Solid Earth*, 96, 16429-16454.
- Silver, P., 1996. Seismic anisotropy beneath the continents: probing the depths of geology, *Annual Review of Earth and Planetary Sciences*, 24, 385-432.
- Simons, F.J., van der Hilst, R.D., Montagner, J.-P. & Zielhuis, A., 2002. Multimode Rayleigh wave inversion for heterogeneity and azimuthal anisotropy of the Australian upper mantle, *Geophysical Journal International*, 151, 738-754.
- Sizova, E., Gerya, T., Stüwe, K. & Brown, M., 2015. Generation of felsic crust in the Archean: A geodynamic modeling perspective, *Precambrian Research*, 271, 198-224.
- Steinberger, B. & Becker, T.W., 2018. A comparison of lithospheric thickness models, *Tectonophysics*, 746, 325-338.
- Swager, C.P., 1997. Tectono-stratigraphy of late Archean greenstone terranes in the southern Eastern Goldfields, Western Australia, *Precambrian Research*, 83, 11-42.

- Thompson, D.A., Kendall, J.M., Helffrich, G.R., Bastow, I.D., Wookey, J. & Snyder, D.B., 2015. CAN-HK: An a Priori Crustal Model for the Canadian Shield, *Seismological Research Letters*, 86, 1374-1382.
- Van Kranendonk, M.J., Ivanic, T.J., Wingate, M.T.D., Kirkland, C.L. & Wyche, S., 2013. Long-lived, autochthonous development of the Archean Murchison Domain, and implications for Yilgarn Craton tectonics, *Precambrian Research*, 229, 49-92.
- Vaucher, A. & Nicolas, A., 1991. Mountain building: strike-parallel motion and mantle anisotropy, *Tectonophysics*, 185, 183-201.
- Vinnik, L.P., Farra, V. & Romanowicz, B., 1989. Azimuthal anisotropy in the Earth from observations of SKS at Geoscope and NARS broadband stations, *Bulletin of the Seismological Society of America*, 79, 1542-1558.
- Watkins, K.P. & Hickman, A.H., 1990. Geological evolution and mineralization of the Murchison Province, Western Australia, edn, Vol. 1, pp. Pages, Department of Mines, Western Australia.
- Wessel, P. & Smith, W.H.F., 1991. Free software helps map and display data, *Eos, Transactions American Geophysical Union*, 72, 441-446.
- Wüstefeld, A. & Bokelmann, G., 2007. Null detection in shear-wave splitting measurements, *Bulletin of the Seismological Society of America*, 97, 1204-1211.
- Wüstefeld, A., Bokelmann, G., Zaroli, C. & Barruol, G., 2008. SplitLab: A shear-wave splitting environment in Matlab, *Computers & Geosciences*, 34, 515-528.
- Xie, Z., Levin, V. & Wu, Q., 2019. Crustal anisotropy beneath northeastern Tibetan Plateau from the harmonic decomposition of receiver functions, *Geophysical Journal International*, 220, 1585-1603.
- Yoshizawa, K., 2014. Radially anisotropic 3-D shear wave structure of the Australian lithosphere and asthenosphere from multi-mode surface waves, *Physics of the Earth and Planetary Interiors*, 235, 33-48.
- Yoshizawa, K. & Kennett, B.L.N., 2015. The lithosphere-asthenosphere transition and radial anisotropy beneath the Australian continent, 42, 3839-3846.
- Yuan, H., 2015. Secular change in Archaean crust formation recorded in Western Australia, *Nature Geoscience*, 8, 808-813.
- Yuan, H., French, S., Cupillard, P. & Romanowicz, B., 2014. Lithospheric expression of geological units in central and eastern North America from full waveform tomography, *Earth and Planetary Science Letters*, 402, 176-186.
- Yuan, H. & Romanowicz, B., 2010. Lithospheric layering in the North American craton, *Nature*, 466, 1063-1068.
- Yuan, H., Romanowicz, B., Fischer, K.M. & Abt, D., 2011. 3-D shear wave radially and azimuthally anisotropic velocity model of the North American upper mantle, *Geophysical Journal International*, 184, 1237-1260.
- Zhang, S. & Karato, S.-i., 1995. Lattice preferred orientation of olivine aggregates deformed in simple shear, *Nature*, 375, 774-777.

3.10 Figure Captions

Figure 1:

Locator maps of the two study areas: a) Yilgarn craton in western Australia, b) Superior craton in eastern North America. Their corresponding locations are marked in the maps in the right corners and the right triangles stand for the sites in each craton. The two letters stand for short names of terranes: a) MC=Murchison Terrane, SW= Southwest Yilgarn Composite Terrane, KL=Kalgoorlie Terrane; b) LG=La Grande Subprovince, OP= Opatika Subprovince, AT=Abitibi Terrane.

Figure 2:

Plots generated by combining the three methods adopted in this study using shear waves for site KMBL in the Yilgarn craton. a) a stereoplot of all shear-wave splitting plotted according to the back-azimuth variations (positive clockwise from N (0°) to S (180°)) from 0° to 360° with a spacing of 15° and incident angles (increase from the center (0°) of the plot to the edge of the plot (18°)) from 0° to 18° with a spacing of 3° . Red bars stand for the non-NUL measurements and black circles stand for the NUL measurements; b) Diagrams of all SI measurements. Red dots stand for the estimated splitting-intensity values with error bars calculated using a 95% confidence interval. Blue sinusoid is determined using all the SI measurements; green sinusoid is plotted based on the averaged fast polarization and delay time using only non-NUL measurements; c) Errors surfaces are plotted against the strength of anisotropy and the azimuths of the fast axes. Within each individual station, errors for each model have been normalized between 0 to 1 using minimum error and maximum error. Contours are plotted with a spacing of 5% of the full error range for the corresponding station. Yellow circles represent models (in only both global and local search) within 2% of the normalized error range from the best-fitting combination shown by a red asterisk. d) corresponding results for averaged observed

splitting parameters, splitting parameters estimated using a weighted SI, and splitting parameters estimated from the best-fitting model in single-layer inversion.

Figure 3:

Distribution of earthquakes adopted in the shear-wave splitting and splitting-intensity analysis. Different colors stand for the depth of the source (from 0 km to 700 km). a) Yilgarn craton, map is centered as the Yilgarn craton; b) Superior craton, map is centered as the Superior craton.

Figure 4.

Selected plots for site MEEK in the Yilgarn Craton as an example of workflow in this study. a) a back-azimuth gather of receiver functions in LTQ coordinates with move-out correction applied; For the visual clarity of the pattern back-azimuth values are arranged from the West (-90°) through North (0°) to East (90°), South (180°) and West (270°). b) back-azimuth gather of receiver functions in LTQ coordinates with move-out correction and migration to 50 km depth; c) epicentral gather of receiver functions for back-azimuth range 0° through 30° ; d) harmonic decomposition of RFs migrated to 50 km and corrected for moveout; e) constant component and vector length amplitudes for 2-lobed (purple) and 4-lobed (orange) components, grey shaded curves are vector length amplitudes of unmodeled components. In all plots grey vertical lines mark 0 delay. In migrated plots (b-e) a grey line marks the time of P-wave arrival (-5.5 s). Green lines – predicted arrival of Ps phase, magenta and cyan – crustal multiples.

Figure 5:

Splitting parameters estimated at four sites in the Yilgarn craton with corresponding statistical metric estimations. Simple-average shear-wave splitting (blue bars) based on

non-NULL measurements and averaged split intensity values (red bars) plotted at the corresponding site. Orientation of the bars stand for the fast polarizations and the lengths are proportional to the delay time (blue bars) or SI values (red bars). a) Cyan circles stand for one standard deviation of the delay time adopted as the error range; b) Green circles stand for one standard deviation of the fast polarization adopted as the error range; c) Yellow circles stand for the percentage NULL measurements at each site.

Figure 6:

Plots generated by combining the three methods adopted in this study using shear waves for all sites (from top to bottom panel: KMBL, MEEK, MORW, MUN) in the Yilgarn craton. For each panel, from left to right: a),d),g),j) a stereoplot of all shear-wave splitting plotted according to the back-azimuth variations (positive clockwise from N (0°) to S (180°)) from 0° to 360° with a spacing of 15° and incident angles (increase from the center (0°) of the plot to the edge of the plot (18°)) from 0° to 18° with a spacing of 3° . Red bars stand for the non-NULL measurements and black circles stand for the NULL measurements; b), e), h), k) Diagrams of all SI measurements. Red dots stand for the estimated splitting-intensity values with error bars calculated using a 95% confidence interval. Blue sinusoid is fit using all the SI measurements; green sinusoid is plotted based on the averaged fast polarization and delay time using only non-NULL measurements; c), f), i), l) Errors surfaces plotted against the strength of anisotropy and the azimuths of the fast axes. Within each individual station, errors for each model have been normalized between 0 to 1 using minimum error and maximum error. Contours are plotted with a spacing of 5% of the full error range for the corresponding station. Yellow circles represent

models (in only both global and local search) within 2% of the normalized error range from the best-fitting combination shown by a red asterisk.

Figure 7:

Splitting parameters estimated at four sites in Superior craton with corresponding statistical metric estimations. All the symbols have the same meanings as those in Figure 5.

Figure 8:

Plots generated by combining the three methods adopted in this study using shear waves for all sites (from top to bottom panel: MATQ, NMSQ, WEMQ, ‘merged’) in the Superior craton. Symbols are the same as in Figure 6.

Figure 9:

Distribution of earthquakes adopted in the receiver-function analysis. Different colors stand for the depth of the source (from 0 km to 700 km). a) Yilgarn craton, map is centered at the Yilgarn craton; b) Superior craton, map is centered at the Superior craton

Figure 10.

Receiver-function plots for site KMBL in the Yilgarn craton. a) Back-azimuth sweeps of receiver functions. The maximum frequency is 0.5 Hz. Multiple observations are combined to form 30° back-azimuth bins with 50% overlap. Receiver functions have been rotated to the LQT coordinates with moveout corrections and migration applied. Time 0 s corresponds to the arrival of the Ps converted wave from 50 km depth. Amplitude scale of T component is twice that of the Q component. b) Customized epicentral gathers of the receiver functions using events with back-azimuth ranges between -60° and 30°. All the other parameters are the same as the back-azimuth sweeps. Amplitude scale of T

component is twice that of the Q component. c) Harmonic stacks for site KMBL. The left panel ‘Anisotropy/Dip’ shows five coefficients calculated by fitting the spectrum of receiver functions to a sum of harmonic functions, and it stands for the expected effects caused by either anisotropy or dipping interfaces; the right panel ‘Unmodelled’ shows corresponding coefficients of those five terms that cannot be fit and thus represent noise and scattering. c) Vector-length plots for site KMBL. Constant component (red-blue waveform) and total amplitudes of energy with a two-lobed back-azimuth pattern (purple) and with a four-lobed pattern (orange). Unmodeled energy for corresponding components shown by grey shading.

Figure 11.

Receiver functions for site MEEK in the Yilgarn craton. Panels a) to d) are the same as Figure 10, except that the range of back azimuths included in the epicentral gather (b) is -60° through 60° .

Figure 12.

Receiver functions for site MORW in the Yilgarn craton. Panels a) to d) are the same as Figure 10, except that the range of back azimuths included in the epicentral gather (b) is 0° through 75° .

Figure 13.

Receiver functions for site MUN in the Yilgarn craton. Panels a) to d) are the same as Figure 10, except that the range of back azimuths included in the epicentral gather (b) is 0 through 30° .

Figure 14.

Receiver functions for site MATQ in the Superior craton. Panels a) to d) are the same as Figure 10, except that the range of back azimuths included in the epicentral gather (b) is -100° through 0° .

Figure 15.

Receiver functions for site NMSQ in the Superior craton. Panels a) to d) are the same as Figure 10, except that the range of back azimuths included in the epicentral gather (b) is -225° through -75° .

Figure 16.

Receiver functions for site WEMQ in the Superior craton. Panels a) to d) are the same as Figure 10, except that the range of back azimuths included in the epicentral gather (b) is -100 through 0° .

Figure 17.

Receiver functions for site QM78 in the Superior craton. Panels a) to d) are the same as Figure 10, except that the range of back azimuths included in the epicentral gather (b) is -90 through -15° .

Figure 18.

An illustration of the anisotropic boundaries identified at both cratons. Each interface (grey bar) is plotted at the corresponding depth. Orange bars stand for the observations of a 2-lobed pattern and purple bars stand for the observations of a 4-lobed pattern. Orientations of both orange and purple bars stand for the horizontal orientation of the symmetry axes calculated from this study. Blue and red triangles stand for positive and negative impedance contrasts at the corresponding boundaries respectively.

Figure 19:

Contours of the depth of the LAB estimated in Steinberger and Becker (2018) for a) the Yilgarn craton and b) the Superior craton. Red triangles stand for corresponding sites in the cratons and the numbers on the contour stand for the depths of the LAB.

Figure 20:

Comparison of the anisotropic boundaries beneath each individual site in the Yilgarn craton from our study with the shear-wave velocity model 3D2018_08Sv from Debayle et al. (2016) and LAT estimations from Yoshizawa (2014) and Yoshizawa and Kennett (2015). From left to right are: a) anisotropic models with interfaces identified from the receiver-function analysis and the corresponding harmonic-decomposition analysis (Conventions are the same as in Figure 18). Red lines stand for the upper and lower boundaries of the Lithosphere-Asthenosphere Transition (LAT) defined in Yoshizawa (2014) and b) depth profile of the isotropic shear-wave velocity (in terms of perturbation). c) peak to peak anisotropy in percentage at the corresponding depth d) azimuth of the fast axis. In b) – d), all cyan curves stand for the profiles for individual sites and the blue one stands for the average. Given the limited resolution of the tomographic models, all parameters are extracted using the closest available grid points in the model instead of the exact geographical locations of the sites.

Figure 21:

Comparison of the anisotropic structures beneath each individual site in the Superior craton with a shear-wave velocity model SAWum_NA2 model from Yuan and Romanowicz (2010). From left to right are: a) anisotropic models with interfaces identified in this study. Red lines stand for MLDs and LABs estimated in the model SAWum_NA2 correspondingly. b) depth profile of the isotropic shear-wave velocity c) depth profile of

the strength of azimuthal anisotropy extracted from the model by interpolation method provided in the dataset d) depth profiles of the azimuths of the fast axes extracted from the model by interpolation method provided in the dataset. In b) – d), all the cyan curves stand for the corresponding files for individual sites and the blue one stands for the average. All the curves are obtained using interpolation method provided inside the model SAWum_NA

Figure 22:

- a) Comparison between the averaged splitting patterns and the APM (orange arrows)
- b) Comparison between the averaged splitting patterns and the tectonic boundaries. The two letters stand for short names of terranes: MC=Murchison Terrane, SW= Southwest Yilgarn Composite Terrane, KL=Kalgoorlie Terrane. In both plots, blue bars are simple-average shear-wave splitting based on non-NUL measurements and red bars are averaged split intensity values plotted at the corresponding site.

Figure 23:

- a) Comparison between the averaged splitting patterns and the APM (orange arrows)
- b) Comparison between the averaged splitting patterns and the tectonic boundaries. The two letters stand for short names of terranes: LG=La Grande Subprovince, OP= Opatika Subprovince

, AT=Abitibi Terrane. Other symbols are the same as those in Figure 22.

Figure 24:

An illustration for craton formation process in Mechanism I.

Figure 25:

An illustration for craton formation process in Mechanism II.

3.11 Supplementary Figure Captions

Supplementary Figure 1:

Distribution of earthquakes adopted in the receiver function analysis at individual sites in Yilgarn craton. Different colors stand for the depth of the source. a) KMBL; b) MEEK; c) MORW; d) MUN

Supplementary Figure 2:

Distribution of earthquakes adopted in the receiver function analysis at individual sites in Superior craton. Different colors stand for the depth of the source. a) MATQ; b) NMSQ; c) QM78; d) WEMQ

3.12 Table Captions

Table 1:

Parameters obtained by carrying out inversions, averaging shear wave splitting measurements and fitting SI curves at stations in the Yilgarn Craton. From left to right are stations names, fast axes and percentage of anisotropy, delay times of the best fitting models evaluated according to Silver (1996); averaged fast polarizations and delay times of non-NUL shear wave splitting measurements; fast polarizations and delay times calculated by fitting a sinusoid to weighted splitting intensity measurements according to the quality of data (good: 100%; fair: 75%; poor: 50%).

Table 2:

Parameters obtained by carrying out inversions, averaging shear wave splitting measurements and fitting SI curves at stations in the Superior Craton. From left to right are stations names, fast axes and percentage of anisotropy, delay times of the best fitting models evaluated according to Silver (1996); averaged fast polarizations and delay times of non-NUL shear wave splitting measurements; fast polarizations and delay times

calculated by fitting a sinusoid to weighted splitting intensity measurements according to the quality of data (good: 100%; fair: 75%; poor: 50%).

3.13 Figures

Figure 1:

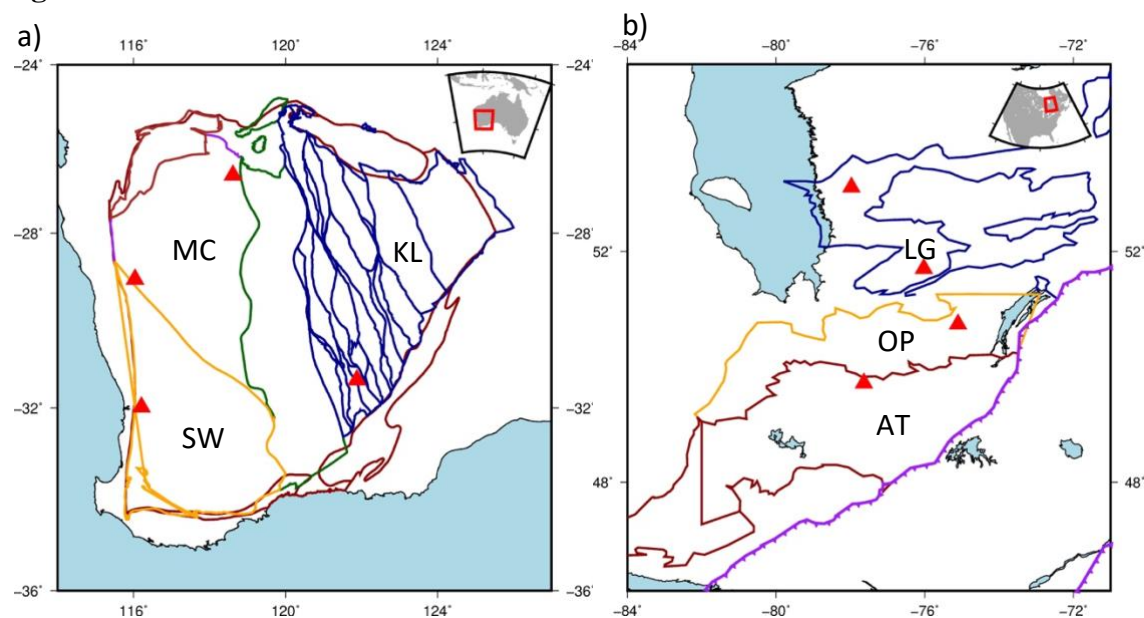
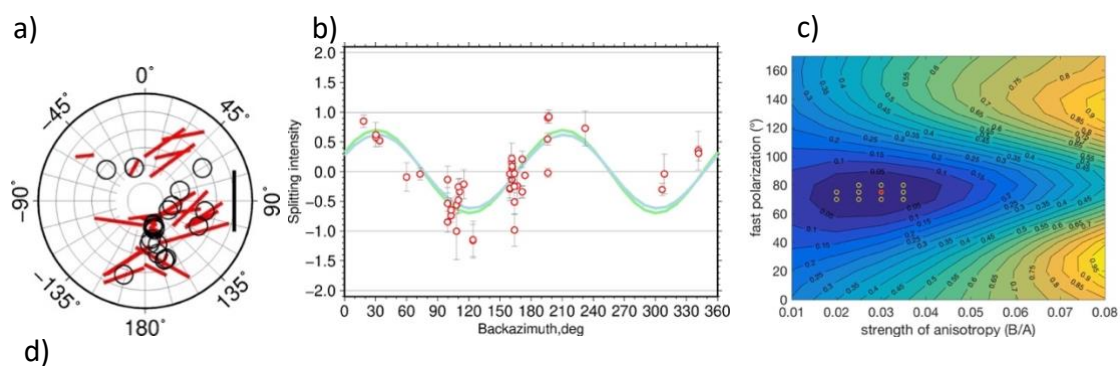


Figure 2:



AU	Averaged Obs		Weighted SI		Best fitting model		
KMBL	76.03°	76.03°	76.43°	0.59 s	75°	3%	0.75 s

Figure 3:

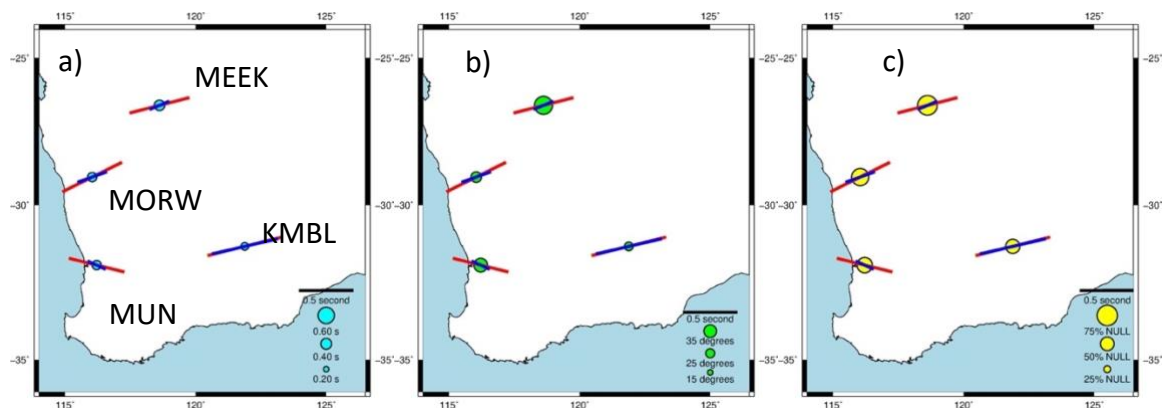
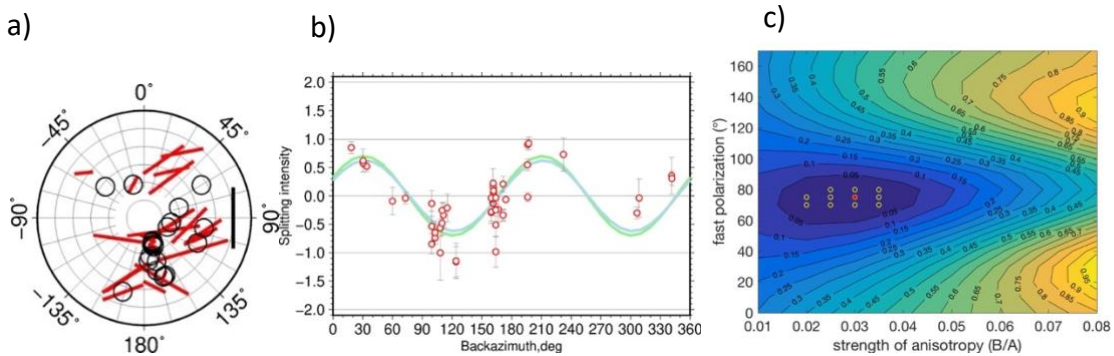
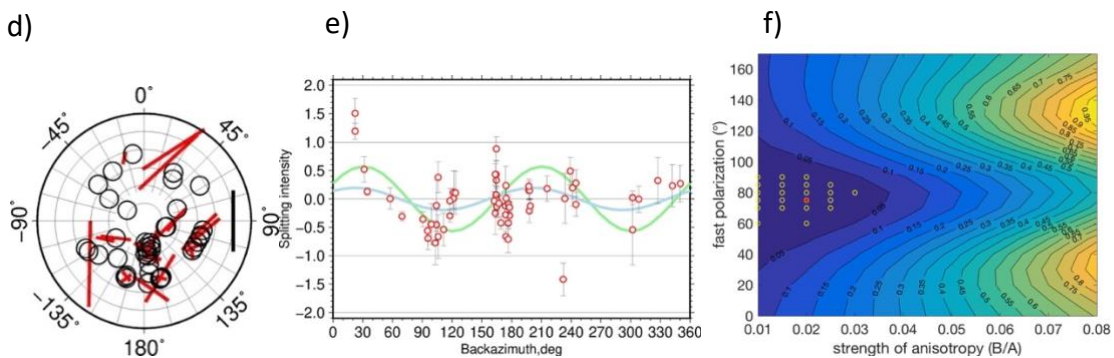


Figure 6:

Site KMBL



Site MEEK



Site MORW

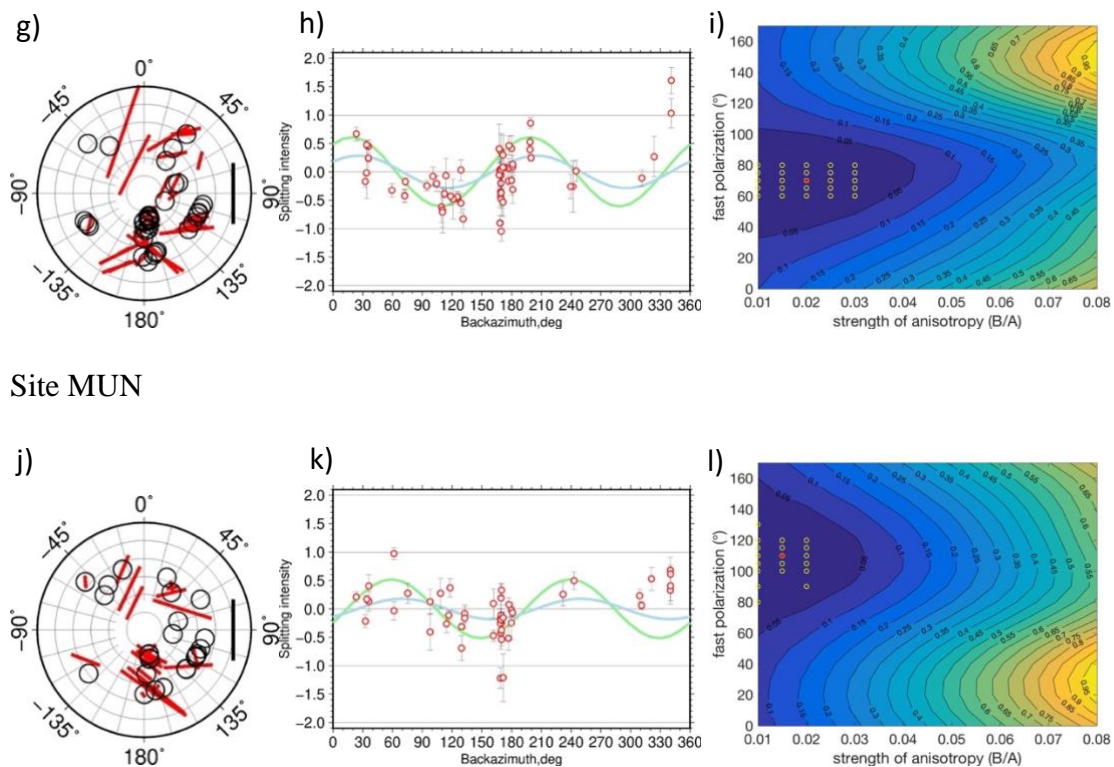


Figure 7:

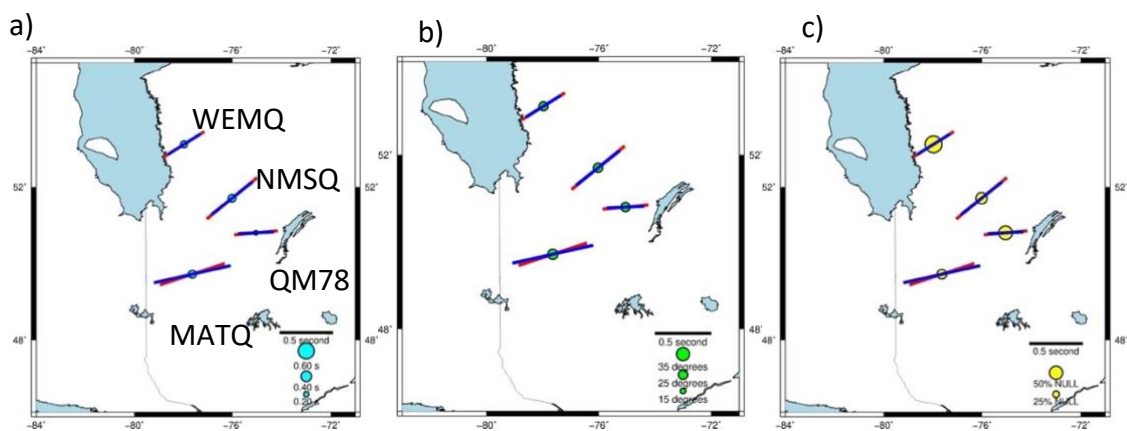
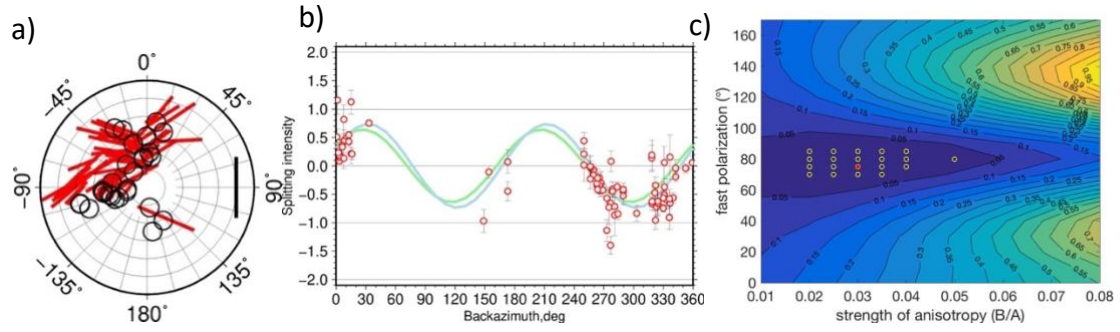
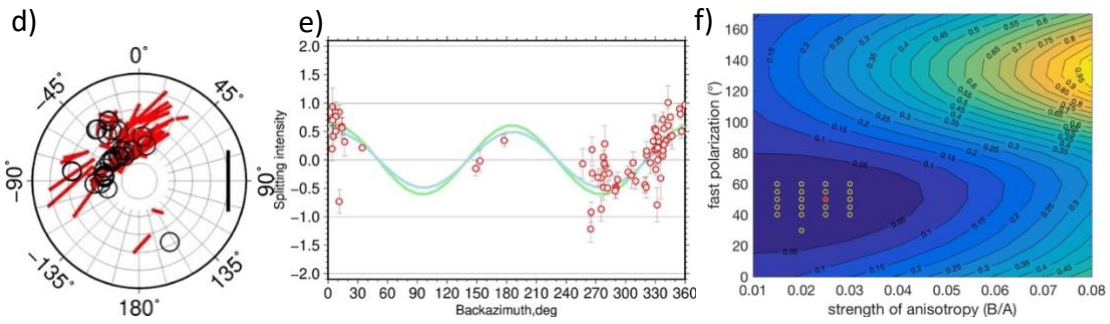


Figure 8:

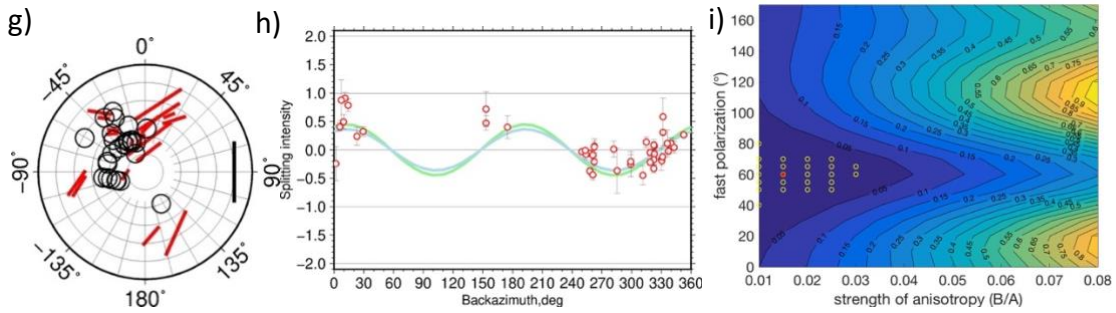
MATQ



NMSQ



WEMQ



'merged'

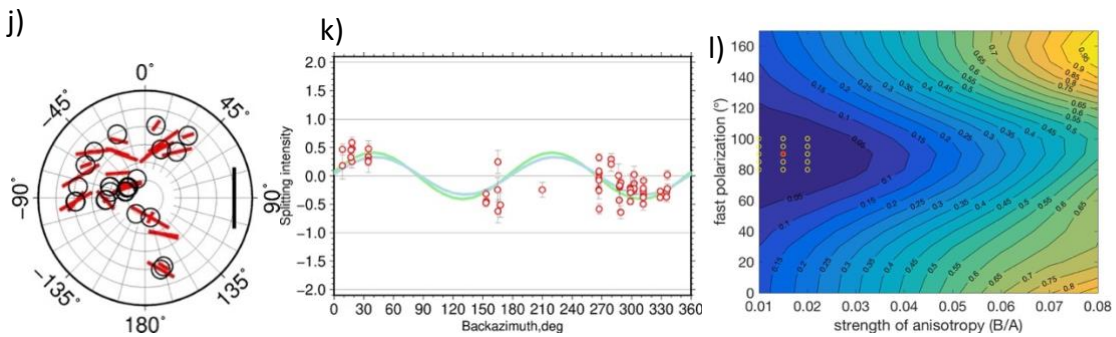


Figure 9:

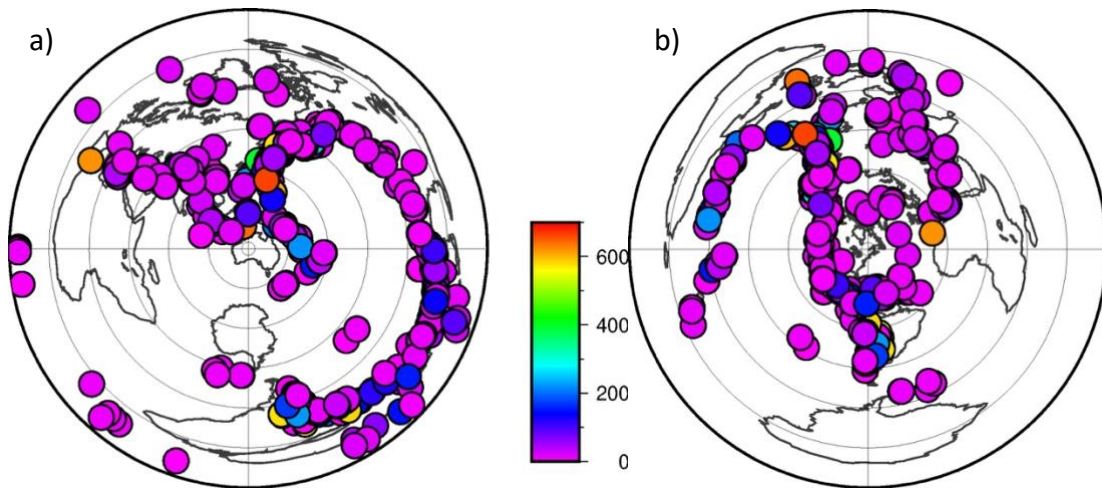


Figure 10:

Site KMBL

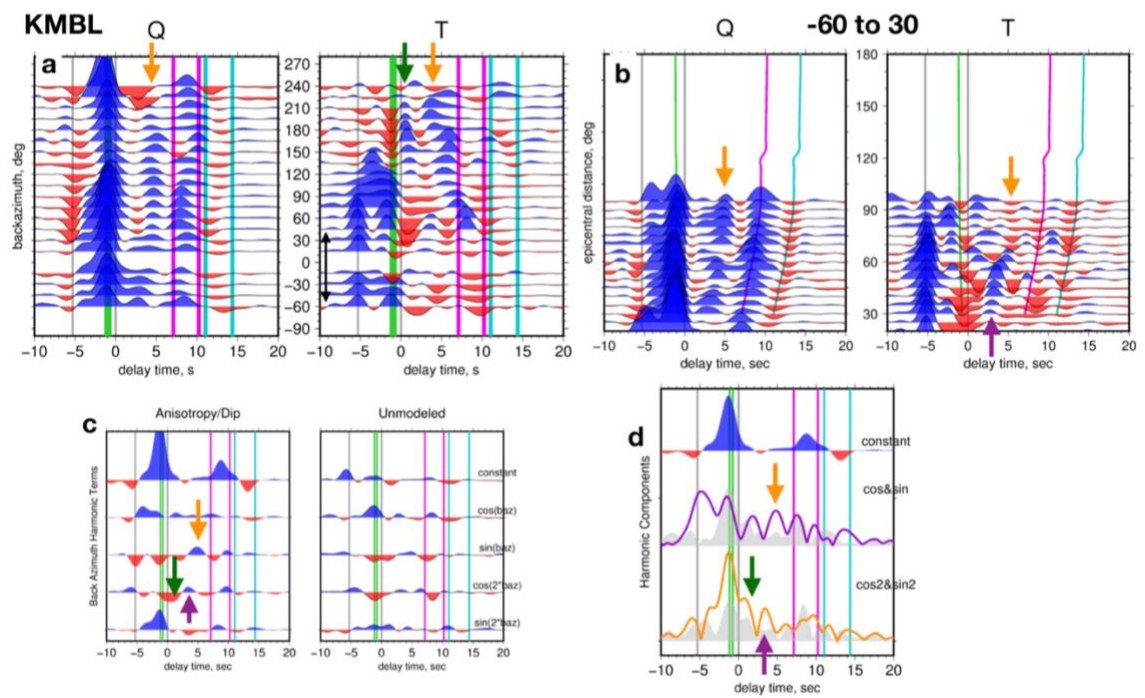


Figure 11:

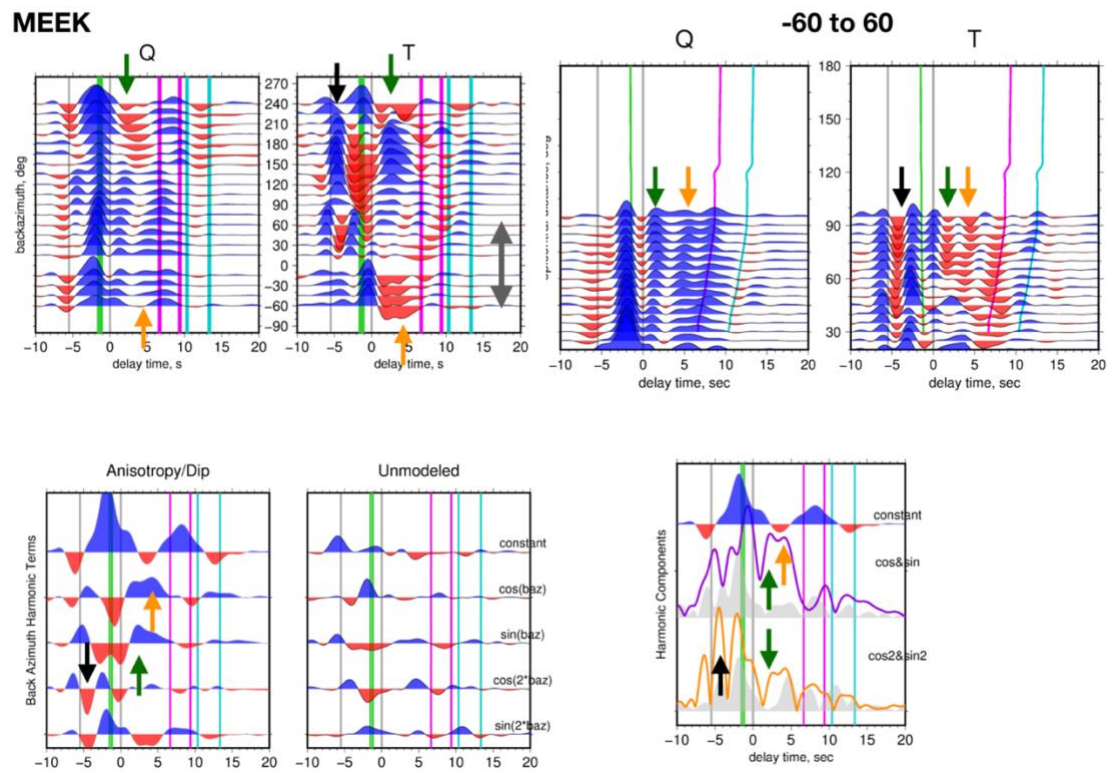
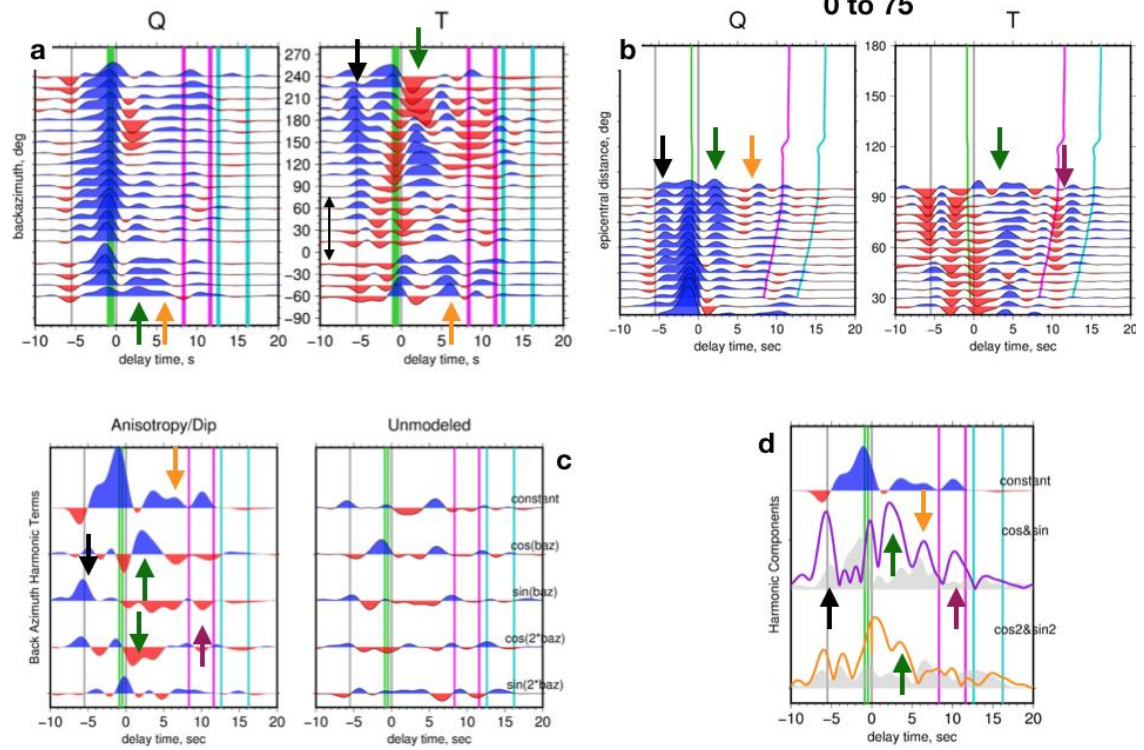
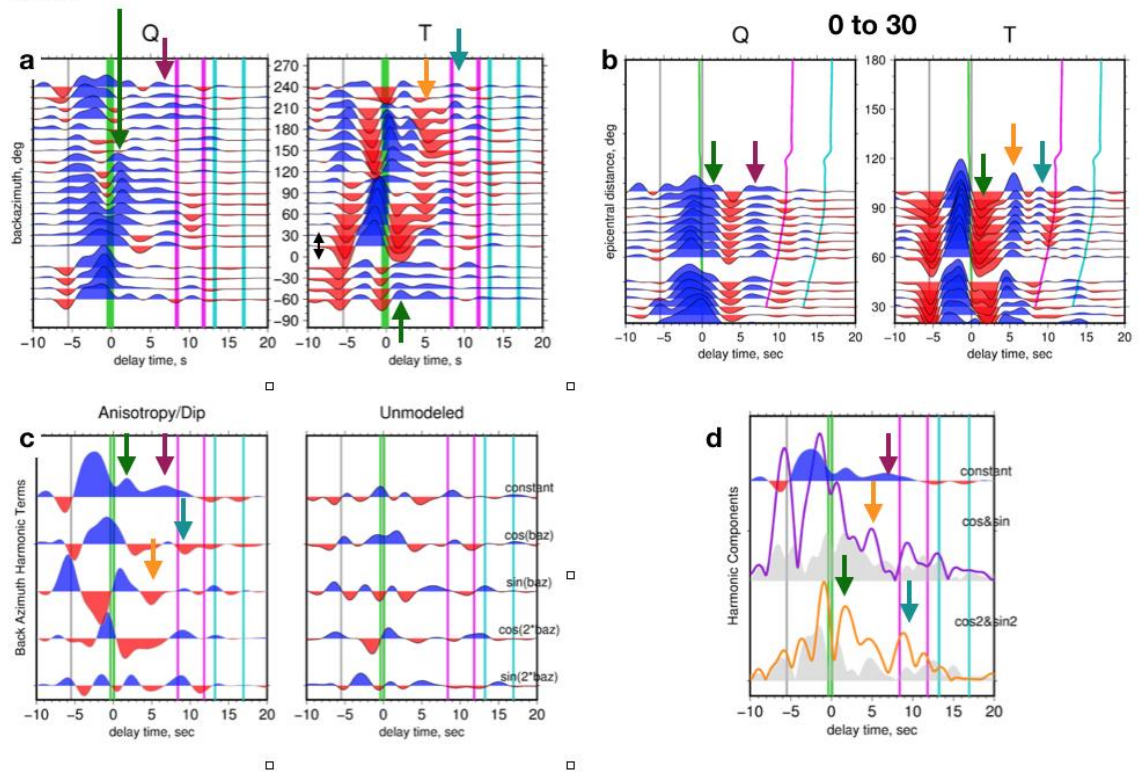


Figure 12:

MORW**Figure 13:**

MUN**Figure 14:**

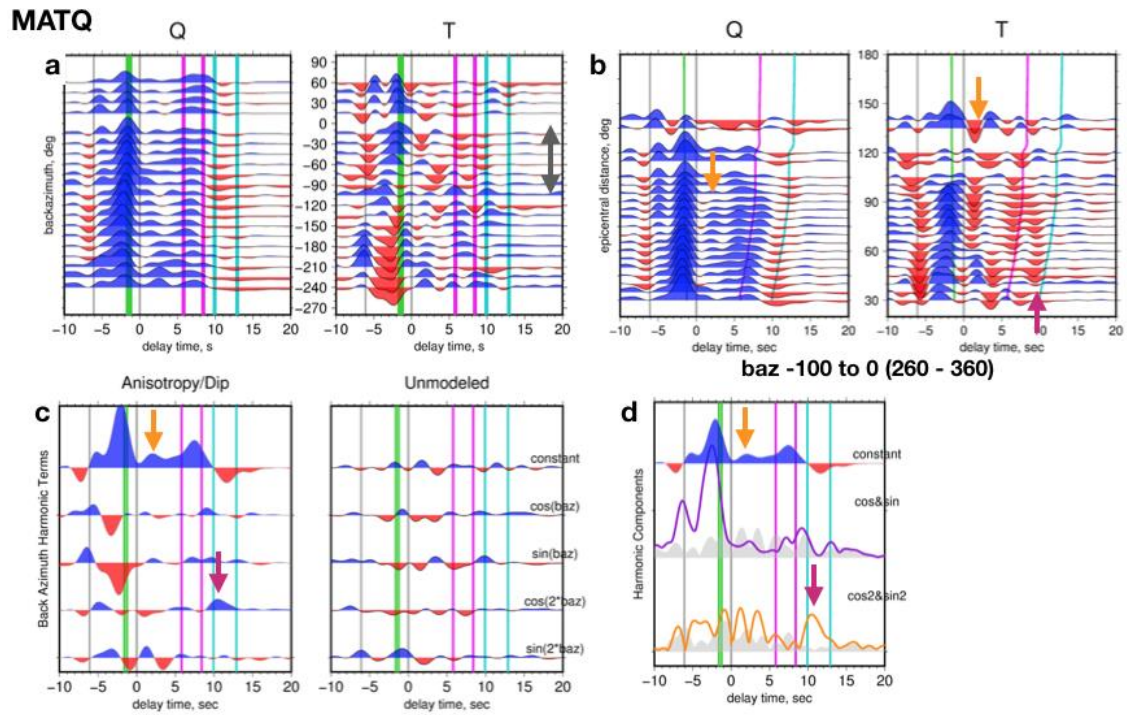


Figure 15:

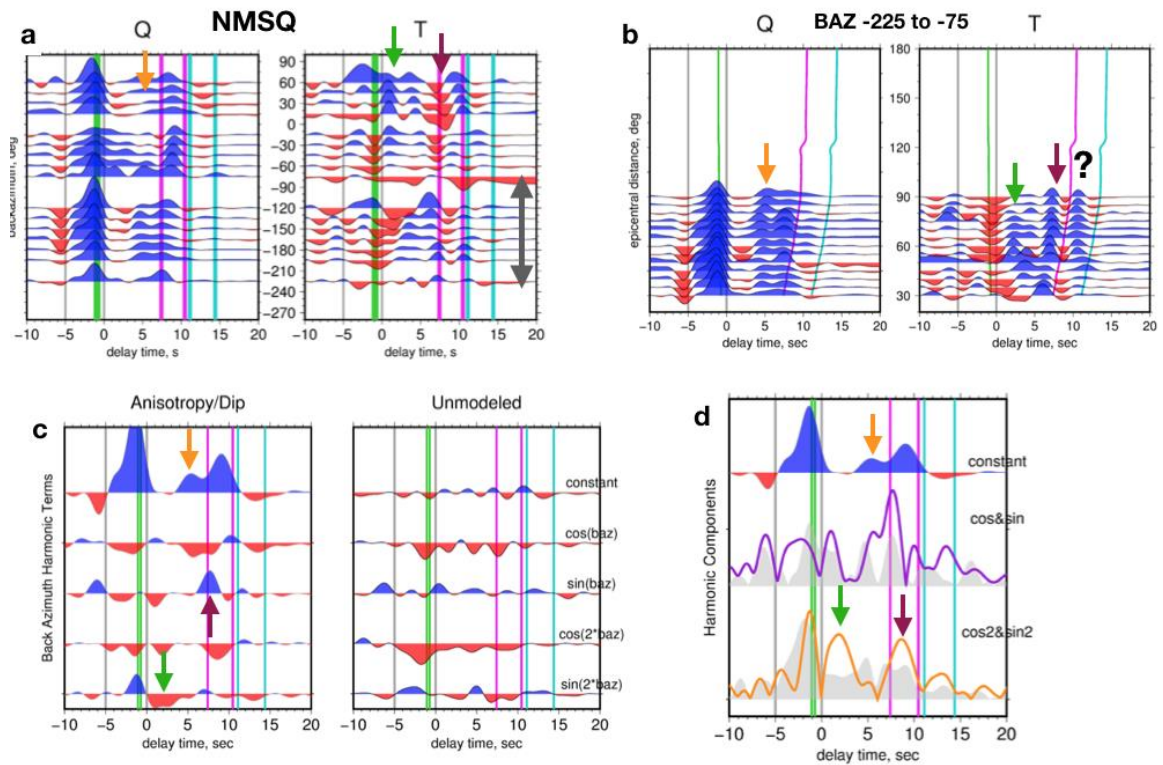


Figure 16:

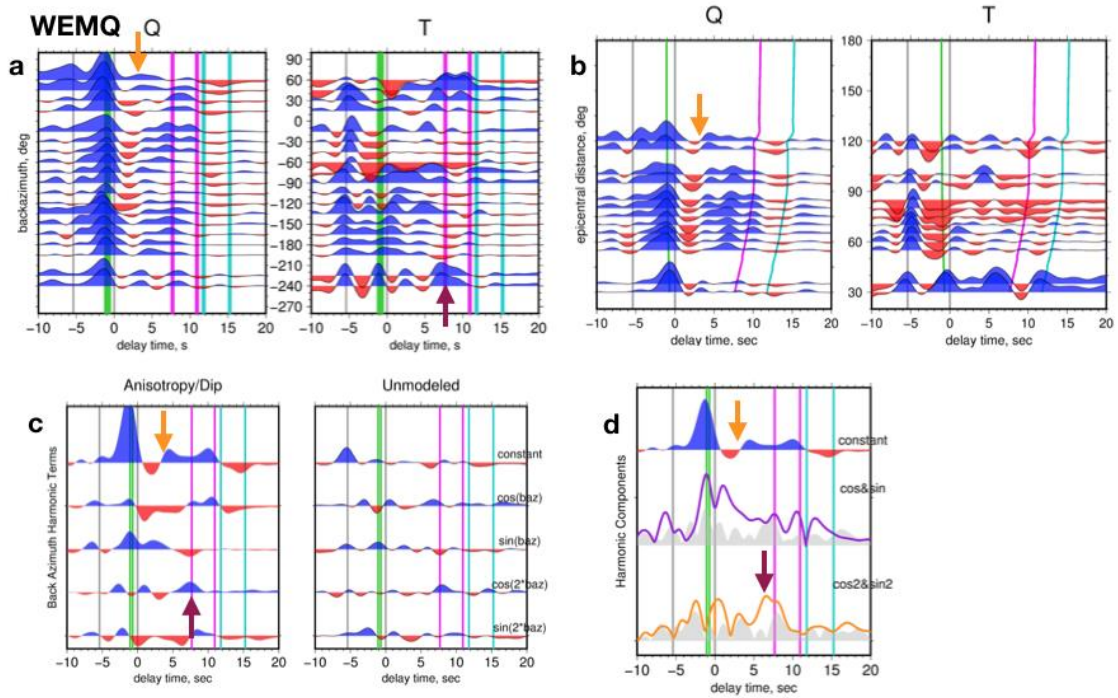


Figure 17:

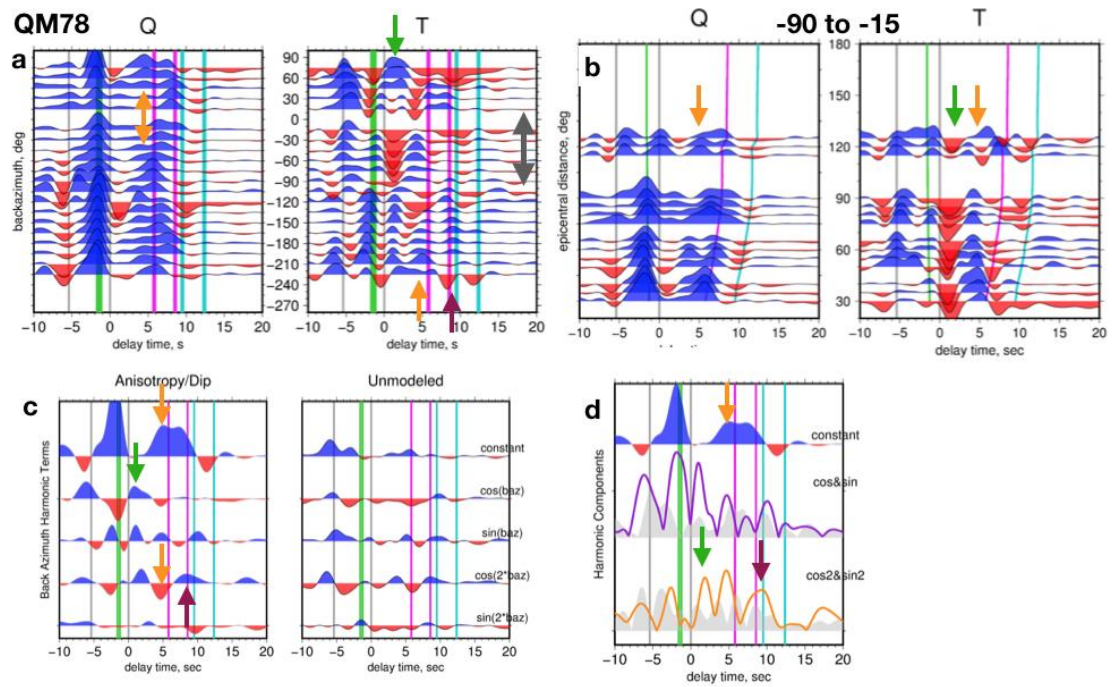


Figure 18:

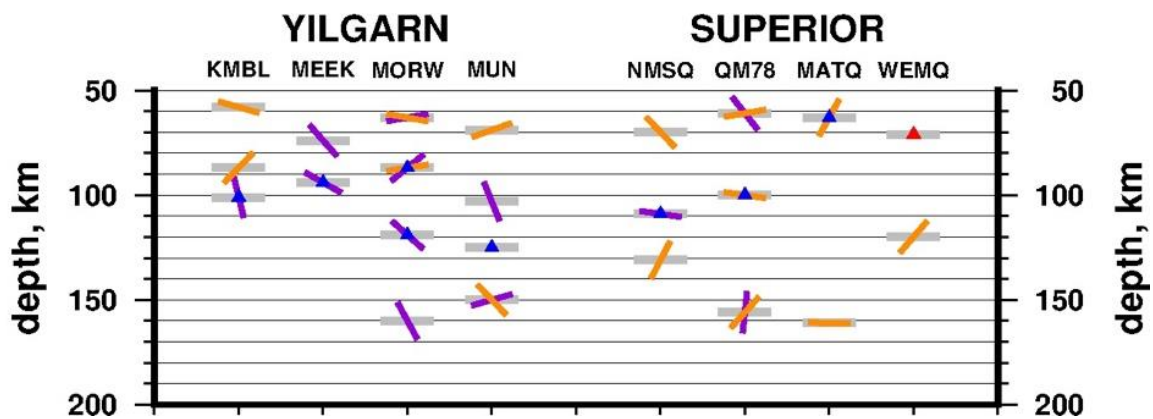


Figure 19:

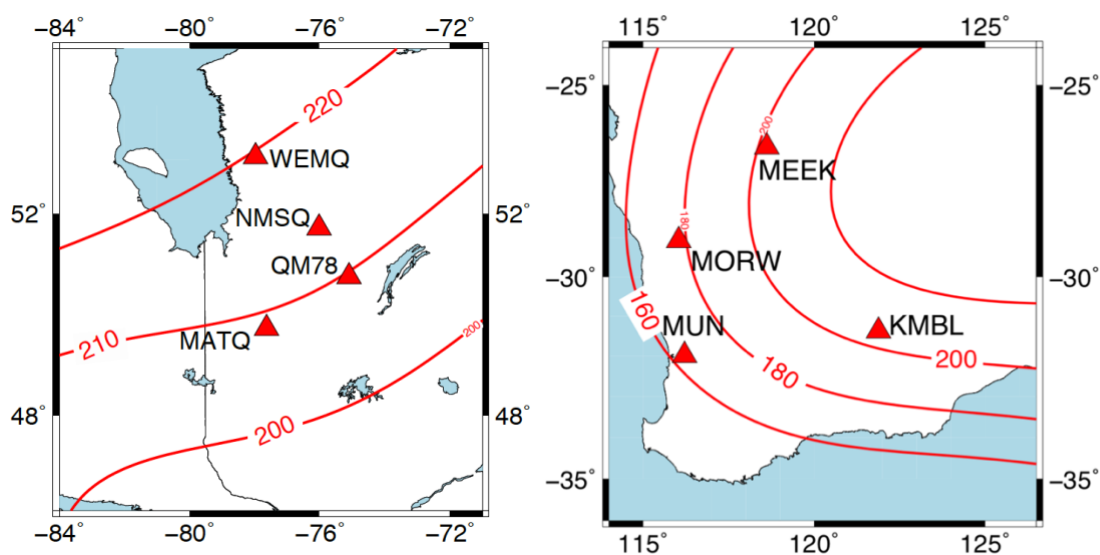


Figure 20:

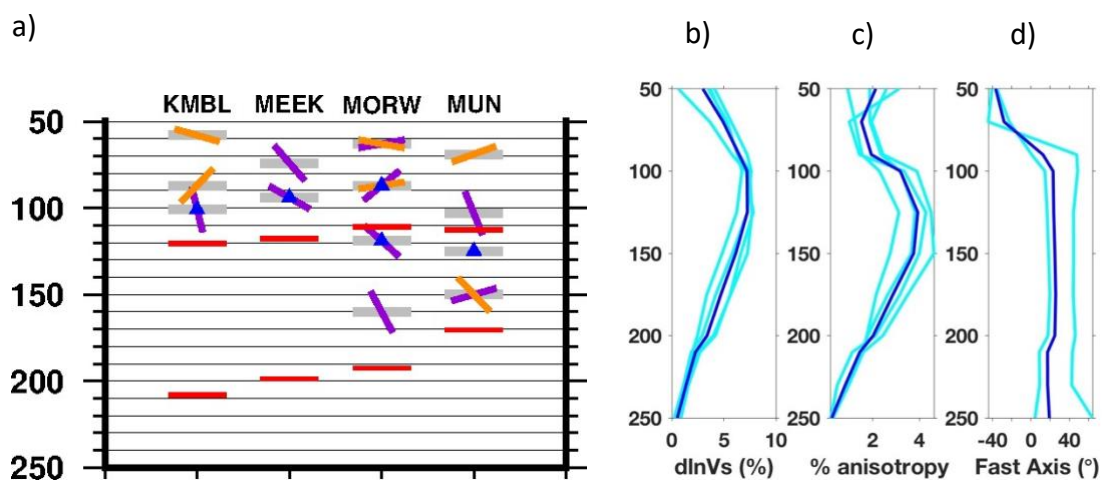
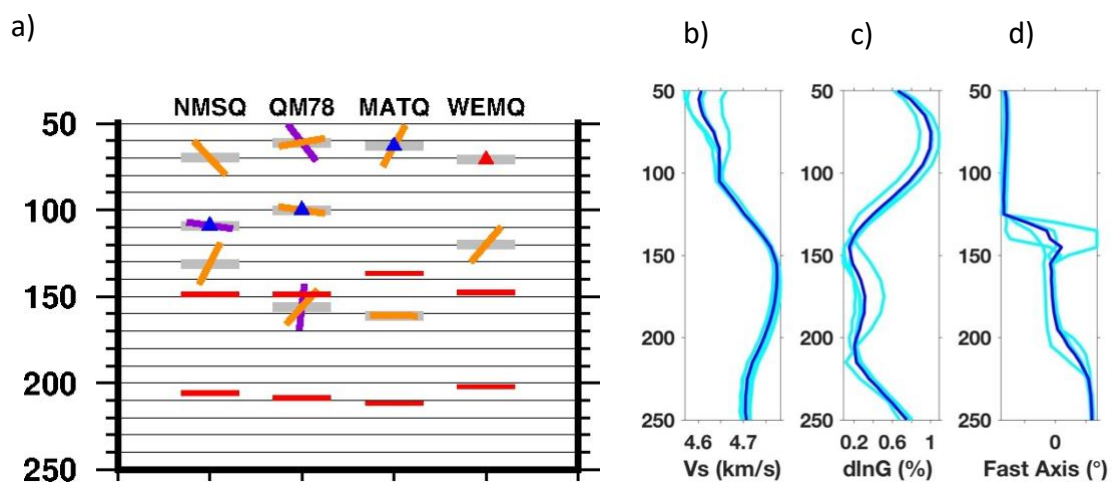
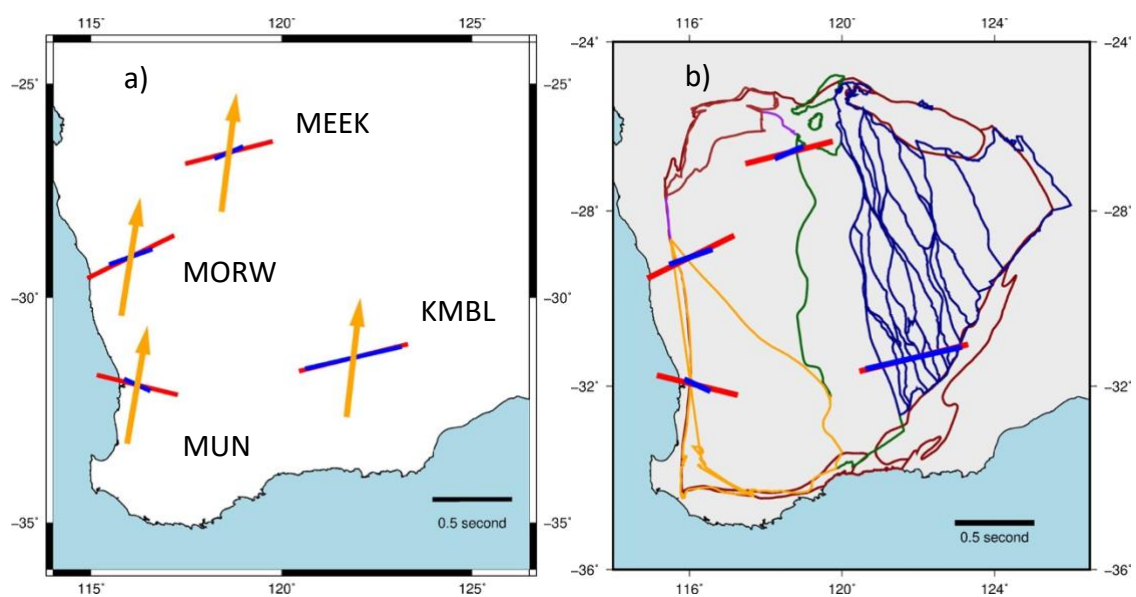


Figure 21:**Figure 22:****Figure 23:**

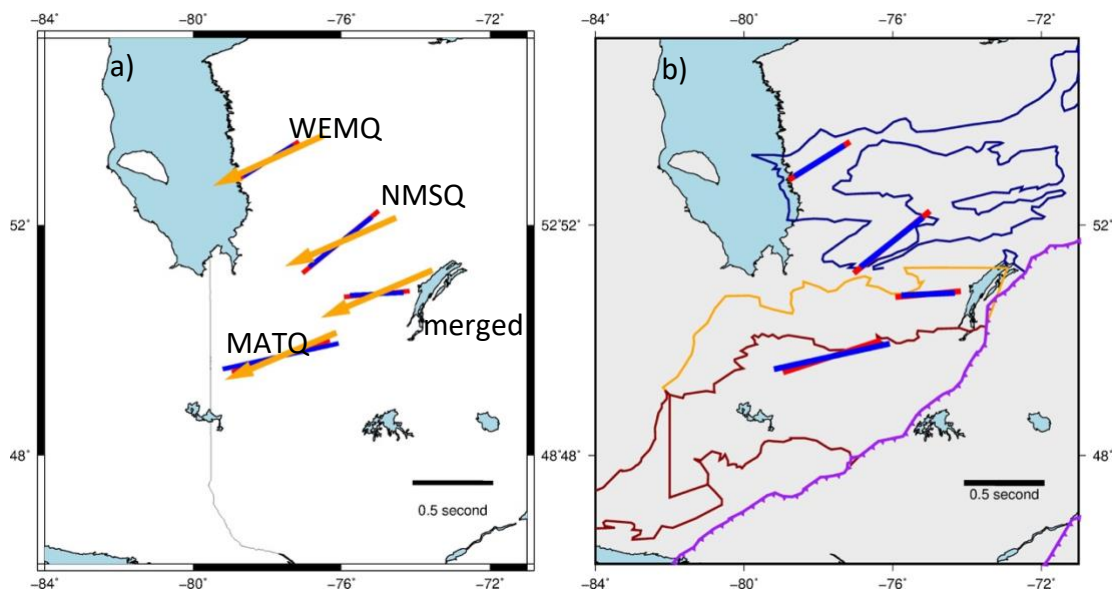


Figure 24:

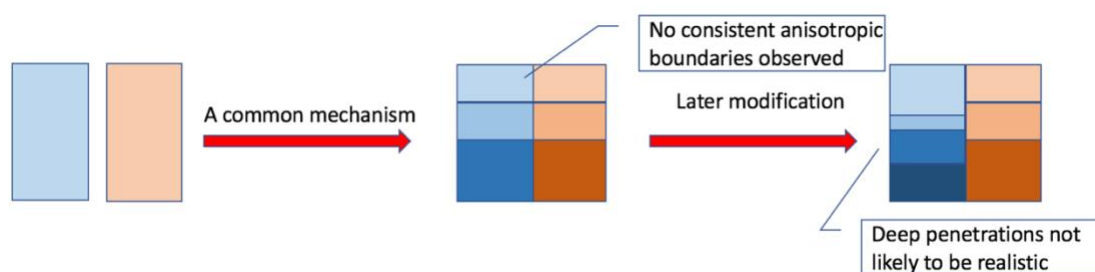
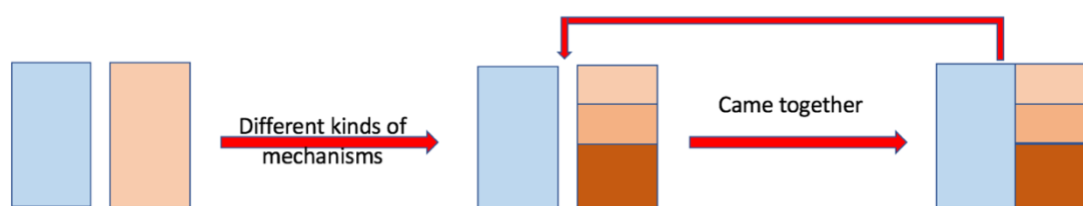
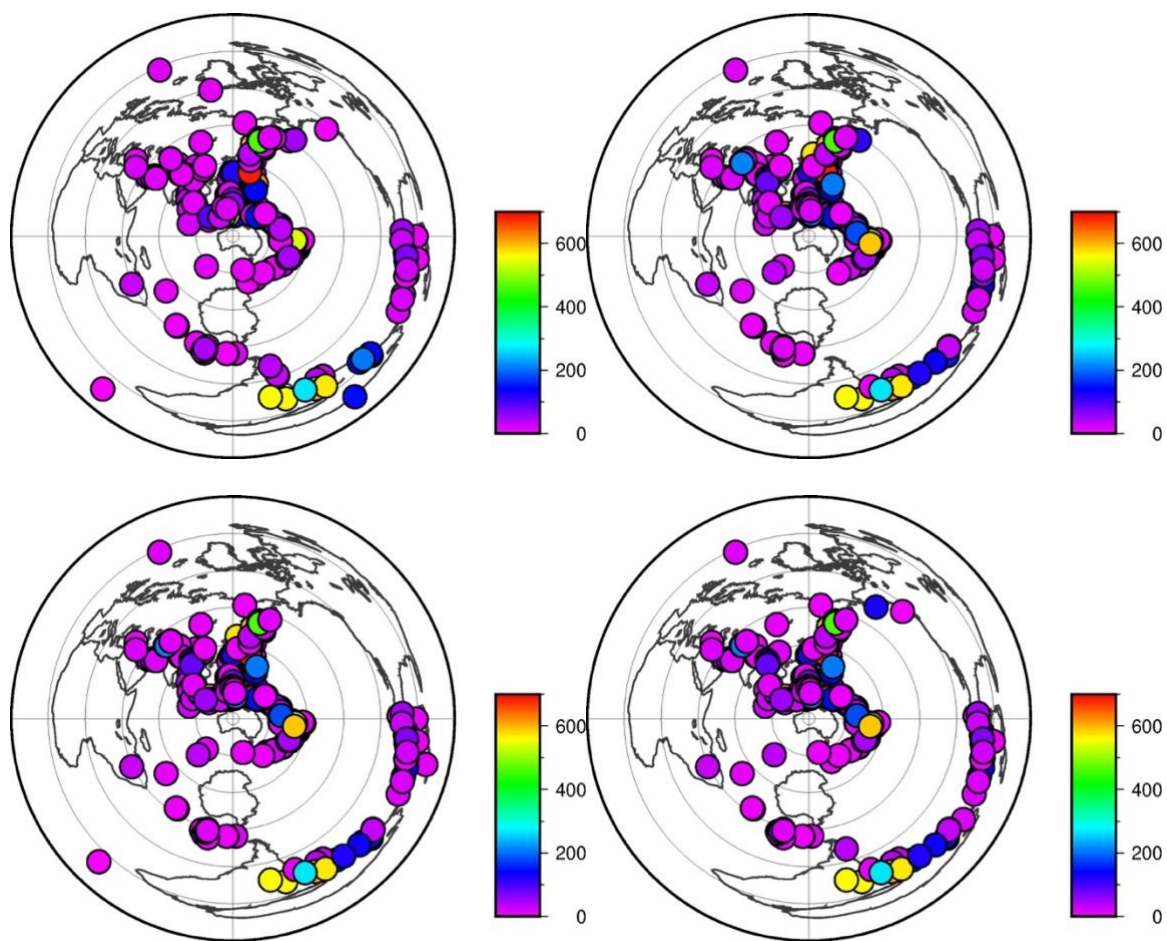


Figure 25:

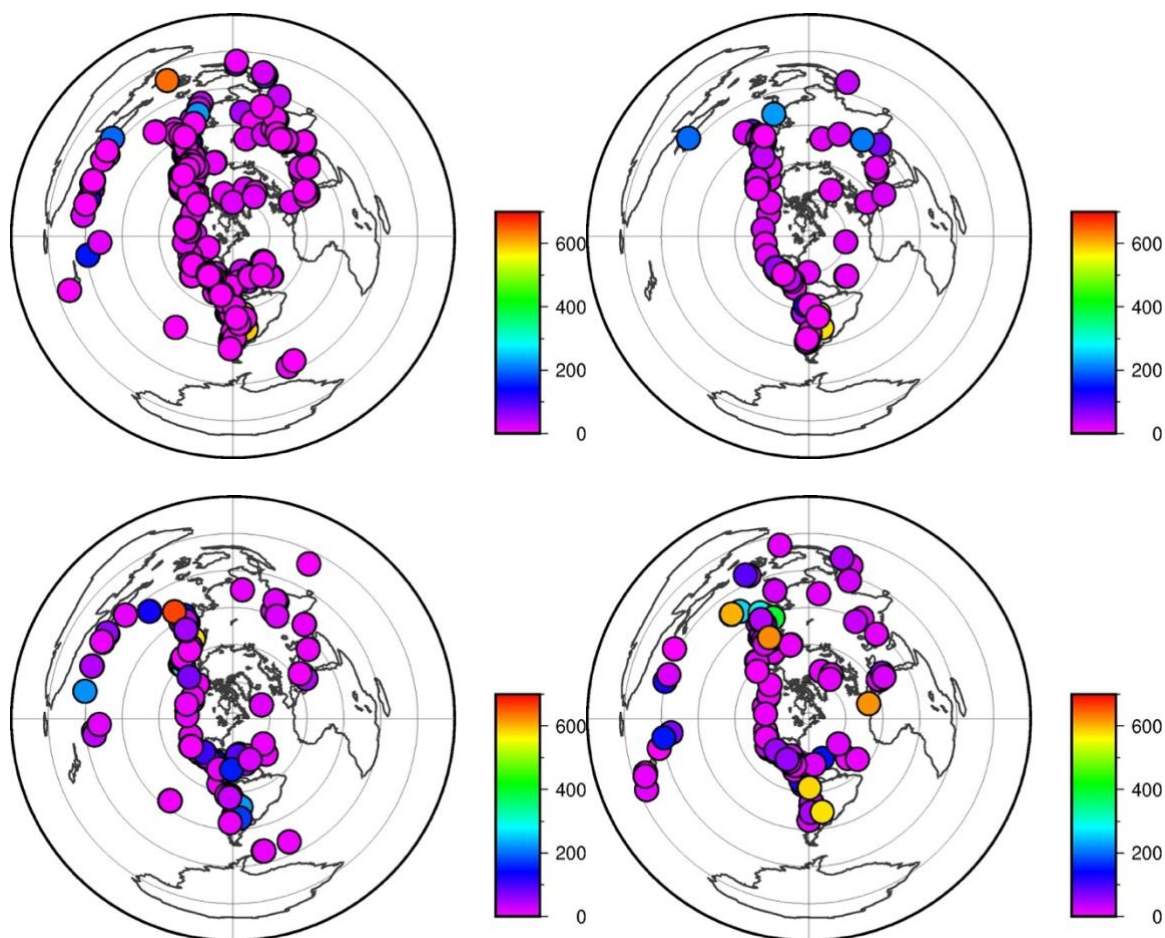


3.14 Supplementary Figures

Supplementary Figure 1:



Supplementary Figure 2:



3.15 Tables

Table 1:

AU	Best Fitting Model			Obs Averages		Weighted Fitted SI	
KMBL	75°	3%	0.75 s	76.03°	0.70 s	76.43°	0.59 s
MEEK	75°	2%	0.50 s	75.58°	0.57 s	68.37°	0.21 s
MORW	70°	2%	0.50 s	63.65°	0.61 s	71.28°	0.30 s
MUN	110°	1.5%	0.375 s	103.92°	0.52 s	113.12°	0.18 s

Table 2:

NA	Best Fitting Model			Obs Averages		Weighted Fitted SI	
MATQ	75°	3%	0.75 s	71.77°	0.64 s	77.55°	0.73 s
NMSQ	50°	2.5%	0.625 s	50.58°	0.61 s	49.80°	0.49 s
WEMQ	60°	1.5%	0.375 s	57.83°	0.45 s	58.23°	0.37 s
merged	90°	1.5%	0.375 s	84.78°	0.41 s	86.39°	0.30 s